Universidad de Granada

Programa de Doctorado en Física y Matemática

PhilosophiæDoctor (PhD) Thesis

Multi-wavelength polarimetric studies of relativistic jets in active galactic nuclei

Carolina Casadio

Instituto de Astrofísica de Andalucía (CSIC)

Director:

Dr. José Luis Gómez Fernández

co-Director:

Dr. Juan Iván Agudo Rodríguez

Granada, 2016

Abstract

This Thesis is focussed on the study of relativistic jets, commonly present in multiple astrophysical sites, from active galactic nuclei (AGN), to microquasars or gamma-ray bursts (GRBs). In the case of AGN, huge amounts of energy across the whole electromagnetic spectrum are released as a consequence of the accretion of material onto a supermassive back hole lurking at their centers. The accretion leads to the formation of a pair of very powerful and highly collimated jets extending far beyond the size of the host galaxy.

We analyzed the correlation between the multi-wavelength emission and the radio jet in three powerful AGN, the radio galaxies 3C 120 and M 87, and the quasar CTA 102. The main goal of this Thesis is to obtain a better understanding of the jet dynamics and the role played by the magnetic field, and to determine what are the sites and mechanisms for the production of the γ-ray emission observed in these sources.

We have performed multi-wavelength studies of the radio galaxy 3C 120 and the blazar CTA 102 during unprecedented γ-ray flares for both sources. The NASA satellite *Fermi* registered in September-October 2012 a bright γ-ray flare in CTA 102, and between December 2012 and October 2014 a prolonged γ-ray activity in the radio galaxy 3C 120. In both studies, to determine where the γ-ray emission is produced, the analysis of *Fermi* data has been compared with a detailed study of the morphology and evolution of the parsec scale jet through a series of extremely-high angular resolution Very Long Baseline Array (VLBA) images at 43 GHz from the Boston University blazar monitoring program, in which our research group is actively participating. In the case of 3C 120 we have also collected 15 GHz VLBA data from the MOJAVE (Monitoring of Jet in Active Galactic Nuclei with

VLBA Experiments) program, extending our study of the radio jet from June 2008 to May 2014. For the study of CTA 102 a total of 80 VLBA images at 43 GHz have been analyzed and compared with observations across the whole electromagnetic spectrum between June 2004 and June 2014. These include observations at millimeter, near-infrared, and optical bands from observatories across the world, as well as ultraviolet and X-ray data from the *Swift* satellite.

Our multi-wavelength observations of 3C 120 and CTA 102 have revealed very similar properties during γ-ray events in both sources, despite representing very different classes of AGN. We found that in both sources the γ-ray flares are associated with the passage of knew superluminal components through the millimeter VLBI core, corresponding to the bright emission at the upstream end of the jet. But not all ejections lead to γ-ray emission; in fact bright superluminal components have been observed crossing the millimeter VLBI core without having a counterpart at γ-ray energies. We have found that in both sources γ-ray flares occurred only when the new component is moving in a direction closer to our line of sight. We located the γ-ray dissipation zone a short distance downstream of the radio core but outside of the broad line region, suggesting synchrotron self-Compton scattering as the probable mechanism for the γ-ray production. In addition, during the multi-wavelength outburst observed in CTA 102 the optical polarized emission displayed intra-day variability and a clear clockwise rotation of the polarization vectors, which we associated with the path followed by the component as it moves along helical magnetic field lines. These results have been reported in two papers published in a high-impact peer-reviewed journal (Casadio et al., 2015a,b) that we present here in their original form.

The location of γ-ray activity close to the radio core and far from the black hole in both 3C 120 and CTA 102 implies that we need a mechanism to reaccelerate particles in situ; this can naturally be explained by identifying the radio core with a recollimation shock. Hence, it is important to understand the physics of recollimation shocks and their observational signatures.

For this purpose we have performed polarimetric studies of the jets in the radio galaxies 3C 120 and M 87 aimed to understand the nature of the peculiar emitting regions known as C80 and HST-1, located hundreds of parsecs from the core of the jet. In Agudo, Gómez, Casadio, et al. (2012) we analyzed polarimetric VLBA observations at 5, 8, 12, and 15 GHz of the jet in 3C 120 revealing that the stationary component C80 corresponds to the peak emission of a larger and more extended emission structure in arc, downstream of which other moving components are observed. The agreement between our observations and numerical simulations led us to conclude that the emitting region C80 corresponds in fact to a recollimation shock located $\sim$190 pc from the core of the jet.

Interestingly, our observations of the peculiar structure HST-1 in the radio-galaxy M 87 revealed a similar structure to that observed in C80 of 3C 120; in Giroletti et al. (2012) we found that HST-1 corresponds to an extended emission structure in which new components appear to be released from the stationary upstream end of HST-1. It has been suggested that very high-energy emission has been originated in the HST-1 region. However, our new VLBA and JVLA observations of M 87 confirmed that HST-1 was in a low energy state between 2011 and 2013, ruling out its implication in the high energy flare in M 87 in March 2012, as we pointed out also in Hada et al. (2014).

In this Thesis we have found that, in both radio galaxies and blazars, the γ-ray flares, often in coincidence with outbursts at other energy bands, are related to the orientation of the jet and to the interaction between a moving and a stationary shock (the core). We observed also that these recollimation shocks are present in many AGN jets and besides the core, as predicted by numerical simulations, they can also be found along the jet as we observed in the radio galaxies M 87 and 3C 120.

Resumen

Esta Tesis está enfocada en el estudio de los jets relativistas, comúnmente presentes en numerosos escenarios astrofísicos, desde los núcleos de galaxias activas (AGN) hasta los microcuásares y las explosiones de rayos gamma (GRBs). En el caso de los AGN, observamos una gran cantidad de radiación emitida a lo largo de todo el espectro electromagnético debida a la acreción de material por parte de un agujero negro supermasivo situado en el interior de estas galaxias. La acreción de material lleva a la formación de dos jets relativistas muy brillantes y bien colimados que se extienden mucho mas allá de la extensión de la propia galaxia.

Hemos analizados la correlación entre la emisión multi-frecuencia y el jet en radio en tres AGN muy brillantes: las radio galaxias 3C 120 y M 87 y el cuásar CTA 102. El objetivo principal de esta Tesis es obtener un mejor conocimiento de la dinámica de los jets y del papel jugado por el campo magnético, así como determinar cuáles son las regiones y los mecanismos de emisión involucrados en la producción de emisión en rayos γ observadas en estas fuentes.

Hemos realizado estudios multi-frecuencia de la radio galaxia 3C 120 y del blazar CTA 102 en coincidencia con extraordinarios flares de rayos γ observados en ambas fuentes. El satélite *Fermi* de NASA ha registrado en septiembre-octubre 2012 un flare γ brillante en CTA 102 y, entre diciembre de 2012 y octubre de 2014, actividad γ prolongada en la radio galaxia 3C 120. En ambos estudios, a fin de determinar dónde se ha producido la emisión γ, el análisis de los datos de *Fermi* ha sido comparado con un estudio detallado de la morfología y evolución del jet a escala del parsec a través de una serie de imágenes interferometricas a muy alta resolución angular

obtenidas con el Very Long Baseline Array (VLBA) a 43 GHz. Estas observaciones forman parte del Boston University blazar monitoring program, en el cuál colabora nuestro grupo de investigación.

En el caso de 3C 120 hemos también recopilado datos VLBA a 15 GHz del programa MOJAVE (Monitoring of Jet in Active Galactic Nuclei with VLBA Experiments), extendiendo así el estudio del jet en radio desde junio de 2008 a mayo de 2014. Respecto al estudio de CTA 102, hemos analizado un total de 80 imágenes a 43 GHz y las hemos comparado con datos a lo largo de todo el espectro electromagnético, cubriendo el periodo de observación desde junio de 2004 hasta junio de 2014. Éstos últimos incluyen observaciones a longitudes de ondas milimetricas, del infrarrojo cercano y en la banda óptica, obtenidas con diferentes observatorios alrededor del mundo, así como datos a frecuencias ultravioleta y rayos X, obtenidos con el satélite *Swift*.

Nuestros estudios multi-frecuencia de 3C 120 y CTA 102 han revelado características muy similares en ambas fuentes durante los flares en rayos γ, de especial relevancia teniendo en cuenta que éstas fuentes representan clases muy distintas de AGN. Hemos encontrado que los flares γ en ambas fuentes están asociados con el paso de una nueva componente superlumínica a través del mm-VLBI core, correspondiente a la región mas brillante desde donde se extiende el jet. No obstante, no todas las eyecciones de componentes producen emisión en γ; de hecho hemos observado eyecciones de nuevas componentes superluminicas sin que produzcan una contrapartida en rayos γ. Hemos observado que en ambas fuentes la emisión en rayos γ se produce solamente cuando la nueva componente se mueve en una dirección cercana a nuestra linea de visión. Hemos determinado que la zona de emisión γ se produce a una pequeña distancia desde el core radio y lejos de la broad line region, y por ello sugerimos el proceso de scattering synchrotron self-Compton como el mecanismo más probable de producción de fotones γ.

Por otra parte, durante el flare multi-frequencia observado en CTA 102 la emisión óptica polarizada muestra una variabilidad en escalas de horas y también una clara rotación del vector de polarización que asociamos al

paso de la componente por la región de aceleración y colimación del jet en el que las lineas del campo magnético tienen una estructura helicoidal. Estos resultados han sido presentados en dos artículos, publicados en una revista internacional con arbitraje y de alto factor de impacto (Casadio et al., 2015a,b), que se incluyen en esta Tesis en su formato original.

La localización de la actividad γ cerca del radio core y lejos del agujero negro tanto en 3C 120 como en CTA 102 implica que necesitamos un mecanismo de aceleración de partículas in situ; esto lleva a considerar el core como un choque de recolimación. Por lo tanto, es importante entender la física de los choques de recolimación y cuáles podrían ser las evidencias observacionales relacionadas con estos choques.

A tal propósito hemos realizado estudios polarimétricos del jet en las radio galaxias 3C 120 y M 87 para estudiar la naturaleza de las regiones de emisión conocidas como C80 y HST-1 y localizadas a cientos de parsec del core del jet. En Agudo, Gómez, Casadio, et al. (2012) hemos analisados observaciones VLBA polarimétricas a 5, 8, 12 y 15 GHZ del jet de 3C 120 que han revelado que la componente estacionaria C80 en realidad corresponde al pico de emisión de una región mas alargada y extensa con forma de arco, detrás de la cuál salen otras componentes que luego viajan a lo largo del jet. La concordancia entre nuestras observaciones y las simulaciones numéricas nos lleva a concluir que la región de emisión C80 corresponde efectivamente a un choque de recolimación situado a $\sim$190 pc desde el core del jet.

Curiosamente, nuestras observaciones de la peculiar estructura HST-1 en la radio galaxia M 87 revelan una estructura similar a la que observamos en la componente C80 en 3C 120; en Giroletti et al. (2012) hemos encontrado que HST-1 corresponde a una región de emisión extensa en la que nuevas componentes parecen originarse desde el extremo estacionario de HST-1. Previos estudios han sugerido que algunos eventos de emisión a altas energías observados en M 87 tienen a HST-1 como origen. Sin embargo, nuestras nuevas observaciones con el VLBA y JVLA de M 87 confirman que, entre 2011 y 2013, HST-1 se encuentra en un estado de baja emisión que excluiría su

implicación en el flare de alta energía observado en M 87 en marzo 2012, como también puntualizamos en Hada et al. (2014).

En esta Tesis hemos visto que, tanto en radio galaxias cuanto en blazars, los flares en rayos γ, muchas veces con contrapartidas a otras frecuencia, están relacionados con la orientación del jet y con la interacción entre una onda de choque que viaja a lo largo del jet y un choque estacionario (el core). Hemos observado también que estos choques de recollimacion están presentes en muchos AGN y que probablemente, como predicen las simulaciones numéricas, además del core los podemos encontrar a lo largo del jet, como hemos visto en las radio galaxias M 87 y 3C 120.

Riassunto

La presente Tesi è incentrata sullo studio dei getti relativistici, comunemente presenti in numerosi scenari astrofisici, dai nuclei di galassie attive (AGN) fino ai microquasar e alle esplosioni di raggi gamma (GRBs). Nel caso degli AGN, osserviamo una grande quantità di radiazione emessa su tutto lo spettro elettromagnetico, dovuta all'accrescimento di materia su un buco nero supermassiccio situato al centro di queste galassie. L'accrescimento di materia porta alla formazione di una coppia di getti relativistici molto brillanti e ben collimati che si estendono ben oltre i confini della galassia stessa.

Abbiamo analizzato la correlazione tra la radiazione multi-frequenza emessa ed il getto radio in tre AGN molto brillanti: le radio galassie 3C 120 e M 87 e il quasar CTA 102. L'obiettivo principale di questa Tesi è ottenere una conoscenza più approfondita della dinamica dei getti e del ruolo del campo magnetico ivi presente, così come determinare quali sono le regioni ed i meccanismi di emissione coinvolti nella produzione di radiazione γ osservata in questi oggetti.

Abbiamo realizzato studi multi-frequenza della radio galassia 3C 120 e del blazar CTA 102 in coincidenza con flares di raggi γ, incredibilmente brillanti, osservati in entrambe le sorgenti. Il satellite *Fermi* della NASA, ha registrato in settembre-ottobre 2012 un flare γ brillante in CTA 102 e, tra dicembre 2012 e ottobre 2014, ha registrato attività γ prolungata proveniente dalla radio galassia 3C 120. In entrambi gli studi, al fine di determinare la zona di produzione dell'emissione γ, l'analisi dei dati *Fermi* è stata comparata con uno studio dettagliato della morfologia ed evoluzione del getto su scala del parsec, attraverso una serie di immagini radio ad alta risoluzione angolare, ottenute con il Very Long Baseline Array (VLBA) a 43

GHz. Tali osservazioni fanno parte del Boston University blazar monitoring program, a cui collabora il nostro gruppo di ricerca.

Nel caso della radio galassia 3C 120 abbiamo inoltre collezionato dati VLBA a 15 GHz facenti parte del programma MOJAVE (Monitoring of Jet in Active Galactic Nuclei with VLBA Experiments), estendendo in tal modo lo studio del getto radio da giugno 2008 a maggio 2014. Riguardo allo studio di CTA 102, abbiamo analizzato un totale di 80 immagini a 43 GHz e le abbiamo comparate con dati su tutto lo spettro elettromagnetico, coprendo il periodo di osservazione da giugno 2004 a giugno 2014. Questi ultimi includono osservazioni a lunghezze d'onda millimetriche, nel vicino infrarosso e in banda ottica, ottenute con telescopi collocati in diverse parti del mondo, così come dati nell'ultravioletto e in banda X ottenuti con il satellite *Swift*.

I nostri studi multi-frequenza di 3C 120 e CTA 102 hanno rivelato caratteristiche similari in entrambe le sorgenti durante i flares γ; un risultato di particolare rilevanza poiché le due sorgenti appartengo a classi di AGN molto diverse tra loro. Abbiamo trovato che i flares γ in entrambe le sorgenti sono associati al passaggio di una nuova componente superluminica attraverso il mm-VLBI core, dove quest'ultimo corrisponde alla regione più brillante dalla quale diparte il getto. Tuttavia, non si osserva emissione γ durante l'eiezione di ogni nuova componente; abbiamo infatti osservato eiezioni di componenti superluminiche che non mostrano controparte a frequenze γ. Abbiamo osservato che in entrambe le sorgenti l'emissione a energie γ si produce soltanto quando la nuova componente si muove in una direzione vicina alla nostra linea di visione. Abbiamo potuto determinare che la zona in cui viene prodotta la radiazione γ si trova ad una piccola distanza dal core radio e lontano dalla broad line region; di conseguenza, suggeriamo il processo di scattering synchrotron self-Compton come meccanismo più probabile per la produzione di fotoni γ.

Inoltre, durante il flare multi-frequenza osservato in CTA 102, l'emissione ottica polarizzata mostra una variabilità in tempi scala dell'ora ed anche una chiara rotazione di vettori di polarizzazione che associamo al passaggio della componente attraverso la regione di accelerazione e collimazione del

getto in cui le linee del campo magnetico hanno una struttura elicoidale. Tali risultati sono stati presentati in due articoli pubblicati in una rivista internazionale con referaggio e con un alto fattore d'impatto (Casadio et al., 2015a,b). Tali articoli sono inclusi in questa Tesi nel loro formato originale.

La localizzazione della attività γ vicino al core radio e lontano dal buco nero, tanto in 3C 120 quanto in CTA 102, richiede un meccanismo di accelerazione di particelle in situ; questo porta a considerare il core come un'onda d'urto di ricollimazione. Per tanto è importante comprendere la fisica delle onde d'urto di ricollimazione e quali potrebbero essere le evidenze osservative relazionate con esse.

A tale proposito abbiamo realizzato studi polarimetrici dei getti delle radio galassie 3C 120 e M 87 al fine di investigare la natura delle regioni di emissione conosciute come C80 e HST-1 localizzate a centinaia di parsec dal core del getto. In Agudo, Gómez, Casadio, et al. (2012) abbiamo analizzato osservazioni polarimetriche con il VLBA a 5, 8, 12 e 15 GHz del getto di 3C 120 che hanno rivelato che la componente stazionaria C80 in realtà corrisponde al picco di emissione di una regione più estesa con forma ad arco, dietro la quale dipartono altre componenti che osserviamo viaggiare lungo il getto. La concordanza tra le nostre osservazioni e le simulazioni numeriche ci porta a concludere che la regione di emissione C80 corrisponde effettivamente ad un'onda d'urto di ricollimazione situato a $\sim$190 pc dal core del getto.

Curiosamente, le nostre osservazioni della peculiare struttura HST-1 nella radio galassia M 87 rivelano una struttura simile a quella osservata nella componente C80 in 3C 120; in Giroletti et al. (2012) abbiamo trovato che HST-1 corrisponde ad una regione di emissione estesa in cui nuove componenti sembrano aver origine dall'estremo stazionario di HST-1. Studi precedenti hanno suggerito che alcuni eventi di emissione alle alte energie osservati in M 87 hanno origine in HST-1. Ciò nonostante, le nostre nuove osservazioni di M 87 con il VLBA ed il JVLA confermano che, tra il 2011 e il 2013, HST-1 si trova in uno stato di debole emissione che escluderebbe la

sua implicazione nel flare ad alta energia osservato in M 87 nel marzo 2012, come già puntualizziamo in Hada et al. (2014).

In questa Tesi abbiamo visto che, tanto nelle radio galassie quanto nei blazars, i flares a energie γ, spesso accompagnati anche da flares in altre bande di energia, sono relazionati con l'orientazione del getto e con l'interazione tra un'onda d'urto che viaggia lungo il getto ed una stazionaria (il it core). Abbiamo osservato anche come queste onde d'urto di ricollimazione siano presenti in molti AGN e probabilmente, come predetto dalle simulazioni numeriche, oltre al core possiamo incontrarli anche lungo il getto, come abbiamo visto nelle radio galassie M 87 e 3C 120.

A mia madre

Il mondo è nelle mani di coloro che hanno il coraggio di sognare e di correre il rischio di vivere i propri sogni. Ciascuno con il proprio talento.

(Paulo Cohelo)

Guardate le stelle e non i vostri piedi. Provate a dare un senso a ciò che vedete, e chiedervi perché l'universo esiste. Siate curiosi.

(Stephen Hawking)

Nella nostra galassia ci sono quattrocento miliardi di stelle, e nell'universo ci sono più di cento miliardi di galassie. Pensare di essere unici è molto improbabile.

(Margherita Hack)

Ringraziamenti

vita ci ha concesso di camminare di nuovo insieme. Ringrazio Granada, perchè mi ha accolta e affascinata ogni giorno di più.

Mi sposto invece in Italia per ringraziare chi da sempre è al mio fianco e con amore incondizionato mi sostiene e mi da forza. Un grazie infinito a mia madre, a mio fratello e ai miei nonni. Grazie a mio padre per avermi trasmesso questa grande sete di conoscenza, per avermi iniziato a tante letture e per insegnarmi a vivere la vita con ebrezza e stupore. Grazie anche ai miei zii, Luca e Laura, per aver sempre creduto in me. Infine grazie a chi, pur essendo entrato in un secondo momento nella mia vita, mi ha incitata e ha gioito per me e per i miei traguardi; grazie a Denni, Mary e i bimbi.

Contents

List of Figures

LIST OF FIGURES

1
Introduction

1.1 Active Galaxies

Black holes (BH) are among the most intriguing objects in astrophysics. They are expected to exist in different sizes: from stellar-mass black holes, the final product of a massive star explosion (supernovae), to supermassive black holes (SMBH), when they have a mass between 10^6 and 10^9 solar masses. SMBH are found in the center of most galaxies, including our own Galaxy, but not all of them show signs of activity. Those galaxies hosting a SMBH and showing nuclear activity (see below) are called active galaxies and they are referred to with the acronym AGN (active galactic nuclei). The two most relevant subclasses of AGN are Seyfert galaxies and quasars. The main difference between these two subclasses is that in Seyfert galaxies the amount of radiation emitted by nuclear regions at visible wavelengths is comparable to the energy emitted by all stars in the galaxy ($\sim 10^{11} M_\odot$), while in quasars it is even larger by a factor of 100 or more. The luminosity coming from these bright nuclei cannot be explained by conventional nuclear fusion like that powering stars.
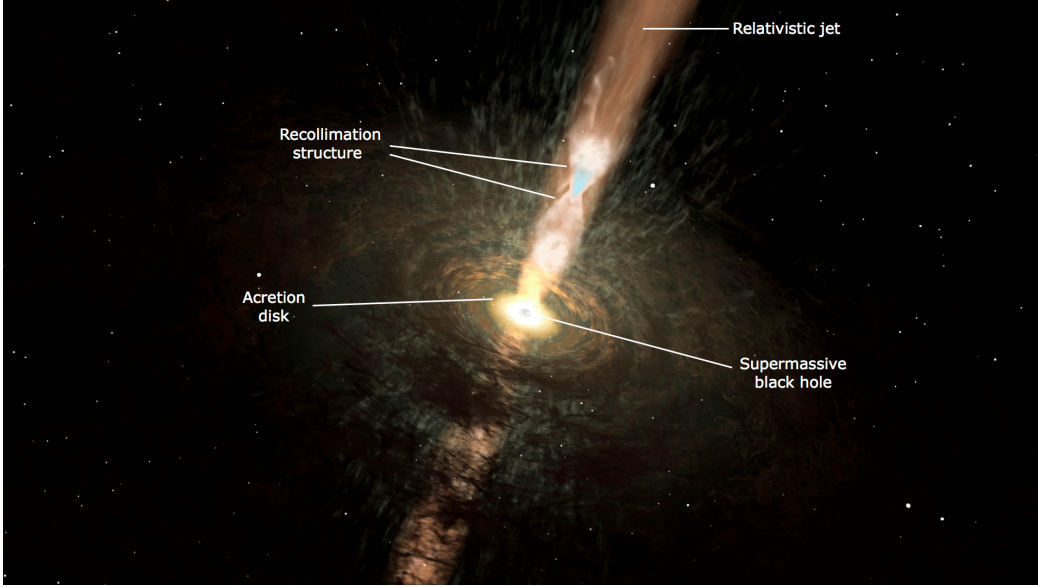
Figure 1.1: Artistic representation of the inner regions of an AGN. Credits: W. Steffen, UNAM & Cosmovision.

The current understanding of AGN is that their emission is produced by the accretion of material onto the central SMBH. Material surrounding the black hole forms a rotating disk that gets heated through the viscous dissipation of gravitational energy and then radiates thermal emission mainly at UV and X-ray energies. In the case of *radio loud* AGN the accretion process also leads to the formation of well collimated jets of plasma propagating in a direction perpendicular to the accretion disk (see Figure 1.1). In the radio-loud AGN case, the radiative power of the jets is a significant fraction of the total bolometric luminosity of these AGN. The jets are launched from a rotating black hole or accretion disk and transport material at relativistic speeds up to distances that can have extensions far beyond the size of the host galaxy (Blandford & Znajek, 1977; Blandford & Payne, 1982). Jets observed in *radio quiet* AGN instead are usually not so powerful and bright.

A useful criterion to distinguish between *radio loud* and *radio quiet* AGN is the ratio (R_{r-o}) of radio (at 6 cm) to optical (at 4400 Å) specific fluxes, being R_{r-o} in the range 10-100 for radio loud objects and $0.1 < R_{r-o} < 1$ for radio quiet ones (Kellermann et al., 1989). This formulation of the criterion leaves some doubts for the range of values 1-10, hence currently $R_{r-o} > 10$ is considered a more reasonable criterion for "radio-

loudness". Seyfert galaxies and radio quiet quasars belong to the *radio quiet* group, while radiogalaxies and blazars are part of the group of *radio loud* AGN. The properties of each of this class of objects are as follows:

- **Seyfert galaxies:** are spiral galaxies with luminous nuclei usually displaying slow, weak and poorly collimated flows. They are divided into two subclasses, type 1 Seyfert galaxies (Sy I) if they show broad (up to 10^4 km s^{-1}) and narrow (several 10^2 km s^{-1}) emission lines in their spectra, or type 2 Seyfert galaxies (Sy II) if they only show narrow emission lines;

- **Quasars:** are the most luminous subclass of AGN and therefore the objects that can be found at the farthest distances in the universe (the most distant quasar is at redshift 7.1). A quasar, for definition, has an optical magnitude M_B<-21.5 + 5*logh$_{100}$ where h$_{100}$=H$_0$/100 [km/s/Mpc] is the Hubble-Lemaître constant, and it appears like a point source, being the host galaxy non-detectable. Narrow lines in their spectra are generally absent or weaker than broad lines;

- **Radiogalaxies:** are typically identified with giant elliptical galaxies, which are very bright at radio wavelengths. Depending on their radio power, radio galaxies are divided into two subclasses, FRI and FRII radio galaxies (Fanaroff & Riley, 1974), where FR I show low 1.4 GHz radio power (P$_{1.4\ GHz}$ < $10^{24.5}$ Watt/Hz) and FR II large radio power (P$_{1.4\ GHz}$ > $10^{24.5}$ Watt/Hz). There are also differences in morphology between these two subclasses: FR II have powerful and well collimated jets that end in bright hot spots surrounded by luminous radio lobes, resulting from the interaction with the ambient medium (see Figure 1.2), while jets in FR I have usually poor collimation and they do not display bright radio lobes at the end (see Figure 1.3). The collimation in FR II jets indicates an efficient transport mechanism of relativistic particles, whereas the dispersion and the darkened edge in FR I jets indicates less energetic relativistic particles that interact more efficiently with the surrounding medium and therefore cool more rapidly. Another classification distinguishes instead between galaxies displaying high-excitation narrow-line optical emission (HEG), to which FRII belong, and low-excitation narrow-line emission (LEG) having also a low accretion rate and

3

probably without a molecular torus (Van der Wolk et al., 2010); mainly FRI and some FRII radio galaxy belong to this last class.
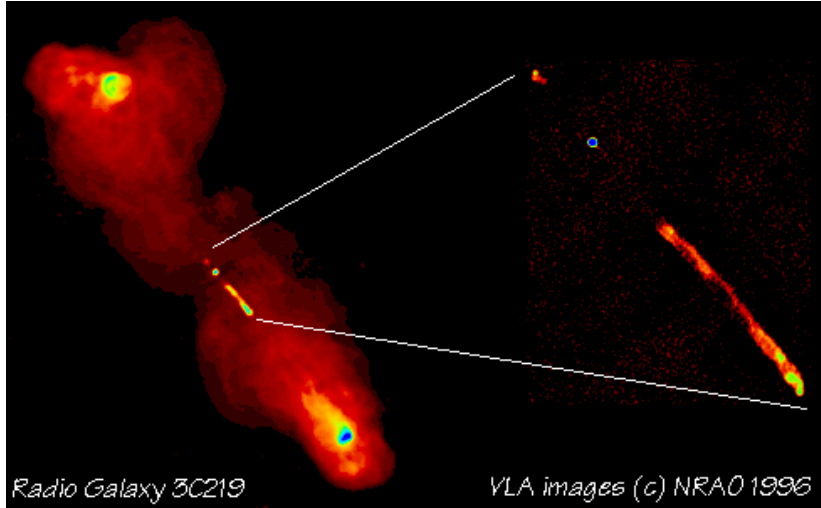
Figure 1.2: FRII radio galaxy. Radio images of the FR II radio galaxy 3C219. *Left:* VLA 1.4 + 1.6 GHz radio images superimposed. *Right:* VLA 8 GHz radio image. Credit: NRAO.

- **Blazars:** are bright, compact, and highly variable AGN. They often display polarized emission at optical and radio frequencies. Variations in total and polarized flux range from less than a day to several months. Blazars get their name from the contraction of names of the two types of sources in which they are subdivided: BL Lacertae objects (BL Lacs) and Flat Spectrum Radio Quasars (FSRQ). BL Lacs are less luminous than FSRQ and they have weak or no lines in their optical spectra, while FSRQ show strong broad emission lines. They differ also in redshifts: BL Lacs objects tend to be located at smaller redshifts ($z \lesssim 0.1$) than FSRQs ($z \gtrsim 0.5$), although this bias most probably depend on our ability to detect further away objects when these are intrinsically more luminous.

Since the discovery of the first quasars it was clear that the identification and classification of a so wide variety of objects was quite complex. Kellermann (2013) provides some interesting historical details about the physics of quasars, highlighting how the different properties of these objects made their classification very confusing.
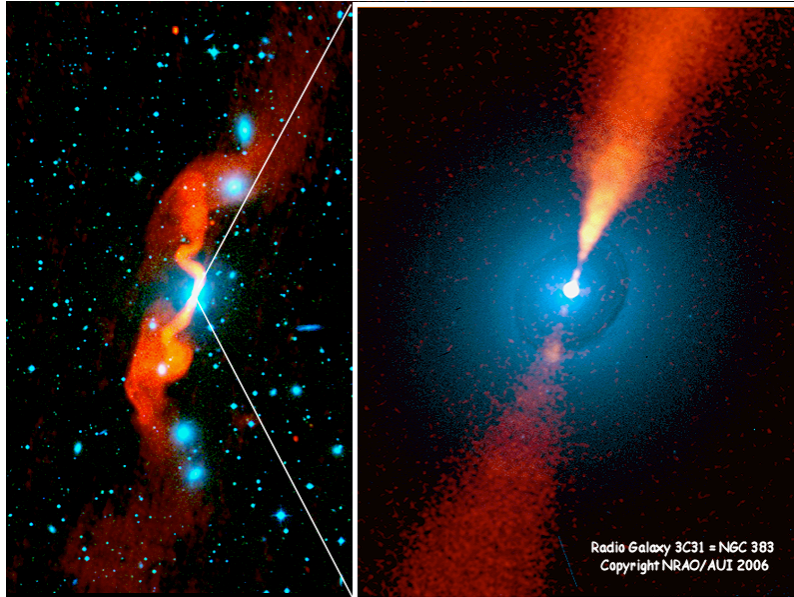
Figure 1.3: FRI radio galaxy. Superposition of an optical (blue) and radio (red) image of the FR I radio galaxy 3C31. The radio images have been taken with the VLA at a wavelength of 1.4 GHz (*left*) and 8.3 GHz (*right*). Credit: NRAO.

In an attempt to find a correspondence between 'blue stellar objects' (BSOs) and the known radio sources, Alan Sandage (1926-2010) noticed that many BSOs had no radio source associated. He also estimated that those BSOs without a counterpart among known radio sources, that he called 'quasi-stellar galaxies' (QSGs), were about 10^3 times more compact than radio sources in the 3C catalog. He reported these findings in a paper sent to *The Astrophysical Journal* (ApJ) on 15 May of 1965. The editor of the journal was so impressed that he delayed the other publications and he published the article in the 15 May issue, without sending it to a referee. This obviously caused some controversy within the astronomical community. Fritz Zwicky (1898 - 1974) in a letter to the editor (Zwicky, 1965) pointed out that:

> "All of the five quasi-stellar galaxies described individually by Sandage (1965) evidently belong to the subclass of compact galaxies with pure emission spectra previously discovered and described by the present writer."

In fact, Zwicky during the April 1963 meeting of the *American Astronomical Society* (AAS) reported that:
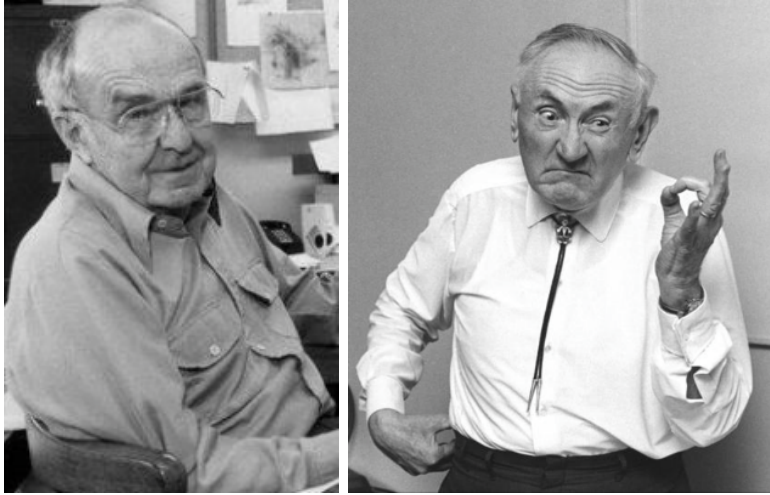
Figure 1.4: *Left:* Alan Sandage (courtesy: Carnegie Observatories) *Right:* Fritz Zwicky (courtesy: Caltech Archives)

> "*Very compact galaxies* have been found.... The objects found form a con-
> tinuos sequence of what appear to be detached red nuclei of galaxies, iso-
> lated in intergalactic space, to exceedingly compact blue objects, which
> show emission lines. Radio stars are thought as lying at the luminous end
> of this sequence" (Zwicky, 1963).

Unlike Sandage's paper, Zwicky's paper on the same subject was rejected by Sub-
rahmanyan Chandrasekhar (1910-1995), the then editor of ApJ, who replied that :
"Communications of this character are outside the scope of this journal."

Afterwards, T. Kinman working at Lick observatory and R. Lynds and C. Villere
working at the Kitt Peak national observatory, suggested that most of the BSO objects
discovered by Sandage were inside our Galaxy, not compact external galaxies. Nowa-
days we know that, apart from radio loud quasars, there is also a radio quiet class of
quasars.

The term 'quasar' was formally accepted by ApJ in 1970, when Maarten Schmidt,
who was the first to observe a quasar (3C 273), wrote in his paper (Schmidt, 1970):

> "We use the term "quasar" for the class of objects of starlike appear-
> ance (or those containing a dominant starlike component) that exhibit
> redshifts much larger than those of ordinary stars in the Galaxy. QSOs
> are quasars selected on the basis of purely optical criteria..."

Since then, the term 'quasar' also started to populate scientific literature and subsequently many subclasses have been defined depending on observational properties, such as, for example, Low-Ionization Nuclear Emission Line Region (LINERS), Broad Absorption Line Quasars (BALQs) based on their optical spectra, or Flat Spectrum Radio Quasars (FSRQs) and Steep Spectrum Radio Quasars (SSRQs) based on their radio spectra and morphology.

1.2   The Unified Model

The previous classification depends mainly on the viewing angle of these objects. The radio emission coming from extended regions, such as that from giant radio lobes, dominates at lower frequencies, thus being responsible for the steep spectrum when we see the extended part of the AGN. The observation of extended regions in AGN at radio wavelength also depends on the viewing angle, as these regions only dominate the total radio emission when the jet is oriented at a large viewing angle. If instead, the jet points almost toward us, as the emission from the jet is beamed and particles move at relativistic speeds, such emission is subject to relativistic effects that have a boosting effect (i.e. the Doppler boosting effect, see § 2.2 for more details). In this case the emission from the jet, whose contribution is greater at higher radio frequencies, dominates over the extended regions and therefore the spectrum is flatter. Hence, the slope of the radio spectrum is a first indication of the viewing angle.

Many other observational properties in AGN seem to depend on the viewing angle, and therefore the viewing angle is the main geometrical factor on which the "unified model" of AGNs, elaborated by Robert Antonucci, Claudia Megan Urry and Paolo Padovani in the 90's (e.g., Antonucci, 1993; Urry & Padovani, 1995), is based. This model unifies all the different types of AGN into a standard model in which the only physical parameter that vary among them is the intrinsic power, while the other observational differences are explained in terms of obscuration and beaming that vary depending on the angle from where the observer sees the source. Figure 1.5 shows a schematic view of this model.

7
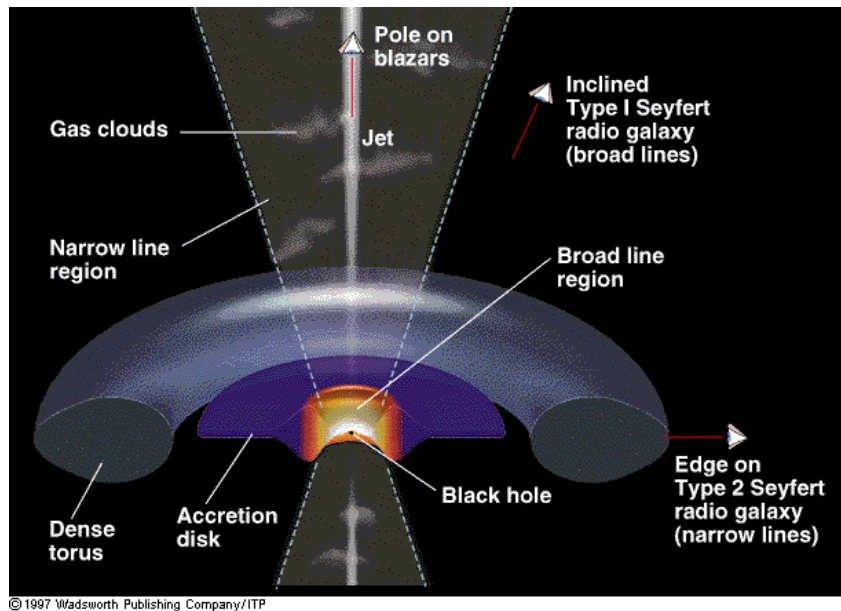
Figure 1.5: AGN model. Artistic representation of the unified AGN model developed by Antonucci R., Urry C. M., and Padovani P. Credit: Wadsworth Publishing Company/ITP
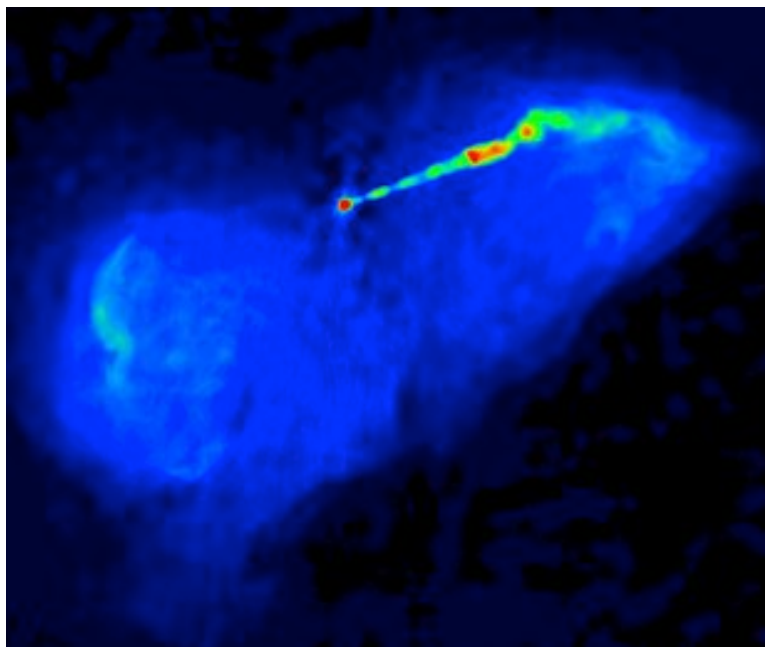
Figure 1.6: M 87. Very Long Array image at 1.4 GHz of the radio galaxy M 87. The field of view in the image is of 5 Kpc. Credit: NRAO.

The AGN feature responsible for obscuration in the system is a molecular torus located at several parsecs from the black hole which partially absorbs the UV radiation from the accretion disk and re-emits it in the infrared. Depending on the viewing angle at which the AGN is observed, the torus could hide some internal zones, such as a region of small clouds located at a distance of $\sim 10^{15}$–10^{18} cm (less than a parsec) from the black hole moving at high speeds (1000-10,000 km s^{-1}), and usually called the Broad Line Region (BLR). These clouds are in fact responsible for the broad emission lines directly observed in AGNs when they are seen almost face-on, or in polarized emission in those AGNs observed almost edge-on, as in this case the torus obscured the BLR. At a greater distance (~ 100 pc) there is another region where slower moving clouds produce narrower emission lines (300-500 km s^{-1}). According to the unified model, Type 1 objects are observed at smaller viewing angles with regard to the direction of the jet and therefore the BLR is easily observed, while Type 2 objects are observed at larger viewing angles and we only have a direct view of the Narrow Line Region (NLR), being the BLR obscured by the molecular torus.

Another phenomena, referred to as relativistic beaming (that is intimately related to the relativistic Doppler boosting), can change the observational properties of AGN jets depending on their viewing angle. This produces an enhancement of the luminosity of the jet that points toward us and a corresponding dimming (de-boosting) of the emission from the jet pointing in the opposite direction, which could be even non-detectable if the viewing angle is sufficiently small, as in the case of blazars, or as we observe in the radio galaxy M 87 (e.g. Figure 1.6). This and other relevant relativistic effects to take into account for the interpretation of the physics of jets in AGN will be discussed in Chapter 2.2.

AGN research also allows us to probe the extreme physics near black holes, to understand the jet formation mechanism, and the production of high energy emission. This makes the study of AGN jets an excellent tool for understanding fundamental physics.

2

The physics of AGN jets

2.1 Emission processes

The non-thermal continuum emission observed in relativistic AGN jets is produced by synchrotron and inverse Compton processes. In this chapter we provide an overview of these two radiative processes and we discuss other aspects related to the physics of AGN jets that are necessary to understand the work contained in this Thesis. A more detailed description of the synchrotron and inverse Compton radiation processes can be found in Pacholczyk (1970), Rybicki & Lightman (1979) and Ghisellini (2013).

2.1.1 Synchrotron emission

According to classical electromagnetism, the power emitted by a charged particle (q) subjected to acceleration (a), is obtained from the Larmor formula:

$$P(t) = -\frac{dE}{dt} = \frac{2}{3}\frac{q^2}{c^3}a^2(t) = \frac{2}{3}\frac{q^2}{m^2c^3}\left(\frac{d\vec{p}}{dt}\right)^2 \tag{2.1}$$

where $\vec{p} = m\vec{v}$ is the particle momentum. We note that the emitted power depends

inversely on the square of the particle mass. This means that an electron or positron radiates $\sim 3 \times 10^6$ times more than a proton. For this reason we focus our attention on electrons, indicating with m_e and e the mass at rest and the charge, respectively.

If the particle is relativistic ($v \approx c$) then the Lorentz factor $\gamma = 1/\sqrt{1-(v/c)^2}$ is significantly larger than one and we need to consider the Lorentz transformations that relate quantities between two different reference frames. We know, however, that the emitted power is Lorentz invariant, hence we can simply write:

$$P = P' = \frac{2}{3}\frac{e^2}{c^3}a'^2 = \frac{2}{3}\frac{e^2}{c^3}\left(a_\parallel'^{\,2} + a_\perp'^{\,2}\right) \tag{2.2}$$

where primed quantities refer to the rest frame of the particle and non-primed ones to the observer's reference frame. In equation 2.2 we have decomposed the acceleration in two terms, parallel and perpendicular to the direction of motion. These are Lorentz transformed as (e.g. Rybicki & Lightman, 1979):

$$a_\parallel' = \gamma^3 a_\parallel \tag{2.3}$$

$$a_\perp' = \gamma^2 a_\perp \tag{2.4}$$

Hence, we can write:

$$P = P' = \frac{2}{3}\frac{e^2}{c^3}\left(a_\parallel'^{\,2} + a_\perp'^{\,2}\right) = \frac{2}{3}\frac{e^2}{c^3}\gamma^4\left(\gamma^2 a_\parallel^2 + a_\perp^2\right) \tag{2.5}$$

For an electron moving in a magnetic field ($\vec{B}$) the only acting force is the Lorentz force:

$$F_L = \frac{d}{dt}(\gamma m_e \vec{v}) = \frac{e}{c}\vec{v} \times \vec{B} = \frac{e}{c}vB\sin\phi \tag{2.6}$$

where ϕ is the *pitch angle*, that is, the angle between the velocity vector and the magnetic field. It follows from the vectorial product that the only acting force is perpendicular to the magnetic field lines. Then the acceleration related to this force is also

perpendicular to the magnetic field and is:

$$a_\perp = \frac{evB\sin\phi}{\gamma m_e c} \tag{2.7}$$

Substituting $a_\perp$ in the generalized Larmor formula (eq. 2.5) and considering $v \approx c$, we obtain the power emitted by an electron subject to the Lorentz force:

$$P_s(\phi) = \frac{2e^4}{3m_e^2 c^3} B^2 \gamma^2 \beta^2 \sin^2\phi \tag{2.8}$$

where the subscript "s" indicates the synchrotron emission process and β is equal to v/c. This can be expressed in terms of the total electron energy ($E = \gamma \mathrm{m}_e \mathrm{c}^2$) as:

$$P_s(\phi) = \frac{2}{3}\frac{e^4}{m_e^2 c^3}\left(\frac{E}{m_e c^2}\right)^2 B^2 \sin^2\phi \tag{2.9}$$

where we can note that the power emitted is proportional to the square of the electron energy and the magnetic field. We can also write equation 2.9 introducing the Thomson scattering cross section, which is given by:

$$\sigma_T = \frac{8\pi}{3}\left(\frac{e^2}{m_e c^2}\right)^2 = 6.65 \times 10^{-25}\mathrm{cm}^2 \tag{2.10}$$

and obtaining for the emitted power by a single relativistic electron the following equation:

$$P_s(\phi) = 2c\sigma_T \gamma^2 \beta^2 \frac{B^2 \sin^2\phi}{8\pi} \tag{2.11}$$

When we deal with an ensemble of mono-energetic particles we can assume an isotropic distribution of pitch angles and average the term $\sin^2\phi$ over the solid angle, hence resulting 2/3. Therefore, in the case of an ensemble of electrons we simply replace $B^2 \sin^2\phi$ with $\frac{2}{3}B^2$. Also knowing that $U_B \equiv B^2/8\pi$ is the magnetic energy density, we can write the power emitted by an ensemble of electrons, as follows:

$$P_s = \frac{4}{3}c\sigma_T U_B \gamma^2 \beta^2 \tag{2.12}$$

For a non-relativistic particle, the pattern of the emitted power over the solid angle has the characteristics of a dipole, as plotted in Figure 2.1. In the relativistic case, we have a dipole radiation pattern only in the reference frame of the electron, where the electron itself is at rest.

a) Rest frame   **a) Observer frame**
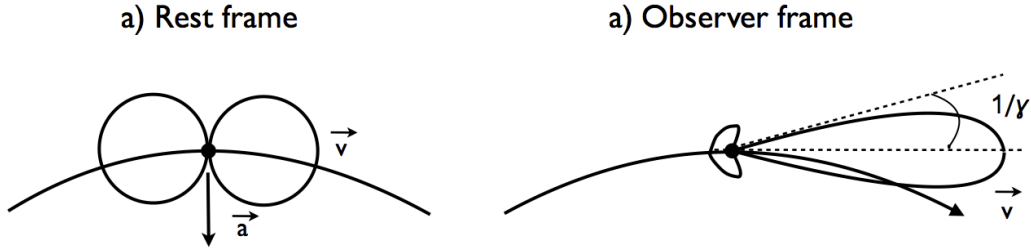
Figure 2.1: Angular distribution of the synchrotron radiation. Diagram showing a) the dipole radiation pattern from a non-relativistic accelerated particle (i.e., in the particle rest frame in the relativistic case), b) the dipole radiation pattern from a relativistic particle as seen by an external observer.

To obtain the angular distribution of radiation in the reference frame of the observer we need to transform the angles between the two reference frames through the relativistic formula of the aberration of light. We indicate with α and α' the angles in the observer and the electron reference frame, respectively, measured with respect to the velocity direction. These are related by (e.g. Ghisellini, 2013):

$$\sin \alpha = \frac{\sin \alpha'}{\Gamma(1 + \beta \cos \alpha')}$$

$$\cos \alpha = \frac{\cos \alpha' + \beta}{1 + \beta \cos \alpha'} \tag{2.13}$$

Only when $\beta=0$ the two angles are the same; in any other case α is smaller than α'. Note that for $\alpha'=90°$ we have $\sin \alpha = 1/\Gamma$ and $\cos \alpha = \beta$.

If we consider a semi-plane in the electron reference system ($\alpha'=\pm 90°$), for $\gamma \gg 1$ we have that $\beta \sim 1$ and then:

$$\alpha \approx \tan\alpha = \frac{1}{\gamma} \qquad (2.14)$$
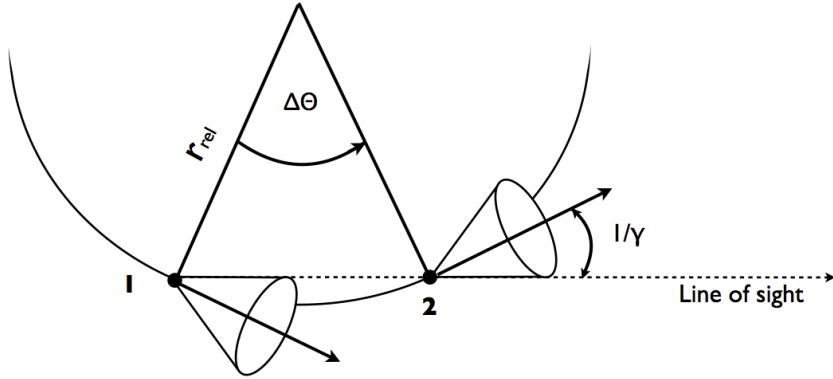
Figure 2.2: Pulse duration. A relativistic electron moving in a circular orbit around magnetic field lines with a pitch angle of 90°. Due to aberration the observer receives the emitted radiation only when the cone of semi-aperture $1/\gamma$ points toward him. The radiation received from a single electron is then in the form of pulses.

Therefore, in the case of relativistic electrons, almost half of the emitted radiation is concentrated in a cone of semi aperture $1/\gamma$ (Figure 2.1). It follows that, as the electron moves on its orbit around magnetic field lines, the observer receives the emitted radiation only when the cone points in his direction, as we observe in Figure 2.2. The emission of a single electron is then received in the form of pulses.

We use Figure 2.2 for a visual description of what happens when the relativistic electron follows its orbit and emits synchrotron radiation. Let us consider $\Delta\theta = 2/\gamma$ the aperture of the cone within which the radiation is emitted. When the electron is in position 1, the cone of emission starts to point toward the observer. The pulse stops when the electron is in position 2. From position 1 to 2 the electron moves by Δl, that is the length of the arc from point 1 to point 2. If we approximate the arc with the

chord whose endpoints are points 1 and 2, we can write $\Delta l \approx \Delta\theta \, r_{rel}$. The radiation emitted in point 1 by the electron, reaches point 2 in $\Delta t_1 = \Delta l/c$, while the electron moves from point 1 to 2 in $\Delta t_2 = \Delta l/v$. Then, the effective duration of the pulse is:

$$\tau = \Delta t_2 - \Delta t_1 \approx \Delta\theta \, r_{rel} \left(\frac{1}{v} - \frac{1}{c} \right) = \frac{\Delta\theta}{\omega_{rel}}(1 - \beta) \tag{2.15}$$

where $\omega_{rel} = v/r_{rel}$ is the frequency of gyration of the relativistic electron along its circular orbit. This is the duration of the pulse of a single emitting electron. Obviously, due to the huge amount of electrons present in a radio source, we do not observe this discontinuity because the sum of pulses emitted by electrons in different times makes the signal continuos in time.
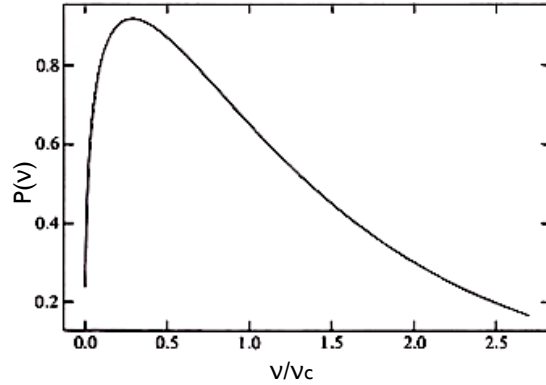
Figure 2.3: Synchrotron spectrum of a single electron. The power radiated by a single relativistic electron as a function of the critical frequency (ν_c). Reproduced from Hughes (1991).

For a non-relativistic motion, the gyration frequency ω_{rel} gives directly the frequency of the emitted radiation $\nu = 2\pi\omega_{rel}$. In the synchrotron case, the spectral distribution of the radiation is mainly concentrated around a *critical frequency* (ν_c), as plotted in Figure 2.3, where ν_c is related to the duration of the pulse (τ) and is given by (Pacholczyk, 1970):

$$\nu_c \sim \frac{1}{\tau} = \frac{3}{4\pi} \frac{eB \sin\phi}{m_e^3 c^5} E^2 \tag{2.16}$$

More specifically, the peak of the emission is centered at a frequency $\nu_p = \nu_c/3$. We note that the critical frequency is proportional to the square of the electron energy, therefore higher energy electrons emit at progressively higher frequencies.

2.1.1.1 Emission from an ensemble of electrons

Now we discuss the case of an ensemble of relativistic electrons. Since the synchrotron process is a non-thermal process, the energy distribution of electrons does not follow a Maxwell-Boltzmann distribution.

We assume a *power law* energy distribution of relativistic electrons:

$$N(E)dE = N_0 E^{-p}dE \qquad (E_{min} \leq E \leq E_{max}) \tag{2.17}$$

where $N(E)dE$ is the number of particles per unit volume having energies between a E and $E + dE$, and p is the exponent of the power law. Now we consider the case in which the source is completely transparent (*optically thin*, see next section for more details) to its own emission and the radiation is not absorbed inside the source. In this case, and considering a homogeneous source, if we integrate $N(E)dE$ times the power emitted by a single electron (eq. 2.9) we obtain the synchrotron emissivity of an ensemble of electrons:

$$j_\nu d\nu = \int P_s(\nu, E) N(E) dE \tag{2.18}$$

where j_ν is specific emissivity, that is the power emitted per unit volume, per unit frequency, per steradian. To simplify the integration of equation 2.18 we can consider $E_{min} = 0$ and $E_{max} = \infty$, obtaining (Pacholczyk, 1970):

$$j_\nu = c_j(p) N_0 (B \sin\phi)^{\frac{p+1}{2}} \nu^{\frac{1-p}{2}} \tag{2.19}$$

where $c_j(p)$ is a constant that depends on p, N_0 is the electron energy density, B the magnetic field, and ϕ the angle between the magnetic field direction and our line of sight. If we integrate the specific emissivity obtained in equation 2.19 over the entire

volume of the source we have the power emitted per unit frequency by all the electrons in the source (for a homogenous source). Hence we have that the synchrotron emission of an ensemble of electrons depends on the frequency as $\nu^{(1-p)/2}$, where $\alpha = \frac{p-1}{2}$ is the *spectral index* of the synchrotron radiation.

In the following section we consider the case in which the source is not completely transparent and part of this radiation is absorbed inside the source.

2.1.1.2   Synchrotron self-absorption

In the previous section we derived the expression for the synchrotron emissivity from an homogenous source in case of no absorption. When instead, the radiation is partially absorbed inside the source, we need to solve the radiative transfer equation:

$$dI_\nu = j_\nu ds - k_\nu I_\nu ds \tag{2.20}$$

where dI_ν is the specific intensity, being the power emitted per unit area, per frequency interval, per steradian. Equation 2.20 tells us that in case of absorption, the specific intensity given by an infinitesimal element of length ds, $j_\nu ds$, is reduced by $k_\nu I_\nu ds$, where k_ν is the *absorption coefficient*. The term $k_\nu ds = d\tau_\nu$ indicates the *optical depth* of the source; when $\tau_\nu > 1$ the source is optically thick, meaning that most of the radiation is absorbed inside the source, while for $\tau_\nu < 1$ is optically thin, and most of the radiation can escape from the source without being absorbed.

Dividing the previous equation by $d\tau_\nu$ we obtain:

$$\frac{dI_\nu}{d\tau_\nu} = S_\nu - I_\nu \tag{2.21}$$

where S_ν is the source function and is equal to $\frac{j_\nu}{k_\nu}$.   To obtain the synchrotron radiation emitted by the source (per unit area) we have to integrate the contribution of each infinitesimal element (equation 2.21) along the line of sight. The solution of the integral for a homogeneous source is given by (Pacholczyk, 1970):

$$I_\nu(\tau_\nu) = S_\nu(1 - e^{-\tau_\nu}) \tag{2.22}$$
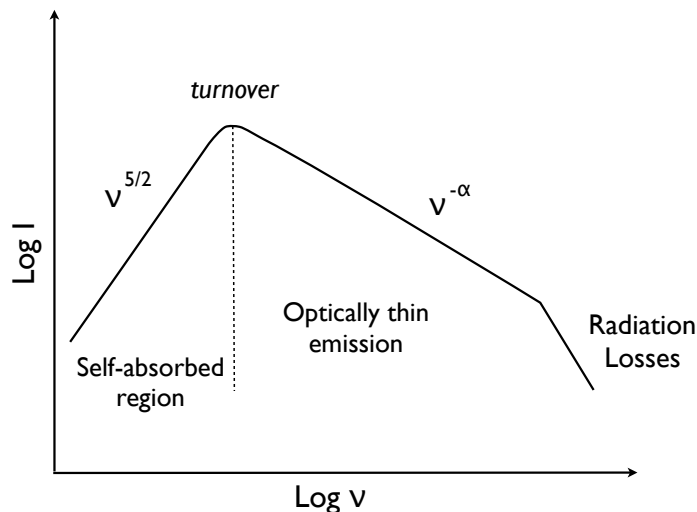
Figure 2.4: Synchrotron spectrum. A plot representing the synchrotron spectrum in the case of a partially self-absorbed source.

In the previous section we obtained the synchrotron emission of an optically thin homogeneous source ($\tau_\nu < 1$) considering an electron energy density distribution as that in equation 2.17. For an optically thick source ($\tau_\nu \gg 1$) the previous equation becomes:

$$I_\nu(\tau_\nu) \approx S_\nu \equiv \frac{j_\nu}{k_\nu} \tag{2.23}$$

If we consider the same energy distribution for relativistic electrons (equation 2.17), the solution for k_ν is found to be (Pacholczyk, 1970):

$$k_\nu = c_k(p) N_0 (B \sin \phi)^{\frac{p+2}{2}} \nu^{\frac{-(p+4)}{2}} \tag{2.24}$$

where $c_k(p)$ is again a constant that depends on p. Given the frequency dependences of j_ν and k_ν, as found in equations 2.19 and 2.24, respectively, from equation 2.23 we obtain the following frequency dependence for the specific intensity:

$$I_\nu(\tau_\nu) \propto \nu^{5/2} \tag{2.25}$$

We note that, in contrast to what it was found for the optically thin case, for an optically thick source the specific intensity follows a power law that does not depend on p.

In Figure 2.4 we display the synchrotron spectrum of a homogeneous, partially absorbed source where we appreciate the frequency dependences found in case of optically thick and optically thin regimes. The frequency at which we have the transition between the two regimes is called the *turnover frequency*. The optically thin part of the spectrum (Figure 2.4) shows also a steepening at high frequencies due to radiative losses of the most energetic electrons that cool more rapidly since energy losses for synchrotron process are proportional to the square of the electron energy, as seen in equation 2.9.

The basic relativistic jet model was developed by (Blandford & Königl, 1979), considering a conical jet in adiabatic expansion. The adiabatic expansion is a simplification that allows us to calculate how some important physical quantities, as the particle energy density and the magnetic field, vary along the jet. In a conical jet in adiabatic expansion, considering that the number of particles and energy are conserved, the electron energy density N_0 decreases along the jet such as: $N_0 \propto r^{-2(p+2)/3}$. In the adiabatic expansion the magnetic field parallel to the jet flow scales as $B_\parallel \propto r^{-2}$, whereas the perpendicular component falls of as $B_\perp \propto r^{-1}$.

In equation 2.19 we have seen that the specific emissivity depends on N_0 and B. From the radial dependences of N_0 and B we infer that the specific emissivity decreases along the relativistic jet.

The absorption coefficient, k_ν, also depends on N_0 and B (equation 2.24). Therefore the opacity decreases with distance along the jet. Moreover, the dependence of k_ν with $\nu^{\frac{-(p+4)}{2}}$ implies that the opacity decreases at progressively higher frequencies and therefore high-frequency (mm-wave band) observations (or even shorter wavelengths) are necessary to probe the innermost jet regions.

2.1.1.3 Polarization

One of the distinguishing features of synchrotron radiation is that it exhibits detectable linear polarization. To investigate this, we consider first the case of the *cyclotron radiation*, produced by a non-relativistic electron on a circular orbit around magnetic

field lines (Fig. 2.5, *left panel*). This is the same as measuring the polarization in the reference frame of the electron in the relativistic case. Observing along the orbital plane, the radiation is completely linearly polarized with the electric vector oscillating perpendicular to the magnetic field line. Observing along the direction of the magnetic field, the radiation is instead completely circularly polarized. If the electron moves at relativistic speed we have shown in § 2.1.1 that the radiation is beamed along the direction of motion in a cone of semi aperture $1/\gamma$ (Fig. 2.5, *right panel*) . In this case the two components of circular polarization, being oriented in opposite directions (right and left hand), will cancel each other out, whereas the linear polarization is conserved.

In the case of an optically thin homogeneous source without Faraday rotation and considering a power law energy distribution of electrons such as that in eq. 2.17, the degree of linear polarization, defined as the ratio between the polarized signal over the total intensity, is (Pacholczyk, 1970):

$$\Pi = \frac{P}{I} = \frac{3p+3}{3p+7} \tag{2.26}$$

From the observed spectral indices we estimate that $2 < p < 3$, implying a maximum theoretical linearly polarized flux of almost 70% (Hughes, 1991). Moreover, any disordering of the magnetic field reduces the degree of polarization, since orthogonal orientations of magnetic field lines produce orthogonal polarization vectors that cancel each other out. We note that the degree of polarization is independent of frequency, and this is true also for optically thick sources, although in the latter case the degree of polarization is smaller than in optically thin sources and can be expressed as follows (Pacholczyk, 1970):

$$\Pi = \frac{3}{6p+13} \tag{2.27}$$

that, for typical values of p, is only $\sim$10%.

Synchrotron radiation may provide a small amount of circular polarization in the most compact regions of radio jets, observed usually close to the synchrotron self-
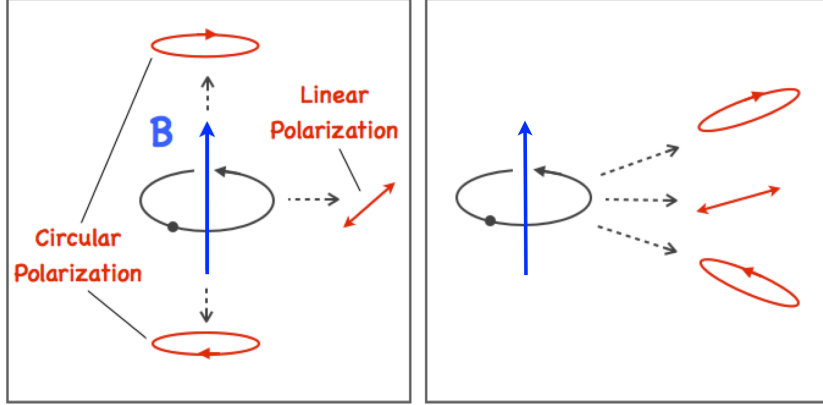
Figure 2.5: Polarization. *Left:* The case of cyclotron radiation. In red we have the polarized emission perceived by the observer from different orientations. *Right:* The case of synchrotron radiation, where the emission is concentrated in a cone of semi-aperture $1/\gamma$. Blue and red lines indicate the same as in *left panel*.

absorbed jet cores with maximum degrees of circular polarization that range between 0.3% and 1% (Homan & Wardle, 1999; Homan et al., 2001).

The polarization properties of an electromagnetic wave are usually characterized in terms of four parameters introduced by Sir George Stokes in 1852. The Stokes parameters are related to the amplitudes of the components of the electric field, E_x and E_y, in the plane perpendicular to the direction of propagation of the electromagnetic wave. Thus, if E_x and E_y are represented respectively by $\epsilon_x(t)\cos(2\pi\nu t + \delta_x(t))$ and $\epsilon_y(t)\cos(2\pi\nu t + \delta_y(t))$, where ϵ_x and ϵ_y are the amplitudes of the vibration while $\delta_x(t)$ and $\delta_y(t)$ are their corresponding phases, the Stokes parameters are defined as follows:

$$
\begin{aligned}
I &= \langle \epsilon_x^2(t) \rangle + \langle \epsilon_y^2(t) \rangle \\
Q &= \langle \epsilon_x^2(t) \rangle - \langle \epsilon_y^2(t) \rangle \\
U &= 2\langle \epsilon_x(t)\epsilon_y(t) \cos(\delta_x(t) - \delta_y(t)) \rangle \\
V &= 2\langle \epsilon_x(t)\epsilon_y(t) \sin(\delta_x(t) - \delta_y(t)) \rangle
\end{aligned}
\tag{2.28}
$$

where the angular brackets denote averages in time. Of the four Stokes parameters, I represents the total intensity, Q and U measure the linearly polarized intensity and V represents the circularly polarized component. From the Stokes parameters we can reproduce the following physical parameters of the polarized signal:

$$\Pi_L = \frac{\sqrt{Q^2 + U^2}}{I} \tag{2.29}$$

$$\Pi_C = \frac{V}{I} \tag{2.30}$$

$$\Pi = \frac{\sqrt{Q^2 + U^2 + V^2}}{I} \tag{2.31}$$

$$\chi = \frac{1}{2} \arctan\left(\frac{U}{Q}\right) \tag{2.32}$$

where Π_L, Π_C and Π are the degrees of linear, circular, and total polarization respectively, and χ is the position angle of the plane of linear polarization, or more commonly the electric vector position angle (EVPA), since it indicates the direction of the oscillation plane of the electric field. This is always perpendicular to the magnetic field and to the direction of propagation of the electromagnetic wave. However, when we try to infer the direction of the magnetic field in the emitting source from the observed direction of the EVPAs we have to consider that we are dealing with different reference frames (the observer and the source frames). Therefore, we have to consider the relativistic Lorentz transformations which establish that the components of the magnetic field perpendicular and parallel to the velocity vector of the plasma transform in different ways (e.g. Blandford & Königl, 1979; Lyutikov et al., 2005). This implies that the orientation of the magnetic field in the emitting source could be different from what we measure in our reference frame. Moreover, there is an additional effect that distorts our view of the linear polarization angle, that can be rotated by the Faraday effect (see next section).

2.1.1.4 Faraday rotation

Faraday rotation of the polarization angle occurs when the electromagnetic wave propagates through a magnetized and non-relativistic plasma containing a considerable population of free electrons, as for example the thermal plasma in the environment of the inner regions of relativistic jets. The linearly polarized electromagnetic wave can be constructed via a superposition of right and left hand circularly polarized waves of

equal amplitudes which propagate with different velocities when they cross the magnetized plasma, causing a rotation in the plane of linear polarization by:

$$\Delta\chi = RM\lambda^2 \tag{2.33}$$

where λ is the wavelength of the electromagnetic wave and RM is the rotation measure defined as (e.g. Gabuzda et al., 2015):

$$RM = \frac{e^3}{8\pi^2\epsilon_0 m_e^2 c^3} \int n_e B_\parallel \, dl \quad [\text{rad m}^{-2}] \tag{2.34}$$

where e is the electron charge, m_e the electron mass, n_e the electron density, ϵ_0 the dielectric constant of the medium, c the speed of light and $B_\parallel$ is the component of the magnetic field along the line of sight. Therefore, the observed EVPAs (χ) affected by Faraday rotation can be expressed as $\chi = \chi_0 + \Delta\chi$, where χ_0 is the intrinsic value of the EVPAs in the source. Due to the dependence of $\Delta\chi$ on the square of the wavelength, in order to obtain the rotation measure values it is necessary to measure χ over a range of frequencies , as shown in Figure 2.6.

The Faraday rotation can be produced either inside or outside the emitting region, in the interstellar or intergalactic medium between the source and the observer. External Faraday rotation follows the λ^2 law (see Figure 2.6), while internal Faraday rotation, although based on the same fundamental mechanism, can be observed following a different functional form (e.g. Gómez et al., 2008; Wardle, 2013). If the Faraday rotation is internal to the emitting source the electromagnetic waves coming from the farthest regions of the source rotate more than those coming from those regions closer to the observer, therefore producing a partial cancelation between each other. The net effect can be a depolarization of the signal and a consequent deviation from the λ^2 law.

2.1.2   Inverse Compton process

The inverse Compton process involves the scattering of low energy photons to high energies by relativistic electrons so that the photons gain and the electrons lose energy. The term *inverse* distinguishes this process from the *direct* Compton scattering,
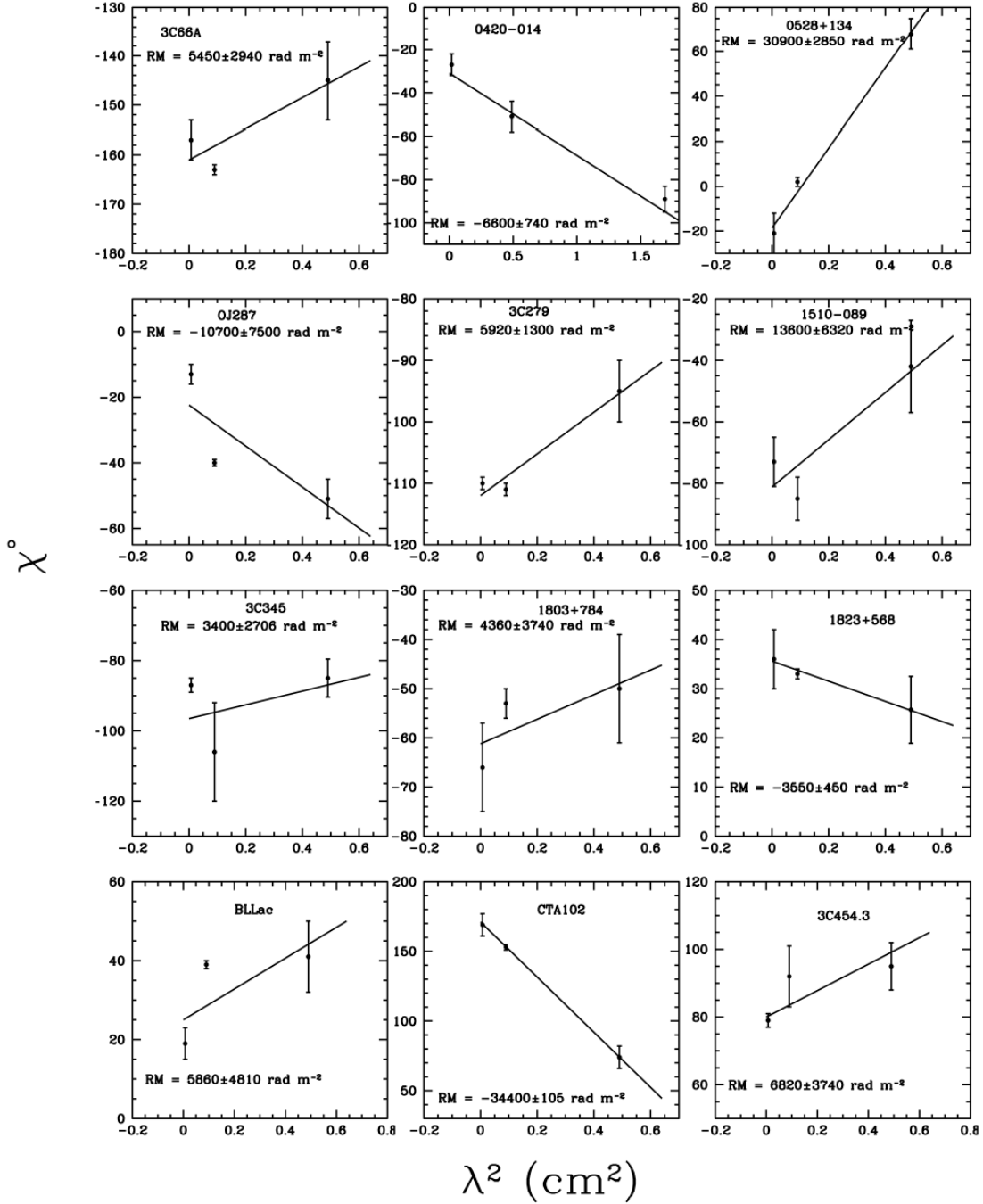
Figure 2.6: Rotation measure determinations of a sample of AGNs. The ordinate axis reports the measured EVPAs and the abscissa the values of the squared wavelengths of observations. The slope of the solid line gives the value of the estimated RM for each source. The image is reproduced from Jorstad et al. (2007)

in which the electron gains energy during the collision while the photon loses part of its energy. During the inverse Compton process the photon can gain sufficient energy to be scattered from frequencies in the optical to X-rays and γ-ray energies if the relativistic electron is sufficiently energetic. Depending on the photon energy in the rest frame of the electron we can distinguish between two scattering cross sections and therefore between two regimes: the *Thomson* and the *Klein-Nishina* regimes. When the energy of the incoming photon in the rest frame of the electron is smaller than the rest mass energy of the electron ($h\nu \ll m_e c^2$) we are in the Thomson regime; in the opposite case ($h\nu \gg m_e c^2$) we are in the Klein-Nishina regime. This is the same as saying that in the classical limit of the problem, when $\lambda \gg \lambda_c$, where λ_c is the *Compton wavelength* and is defined by (Rybicki & Lightman, 1979):

$$\lambda_c \equiv \frac{h}{mc} = 0.02426\,\text{Å} \quad (\text{for electrons}) \tag{2.35}$$

we are in the Thomson regime; otherwise we have to consider the quantum approach of the Klein-Nishina regime. The principal effect in the Klein-Nishina regime is the reduction of the scattering cross section with respect to the classical value, leading to a lower probability of scatter than in the classical case, although in this case the recoil of the electron is not negligible and the electron loses most of its energy during the collision. Due to the low probability of having Klein-Nishina interactions the quantum effects on the inverse Compton process are usually neglected.

2.1.2.1 Thomson regime

In the rest frame of the electron the scattering is closely elastic and we can assume that there is no change in the photon energy. But, this is not true in the observer rest frame where, during the collision, the photon gains energy and its final energy ranges between $x/4\gamma^2$ and $4\gamma^2 x$, where x is the energy of the photon before the collision (see for example Ghisellini, 2013). The maximum gain occurs when the angle between the electron velocity and the incoming photon is π (*head-on collision*) and the minimum gain occurs when the angle is $0°$, meaning that the photon comes from behind (*tail-on collision*). Considering an isotropic distribution of incoming photons, the mean photon energy after the scattering is $\frac{4}{3}\gamma^2 x$.

The energy loss rate of electrons during the scattering in the Thomson regime is given by (Rybicki & Lightman, 1979):

$$P_c = \frac{dE}{dt} = \frac{4}{3}\sigma_T c \gamma^2 \beta^2 U_{ph} \tag{2.36}$$

where σ_T is the Thomson scattering cross section and U_{ph} is the initial photon energy density.

There are many analogies among the energy loss rate of electrons due to synchrotron and inverse Compton processes, as seen from comparison of eq. 2.11 and 2.36. If in eq. 2.36 we replace U_{ph} with U_B, the magnetic energy density, we obtain eq. 2.11. Then if electrons travel in a medium embedded in radiation and magnetic fields, they will emit both by the synchrotron and the inverse Compton process.

Another analogy is the spectral distribution of photons after the inverse Compton scattering and that one resulting from the synchrotron process. If we consider an initial power law distribution for the population of relativistic electrons, as that in eq. 2.17, the spectral distribution of photons after inverse Compton scattering will again be a power law with spectral index $\alpha = (p-1)/2$, as in the synchrotron process for optically thin emission.

2.1.3 The SED

The broad band spectral energy distribution (SED) of most radio loud AGNs has the typical double-hump shape as the one shown in Figure 2.7.

The first peak falls in the range of mm and soft X-ray frequencies (depending on the spectral properties of the emitting source) and the corresponding second peak at γ-ray frequencies, in the MeV-TeV energy range. The first hump is produced by the synchrotron process and the second one by the inverse Compton scattering of the same photons produced by synchrotron emission (*Synchrotron Self Compton, SSC*) or the inverse Compton scattering of an external photon field (*External Compton, EC*). The candidates for the external photon field are the accretion disk (e.g. Dermer et al., 1992), the broad line region (e.g. Sikora et al., 1994), the dusty torus (e.g. Tavecchio et al., 2011), or a relatively slow sheath surrounding the jet (e.g. Marscher et al., 2010).

The series of SEDs, for different sources, reported in Figure 2.7 represent the spectral sequence of blazars and, as noted by Fossati et al. (1998), when the luminosity increases the two peaks shift to lower frequencies and the high energy peak becomes more prominent. This sequence also marks the difference between the more powerful FSRQs, that are represented by the SEDs at higher luminosities in Figure 2.7, and BL Lacs, less powerful, represented by SEDs at lower luminosities. This differentiation was interpreted by Ghisellini et al. (1998) as due to a more severe cooling suffered by FSRQs than by BL Lacs. FSRQs are more powerful sources than BL Lacs and electrons suffer a stronger inverse Compton cooling due to the presence of external photon fields (disk, BLR and molecular torus) observed in FSRQs and not in BL Lacs. Hence, typical electron energies in FSRQs are smaller than in BL Lacs and the second peak, due to the Compton scattering, is more prominent.
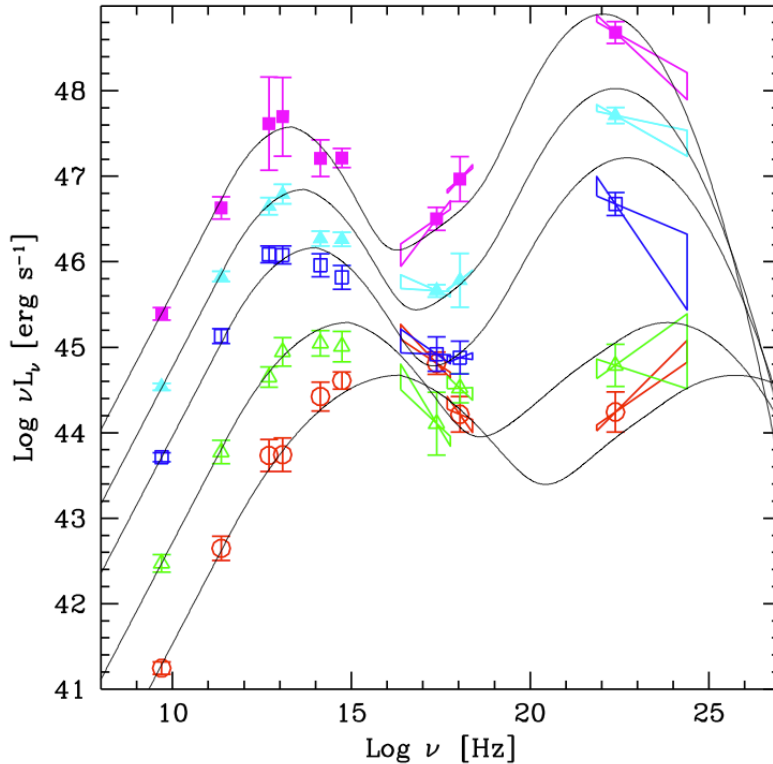
Figure 2.7: Collection of different blazar SED. Sequence of different average blazar SED taken from a big sample as reported in Donato et al. (2001) and adapted from Fossati et al. (1998).

2.2 Relativistic effects in jets

Special relativity teaches us that lengths and times measured in two different reference frames differ from each other. If we measure a ruler when it is at rest and when it is moving we find that the ruler is shorter when it is moving. The opposite effect is observed in the case of intervals of time, which are longer when the reference frame is moving.

Furthermore, if we measure the distance travelled by an emitting source that moves at relativistic speeds we must take into account the different travel paths of photons, relevant when the source is moving in a direction that forms an angle different from 90° with regard to our line of sight. This is what happens in AGN, where information is carried to the observer by photons and the plasma in the jet moves relativistically. Besides usual Lorentz transformations we have to consider also the *Doppler factor* (δ), a parameter related to both, the velocity and the viewing angle of the jet, of special relevance for the understanding of several observed properties of radio loud AGN. Through these considerations we can explain for example apparent superluminal motions observed in many blazars (e.g Jorstad et al., 2005; Lister et al., 2009) and radiogalaxies (e.g Gómez et al., 2000; Lister et al., 2013) as well as intraday variability observed in total and polarized flux in many sources (see e.g. reviewed by Wagner & Witzel, 1995).

2.2.1 Superluminal motions

A peculiar phenomenon observed commonly in blazars is the one of apparent superluminal motions, namely velocities larger than the speed of light as measured projected on the plane of the sky. These apparent superluminal velocities are observed in bright regions of the jet commonly known as "components" (see § 2.3 for more details). These components, which move relativistically toward the observer, run after their own emitted photons and this makes the observed time lapse smaller and the apparent velocity larger than c in the observer's frame. Superluminal motions were first predicted by Sir Martin Rees in his PhD thesis (1966) and then actually measured in 1971 (Whitney et al., 1971) thanks to the first Very Long Baseline Interferometer (VLBI) observations at radio wavelength, the only observing technique capable to achieve the necessary angular resolution to discern this phenomenon.

To understand it better, we consider the artistic reproduction in Figure 2.8, where we have a jet oriented at a viewing angle θ, in which we distinguish the motion of a bright component. This component emits radiation in two different instants separated by an interval of time Δt. The first pulse, that moves at the speed of light, c, in the interval of time Δt covers a distance $c\Delta t$; at the same time the component moves along the jet a distance $v\Delta t$. As a consequence, the second pulse has to travel a shorter distance to reach us with regard to the distance traveled by the first pulse (see Figure 2.8).
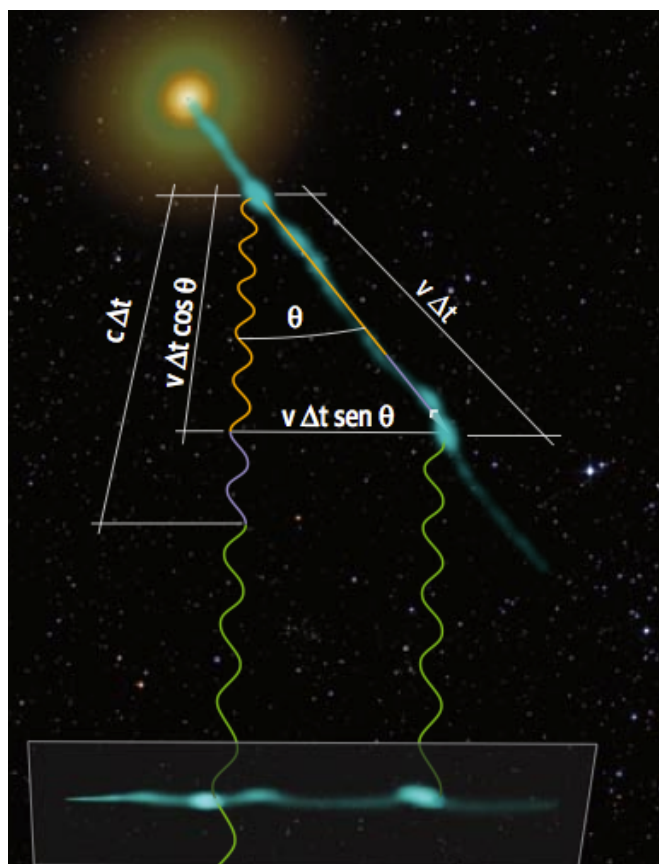

Figure 2.8: Conceptual illustration of apparent superluminal motions. Artistic view of a moving component along a jet oriented at viewing angle θ. This component emits radiation in two separated instants of time. The time measured between the two pulses by the observer differs from the real time lag Δt. Reproduced from Gómez & Steffen (Investigación y Ciencia, 2009).

This results in a time interval between the two pulses, as measured by the observer, shorter than the real time interval at which the source has emitted the two pulses. More precisely, the time interval in the observer's reference frame is equal to the time spent by the second pulse to reach the first pulse (the path in violet in Figure 2.8). The path difference is equal to cΔt - vΔt$\cos\theta$, hence the time needed for the second pulse to reach the first one is (cΔt - vΔt$\cos\theta$)/c, that is Δt(1 - $\frac{v}{c}\cos\theta$). This allows us to obtain the apparent velocity measured by the observer in the plane of the sky, that we calculate dividing the distance traveled by the component between the two pulses projected in the plane of the sky (vΔt$\sin\theta$), by the time interval between the pulses as measured in the observer's frame Δt(1 - $\frac{v}{c}\cos\theta$):

$$v_{app} = \frac{v\Delta t \sin\theta}{\Delta t(1 - \frac{v}{c}\cos\theta)} \tag{2.37}$$

If we express the apparent velocity in units of c we obtain the usual formula:

$$\beta_{app} = \frac{\beta\sin\theta}{1 - \beta\cos\theta} \tag{2.38}$$

where the observed apparent velocity (projected on the plane of the sky) depends on the speed of the component in the jet and the angle between its velocity vector and the line of sight. It is easy to see that when θ=90° the apparent velocity is equal to the real velocity of the component, since in this case all photons travel along the same path.

In Figure 2.9 we plot the values of β_{app} for different viewing angles and Lorentz factors, Γ. It is easy to see that for each Γ there is a value of viewing angle for which the apparent velocity is maximum, and this value corresponds to θ_{max}=arccosβ. For viewing angles below the peak the apparent velocity decreases, because of projection effects.

From eq. 2.38 we can derive some constraints on the physical parameters of relativistic jets using the observed apparent velocity of the components. For example, for a certain β_{app} we can calculate the upper limit of the viewing angle of the jet, θ_{sup}, which is obtained considering that the component is moving at the maximum possible

speed ($\beta = 1$). In this case we have:

$$\beta_{app} = \frac{\sin\theta_{sup}}{1 - \cos(\theta_{sup})} = \frac{1}{\tan(\theta_{sup}/2)} \tag{2.39}$$

and a corresponding upper limit of $\theta_{sup} = 2\arctan(1/\beta_{app})$.
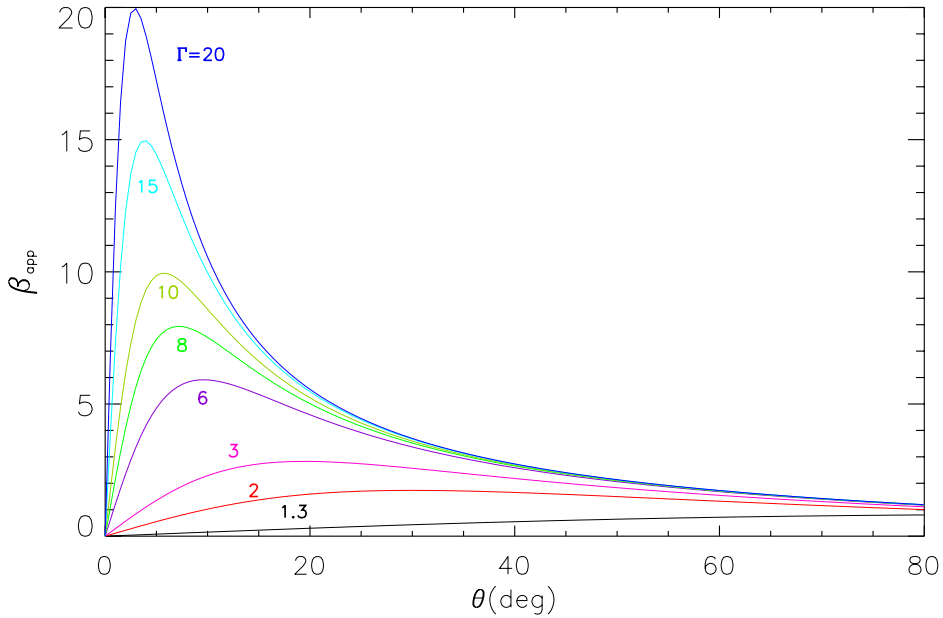
Figure 2.9: Apparent velocity trend. The apparent velocity as a function of the viewing angle (θ) and the Lorentz factor (Γ).

For example, for an observed apparent velocity of $\beta_{app} = 5$, the jet has to be oriented at a viewing angle $\leq 23°$. From similar considerations we can also put a constraint on the minimum value of β necessary to have an observed β_{app}, independently of the viewing angle of the jet, as we can also appreciate in Figure 2.9. The value of β_{min} for a given β_{app} is obtained for $\theta = \theta_{max}$, as follows:

$$\beta_{min} = \frac{\beta_{app}}{\sqrt{1 + \beta_{app}^2}} \tag{2.40}$$

Therefore, for $\beta_{app} = 5$, for example, we have $\beta_{min} = 0.98$ and a corresponding $\Gamma_{min} = 5$.

In some blazars superluminal components with speeds up to 40 times the speed of light are routinely measured (Jorstad et al., 2005), although more moderate superluminal motions up to $\sim 10c$ are more typical for this class of AGNs (e.g. Gómez et al., 2001a; Marscher et al., 2008; Agudo et al., 2011a; Ramakrishnan et al., 2014). Superluminal motions are not common in radiogalaxies, but some of them, such as the radiogalaxies 3C 120 (Gómez et al., 1998, 2001b; Casadio et al., 2015a), 3C 111 (Chatterjee et al., 2011) and M 87 (Cheung et al., 2007; Giroletti et al., 2012) also display these kind of motions.

2.2.2 Doppler boosting

We consider for example the component in Figure 2.8 that moves with a velocity v=βc along the jet oriented at viewing angle θ. This component emits a pulse at a frequency ν'. Due to the relativistic time dilation the frequency will be redshifted by a factor $1/\Gamma$, while the Doppler effect causes a shift in frequency by a factor $(1-\beta\cos\theta)^{-1}$. The latter rescales the frequency to higher values (blu-shift) if the source is moving toward us and to lower values (red-shift) if the source is moving in the opposite direction. Considering both effects, we obtain the frequency in our reference frame, that is:

$$\nu = \nu'\frac{1}{\Gamma}\frac{1}{(1-\beta\cos\theta)} = \nu'\delta \tag{2.41}$$

where δ is the *Doppler factor*.

We are also interested in determining how the intensity Lorentz transforms between the fluid and observers' reference frames. The specific intensity that we already discussed in sec. 2.1.1.2, is the energy emitted per unit of time (the power), per unit area, per frequency interval and solid angle ($d\Omega$):

$$I_\nu = \frac{h\nu dN}{dt dA d\nu d\Omega} \qquad [\text{erg cm}^{-2}\text{ s}^{-1}\text{ Hz}^{-1}\text{ ster}^{-1}] \tag{2.42}$$

where we have considered an ensemble of photons (dN) with energy ($h\nu$). The only

invariant quantities between the two reference frames are dN, as it is a number, and dA, that is a surface and only rotates due to relativistic effects. Therefore the specific intensity Lorentz transforms as:

$$I_\nu = \frac{h\delta\nu' dN'}{(dt'/\delta)\delta d\nu'(d\Omega'/\delta^2)dA'} = \delta^3 I'_{\nu'} \tag{2.43}$$

where we introduced the transformation of the solid angle between the two reference frames ($d\Omega = d\Omega'/\delta^2$), as well as those of the time intervals and frequencies discussed previously.

Depending on the value of the *Doppler factor* (δ), the specific intensity can be significantly amplified by the δ^3 factor, favoring the observation of faint sources or components when their jets point toward us.

2.3   Theoretical model of relativistic jets in AGN

Relativistic jets are the product of accretion onto black holes. Despite many years of observations and theoretical studies, their most fundamental aspects are still not fully understood. It is still unclear how relativistic jets are launched, accelerated and collimated up to large distances from the nucleus of the host galaxy; why some AGN produce prominent and powerful jets, while others not; and whether such relativistic jets are dynamically dominated by matter or by the magnetic fields that thread their plasma. Also high-energy outbursts, sometimes in coincidence with flares at the other wavebands and sometimes not, observed in many AGN are still a matter of debate. Many models are able to make a successful interpretation of the physics involved on the formation of jets, but we have yet to confirm observationally which one of these models better explains the wide variety of AGN properties.

The first very long baseline interferometric (VLBI) observations of AGN suggested that the radio emission may arise from relativistic jets where relativistic electrons emit at radio frequencies through synchrotron process (e.g. Readhead et al., 1979). Before their early observations, such scenario had been proposed theoretically by Blandford & Rees (1978) and Blandford & Königl (1979). The most promising model for launching relativistic jets in AGN involves the rotation of large-scale magnetic fields (Blandford & Payne, 1982; Blandford & Znajek, 1977). The differential rotation of plasma in the

accretion disk or black hole magnetosphere causes the polar component of magnetic field lines to wind up into a helix.
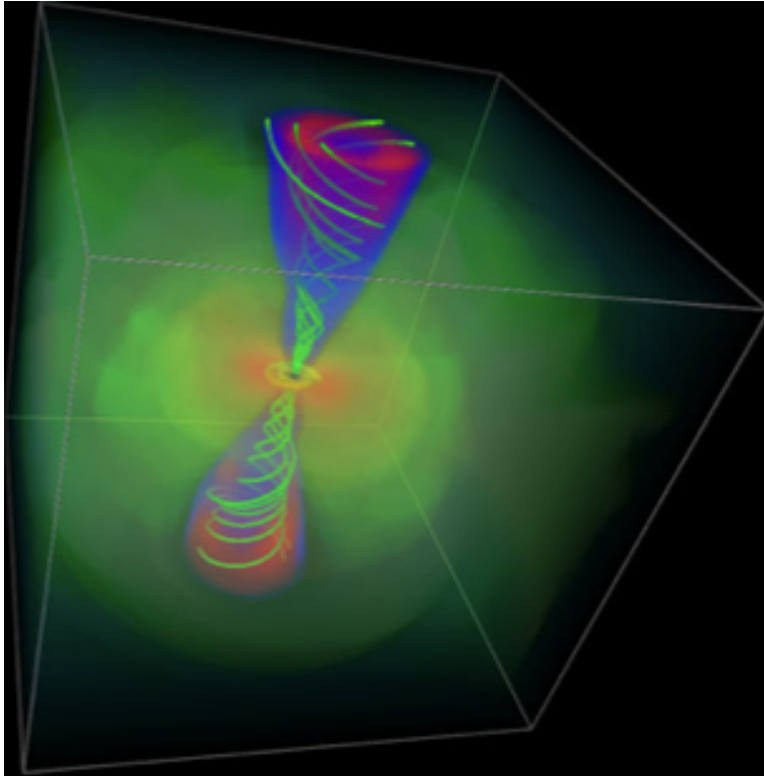
Figure 2.10: Magnetic tower. Helical magnetic fields driving magnetized plasma into the jets. Reproduced from McKinney & Blandford (2009)

The toroidal component of the magnetic field provides a force directed toward the jet axis that allows the jet confinement. This effect is complemented by the pressure provided by an external (high relative pressure) envelop of dense material such as a wind from the accretion disk. The expansion of the magnetic field with distance from the black hole reduces the magnetic pressure, hence creating a pressure gradient along the jet that drives the flow. Such outflow can become relativistic if the magnetic energy density exceeds the rest mass energy density. Therefore, the jet is initially dominated by Pointing flux; later on most of the energy is transferred to the kinetic flux of the particles until reaching the equipartition between the kinetic and the magnetic energy density. Magnetic acceleration and gas dynamical models predict also that the intrinsic

opening angle of the jet is inversely proportional to the Lorentz factor of the flow, as observed in many AGN jets (Jorstad et al., 2005).

Therefore, the scenario that emerges from these theoretical models is that of a jet formed by an electron-proton or electron-positron plasma (or a combination of both) that is driven and collimated by a toroidal magnetic field. The plasma is accelerated to a high bulk Lorentz factor by a decreasing magnetic pressure gradient, although where this occurs, if close to the black hole or at hundreds or thousands of Schwarzshild radii, is still unclear. The plasma is also eventually subject to internal instabilities, causing sometimes local enhancements of the emission. These enhancements of emission can be produced by different kinds of physical processes. In the next section we outline the most relevant ones among these.

2.3.1   Shock waves and related polarization

Variations in the velocity or energy density of the particles injected into the jet can produce internal shock waves that increases the density of plasma, compresses the magnetic field component parallel to the shock front and accelerates particles (e.g. Marscher, 2009). This produces a region with enhanced emission with regard to that of the underlying plasma. That is usually called a jet emission component (or simply a *component*) in the VLBI argot.

The density of the shocked plasma is increased by a factor $1/\eta$ (see Figure 2.11), where η is <1 and is given by (Hughes et al., 1989; Gómez et al., 1993):

$$\eta = \frac{n_u}{n_d} = \Gamma'_u (8\Gamma'^{\,4}_u - 17\Gamma'^{\,2}_u + 9)^{-0.5} \qquad (2.44)$$

with n_u and n_d being the particle density upstream and downstream, respectively, and Γ'_u the Lorentz factor of the upstream flow in the shock's frame. The upstream flow is the quiescent flow that has not crossed yet the shock front, while the downstream flow is the one already processed by the shock front.

The magnetic field component that lies parallel to the shock front is compressed by the shock and increases its intensity by the same $1/\eta$ factor, while the component transverse to shock front direction, and mostly parallel to the jet axis, does not change significantly. Therefore, plane perpendicular shock fronts produce a level or order of

magnetic field, even on initial fully tangled configurations. This is relevant, because the geometry and degree of order of the magnetic field are key indicators of the physical conditions of the plasma, and can therefore be estimated in shocks from polarimetric observations.
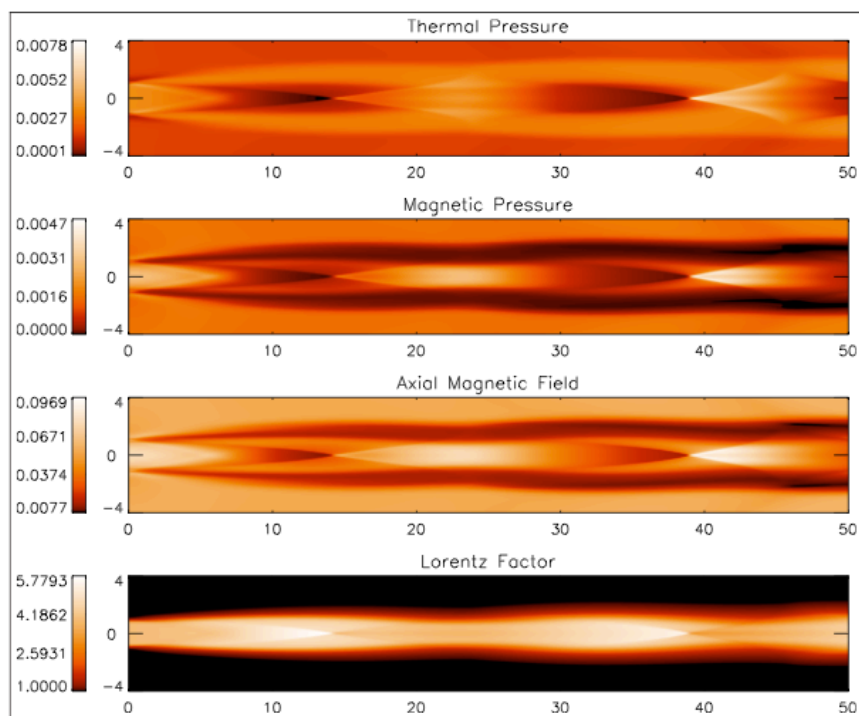
Figure 2.11: RMHD simulations. Relativistic magnetohydrodynamical simulation of a jet with a poloidal magnetic field. A series of recollimation shocks form along the jet. Reproduced from Mar Roca-Sogorb's PhD thesis.

There is another type of shock, most commonly known as "recollimation" or "external" shocks, since they are related to instabilities coming from outside the jet, unlike "internal" ones. A jet in equilibrium tends to reach pressure balance with the external medium. If that equilibrium is not the initial condition at the location of the jet launching region, a series of oscillating expansion and contraction cycles happen in the cross section of the jet. Since both the external medium and the plasma inside the jet are subject to variations of pressure, they can undergo local mismatches in pressure between each other (see Figure 2.11). The jet edges experience first the mismatch and communicate it to the interior of the jet through sound waves. When the mismatch

is large enough, a shock wave forms to adjust the imbalance more rapidly. These recollimation shocks are observed to be oblique shocks waves (Gómez et al., 1995; Marti et al., 1995) or conical shocks if the jet is circularly symmetric (Cawthorne & Cobb, 1990; Cawthorne, 2006).

In optically thin regions, the observed polarization vectors (EVPAs) and the associated magnetic fields must be orthogonal to each other (see § 2.1.1.3). Therefore, in plane perpendicular moving shocks, that are expected to have the shock front perpendicular to the jet axis (Marscher & Gear, 1985; Hughes et al., 1985) the EVPAs are expected to be aligned with the jet axis while in conical shock models (Cawthorne & Cobb, 1990; Cawthorne, 2006) EVPAs are expected to cover a wide range of angles depending on the opening angle of the cone and the viewing angle. Therefore, the information provided by the direction of the EVPA in shocks, together with the linear polarization degree, is of great relevance to infer the physical properties of the jet, via modeling of the observational properties of the shocks.

2.3.2   Models for the core, stationary, and superluminal knots

The most prominent features on VLBI images of jets in radio loud AGN are the *core* and the so called *knots* or *components* in the jets (mentioned in the previous section). The radio *core* is usually the brighter feature at the upstream end of a one-sided jet, and is tipically the most compact feature at any observing frequency in the jet. The core may correspond to the transition region between optically thick and thin emission (see Konigl, 1981) or to the first "recollimation" shock as obtained in numerical simulations (i.e., Gómez et al., 1995, 1997, see also Figure 2.11). In the first case, the position of the core should move toward the central engine with increasing observing frequency, see Figure 2.12 for a sketch. This effect, called opacity core-shift, has been observed in some objects (e.g., Lobanov, 1998; Hada et al., 2011) but not in all of them (e.g., Mittal et al., 2006).

Besides the core, there are often other kinds of bright features (i.e. emission components) observed in the jet that could be either stationary or moving at subluminal, or even superluminal apparent speeds. Stationary components can be produced by recollimation shocks or instabilities in the jets that compress the flow, accelerate particles and amplify the magnetic field, therefore enhancing the output emission. Stationary

features can also be produced by bends in the jet through the differential Doppler boosting (Gómez et al., 1994).
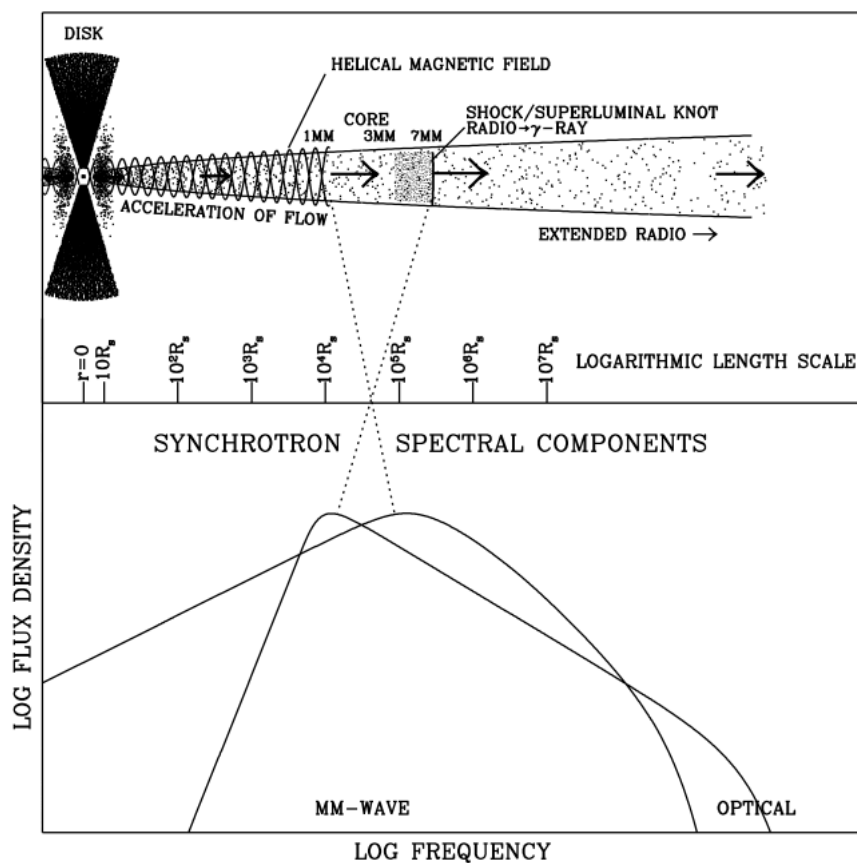
Figure 2.12: Shock-in-jet model. Reproduced from Jorstad et al. (2007)

Many theoretical models are able to reproduce the time variability of the flux, polarization and continuum spectra of blazars (e.g. Hughes et al., 1985; Marscher & Gear, 1985) identifying moving knots with shocks that propagate along the jet. In the shock-in-jet model of Marscher & Gear (1985) for example, electrons are accelerated at the shock front and they lose energy because of expansion and cooling as the shock propagates downstream the jet flow where they are embedded. This results in energy stratification of electrons, with higher energy electrons located in a thin layer close to the shock front and progressively lower energy electrons occupying larger volumes because of the longer cooling times of lower energy particles. When applied to an outburst or a

flare, this leads to time lags among different peaks of emission at different frequencies with higher frequency variations leading those at lower frequencies.

3
Multi-wavelength studies of AGN

3.1 High-energy emission in AGN

Most extragalactic sources detected so far at γ-ray frequencies are active galactic nuclei, γ-ray bursts and starburst galaxies. As expected, the majority of detected AGN (98%, Acero et al., 2015) are blazars. Their radiation is expected to be enhanced and shifted to higher frequencies by Doppler boosting effects (see § 2.2). However, other AGN classes with their jets at larger viewing angles than those of blazars have also been detected at gamma rays, although these are only a small fraction of the entire population of gamma ray emitting AGN. Radio galaxies, of both type I (FRI) and type II (FR II), belong to this group of non-blazar misaligned AGN (MAGN).

The γ-ray space observatory EGRET (1991-2000), that observed in the energy range from 20 MeV to 30 GeV, allowed to catalog for the first time the extragalactic sky at γ-ray energies. But it has been the current high sensitivity generation of MeV-GeV space observatories (i.e., *Fermi* and AGILE) and ground based Cherenkov telescope array in the TeV range (HESS, MAGIC and VERITAS), that have produced an actual revolution in the field of the γ-ray astronomy.

One of the major challenges on physics of high-energy emission in AGN concerns the location of γ-ray emission site. The debate lies in whether γ-ray are produced close to the central engine, as proposed in the pair cascade model of Blandford & Levinson (1995), or in shocks located in the parsec-scale jets (i.e., the mm-VLBI *core*) as proposed in Jorstad et al. (2001).
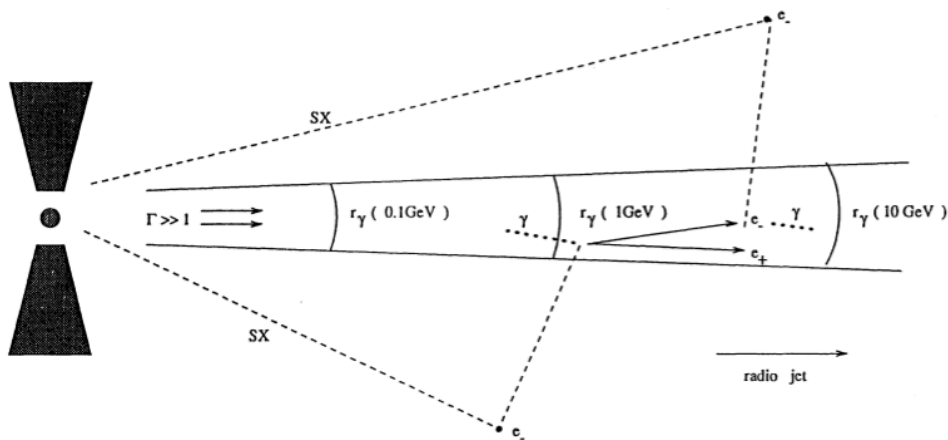
Figure 3.1: Sketch of the pair cascade model. Reproduced from Blandford & Levinson (1995)

In Blandford & Levinson (1995) model, soft X-ray photons coming from regions near the black hole are Thomson-scattered by electrons in the surrounding medium. As a consequence, they interact with electron/positrons or other γ-ray photons already in the jet. The interaction with another γ-ray photon, if the sum of their energies exceeds 1.022 MeV (the sum of the rest mass energies of an electron and positron), produces an electron positron pair. The interaction with electrons or positrons instead can produce γ-ray photons through inverse Compton scattering. In this way a pair cascade can develop, leading to pair-production opacity. This opacity is energy dependent and gives rise to unity opacity surfaces for the γ-ray photons, whose radius increases with energy. This means that the lower energy photons come from regions closer to the black hole. In Figure 3.1 we show a schematic representation of this model.

The scenario that locates the γ-ray dissipation zone in the parsec scale jet (Jorstad et al., 2001; Marscher, 2005), considers that the radio and γ-ray emission originate from the same shocked area, and that this is located close to the radio core rather

than near the central engine. The electrons, that are accelerated in shocks, scatter IR-optical photons to γ-ray energies via the synchrotron self Compton or external Compton mechanisms (see § 2.1.2 and § 2.1.3).

The fast variability observed at high energies initially pointed to a location of the emission site close to the black hole, where the jet has a smaller cross-section (e.g. Tavecchio et al., 2010). However, the short time scales of variability only imply the compactness of the emitting region, which has to be R $< c\Delta t\delta$, being c the speed of light, Δt the variability time scale, and δ the Doppler factor. Therefore, emitting regions far away from the central engine cannot be discarded if γ-ray emission can be associated to compact knots in the jet (e.g. Tavecchio et al., 2011) or if the jet is treated as composed by many turbulent cells (Marscher, 2014). Depending on the location of the high-energy dissipation zone, the production mechanism of this emission could be different. Some authors suggest external Compton emission with external photons coming from the broad line region (Ghisellini et al., 2010), while others locate the emission at parsecs scale with external IR and optical photons coming from the dusty torus, or synchrotron self Compton emission if we have no contribution from an external photon field (Sikora et al., 2009; Bonnoli et al., 2015). However, in many cases spectral energy distribution modeling does not provide a unique answer to the above questions and more observational constraints are needed.

3.2 Combining high spatial resolution radio observations with high energy data: the multi-waveband tools.

Many studies of AGN involve a single technique and at only one waveband, which is usually inadequate to reveal the complex physics behind these objects that are well known to radiate in the entire electromagnetic spectrum. Our understanding has improved with the increase of available data sets from many astronomical facilities at different wavelengths. Multi-waveband polarimetric observations of individual objects that undergo high energy events can provide a wealth of informations on the physics of jets through the following tools:

· *creation of the spectral energy distribution (SED) at several epochs using measurements of flux density at different frequencies*: this provides information on the

emission processes and helps separating components responsible for the emission at the different observing epochs;

· *study of the variability at different wavelengths*: the minimum time scale observed in flux variations at any wavelength is related to the maximum size of the emitting region; cross-frequency time lags help to establish the relative location of the emission region at different frequencies;

· *radio interferometric imaging (in particular, mm-VLBI images)*: we can study the evolution of the parsec to kiloparscec scale jet with angular resolutions of 0.1 milliarcseconds or less. This provides information on superluminal motions inside the jet, appearance or disappearance of radio knots that could be related to high energy flares and peculiar changes of the polarized flux on very small angular scales;

· *study of the polarized flux at different wave-bands*: polarization provides information on the degree of ordering of the magnetic field and the mean direction of the field, and it is also an additional tool for the cross-frequency identification of emission regions.

Radio interferometric images and, in particular, millimeter-VLBI images are a key tool among those mentioned above. Infrared and high energy observations have worst angular resolutions with regard to those of mm-VLBI observations and therefore multi-epoch VLBI images are necessary to determine where flares take place in the jet. Moreover, comparing the time scale of variability of radio knots with their size we can infer the Doppler factor related to each observed knot (e.g. Jorstad et al., 2005). This allows deriving the Lorentz factor and the angle between the direction of these knots and the line of sight. The Doppler factor, the Lorentz factor, and the viewing angle are key parameters in revealing changes in the jet that can be related to events at the remaining observing frequencies.

In the studies presented in this thesis we compile data at different wavebands and we performed the analysis of data making use of all techniques outlined above. In particular, the γ-ray data come from NASA's *Fermi* space observatory and the VLBI data from observations at different frequencies obtained with the Very Long Baseline

Array (VLBA). Also, low resolution observations with the Karl G. Jansky Very Large Array (JVLA) have been performed in the analysis of M 87 jet (see Chapter 5).

In the coming sections, after a brief description of the main instruments involved in our studies, we explain how the calibration process of VLBI data was performed. In fact, while the calibration of *Fermi* data is well explained in both studies where we used γ-ray data (Casadio et al., 2015a,b), the calibration of VLBA data is not explained in detailed in any of the three publications presented in this thesis.

3.2.1 The *Fermi* gamma-ray Space Telescope

The *Fermi* satellite was launched by NASA on 11 June 2008 as the γ-ray Space Telescope (GLAST) and renamed *Fermi γ-ray Space Telescope* when the mission started (04 August 2008). It orbits the Earth at $\sim$565 km altitude with an orbital period of about 96 minutes (a Low Earth Orbit in the space mission argot).
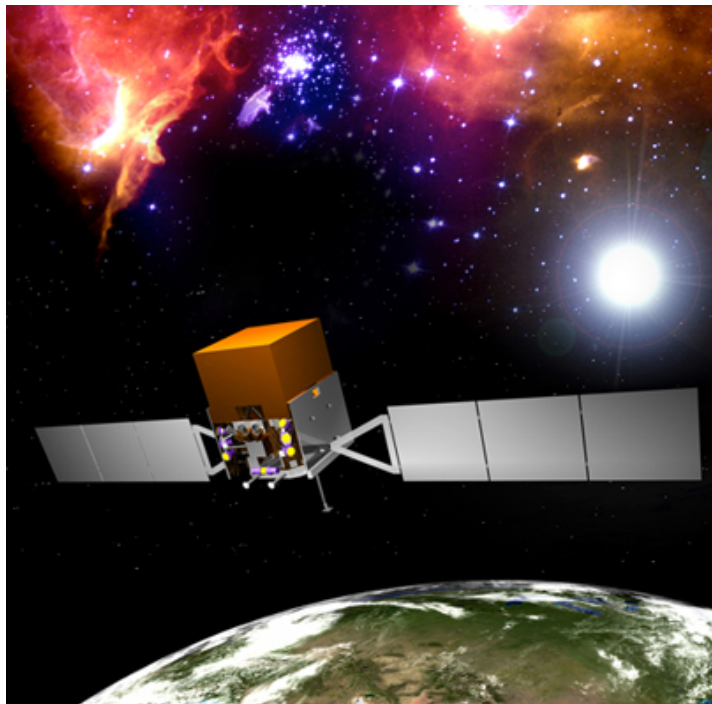

Figure 3.2: The Artistic representation of the NASA's *Fermi* gammma-ray Space Teelescope. An artistic image of the NASA's space telescope Fermi. Credit: NASA artist's concept.

There are two scientific instruments on board, the Large Area Telescope (LAT) and the γ-ray Burst Monitor (GBM). The LAT is a pair-conversion telescope designed to measure the direction, energy (from 20 MeV to 300 GeV) and arrival time of γ-ray photons over a large field of view ($\sim 20\%$ of the sky at 1GeV), while rejecting the background of cosmic rays. In order to take full advantage of the LAT large field of view, *Fermi* operates primarily in scanning survey mode in which the telescope is pointed north and south of zenith in alternate orbits. As a result, after two orbits, about 3 hours, an almost uniform sky exposure is obtained. Making use of the observing results from its survey mode, the *Fermi*-LAT collaboration have produced so far three catalogs with the detected γ-ray sources and the corresponding counterparts at lower energies (if available), where the third catalog (3FGL; Acero et al., 2015) is the most updated and complete one. In addition to these catalogs containing all the γ-ray sources detected by *Fermi*, others catalogs containing only the AGN lists and related studies have been reported in the LAT Bright AGN Sample (LBAS; Abdo et al., 2009), and three LAT AGN catalogs (Abdo et al., 2010; Ackermann et al., 2011, 2015), where the last one, 3LAC, is the most updated and complete one.

The 3FGL catalog includes 2192 γ-ray sources detected at Galactic latitudes larger than $10°$. Among these 2192 sources, 71% of them are associated with AGN and form the 3LAC. Only 2% of these AGN are non-blazar AGN, and among this 2% the majority of them are radio galaxies. Radio galaxies, that belong to the misaligned AGN class, are not favored GeV sources, as previously explained at the beginning of this Chapter.

3.2.2   The Very Long Baseline Array

The VLBA consists in 10 antennas of 25 meters in diameter, located across the USA territory and controlled remotely from the National Radio Astronomy Observatory in Socorro (New Mexico).

The antennas are distributed in such a way that there is a reasonably number of them with short baselines (distances between them), which is necessary to image extended and weak structures, as well as with long baselines to map the observed sources at the finest angular resolutions. In interferometry the maximum baseline length between two antennas represents the "equivalent diameter" (D) of the instrument, which provides an estimate of the angular resolution (θ) that can be achieved by the instrument according to the Airy formalism $\theta \propto \lambda/D$, being λ the observed wavelength.

The sites hosting the antennas are: Mauna Kea (Hawaii), Brewster (Washington), Owens Valley (California), Kitt Peak (Arizona), Pie Town (New Mexico), Los Alamos (New Mexico), Fort Davis (Texas), North Liberty (Iowa), Hancock (New Hampshire), St. Croix (Virgin Islands). The maximum baseline length of the VLBA is about 8600 km and corresponds to the baseline between Mauna Kea and St. Croix antennas, providing for 7 mm observations an angular resolution of ∼0.15 mas.
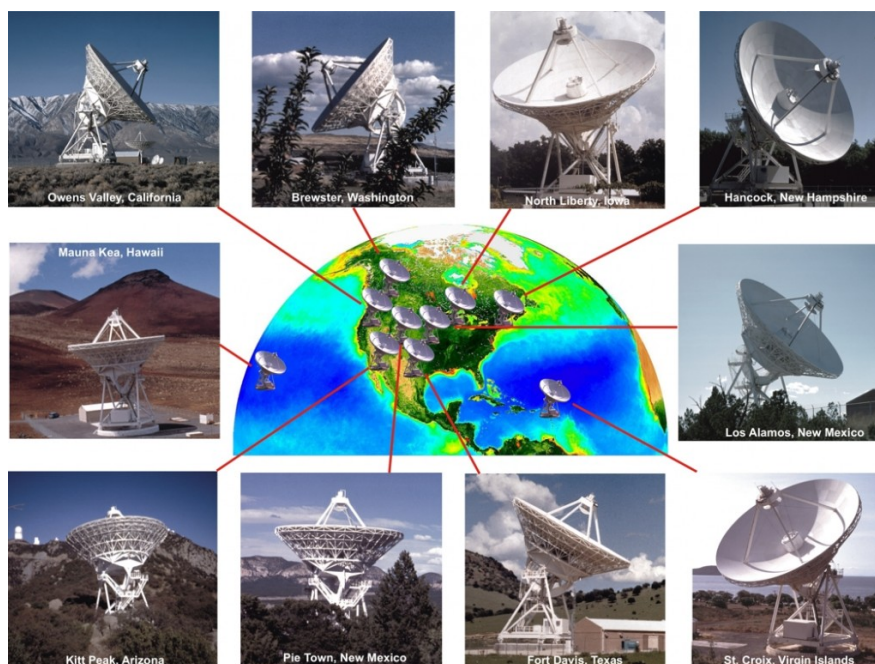
Figure 3.3: The Very Long Baseline Array. Panoramic view and localization of the 10 antennas forming the VLBA. Credit: NRAO/AUI and for the Earth image, the SeaWiFS Project NASA/GSFC and ORBIMAGE.

3.2.3   The Jansky Very Large Array

The Very Large Array (VLA), built at the end of the 70's in Socorro (New Mexico, USA), is one of the oldest astronomical radio observatories in the world. It is formed by 27 antennas, each with a diameter of 25 meters and arranged along the arms of an upside-down Y, as seen in Figure 3.4. The antennas can move along the arms forming four different configurations denoted as D, C, B and A, from the most compact to the most extended one. All VLA antennas have eight receivers providing continuous

frequency coverage from 1 to 50 GHz thanks to a recent improvement of the receivers to extend their bandwidth and sensitivity. The new improved VLA was renamed Karl G. Jansky Very Large Array (JVLA) in honor of the famous radio astronomer.

Figure 3.4: The Jansky Very Large Array. Part of the JVLA antennas in Socorro (New Mexico) at the twilight. Credit: NRAO.

3.2.3.1 Interferometric data

Each antenna forming the interferometer register the electromagnetic waves coming from the observed source. Afterwards, all signals coming from the antennas are collected at the correlator center, where they are combined and corrected for time delays due to the different arrival times at the different sites where the antennas are located, therefore forming a partly-sampled synthetic wave-front. The output of the correlator is a complex function called "fringe visibility function" or more simply "visibility function", whose amplitude and phase are the Fourier components of the sky brightness convolved with the *beam* of the instrument. The *beam* or *power pattern* or *Point Spread Function* (PSF), the latter mainly used at optical wavelength, is the response of the antenna to the observation of a point source at the center of the field and describes how the energy of a plane wavefront is distributed on the focal plane of the instrument. An
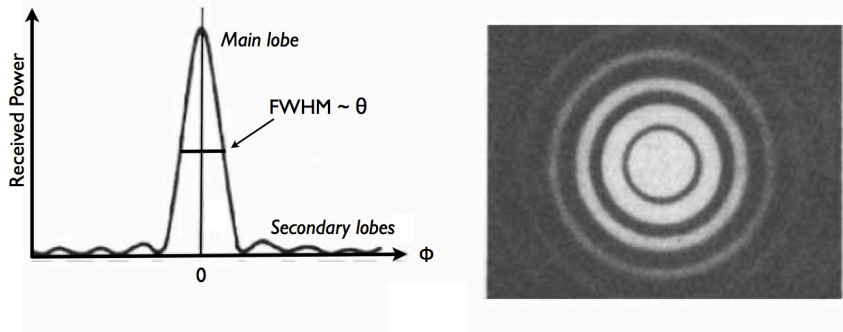
Figure 3.5: The antenna power pattern. In both figures we appreciate the main lobe and the secondary lobes of the diffraction pattern produced by the observation of a point source by a radio telescope. In the graphic, the x-axis represents the angular distance with regard to the axis of the antenna and the y-axis represent the power received by the antenna. The FWHM gives an estimate of the resolution of the antenna (θ).

example of power pattern is shown in Figure 3.5, where the full width half maximum (FWHM) of the main lobe gives an estimate of the resolution of the instrument (θ).

The visibility function, V(u,v), depends on coordinates of the uv plane, which is the reference plane tangent to the celestial sphere in the direction of the observed source (i.e. the Fourier conjugate of the image celestial plane). On the uv plane, the baselines distances between all antennas as are seen from the source represent the uv coverage (Figure 3.6).

The u-axis represents the East-West direction and the v-axis the North-South direction. The rotation of the Earth makes the locations of the antennas, as seen by the source, to change with time and this produces a better coverage of the uv plane that later translates into a better image fidelity. Indeed a better coverage of the Fourier space should translate on a better reconstruction of the image plane.

After correlation, the data are still not ready to produce a final image. Before that, the amplitudes and phases of the visibility function still need further corrections. Calibration of amplitudes is important because errors in amplitude can produce non-real structures. Even more important, the phases of the visibility function are still subject to variations in time (rates) and in frequency inside the observing bandwidth (group delays) because of many instrumental and atmospheric causes: changes in the electronic of the instrument related to changes in temperature, extra path introduced by different antennas cables, changes in atmospheric conditions, imprecisions in pointing

of some antennas, delays due to the ionosphere, etc.
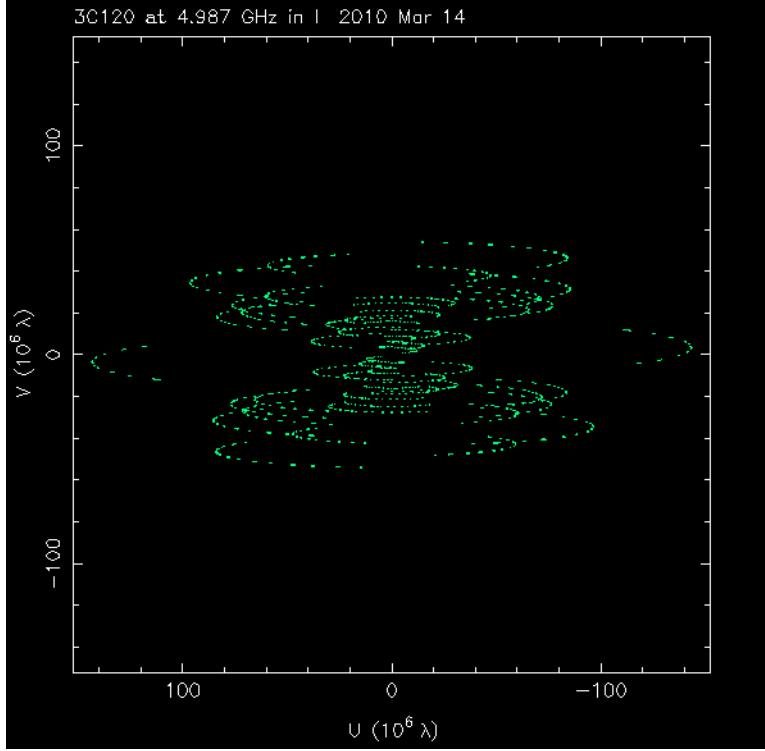
Figure 3.6: The UV plane. The UV plane coverage corresponding to the observation (presented in this thesis) made on 14th March 2010 of the radio galaxy 3C 120 with the VLBA at 5 GHz.

3.2.3.2 Amplitude and phase calibration

Calibration of the VLBA data has been performed within the Astronomical Image Processing System (`AIPS`) following the standard procedure for VLBI polarimetric observations (Leppanen et al., 1995).

Phases were first corrected for the dispersive delays introduced by the ionosphere using Global Position System (GPS) models of the electron content in the ionosphere. Time dependent corrections of the Earth Orientation Parameters (EOPs), which take into account the different orientation of the antennas with time with regard to the source because of the earth rotation, were then applied. Afterwards the amplitude calibration, which uses informations contained in two calibration channels, the GC

50

(Gain Curve) and TY (System Temperature) table, was applied. The GC table contains measurements of the efficiency of each antenna, which depends mainly on the elevation of the antenna and hence on the position of the source in the sky. The TY table contains measurements of the system temperature of the antennas. These are related to weather conditions and performance of the receiver. The amplitude calibration also converts the amplitude values of the visibility function into physical units.
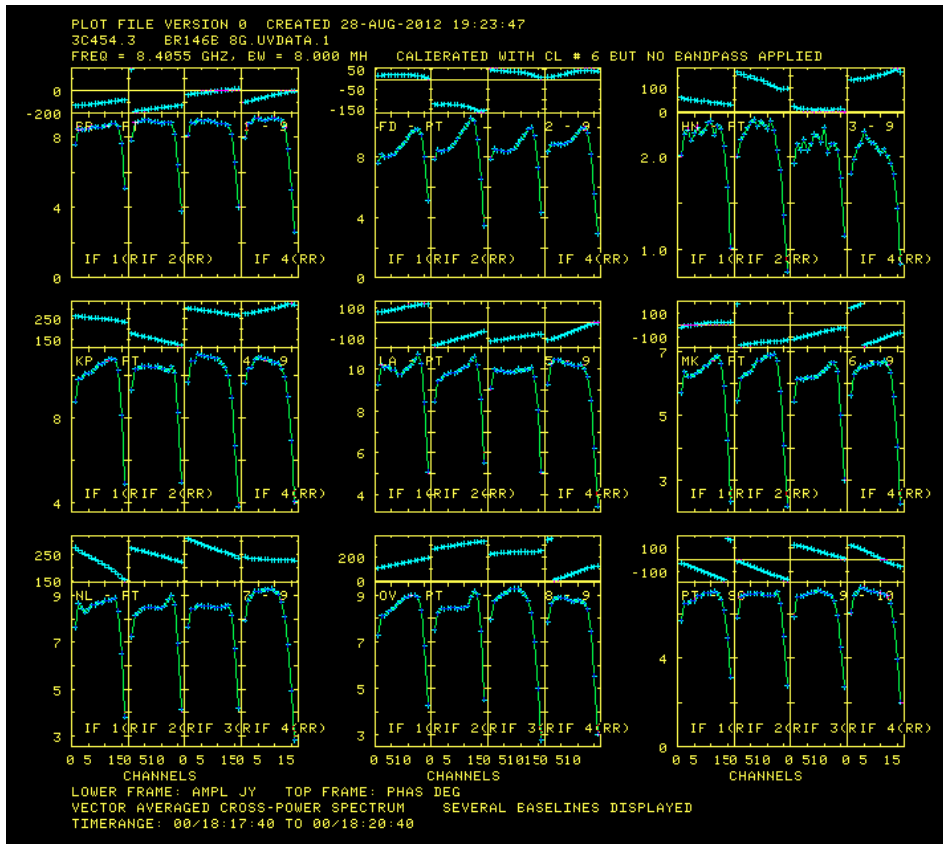
Figure 3.7: VLBI visibility data with phases affected by delays. The data presented in this figure were taken from one of the 8 GHz VLBA observations of 3C 120 presented in this thesis. The nine plots represent the visibility data for baselines between the antenna in Pie Town and the remaining 9 VLBA antennas. Every one of the nine insets shows the phases (panels above) and the amplitudes (panels below) of the visibility function for every baseline. The bandwidth of the receiver for each baseline is divided into four sub-bands (usually called intermediate frequencies [IF]) and each IF is subdivided into 16 channels (represented by each of the blue points). The phases here are affected by delays.

At this point, if the amplitude calibration is satisfactory, the calibration of the phases of the visibility data is the next step to do. First the phases are corrected considering the parallactic angle of each antenna, which changes in time with the source tracking. This calibration is important for polarimetric observations because the two (orthogonally polarized) receivers involved in a polarimetric observation, the right circularly polarized (RCP) and the left circularly polarized (LCP) one, rotate in position angle with regard to the source during the observation and this introduces a geometric effect that has to be corrected.
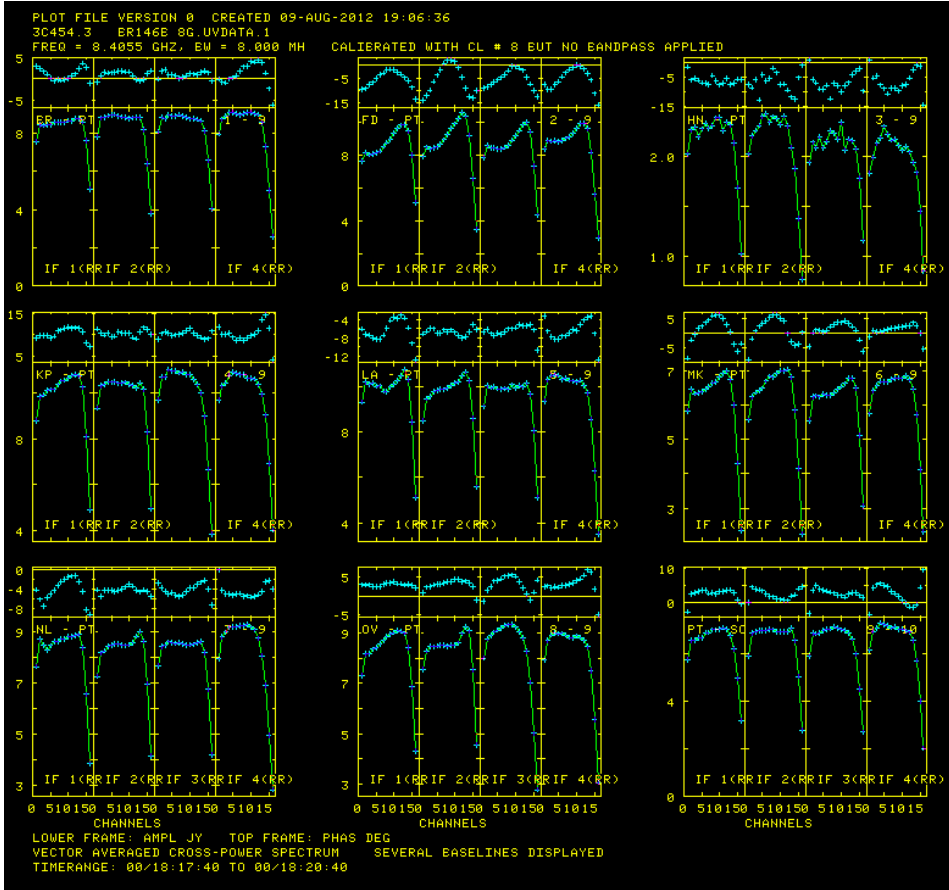
Figure 3.8: The visibility data with phases corrected for delays. The visibility data of the scan in Figure 3.7 after the correction using the pulse calibration. The phases now do not exhibit large changes among the IFs (note the different scales of the plot for phases with regard to Figure 3.7.)

The next step is to correct phase variations along the observing frequency bandwidth (the delays) introduced by the passage of the signal thought the different electronics on each of the VLBA backends. An example of data affected by these delays is shown in Figure 3.7. These delays are removed using the "pulse-cal" system, which consists of a series of pulses of well-known time and frequency interval introduced during the observation yielding a pulse-cal (PC) table to apply to the data. In Figure 3.8 we appreciate how phases displayed in Figure 3.7 have been corrected by the pulse calibration.

The phases after the pulse calibration can still exhibit residual rates and second order delays. The last step of the phase calibration is the *global fringe-fitting* as described by Schwab & Cotton (1983). The global fringe-fitting searches peaks in amplitude and phase (the fringes) in a determined integration time. The integration time used to search for fringes, usually between 1 and 3 minutes, has to be sufficiently large to have a good signal to noise ratio, and not so large to avoid coherence losses in the signal because of ionospheric and tropospheric variations. When the source of interest is bright enough, as in our case, the fringe fitting can be done directly on the source, while in case of weak sources a phase calibrator is needed. After applying fringe-fitting solutions the visibility data are ready for imaging and self-calibration using a combination of `AIPS` and the Differential Mapping (`Difmap`) packages.

3.2.3.3   Imaging and self-calibration

The amplitudes and phases of the data can still display minor errors which, together with secondary lobes (due to the *beam*) and grating lobes (due to lack of points in the uv plane), produces an imperfect image (the dirty image). This implies a difficult image reconstruction process where it is necessary to pay special attention to the iterative process. This is because there is not a unique solution and it is necessary to make sure that the process converges adequately from the beginning. The main difficulty in image reconstruction consists in choosing plausible visibility distributions for those points of the uv plane where we do not have information because of the incomplete coverage of the uv plane. At the same time, it is necessary to take care of any spurious emission in the dirty image produced by secondary lobes.

There are many methods to reconstruct an image but the most widely used is the CLEAN algorithm (Högbom, 1974). CLEAN starts selecting the region containing the source and choosing the number of iterations to perform. In each iteration, the

CLEAN algorithm searches for the intensity peak inside the selected region and, after convolving it with the dirty beam, it is subtracted from the dirty map. In this way the CLEAN algorithm removes the intensity peaks of the map together with secondary lobes due to the beam, and it also records the position and values of the point sources subtracted in a model. This process stops when the maximum value of the residual map (the image containing the remained flux after subtraction) is smaller than the estimated noise of the image. Afterwards, the image is reconstructed by adding to the last residual map the components found by CLEAN on previous iterations but only after having convolved them with a clean beam, usually a Gaussian function with the same FWHM of the dirty beam, in order to maintain the correct angular resolution of the image.

The CLEAN components generate a source model used to self-calibrate visibility data, usually in an iterative process. When the differences between the model and the visibility data are no longer considerable we consider that we have obtained the final image.

3.2.3.4 Polarization calibration

The phases and delays corrected in previous steps were mainly related to the correlation Right–Right (RR) and Left–Left (LL) for different antennas (forming every pair of them a baseline). Also, corrections of cross-hand circular polarization correlations (this is, Right–Left and Left–Right circular polarization correlations) phases and delays are important. The calibration of RL and LR data are necessary for polarimetric imaging, since both the Q and U Stokes parameters images are obtained from the RL and LR correlations. Moreover, the determination of the R-L phase difference is equivalent to the determination of the polarization position angle (mentioned in § 2.1.1.3). We use a specific task in `AIPS` named RLDLY to correct R-L delays differences and after that the RL and LR phases should be continuos over the bandwidth and flat if the RR and LL phases are flat, meaning without residual delays.

Once the cross-hand phase calibration has been completed it is also necessary to correct for the instrumental polarization, also known as "D-terms", i.e. the crosstalk polarization terms between the different receivers at each station. In `AIPS` there are many tasks that correct for D-terms and they all write corrections in the antenna table (AN) that is later on applied to the data. Then, after executing one of these tasks,

the AN table contains corrections for D-terms associated to each antenna. The D-terms are instrumental terms, and therefore they are not expected to change with time unless the receiver system has changed (either programmed by the observatory or not). Therefore, as shown in Gómez et al. (2002), the D-terms can be used to calibrate the absolute orientation of EVPA across different VLBI observation. Ideally, the absolute orientation of the polarization would be obtained by observing a calibrator with stable EVPAs. However, this type of sources are almost non-existent for VLBI observations since the brightest sources (and therefore more suitable as calibrators), are blazars jets, which are characterized by a highly variable structure on milliarcseconds scales.

When quasi-simultaneous low resolution observations, as those performed with the JVLA or single-dish observatories, are available we achieve the absolute calibration of the EVPA by comparing the EVPA in low resolution observations with an integrated value of the EVPA in the VLBI images. Once we have the absolute orientation of the EVPA in at least one epoch, we can use the D-terms to obtain the absolute calibration at all the other epochs, after making sure that there were no instrumental changes in any of the stations forming the interferometer.

For the polarimetric study on the radio galaxy 3C 120 presented in this thesis, where we analyzed VLBA observations at three different frequencies (5, 8 and 12 GHz) during three observing epochs (December 2009, March and June 2010), we make use of both techniques as explained above. As described in detail in § 5.1, we performed the absolute calibration of the EVPA at 5 and 8 GHz in the first epoch (December 2009) taking advantage of the information contained in the VLA/VLBA Polarization Calibration Program [1] and we used the D-term method for the relative calibration at 5 and 8 GHz EVPAs in May and June 2010. The VLA/VLBA Polarization Calibration Program, started in 1999 and stopped producing public results in 2009 when the new JVLA started operating, was planned to offer continuous VLA monitoring of VLBA polarization calibrators. The lack of 12 GHz data in this program led us to use another method: we extrapolated the value of 12 GHz EVPAs from the Faraday rotation profile (described in § 2.1.1.4) where we included EVPA values at 5, 8 and 15 GHz; the latter obtained from the MOJAVE[2](Monitoring of Jets in Active Galactic Nuclei with VLBA

---

[1]http://www.vla.nrao.edu/astro/calib/polar/
[2]http://www.physics.purdue.edu/MOJAVE/

Experiments) program. Moreover, also in this case, the D-terms stability among epochs at 12 GHz has been used as further proof for the EVPA calibration.

In both multi-wavelength studies presented here (Casadio et al., 2015a,b), we also used 43 GHz VLBA data from our sources of interest (3C 120 and CTA102) from the Boston University Blazar monitoring program at the VLBA (VLBA-BU-BLAZAR)[1] which includes regular monthly observations of them, and other 35 bright radio AGN. The calibration of total intensity and polarization intensity of the entire data set was performed simultaneously for all objects in the Boston University sample. In this case, we inferred the mean values of the D-terms from sources that we considered better polarization calibrators and we applied them to all sources in the sample. We compared the mean D-terms among epochs for the relative calibration of the electric vector position angles and, in addition, we took a look at some strong calibrators in the sample having knots in their jets with reasonably stable EVPAs which provide an additional comparison method.

A more detailed explanation on the data set analyzed in each study is included in the corresponding section for each independent work shown below.

3.3   Previous multi-wavelength studies.

The first studies of variability at radio wavebands in connection with the γ-ray activity were carried out by Valtaoja & Terasranta (1995) and Valtaoja & Teraesranta (1996). They compared sources observed at 22 and 37 GHz with the 13.7 meter Metsähovi Radio Telescope with γ-ray detections by EGRET. They found a correspondence between γ-ray detections and radio activity and they interpreted this result as evidence for the common spatial location of the radio and γ-ray emission regions. Later on, radio monitoring using the VLBA at 22 and 43 GHz was compared with γ-ray measurements with EGRET in Jorstad et al. (2001). In this work the authors found that in most cases γ-ray flares were related to the appearance of new superluminal components.

Currently the two most comprehensive VLBI monitoring programs of the northern hemisphere are the VLBA−BU−BLAZAR program and the MOJAVE program, both of them sensitive to both total and polarized intensity.. The VLBA-BU-BLAZAR program is pioneering in mm-VLBI and multi-frequency studies of AGN. It consists

---

[1]https://www.bu.edu/blazars/VLBAproject.html

of monthly polarimetric observations of 36 γ-ray blazars and radio galaxies with the VLBA at 43 GHz (7 mm) plus observations of the 17 brightest AGN of the sample with the Global mm-VLBI Array (GMVA) at 90 GHz (3 mm) every 6 months (e.g. Jorstad et al., 2013). Moreover, several research groups collaborate to this program with data from many telescopes and at different wavelength in order to extend the monitoring of these 37 AGN to the entire electromagnetic spectrum. The research group in Granada participates in the collaboration with the ongoing polarimetric programs MAPI and POLAMI, where we observe the sources at 1 and 3mm with the 30m Telescope of the Institut de Radioastronomie Millimétrique (IRAM) located at the Pico Veleta Observatory in Sierra Nevada (Granada, Spain), and with the MAPCAT program, where the same sample is observed with the 2.2m Optical Telescope of the Calar Alto Observatory in Almeria (Spain). Both programs observe both, in total flux and in polarimetric data. In the case of the IRAM 30m Telescope, even circular polarimetric data is recorded. During my PhD, I performed about half of the observations carried out with the IRAM telescope. I also reduced a relevant part of the optical data obtained from the Calar Alto telescope. The MOJAVE program provides long-term systematic monitoring of an extended sample of AGN with the VLBA at 15 GHz (2 cm) (e.g. Lister et al., 2009). One of the main goals of this program is to characterize the kinematics and polarization evolution of AGN jets, providing also parsec-scale structural informations on over 100 AGN jets observed with the *Fermi* γ-ray space telescope.

Statistical studies between the MOJAVE sample and *Fermi* catalogs reveal that, among the brightest radio loud blazars in the sample, AGN non-detected by *Fermi* have lower Doppler factors with regard to other AGN displaying prominent γ-ray emission. Also larger Doppler factors are in many cases related to jets oriented at smaller viewing angles (Pushkarev et al., 2014). Another result from the MOJAVE program is that synchrotron self Compton mechanism is favored for the γ-ray emission in BL Lac objects (Lister et al., 2011). We also found a similar result in Williamson et al. (2014), where we analyzed 4 years of multi-wavelength data of a sample of 33 γ-ray bright blazars. In Williamson et al. (2014) we also reported how FSRQ display the highest amplitudes of γ-ray outbursts and the largest variations of γ-ray spectral indices between quiescent and active states. In contrast, in BL Lacs where different activity states have similar characteristics, the same mechanism should be responsible for the quiescent and flaring γ-ray states. From statistical studies on the AGN sample of the VLBA−BU−BLAZAR

program it is found that more than 50% of γ-ray flares occurred in the mm-core, which lies parsecs away from the black hole in luminous blazars, and are associated with the ejection of a new superluminal component (Marscher et al., 2012). This confirms previous results from VLBA and EGRET observations (Jorstad et al., 2001). Also, X-ray emission in blazars seems to come predominantly from regions close to the mm-core (Marscher et al., 2004; Sokolov et al., 2004).

However, we also observe cases of AGN where γ-ray or X-ray and optical flares occur before any variability in the mm-VLBI core is obtained (e.g. Jorstad et al., 2005), or where the γ-ray spectral break at few GeVs probably due to pair production opacity (see S 3.1 for more details) is observed (Poutanen & Stern, 2010). The photon-photon pair production is expected to occur where a high density of atomic nuclei is present (i.e., the BLR). These evidences point to a location of the high energy site closer to the central engine than what our work predicts. A significant progresses toward revealing the location and mechanism of high energy emission in AGN have been obtained through multi-waveband monitoring observations. However, the variety of objects and characteristics displayed is so wide that still more information is necessary to obtain a complete model.

4

Multi-wavelength polarimetric studies of the radio galaxy 3C 120 and the blazar CTA 102

In this chapter we present the multi-wavelength and polarimetric studies performed on the radio galaxy 3C 120 and the blazar CTA 102 in their original format, as published in the international, hight-impact, peer-reviewed journal *The Astrophysical Journal*.

Both sources have been observed in coincidence with unprecedented γ-ray flares registered by the *Fermi* satellite. The *Fermi* LAT registered in September-October 2012 an extraordinary bright γ-ray outburst in the quasar CTA 102, and between December 2012 and October 2014 a prolonged γ-ray activity in the radio galaxy 3C 120. In CTA 102, also very bright flares at both optical and near infrared wavelengths have been observed in the same period. In both studies the analysis of γ-ray data has been compared with a series of 43 GHz VLBA images from the VLBA-BU-BLAZAR program, providing the necessary spatial resolution to probe the parsec scale jet evolution during the high energy events. In the case of 3C 120, to extend the observing period covered by radio data, we also used 15 GHz VLBA data from the MOJAVE sample. For the CTA 102 study we extend the analysis to the entire electromagnetic spectrum, collecting data from many ground telescopes and satellites.

4.1 The Connection between the Radio Jet and the Gamma-ray Emission in the Radio Galaxy 3C 120

The following article has been published in *The Astrophysical Journal* on August 1st, 2015 and it is reproduced here in its entirety an in its original format.

The reference for this article is: Casadio C., Gómez J. L., Grandi P., et al., 2015, ApJ, 808, 162.

The authors are: Carolina Casadio, José L. Gómez, Paola Grandi, Svetlana G. Jorstad, Alan P. Marscher, Matthew L. Lister, Yuri Y. Kovalev, Tuomas Savolainen and Alexander B. Pushkarev.

THE CONNECTION BETWEEN THE RADIO JET AND THE GAMMA-RAY EMISSION IN THE RADIO GALAXY 3C 120

Carolina Casadio[1], José L. Gómez[1], Paola Grandi[2], Svetlana G. Jorstad[3,4], Alan P. Marscher[3], Matthew L. Lister[5], Yuri Y. Kovalev[6,7], Tuomas Savolainen[8,7], and Alexander B. Pushkarev[7,9,10]

[1] Instituto de Astrofísica de Andalucía, CSIC, Apartado 3004, E-18080, Granada, Spain
[2] Istituto Nazionale di Astrofisica-IASFBO, Via Gobetti 101, I-40129, Bologna, Italy
[3] Institute for Astrophysical Research, Boston University, 725 Commonwealth Avenue, Boston, MA 02215, USA
[4] Astronomical Institute, St. Petersburg State University, Universitetskij Pr. 28, Petrodvorets, 198504 St. Petersburg, Russia
[5] Department of Physics, Purdue University, 525 Northwestern Avenue, West Lafayette, IN 47907, USA
[6] Astro Space Center, Lebedev Physical Institute, Russian Academy of Sciences, Profsoyuznaya str. 84/32, Moscow 117997, Russia
[7] Max-Planck-Institut für Radioastronomie, Auf dem Hügel 69, D-53121 Bonn, Germany
[8] Aalto University Metsähovi Radio Observatory, Metsähovintie 114, FI-02540 Kylmälä, Finland
[9] Pulkovo Observatory, Pulkovskoe Chaussee 65/1, 196140 St. Petersburg, Russia
[10] Crimean Astrophysical Observatory, 98409 Nauchny, Crimea, Russia

ABSTRACT

We present the analysis of the radio jet evolution of the radio galaxy 3C 120 during a period of prolonged γ-ray activity detected by the *Fermi* satellite between 2012 December and 2014 October. We find a clear connection between the γ-ray and radio emission, such that every period of γ-ray activity is accompanied by the flaring of the millimeter very long baseline interferometry (VLBI) core and subsequent ejection of a new superluminal component. However, not all ejections of components are associated with γ-ray events detectable by *Fermi*. Clear γ-ray detections are obtained only when components are moving in a direction closer to our line of sight. This suggests that the observed γ-ray emission depends not only on the interaction of moving components with the millimeter VLBI core, but also on their orientation with respect to the observer. Timing of the γ-ray detections and ejection of superluminal components locate the γ-ray production to within ∼0.13 pc from the millimeter VLBI core, which was previously estimated to lie about 0.24 pc from the central black hole. This corresponds to about twice the estimated extension of the broad line region, limiting the external photon field and therefore suggesting synchrotron self Compton as the most probable mechanism for the production of the γ-ray emission. Alternatively, the interaction of components with the jet sheath can provide the necessary photon field to produced the observed γ-rays by Compton scattering.

Key words: galaxies: active – galaxies: individual (3C120) – galaxies: jets – radio continuum: galaxies

Supporting material: machine-readable tables

1. INTRODUCTION

In the unified scheme of active galactic nuclei (AGNs), Fanaroff–Riley radio galaxies of type I (FRI) and II (FRII) are considered the parent population of BL Lacs and flat spectrum radio quasars (FSRQs), respectively. FRI and FRII radio galaxies belong to the misaligned AGN class, as they are oriented at larger viewing angles than blazars (the most luminous and variable BL Lac objects and FSRQs). Relativistic beaming amplifies the emission of jets pointing toward the observer, making blazars the brightest objects in the extragalactic sky also in the γ-ray band. In fact, among the more than 1000 extragalactic sources detected by the Large Area Telescope (LAT) on board the *Fermi* Gamma-Ray Space Telescope in 2 years, only 3% of them are not associated with blazar objects. FRI and FRII radio galaxies fall inside this 3%, with the predominance of nearby radio galaxies of type I (Grandi et al. 2012a). FRII radio galaxies with GeV emission are rare, 3C 111 being the only FRII so far with a confirmed *Fermi* counterpart. 3C 111 is also the first FRII radio galaxy where a γ-ray flare has been associated with the ejection of a new bright knot from the radio core (Grandi et al. 2012b). The simultaneity of the observed flare in millimeter, optical, X-ray and γ-ray bands led Grandi et al. (2012b) to claim that the GeV dissipation region is located at a distance of about 0.3 pc from the central black hole (BH).

The rapid γ-ray variability observed in FRI radio galaxies, with time scales of months in the case of NGC 1275 (Abdo et al. 2010; Kataoka et al. 2010), or even days for the case of the TeV variability in M87 (Aharonian et al. 2006; Harris et al. 2011), suggests that the γ-ray emission in these sources originates also in a very compact jet region. Results from over 10 years of multiwavelength observations of M87 (Abramowski et al. 2012) suggest that the very high energy flares may take place in the core (for the case of the 2008 and 2011 TeV flares), or in the HST-1 complex, about $0\rlap{.}''8$ downstream of the jet (in the case of the 2005 TeV flare). More recently, Hada et al. (2014) found that the last TeV flare occurred in M87 in 2012 originates in the jet base, within 0.03 pc from the BH, but no correlation with the MeV–GeV light curve obtained by *Fermi* has been found.

Recently, the LAT detected an unprecedented γ-ray flare from the FRI radio galaxy 3C 120 on 2014 September 24th, when the source reached a daily flux ($E > 100\,\mathrm{MeV}$) of $1.0 \pm 0.3 \times 10^{-6}\,\mathrm{photon\,cm^{-2}\,s^{-1}}$, as reported in Tanaka et al. (2014). This recent flare appears to be associated with a higher state of γ-ray activity in the source. In fact, since 2012 December the radio galaxy 3C 120 registered a series of γ-ray events, indicating a flaring activity that lasted until at least our last data were analyzed, in 2014 October 4.

1

The radio galaxy 3C 120 ($z = 0.033$) presents an FRI morphology, but it also has a blazar-like radio jet, showing multiple superluminal components at parsec scales (Gómez et al. 2000, 2001, 2011), as well as at distances as large as 150 pc in projection from the core (Walker et al. 2001). This radio galaxy also reveals X-ray properties similar to Seyfert galaxies, with the X-ray spectral slope increasing with intensity (Maraschi et al. 1991), and a prominent iron emission line at a photon energy of 6.4 KeV. This implies that most of the X-ray emission comes from or near the accretion disk, rather than in the jet. In addition, the observed strong correlation between dips in the X-ray emission and the ejection of new super-luminal components in the radio jet (Marscher et al. 2002; Chatterjee et al. 2009) reveals a clear connection between the accretion disk and the radio jet.

In this paper we present the first association of γ-ray emission and the ejection of new superluminal components in a FRI radio galaxy, 3C 120. This resembles the recent findings on the FRII radio galaxy 3C 111 (Grandi et al. 2012b). We present the radio data set analyzed in this study, as well as methods used to reduce radio data in Section 2; in Section 3 we present the analysis and results of the *Fermi*-LAT data; in Section 4 we study the radio emission at 15 and 43 GHz in the parsec scale jet; Section 5 presents the connection between the γ-ray and radio emission, and in Section 6 we discuss our findings.

The cosmological values adopted from Planck's results (Planck Collaboration et al. 2014) are $\Omega_m = 0.3$, $\Omega_\Lambda = 0.7$, and $H_0 = 68$ km s^{-1} Mpc^{-1}. With these values, at the redshift of 3C 120 ($z = 0.033$) 1 mas corresponds to a linear distance 0.67 pc, and a proper motion of 1 mas yr^{-1} corresponds to an apparent speed of $2.21c$.

2. RADIO DATA ANALYSIS

To study the structure of the radio jet in 3C 120 we have collected data from two of the most extended Very Long Baseline Array (VLBA) monitoring programs: the MOJAVE[11] and the VLBA-BU-BLAZAR programs.[12] This radio data set consists of 46 epochs of VLBA data at 15 GHz taken from the MOJAVE survey, covering the observing period from 2008 June to 2013 August, and 21 epochs of VLBA data at 43 GHz from the VLBA-BU-BLAZAR program, covering the period from 2012 January to 2014 May.

The reduction of the VLBA 43 GHz data has been performed using a combination of AIPS and Difmap packages, as described in Jorstad et al. (2005). VLBA data at 15 GHz have been calibrated by the MOJAVE team, following the procedure described in Lister et al. (2009a). For comparison across epochs all the images have been convolved with a mean beam of 0.3×0.15 and 1.2×0.5 mas for the VLBA-BU-BLAZAR and MOJAVE programs, respectively.

To determine the structural changes in the radio jet we have modeled the radio emission through fitting of the visibilities to circular Gaussian components using Difmap (Shepherd 1997). Fitted values for each component are the flux density, separation and position angle (PA) from the core, and size. These are tabulated in Tables 1 and 2 for the 15 and 43 GHz data, respectively.

3. *FERMI*-LAT DATA ANALYSIS

The LAT data collected during 72 months of operation (from 2008 August 4 to 2014 August 4)[13] were analyzed using the *Fermi*-LAT ScienceTools software (version v9r32p5) and the P7REP_SOURCE_V15 set of instrument response functions (Ackermann et al. 2012).[14] The time intervals when the rocking angle of the LAT was greater than 52° were rejected and a cut to select a maximum zenith angle of 100° of the events was applied to exclude γ-rays originating from cosmic ray interactions with the Earth's atmosphere.

The detection significance of a source is provided by the TS $= 2[\log L(\text{source}) - \log L(\text{no source})]$, where $L(\text{source})$ is the maximum likelihood value for a model with an additional source at a specified location and $L(\text{no source})$ is the maximum likelihood value for a model without the additional source (Mattox et al. 1996). When the TS is less than 10 or the ratio of the flux uncertainty to the flux is more than 0.5, a 2σ upper limit of the flux is provided. Depending on the TS value, the upper limits are calculated using the profile (TS $\geqslant 1$) or the Bayesian (TS < 1) method as described in the second LAT catalog (2FGL catalog; Nolan et al. 2012). All errors reported in the figures or quoted in the text are 1σ statistical errors. The estimated systematic errors on the flux, 10% at 100 MeV, decreasing to 5% at 560 MeV, and increasing to 10% at 10 GeV, refer to uncertainties on the effective area of the instrument.[15]

3.1. The 72 Month Average Spectrum

We performed both binned and unbinned likelihood analyses following the standard LAT data analysis procedures, obtaining consistent results. Here we present results from binned analyses to be consistent with published data (Ackermann et al. 2011). We accumulated 72 months of data to obtain the average γ-ray spectral properties of the source. The adopted model included all 2FGL sources within 15° of 3C 120 (R.A. (J2000) $= 68°.2962313$, decl.(J2000) $= 5°.3543389$). The studied source was modeled with a power law. All spectral parameters of the sources more than 10° from the center of the Region of Interest (RoI) were fixed to the 2FGL values. The Galactic diffuse emission was modeled using the standard diffuse emission model *gll_iem_v05_rev1.fit* while isotropic γ-ray emission and the residual cosmic ray contamination in the instrument were modeled using the template *iso_source_v05.txt*.

3C 120 was detected in the 100 MeV–100 GeV band with a TS value of 107 ($\sim 10\sigma$). The source is steep (photon index $\Gamma = 2.7 \pm 0.1$) and weak with a flux of $F_{>100\text{MeV}} = 2.5 \pm 0.4 \times 10^{-8}$ photon cm^{-2} s^{-1}, in agreement with the result of Abdo et al. (2010). As noted by the same authors, a Flat Spectrum Quasar, PKS 0423+05, is located at only ~ 1.6 degrees from the radio galaxy. In our analysis, the blazar is soft ($\Gamma = 2.6 \pm 0.1$) and slightly fainter ($F_{>100\text{MeV}} = 1.77 \pm 0.36) \times 10^{-8}$ photon cm^{-2} s^{-1}) than 3C 120.
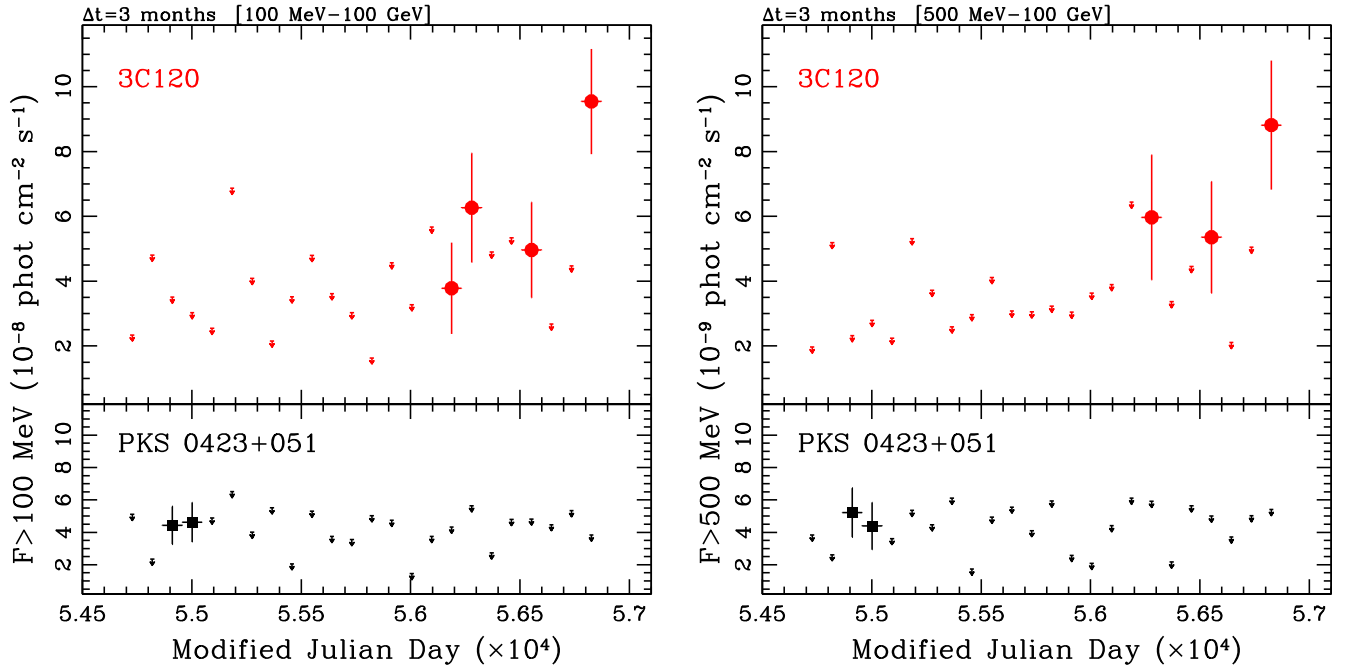
2

Figure 1. *Fermi*-LAT light curves of 3C 120 covering 72 month of survey (from 2008 August 4 to 2014 August 6) obtained considering two different energy bands: 100 MeV–100 GeV (left panel) and 500 MeV–100 GeV (right panel). A bin width of 3 months is adopted. A 2σ upper limit flux is shown (arrow) when the source is not detected (TS < 10). For comparison the light curves of the nearby FSRQ (PKS 0423+051) at $1°\!.6$ from 3C 120 are also shown in the same energy ranges. There is not significant overlapping, as 3C 120 and PKS 0423+051 appear to be active in different time intervals.

Table 1
VLBA 15 GHz Model-fit Components' Parameters

Epoch (year)	Epoch (MJD)	Name	Flux (mJy)	Distance From C0 (mas)	Pos. Angle (°)	FWHM (mas)
				VLBA 15 GHz		
2008.48	54642.50	C0	768 ± 38	⋯	⋯	0.31 ± 0.20
⋯		C1	271 ± 14	0.65 ± 0.08	-115.2 ± 6.7	0.49 ± 0.16
⋯		E0	117 ± 6	3.51 ± 0.24	-112.1 ± 3.6	0.79 ± 0.47
⋯		E1	392 ± 20	1.50 ± 0.04	-109.3 ± 1.4	0.32 ± 0.08
⋯		E1a	429 ± 21	1.14 ± 0.04	-106.2 ± 1.7	0.33 ± 0.08
2008.58	54677.50	C0	604 ± 30	⋯	⋯	0.22 ± 0.17
⋯		C1	443 ± 22	0.35 ± 0.03	-115.8 ± 5.3	0.31 ± 0.07
⋯		E0	123 ± 6	3.77 ± 0.26	-111.2 ± 3.7	0.88 ± 0.53
⋯		E1	455 ± 23	1.75 ± 0.04	-109.9 ± 1.3	0.38 ± 0.09
⋯		E1a	740 ± 37	1.31 ± 0.04	-110.0 ± 1.7	0.48 ± 0.09

(This table is available in its entirety in machine-readable form.)

3.2. Light Curves

Gamma-ray light curves were produced by dividing the analyzed time interval in temporal segments and repeating the likelihood analysis with only the normalizations of the sources within 10° free to vary. The spectral slopes of all the sources in the RoI were kept fixed to the best fit values of the 72 month likelihood analysis.

At first we produced a light curve from 2008 August 4 to 2014 August 4 with a bin size of 3 months in the 100 MeV–100 GeV energy band. The light curve shown in Figure 1 (left upper panel) indicates that 3C 120 was active starting from 2012. Abdo et al. (2010) reported also a detection between 2008 November and 2009 February. Our new analysis, which was performed with up-dated background files and new instrument response functions, provides only a flux upper limit for the same time interval (second bin of the light curve). Although we cannot claim a detection, the calculated TS value is however high (TS = 9.2, corresponding to ~3σ) and only slightly below the usually adopted detection threshold (TS = 10).

Considering that PKS 0423+051 is at only $1°\!.6$ from 3C120, that both sources have steep spectra and, that the LAT point-spread function (PSF) is very broad at MeV energies, we decided to explore the 3 month light curve of the quasar to check for possible confusion effects. As shown in Figure 1, PKS 0423+051 and 3C 120 flare in different periods and exhibit light curves with different patterns, suggesting a negligible (mutual) contamination.
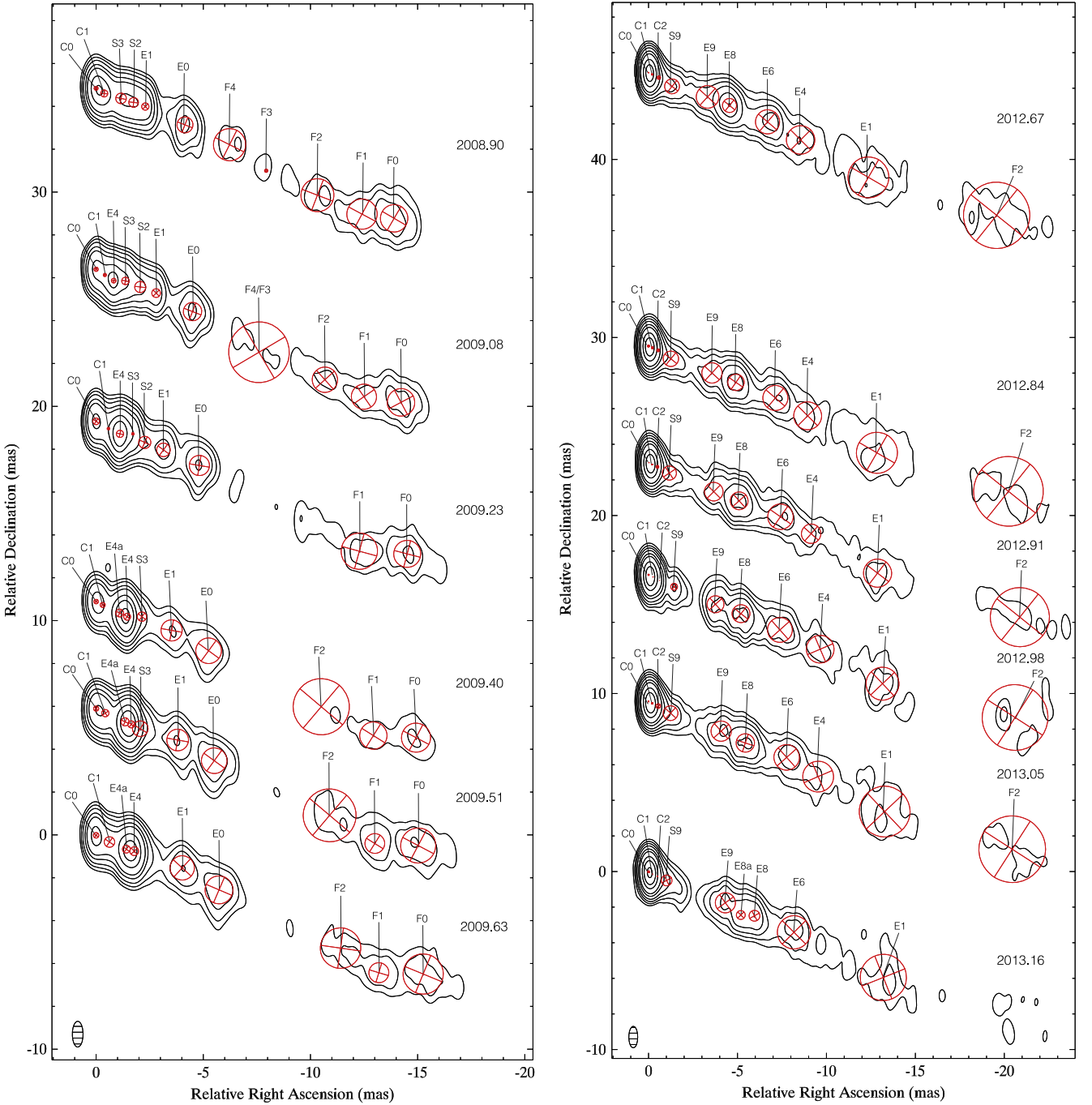
3

Figure 2. Sequence of total intensity 15 GHz VLBA images from the MOJAVE monitoring program of 3C 120 with a common restoring beam of 1.2 × 0.5 mas at 0°. The separation among images is proportional to the time elapsed between observing epochs. Contours are traced at 0.0015, 0.004, 0.009, 0.02, 0.05, 0.1, 0.3, 0.6, 1.2 Jy. Red circles represent model-fit components.

As further test, we also performed a variability study considering only photons with energy >500 MeV. Above this energy, the 68% containment angle (i.e., the radius of the circle containing 68% of the PSF) is indeed comparable or smaller than the separation of the two sources. The 500 MeV−100 GeV light curves (Figure 1, right panel) are similar to those obtained taking also into account softer photons, supporting the previous conclusion on negligible confusion effects.

Finally, we reduced the integration time interval of each bin to 15 days to better constrain the time of the γ-ray detections, shown in Table 3. In this case the analysis has been extended

until 2014 October to confirm the flare at the end of 2014 September reported in Tanaka et al. (2014). Our analysis yields a γ-ray flux of $2.52 \pm 0.86 \times 10^{-8}$ photon cm^{-2} s^{-1} in MJD 56924–56939 for the 2014 September event (see Table 3).

4. THE PARSEC SCALE JET AT 15 AND 43 GHz

4.1. VLBA Data at 15 GHz

The study of the jet evolution at 15 GHz has been performed on the series of 46 VLBA images obtained by the MOJAVE monitoring program—a subset of these images is displayed in
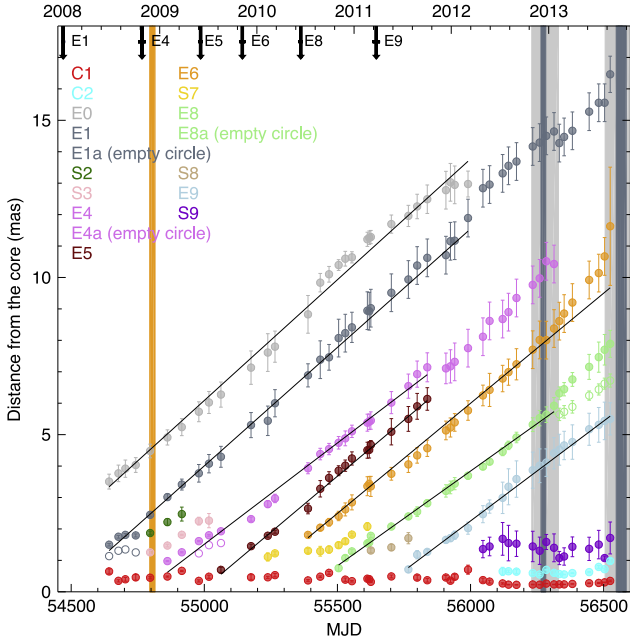
Figure 3. Distance from the core vs. time for the 15 GHz model-fit components with linear fits overlaid. Downward black arrows mark the time of ejection of each component. Gray vertical lines indicate γ-ray detections in the 15 day bin (dark gray) and 3 month bin (light gray) light curves in the energy band 500 MeV–100 GeV. The orange vertical line marks the optical flare reported in Kollatschny et al. (2014) (see text).
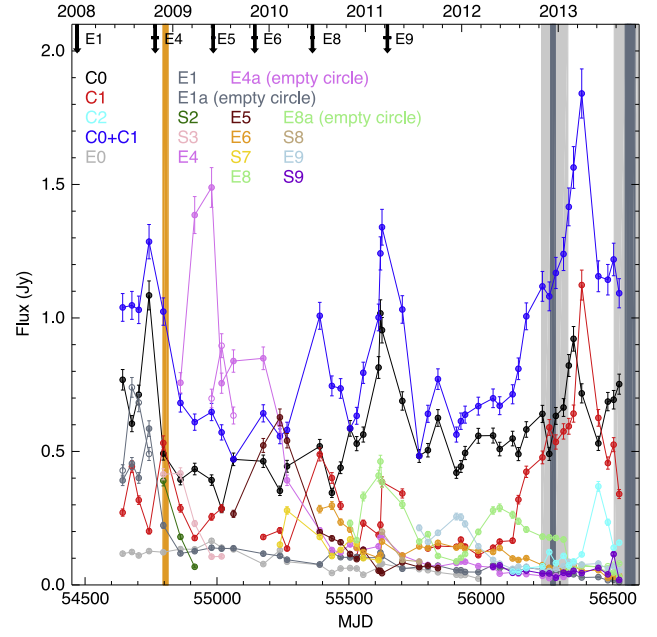
Figure 4. Light curves of the 15 GHz model-fit components, including the added total flux density of the core and component C1 (C0+C1). Arrows and vertical lines are as indicated in Figure 3.

Table 2
VLBA 43 GHz Model-fit Components' Parameters

			VLBA 43 GHz			
Epoch (year)	Epoch (MJD)	Name	Flux (mJy)	Distance From c0 (mas)	Pos. Angle (°)	FWHM (mas)
2012.07	55953.50	c0	708 ± 43	…	…	0.08 ± 0.03
…	…	d7	34 ± 13	0.13 ± 0.01	−124.8 ± 11.2	0.13 ± 0.04
…	…	d10	346 ± 26	0.13 ± 0.01	−123.7 ± 8.6	0.13 ± 0.03
2012.18	55991.50	c0	756 ± 45	…	…	0.08 ± 0.03
…	…	d7	66 ± 16	0.28 ± 0.05	−123.7 ± 20.4	0.16 ± 0.03
…	…	d10	264 ± 22	0.13 ± 0.02	−126.2 ± 11.5	0.14 ± 0.03
2012.25	56019.50	c0	372 ± 26	…	…	0.06 ± 0.03
…	…	d7	42 ± 13	0.41 ± 0.08	−122.8 ± 14.2	0.18 ± 0.03
…	…	d10	186 ± 18	0.13 ± 0.01	−113.1 ± 6.1	0.08 ± 0.03

(This table is available in its entirety in machine-readable form.)

Figure 2, where contours represent the total intensity with model-fit components (red circles) overlaid.

We detected in total 25 components, apart from the core, although some of them characterize more probably the underlying flux density than knots that have been ejected from the core and move along the jet. The radio core is usually defined as the bright, compact feature at the upstream end of the jet, which may correspond to a recollimation shock (i.e., Gómez et al. 1997) at millimeter wavelengths and to the optically thin–thick transition at centimeter wavelengths.

Components E-F and C are robustly identified moving and standing features, respectively, and the rest of the model-fit components are required by the data, but cannot be cross-identified across the epochs and may represent, e.g., emission

from the underlying jet flow. The core, identified with component C0, is considered stationary across epochs. Plots of the separation from the core and flux density evolution of the fitted components are shown in Figures 3 and 4, respectively.

We fit the trajectories with respect to the core for all the superluminal knots that can be followed for a significant number of epochs, as plotted in Figure 3. In order to have a better determination of the time of ejection of each component, namely the time when a new knot crosses the radio core, we use linear fits for the component separation versus time. Note that in some cases we have found evidence for components merging, splitting, or a clear acceleration in their motion (e.g., Homan et al. 2009, 2015). In those cases we have considered only the initial epochs with a clear linear fit, as we are mainly

interested in determining the time of ejection of each component. The time of ejection, angular and apparent velocities of the components are tabulated in Table 4.

We find that superluminal components move with apparent velocities between 5 and 6c, in agreement with previous findings (Gómez et al. 2001, 2008, 2011; Jorstad et al. 2005). This agrees also with recent MOJAVE results (Lister et al. 2013) where the 3C 120 kinematics, together with the radio galaxy 3C 111, departs from the others in the sample. These two radio galaxies seem to be the only ones displaying clear superluminal motions and with apparent speeds that do not commonly change with distance from the core.

From 2008 June to the beginning of 2012a stationary feature, C1, is found at a distance that shifts between ∼0.4–0.7 mas from the core. We identify this component with that reported by León-Tavares et al. (2010) at 0.72 ± 0.25 mas from the core, which is assumed by the authors to be related to optical flares when new components cross its position. Starting in 2012 the innermost 1 mas region of the jet changes, so that two stationary components can be found, C1 and C2. An extra component, labeled S9, is also required to fit some extended and weak flux density at ∼1.5 mas from the core.

As can be seen in Figures 2 and 4, the presence of two stationary components (C1 and C2) within the innermost 1 mas is associated with an increase in flux density and a more extended structure of the core. Component C1 is observed to progressively increase its flux density between mid 2012 and the beginning of 2013, when both the core and C1 are in a high flux density state. Three months later component C2 also shows an increase in flux density. These changes in the innermost structure of the jet are associated with the ejection of a new component, d11, revealed by the 43 GHz VLBA data (see Section 4.2), which extends our study of the jet until 2014 May.

Two other radio flares in the core have been also observed, one at the end of 2008 (2008.76 ± 0.10 year) and a second one at the beginning of 2011 (2011.15 ± 0.05 year). The flare in 2011 is associated with the ejection of a weak radio component from the core, E9, for which we estimate the time of ejection in 2011.23 ± 0.04.

The radio core flare at the end of 2008 is instead associated with the ejection of a bright superluminal knot, E4, in 2008.82 $\pm$ 0.04 year. The light curves of the different components shown in Figure 4 reveal the unusually large flare experienced by E4. By mid 2009 it has doubled its flux density, reaching a peak of ∼1.5 Jy and becoming brighter than the core itself. During the high state of flux density of E4 another component, named E4a, appears very close to it, suggesting an increase in extension of component E4 during the flare, as can be seen in Figures 2–4. In this case we consider more appropriate to take into account a flux-density-weighted distance between that of E4 and E4a to estimate the distance from the core of the new component E4 during its high state of flux density. The same method is used for components E1 and E1a, as we considered E1a an extension of E1 soon after this component is ejected from the core at the beginning of 2008. A similar splitting of components was also observed previously in 43 GHz VLBA images of 3C 120 (Gómez et al. 2001).
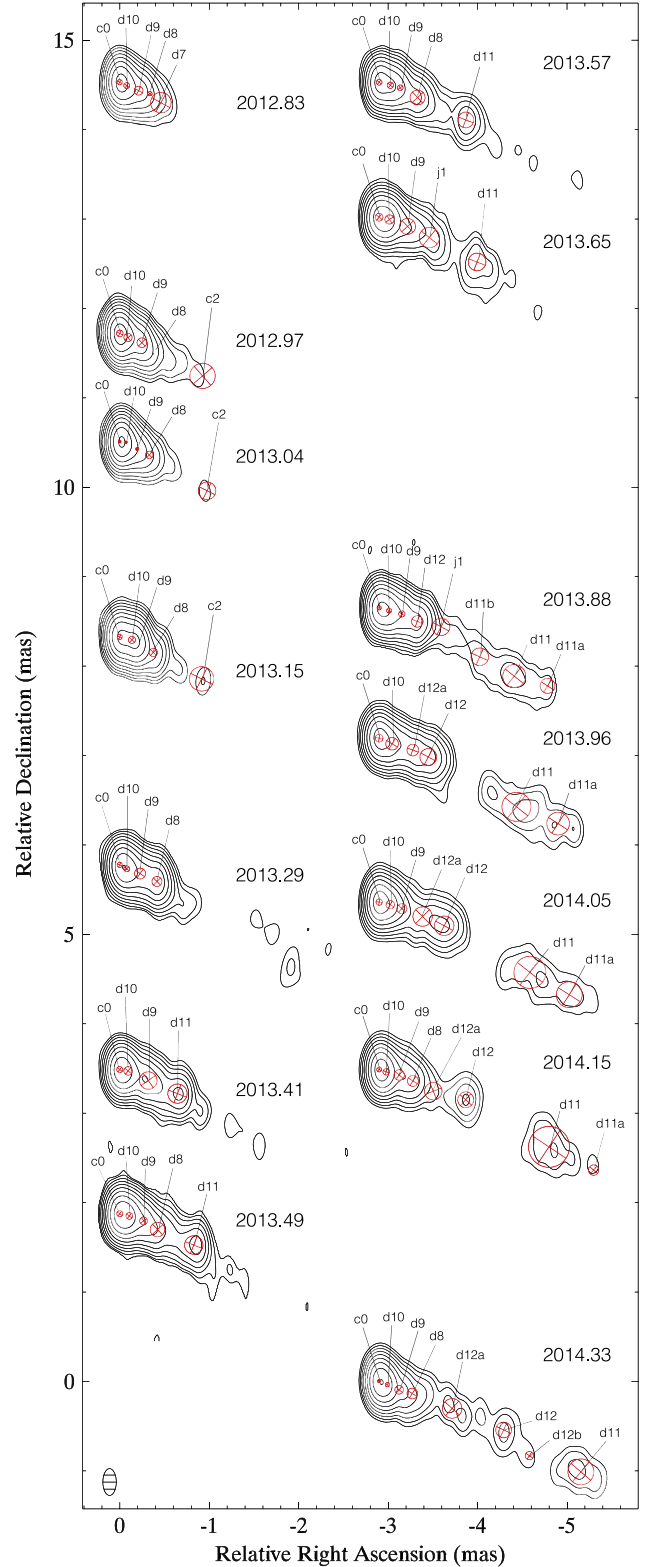

Figure 5. Sequence of total intensity 43 GHz VLBA images from the VLBA-BU-BLAZAR monitoring program of 3C 120 with a common restoring beam of 0.3×0.15 mas at 0°. Red circles represent modelfits components. Contours are traced at 0.16%, 0.35%, 0.77%, 1.7%, 3.77%, 8.33%, 18.41%, 40.71%, 90% of the peak intensity, 1.82 Jy beam^{-1}.
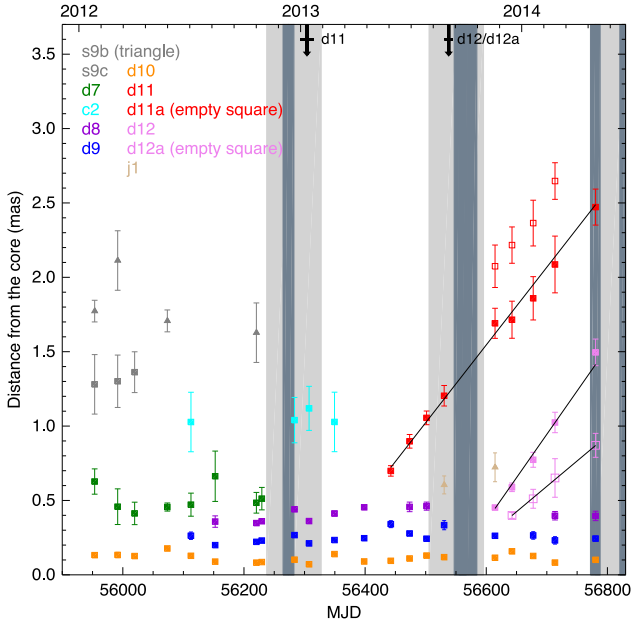
6

Figure 6. Distance from the core vs. time for the 43 GHz model-fit components with linear fits overlaid. Downward black arrows mark the time of ejection of each component. Gray vertical lines indicate γ-ray detections in the 15 day bin (dark gray) and 3 month bin (light gray) light curves in the energy band 500 MeV–100 GeV.
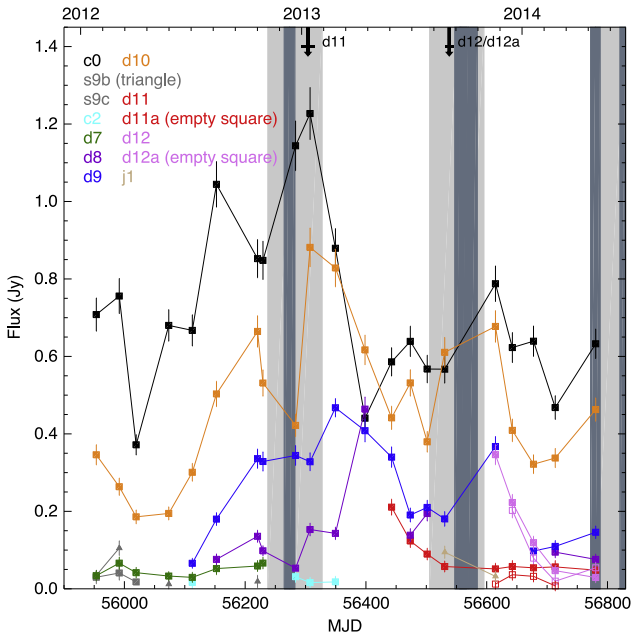

Figure 7. Light curves of the 43 GHz model-fit components. Arrows and vertical lines are as indicated in Figure 6.

The extended emission structure of components E1 and E4 (associated with components E1a and E4a) is consistent with Aloy et al. (2003) relativistic hydrodynamic simulations, where the passage of a new perturbation from a series of recollimation shocks results in extended emitting regions due to light-travel time delays between the front and the back of the perturbation.

Figure 4 shows also the light-curve obtained from adding the flux densities of C0 and C1. The stationary component C1 is usually located at a distance from the core of the order or

smaller than the observing beam, therefore in many epochs it is difficult to disentangle its flux density from that of the core. For instance, the combination of the C0+C1 flux density reveals a high state leading to the ejection of component E8 in mid 2010. It is also particularly remarkable the increase in flux density of the C0+C1 complex in mid 2013 leading to the ejection of a new component, d11, seen at 43 GHz (see below).

4.2. VLBA Data at 43 GHz

We modeled the 43 GHz jet in the same manner as for the 15 GHz data, finding a total of 16 components, although as in the case of the 15 GHz data, some of them are most probably related to the underlying continuum flow and it is difficult to follow them along the jet. In each epoch we identify the core with c0 and we consider it a stationary feature.

Figure 5 shows a sequence of VLBA 43 GHz images in total intensity, where red circles represent model-fit components. The displayed images cover the observing period from 2012 October to 2014 May, when 3C 120 was detected at γ-ray frequencies.

As observed in the 15 GHz data, starting in mid 2012 we find an increase in the flux density and extension of the core, requiring up to three stationary components, d10, d9, and d8, to model the innermost 0.5 mas structure (see Figures 6 and 7). Because of the different angular resolution and opacity with respect to that obtained at 15 GHz, it is difficult to establish a one-to-one connection among the components at 43 and 15 GHz for the innermost jet region. We tentatively identify components s9b and s9c with substructures of component S9 seen at 15 GHz. Furthermore, during the enhanced activity of the source starting in mid 2012 it is not clear whether d10, d9, and d8 at 43 GHz—and C1, C2 at 15 GHz—correspond to actual physical structures in the jet, like recollimation shocks, or they trace the underlying emission of the jet.

The radio core persists in a flaring state until 2013 January. After this, the peak in flux density moves from the core along the jet, crossing progressively the three stationary features close to it (d10, d9 and d8). When the perturbation crosses the last stationary component, d8, we can clearly discern a new knot, d11, that emerges from the first 0.5 mas in 2013.4 years (see Figure 5). From the progressive flaring of stationary features close to the core we can infer the extension of the crossing emitting region, obtaining ∼0.35 mas. This is significantly larger that the FWHM obtained from the model-fit of d11 (see Table 2), which suggests that d11 is in fact part of a more extended region, resembling the results obtained from relativistic hydrodynamical simulations (Aloy et al. 2003). Fitting of the separation versus distance for d11 yields a proper motion of 1.91 ± 0.09 mas yr^{-1}, which corresponds to an apparent velocity of $4.22 \pm 0.22c$. The estimated time of ejection, that is, when component d11 crossed the radio core at 43 GHz, is 2013.03 ± 0.03.

A similar situation takes place also in the second half of 2013, when the core, together with components d10 and d9, starts to bright and a new component, d12, appears at ∼0.45 mas. We note also that another component, d12a, appears very close in time and position to component d12, although it displays a significantly slower proper motion. Component d12 moves at 2.1 ± 0.2 mas yr^{-1} ($4.7 \pm 0.3c$), while component d12a moves at 1.2 ± 0.2 mas yr^{-1} ($2.6 \pm 0.5c$). We note, however, that the estimated time of ejection for d12 and d12a, 2013.67 ± 0.02 year and 2013.64 ± 0.07 year,

7

Table 3
γ-ray Detections of 3C 120 in the Energy Range 0.5–100 GeV with a Bin Size of 15 Days

MJD	Date	Flux	Err	TS
56264–56279	2012 Dec 03–2012 Dec 18	1.41	0.60	10.6
56549–56564	2013 Sep 14–2013 Sep 29	1.65	0.54	21.6
56564–56579	2013 Sep 29–2013 Oct 14	1.31	0.53	13.3
56774–56789	2014 Mar 27–2014 May 12	1.15	0.52	10.4
56819–56834	2014 Jun 11–2014 Jun 26	1.47	0.59	13.8
56924–56939	2014 Sep 24–2014 Oct 09	2.52	0.86	18.4

Notes. We report the integration time in MJD and date, the flux with the corresponding error in 10^{-8} photon cm^{-2} s^{-1} and the TS value associated to each γ-ray detection.

respectively, is the same within the uncertainties. Both components therefore originated simultaneously in the millimeter very long baseline interferometry (VLBI) core, although they propagate at quite different velocities afterwards.

Time delays stretch the shocked emission in the observer's frame, so that with the necessary angular resolution multiple sub-components associated with a single shock could be distinguished in the jet, but in this case they would have similar apparent velocities, in contrast with what it is observed for components d12 and d12a. Trailing components have a smaller velocity than the leading perturbation, but they are released on the wake of main perturbation (Agudo et al. 2001), instead of being ejected from the core, as occurs for component d12a. On the other hand, relativistic hydrodynamic simulations show that a single perturbation in the jet inlet leads to the formation of a forward and reverse shock (Gómez et al. 1997; Aloy et al. 2003; Mimica et al. 2009). Therefore, the fact that components d12 and d12a are ejected from the core at the same time but with different velocities suggests that they may correspond to the forward and reverse shock of a perturbation.

5. CONNECTION BETWEEN γ-RAY AND RADIO EMISSION

Our analysis of the *Fermi*-LAT data (see Figure 1 and Table 3) shows a prolonged γ-ray activity in the radio galaxy 3C 120 between 2012 December and 2014 September–October, when the source reaches a flux of $F_{>500\mathrm{MeV}} = 2.5 \pm 0.8 \times 10^{-8}$ photon cm^{-2} s^{-1}, about an order of magnitude larger than in previous detections. Three clear periods of γ-ray activity are found at the end of 2012 (56264–56279 MJD), 2013 September–October (56549–56579 MJD), and 2014 May–October (56774–56939 MJD).

The γ-ray activity in 2012 December is accompanied by an increase in the radio core flux density, as well as in the innermost stationary components, at both 15 and 43 GHz (see Figures 4 and 7), leading to the ejection of component d11 in 2013.13 ± 0.03 (see also Figure 6). From the estimated proper motion of d11 we infer that in the last epoch of the 15 GHz data this component is still in the innermost region of the jet as imaged at 15 GHz, crossing the stationary component C2.

After this first γ-ray detection the source remains in a quiescent state until 2013 August, when another γ-ray event covering the period from 2013 August to October is detected. The 15 days binning analysis (see Table 3) constrains the main flaring activity to 2013 September–October (56549–56579 MJD), coincident with the flaring of the radio core at 43 GHz

Table 4
Time of Ejection, Proper Motions and Apparent Velocities of Model-fit Components at 15 GHz

Name	T_{ej} (year)	μ (mas yr^{-1})	β_{app}
E0	2007.29 ± 0.06	2.81 ± 0.05	6.21 ± 0.11
E1	2008.01 ± 0.02	2.76 ± 0.05	6.10 ± 0.11
E4	2008.82 ± 0.04	2.35 ± 0.05	5.19 ± 0.11
E5	2009.42 ± 0.02	2.60 ± 0.06	5.75 ± 0.13
E6	2009.85 ± 0.03	2.56 ± 0.05	5.66 ± 0.11
E8	2010.45 ± 0.02	2.20 ± 0.03	4.86 ± 0.07
E9	2011.23 ± 0.04	2.32 ± 0.09	5.12 ± 0.19

and the ejection of the d12–d12a pair of components (see Figures 5–7).

There is also indication of the beginning of a new flaring activity in the 43 GHz radio core associated with the last γ-ray flaring activity starting in 2014 May, but further VLBI images are required to confirm the ejection of a new component in this event.

We therefore can conclude that there is a clear association between the γ-ray and radio emission in 3C 120, such that every period of γ-ray activity is accompanied by flaring of the VLBI radio core and subsequent ejection of a new super-luminal component in the jet. However, not all ejections of superluminal components are related to enhanced γ-ray emission, detectable by *Fermi*-LAT, as occurred for components E4, E5, E6, E8, and E9. The case of component E4 is particularly interesting. Abdo et al. (2010) report a γ-ray detection in 2008 December, coincident with an increase of the 15 GHz radio core flux, leading to the ejection of E4 in 2008.82 ± 0.04. This is also coincident with an optical flare in 2008 December, as reported by Kollatschny et al. (2014). We also note that E4 reached a peak flux of ~1.5 Jy, significantly larger than any other component seen in our analysis. Despite this intense activity in the optical and radio core, our analysis of the *Fermi* data during this period does not provide a clear detection in γ-rays, although the calculated TS (corresponding to ~3σ) is only slightly smaller than the usually adopted detection threshold.

6. DISCUSSION

6.1. Motion of Components Along the Jet

The debate on the origin and location of the γ-ray emission in blazars has gained added interest since the launch of the *Fermi* satellite. Much of the current discussion lies in whether γ-rays are produced upstream of the millimeter VLBI core, as suggested by some γ-ray and radio correlations (e.g., Rani et al. 2013a, 2014) and the observed γ-ray spectral break at few GeVs (Abdo et al. 2009; Finke & Dermer 2010; Poutanen & Stern 2010; Tanaka et al. 2011; Rani et al. 2013b) or downstream, as suggested by coincidence of γ-ray flares with either the appearance of new superluminal components (e.g., Jorstad et al. 2010, 2013) or the passage of moving components through a stationary jet feature (Schinzel et al. 2012; Marscher 2013).

As observed in several blazars (Jorstad et al. 2010, 2013; Ramakrishnan et al. 2014), the interaction between traveling features and the stationary radio core appears to be a necessary condition for the production of γ-ray photons in 3C 120, but it is clearly not enough. Therefore, to understand the γ-ray
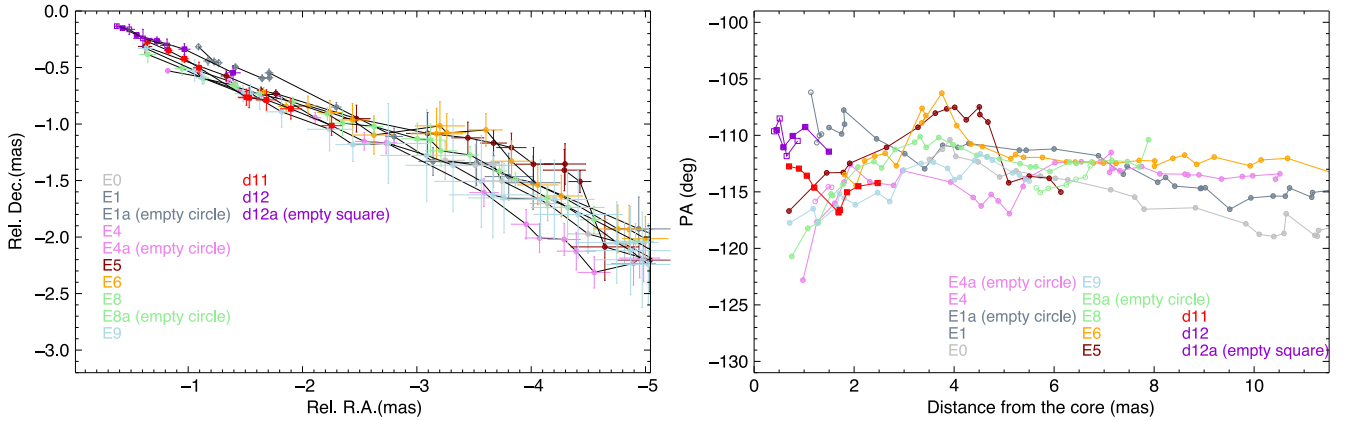
8

Figure 8. Positions (*l*eft) and position angles as a function of distance from the core (*r*ight) for the model-fit components at 15 (circles) and 43 GHz (squares). For clarity errors bars are shown only in the plot of the components' position.

emission in 3C 120, and more generally in AGN, it is necessary to address the question of what physical changes in the jet can produce γ-ray emission.

We note that the beginning of the γ-ray activity in 3C 120 occurs after a sustained period of low activity in the jet. As indicated in Table 4, during the time period analyzed new components are seen in the jet of 3C 120 roughly every 8 months; however, no new components are detected in the jet between the ejection of E9 in 2011.23 ± 0.04 and component d11 in 2013.03 ± 0.03, implying a lack of activity in the jet for almost 2 years. Note that after the ejection of d11 the source resumes its activity with the ejection of component d12, again roughly 8 months later.

Analysis of the components' proper motions (see Table 4) reveals a clear pattern of decreasing apparent velocities, from the 6.21 ± 0.11c of E0 to 5.12 ± 0.19c of E9. Furthermore, when the core resumes the ejection of components after a 2 years inactivity, the apparent velocities measured for d11 and d12 have further decreased to 4.22 ± 0.22c and 4.70 ± 0.31c, respectively. Component d12a shows an even smaller velocity of 2.75 ± 0.45c, but we believe this component differs for the other components seen previously in 3C 120 in which it is probably associated with a reserve shock.

Note that model-fits at 43 and 15 GHz trace the motion of components continuously throughout the jet. We also find no evidence for acceleration (only component E6 shows a clear acceleration at ∼8 mas from the core), hence we consider that the proper motions measured at 43 GHz provide a good estimation for the expected values should these components be detected later on at 15 GHz, reassuring our finding for a progressive decrease in the apparent velocity of the components from ∼6.2c to 4.2c in a time span of approximately 6.4 years, from 2007.3 to 2013.7. This progressive change in the apparent velocity of components could be due to a change in the velocity and/or orientation of the components. Considering that the 6.4 years time span measured roughly agrees with the 12.3 ± 0.3 year full period determined by the precessing jet model of Caproni & Abraham (2004), we favor the case in which it is produced by a change in the orientation of the components with respect to the observer.

Figure 8 shows the motion of components along the jet, as well as their PA with distance from the core. We observe that components E1-E1a (and presumably E0) are ejected with a PA of around −110° and they travel toward the southwest

direction while the other components at 15 GHz are ejected with a PA between −117° and −123° and move initially in a less southern direction. Components E5 and E6 present a significant change in their velocity vectors at a distance of ∼3 mas from the core, as observed previously for other components and interpreted as the interaction with the external medium or a cloud (Gómez et al. 2000, 2008). Components d11 and d12–d12a are ejected with a PA of around −110°, similar to that observed previously for E1-E1a. Note that in a precession model components E1 and d12 would have similar projected velocity vectors while differing in their orientation with respect to the observer. Despite the initially different PAs, components move following parallel paths after the initial ∼4–5 mas. Rather than a precession of the whole jet, we therefore favor the model in which the jet consists of a broad funnel through which components—not filling the whole jet width—are ejected and travel at differ PAs, as supported also by previous observations of 3C 120 (Gómez et al. 2011) and other sources in the MOJAVE sample (Lister et al. 2013).

Considering that the slower apparent velocities of d11 and d12 are related to the first γ-ray detections, we conclude that these components are most likely ejected with a smaller viewing angle. This should increase the Doppler factor, leading to the enhanced γ-ray emission measured since the end of 2012, and a significant increase in the total flux of the core and innermost stationary features (see Figure 7). However, we cannot completely rule out the possibility that the smaller apparent velocities are just due to greater viewing angles, or slowing of the components' velocity.

It is possible to estimate the required minimum Lorentz factor, $\Gamma_{\min} = (1 + \beta_{\text{app}}^2)^{1/2} = 6.3$, using the observed maximum apparent velocity of 6.2c. To minimize the required reorientation of the components, we can assume that the maximum apparent velocity is obtained for the angle that actually maximizes the apparent velocity, given by $\theta = \arccos(\beta)$, where β is the component's velocity in units of the speed of light. Using our previous estimation of $\Gamma_{\min} = 6.3$, we obtain a viewing angle of $\theta \sim 9°2$ for the maximum apparent velocity of 6.2c measured for component E0, in agreement with Hovatta et al. (2009). Given that the observed decrease in the apparent velocity is probably produced by a decrease in the viewing angle, the smallest observed apparent velocity of 4.2c for d11 requires $\theta \sim 3°6$. These values agree with the precession model of Caproni &

9

Abraham (2004), for which the authors estimate $\Gamma = 6.8 \pm 0.5$ and a variation of the viewing angle between $(6.3 \pm 0.^{\circ}8)$ and $(3.3 \pm 0.^{\circ}8)$. We should note however that our measured change in the apparent velocities is shifted from the periodicity phase predicted by Caproni & Abraham (2004) model.

This change in the orientation from $\theta \sim 9.^{\circ}2$ to $\theta \sim 3.^{\circ}6$ would lead to an increase in the Doppler factor from $\delta \sim 6.2$ to $\delta \sim 10.9$, enhancing the γ-ray emission above the flux detectable by *Fermi*.

In summary, all these evidence suggest that the observed γ-ray emission in 3C 120 depends strongly on the orientation of component's motion with respect to the observer, so that only when they are best oriented *and* a new superluminal component pass through the radio core a clear γ-ray detection is obtained.

Superluminal components are associated with shocks moving along the jet, hence the inferred values for the velocity—provided there is an estimation of the jet orientation—correspond to the pattern velocity of the shock, not the actual flow velocity. The detection of the forward and reserve shocks of the perturbation associated with d12 and d12a, respectively, allows to obtain a direct calculation of the jet bulk flow velocity. For the estimated viewing angle of $\sim 3.^{\circ}6$ during the ejection of components d12 and d12a we obtain the corresponding pattern velocities of $\Gamma_{d12} = 6.7$ and $\Gamma_{d12a} = 5$. Hence, we can conclude that the jet bulk flow velocity is restricted to be $5 \leqslant \Gamma_j \leqslant 6.7$.

6.2. Gamma-ray Location and Emission Mechanism

Our first γ-ray detection at the end of 2012 is associated with the passage of component d11 through the millimeter VLBI core, whose time of ejection is coincident with the 3 months-bin γ-ray detection, and is ~ 34 days (0.09 year) after the 15 days-bin γ-ray detection. On the other hand, Marscher et al. (2002) and Chatterjee et al. (2009) have measured a mean delay of 0.18 year (~ 66 days) between X-ray dips and the ejection of new superluminal components. Considering that most of the X-ray emission in 3C 120 originates from the disk-corona system, close to the central BH, we can consider this time delay as the distance in time between the BH and the millimeter VLBI core. A mean apparent motion of ~ 2 mas yr^{-1} corresponds to a rate of increase in projected separation from the core of ~ 0.24 pc yr^{-1}—or slightly smaller if we allow for some initial acceleration of the components.

The measured delay of 34 days between the 15 days-bin γ-ray detection and the passage of d11 from the millimeter VLBI core locates the γ-ray emission upstream of the millimeter VLBI core, at a distance about half of that between the BH and the core. Relativistic 3D hydrodynamic simulations of Aloy et al. (2003) show that time delays stretch significantly the observed size of components, so that our VLBI observations could detect only some portions of the component, depending on the strength of the forward/reverse shock and Doppler factor (i.e., viewing angle). Considering also that we have estimated for component d11 a size of ~ 0.35 mas (0.2 pc) once it is clearly detached from the core, it is possible that the 15 days-bin γ-ray detection could correspond to the passing of the forward section of the d11 perturbation through the millimeter VLBI core, while later on our VLBI images identify only the back section, as it is precisely seen in the numerical simulations of Aloy et al. (2003). In this case the flaring in γ-rays would more closely mark the crossing of the d11 perturbation through the millimeter VLBI core.

The second γ-ray event is instead associated with the ejection of components d12 and d12a. In this case the time of ejection of these two components is also coincident with the 3 months bin γ-ray detection, but the finer time sampling of the 15 day γ-ray light curve constrains the γ-ray production to ~ 33 days after. Hence we conclude that in the second γ-ray event the high energy emission is produced downstream of the millimeter VLBI core, at a projected distance of ~ 0.13 pc from its position—smaller if we consider that the shock responsible for the γ-ray emission is the slower moving d12a.

Reverberation mapping studies of the broad-line-region (BLR) in 3C 120 suggest an inclined disk model with an extension from 12 ± 7 light days (~ 0.01 pc) to 28 ± 9 light days (~ 0.025 pc), from the BH (Grier et al. 2013; Kollatschny et al. 2014). These studies also found evidence of radial stratification in the BLR as well as infall and rotation related to the BH gravity. Therefore the BLR extends to about half of the estimated distance between the BH and the millimeter VLBI core, severely limiting the external photon field from the BLR at the location of the millimeter VLBI core. Hence we favor synchrotron self Compton as the mechanism for the production of γ-ray photons in the case of the second γ-ray event in late 2013, although we cannot discard the contribution from another external photon field, such the sheath or the external ionized cloud.

The external Compton process with photons coming from the BLR could be instead a possibility for the first γ-ray event, as our findings point to a γ-ray dissipation zone between the BH and the radio core, on the limit of the extension of the BLR.

The different orientation of the components within the broader jet funnel supports also a model in which they interact with the sheath of the jet (see also Gómez et al. 2000, 2008). In this case the observed γ-ray activity can be produced by Compton scattering of photons from the jet sheath, as proposed by Marscher et al. (2010) to explain the γ-ray activity seen in PKS 1510–089.

Grandi et al. (2012b) obtain similar results for the FRII radio galaxy 3C 111, associating the γ-ray activity with the ejection of a new radio component from the core, and confining the γ-ray dissipation region within 0.1 pc at a distance of almost 0.3 pc from the BH. These two radio galaxies have other similarities as they are both BLRGs and they show a connection between the radio jet and the corona-disk system (Marscher et al. 2002; Chatterjee et al. 2011). In addition, the apparent motions of superluminal components detected in their jets detach from those of the other radio galaxies in the MOJAVE sample (Lister et al. 2013).

10

REFERENCES

Abdo, A. A., Ackermann, M., Ajello, M., et al. 2009, ApJ, 707, 1310
Abdo, A. A., Ackermann, M., Ajello, M., et al. 2010, ApJ, 720, 912
Abramowski, A., Acero, F., Aharonian, F., et al. 2012, ApJ, 746, 151
Ackermann, M., Ajello, M., Albert, A., et al. 2012, ApJS, 203, 4
Ackermann, M., Ajello, M., Allafort, A., et al. 2011, ApJ, 743, 171
Agudo, I., Gómez, J.-L., Martí, J.-M., et al. 2001, ApJL, 549, L183
Aharonian, F., Akhperjanian, A. G., Bazer-Bachi, A. R., et al. 2006, Sci, 314, 1424
Aloy, M.-Á., Martí, J.-M., Gómez, J.-L., et al. 2003, ApJL, 585, L109
Caproni, A., & Abraham, Z. 2004, MNRAS, 349, 1218
Chatterjee, R., Marscher, A. P., Jorstad, S. G., et al. 2011, ApJ, 734, 43
Chatterjee, R., Marscher, A. P., Jorstad, S. G., et al. 2009, ApJ, 704, 1689
Finke, J. D., & Dermer, C. D. 2010, ApJL, 714, L303
Gómez, J. L., Marscher, A. P., Alberdi, A., Jorstad, S. G., & Agudo, I. 2001, ApJL, 561, L161
Gómez, J. L., Marscher, A. P., Alberdi, A., Jorstad, S. G., & García-Miró, C. 2000, Sci, 289, 2317
Gómez, J. L., Marscher, A. P., Jorstad, S. G., Agudo, I., & Roca-Sogorb, M. 2008, ApJL, 681, L69
Gómez, J. L., Martí, J. M., Marscher, A. P., Ibáñez, J. M., & Alberdi, A. 1997, ApJL, 482, L33
Gómez, J. L., Roca-Sogorb, M., Agudo, I., Marscher, A. P., & Jorstad, S. G. 2011, ApJ, 733, 11
Grandi, P., Torresi, E., & FERMI-LAT Collaboration 2012a, arXiv:1205.1686
Grandi, P., Torresi, E., & Stanghellini, C. 2012b, ApJL, 751, L3
Grier, C. J., Peterson, B. M., Horne, K., et al. 2013, ApJ, 764, 47
Hada, K., Giroletti, M., Kino, M., et al. 2014, ApJ, 788, 165
Harris, D. E., Massaro, F., Cheung, C. C., et al. 2011, ApJ, 743, 177
Homan, D. C., Kadler, M., Kellermann, K. I., et al. 2009, ApJ, 706, 1253
Homan, D. C., Lister, M. L., Kovalev, Y. Y., et al. 2015, ApJ, 798, 134
Hovatta, T., Valtaoja, E., Tornikoski, M., & Lähteenmäki, A. 2009, A&A, 494, 527
Jorstad, S. G., Marscher, A. P., Larionov, V. M., et al. 2010, ApJ, 715, 362
Jorstad, S. G., Marscher, A. P., Lister, M. L., et al. 2005, AJ, 130, 1418
Jorstad, S. G., Marscher, A. P., Smith, P. S., et al. 2013, ApJ, 773, 147
Kataoka, J., Stawarz, Ł., Cheung, C. C., et al. 2010, ApJ, 715, 554
Kollatschny, W., Ulbrich, K., Zetzl, M., Kaspi, S., & Haas, M. 2014, A&A, 566, A106
León-Tavares, J., Lobanov, A. P., Chavushyan, V. H., et al. 2010, ApJ, 715, 355
Lister, M. L., Aller, H. D., Aller, M. F., et al. 2009a, AJ, 137, 3718
Lister, M. L., Aller, M. F., Aller, H. D., et al. 2013, AJ, 146, 120
Lister, M. L., Cohen, M. H., Homan, D. C., et al. 2009b, AJ, 138, 1874
Maraschi, L., Chiappetti, L., Falomo, R., et al. 1991, ApJ, 368, 138
Marscher, A. P. 2013, in American Astronomical Society Meeting Abstracts, 221, 339.53
Marscher, A. P., Jorstad, S. G., Gómez, J.-L., et al. 2002, Nature, 417, 625
Marscher, A. P., Jorstad, S. G., Larionov, V. M., et al. 2010, ApJL, 710, L126
Mattox, J. R., Bertsch, D. L., Chiang, J., et al. 1996, ApJ, 461, 396
Mimica, P., Aloy, M.-A., Agudo, I., et al. 2009, ApJ, 696, 1142
Nolan, P. L., Abdo, A. A., Ackermann, M., et al. 2012, ApJS, 199, 31
Planck Collaboration, Ade, P. A. R., Aghanim, N., et al. 2014, A&A, 571, A16
Poutanen, J., & Stern, B. 2010, ApJL, 717, L118
Ramakrishnan, V., León-Tavares, J., Rastorgueva-Foi, E. A., et al. 2014, MNRAS, 445, 1636
Rani, B., Krichbaum, T. P., Fuhrmann, L., et al. 2013a, A&A, 552, A11
Rani, B., Krichbaum, T. P., Lott, B., Fuhrmann, L., & Zensus, J. A. 2013b, Advances in Space Research, 51, 2358
Rani, B., Krichbaum, T. P., Marscher, A. P., et al. 2014, A&A, 571, L2
Schinzel, F. K., Lobanov, A. P., Taylor, G. B., et al. 2012, A&A, 537, A70
Shepherd, M. C. 1997, in ASP Conf. Ser. 125, Astronomical Data Analysis Software and Systems VI, ed. G. Hunt & H. Payne, 77
Tanaka, Y. T., Cutini, S., Ciprini, S., et al. 2014, The Astronomer's Telegram, 6529, 1
Tanaka, Y. T., Stawarz, Ł., Thompson, D. J., et al. 2011, ApJ, 733, 19
Walker, R. C., Benson, J. M., Unwin, S. C., et al. 2001, ApJ, 556, 756

11

4.2   A multi-wavelength polarimetric study of the blazar CTA 102 during a Gamma-ray flare in 2012

The following article has been published in *The Astrophysical Journal* on November 1st, 2015 and it is reproduced here in its entirety and in its original format.

    The reference for this article is: Casadio C., Gómez J. L., Jorstad S. G., et al., 2015, ApJ, 813, 51.

    The authors are: Carolina Casadio, José L. Gómez, Svetlana G. Jorstad, Alan P. Marscher, Valeri M. Larionov, Paul S. Smith, Mark A. Gurwell, Anne Lähteenmäki, Iván Agudo, Sol N. Molina, Vishal Bala, Manasvita Joshi, Brian Taylor, Karen E. Williamson, Arkady A. Arkharov, Dmitry A. Blinov, George A. Borman, Andrea Di Paola, Tatiana S. Grishina, Vladimir A. Hagen-Thorn, Ryosuke Itoh, Evgenia N. Kopatskaya, Elena G. Larionova, Liudmila V. Larionova, Daria A. Morozova, Elizaveta Rastorgueva-Foi, Sergey G. Sergeev, Merja Tornikoski, Ivan S. Troitsky, Clemens Thum, Helmut Wiesemeyer.

A MULTI-WAVELENGTH POLARIMETRIC STUDY OF THE BLAZAR CTA 102 DURING A GAMMA-RAY FLARE IN 2012

CAROLINA CASADIO[1], JOSÉ L. GÓMEZ[1], SVETLANA G. JORSTAD[2,3], ALAN P. MARSCHER[2], VALERI M. LARIONOV[3,4], PAUL S. SMITH[5], MARK A. GURWELL[6], ANNE LÄHTEENMÄKI[4,7], IVÁN AGUDO[1], SOL N. MOLINA[1], VISHAL BALA[2], MANASVITA JOSHI[2], BRIAN TAYLOR[2], KAREN E. WILLIAMSON[2], ARKADY A. ARKHAROV[8], DMITRY A. BLINOV[3,9], GEORGE A. BORMAN[10], ANDREA DI PAOLA[11], TATIANA S. GRISHINA[3], VLADIMIR A. HAGEN-THORN[3], RYOSUKE ITOH[12], EVGENIA N. KOPATSKAYA[3], ELENA G. LARIONOVA[3], LIUDMILA V. LARIONOVA[3], DARIA A. MOROZOVA[3], ELIZAVETA RASTORGUEVA-FOI[4,13], SERGEY G. SERGEEV[10], MERJA TORNIKOSKI[4], IVAN S. TROITSKY[3], CLEMENS THUM[14], AND HELMUT WIESEMEYER[15]

[1] Instituto de Astrofísica de Andalucía, CSIC, Apartado 3004, E-18080 Granada, Spain
[2] Institute for Astrophysical Research, Boston University, 725 Commonwealth Avenue, Boston, MA 02215, USA
[3] Astronomical Institute, St. Petersburg State University, Universitetskij Pr. 28, Petrodvorets, 198504 St. Petersburg, Russia
[4] Aalto University Metsähovi Radio Observatory, Metsähovintie 114, FI-02540 Kylmälä, Finland
[5] Steward Observatory, University of Arizona, Tucson, AZ 85716, USA
[6] Harvard-Smithsonian Center for Astrophysics, Cambridge, MA 02138, USA
[7] Aalto University Department of Radio Science and Engineering, P.O. Box 13000, FI-00076 Aalto, Finland
[8] Pulkovo Observatory, St. Petersburg, Russia
[9] University of Crete, Heraklion, Greece
[10] Crimean Astrophysical Observatory, Nauchnij, Ukraine
[11] INAF, Osservatorio Astronomico di Roma, Roma, Italy
[12] Department of Physical Sciences, Hiroshima University, Higashi-Hiroshima, Hiroshima 739-8526, Japan
[13] School of Maths Physics, University of Tasmania, Private Bag 37, Hobart, TAS 7001, Australia
[14] Instituto de Radio Astronomía Milimétrica, Granada, Spain
[15] Max-Planck-Institut für Radioastronomie, Bonn, Germany

ABSTRACT

We perform a multi-wavelength polarimetric study of the quasar CTA 102 during an extraordinarily bright γ-ray outburst detected by the *Fermi* Large Area Telescope in 2012 September–October when the source reached a flux of $F_{>100\,\mathrm{MeV}} = 5.2 \pm 0.4 \times 10^{-6}$ photons cm^{-2} s^{-1}. At the same time, the source displayed an unprecedented optical and near-infrared (near-IR) outburst. We study the evolution of the parsec-scale jet with ultra-high angular resolution through a sequence of 80 total and polarized intensity Very Long Baseline Array images at 43 GHz, covering the observing period from 2007 June to 2014 June. We find that the γ-ray outburst is coincident with flares at all the other frequencies and is related to the passage of a new superluminal knot through the radio core. The powerful γ-ray emission is associated with a change in direction of the jet, which became oriented more closely to our line of sight ($\theta \sim 1°.2$) during the ejection of the knot and the γ-ray outburst. During the flare, the optical polarized emission displays intra-day variability and a clear clockwise rotation of electric vector position angles (EVPAs), which we associate with the path followed by the knot as it moves along helical magnetic field lines, although a random walk of the EVPA caused by a turbulent magnetic field cannot be ruled out. We locate the γ-ray outburst a short distance downstream of the radio core, parsecs from the black hole. This suggests that synchrotron self-Compton scattering of NIR to ultraviolet photons is the probable mechanism for the γ-ray production.

Key words: galaxies: active – galaxies: jets – quasars: individual (CTA 102) – techniques: interferometric – techniques: photometric – techniques: polarimetric

Supporting material: machine-readable tables

1. INTRODUCTION

The Blazar CTA 102 (B2230+114) is classified as a highly polarized quasar, characterized by optical polarization exceeding 3% (Moore & Stockman 1981). Its high variability at optical wavelengths (Pica et al. 1988; Osterman Meyer et al. 2009) and its spectral properties also identify it as an optically violent variable quasar (Maraschi et al. 1986). Microvariability of CTA 102 at optical wavelengths has been investigated by Osterman Meyer et al. (2009), who found that faster variability is associated with higher flux states.

The variability in this source occurs at other frequencies as well: flares at centimeter and millimeter wavelengths have been registered in the past, as well as an X-ray flare detected by the *Rossi X-ray Timing Explorer* in late 2005 (Osterman Meyer et al. 2009). A radio flare in 1997 was related to the ejection of a new knot from the core (Savolainen et al. 2002; Rantakyrö et al. 2003; Jorstad et al. 2005), and another, in 2006, was connected with both the ejection of a new superluminal feature and the interaction between this component and a recollimation shock at 0.1 mas (Fromm et al. 2011).

The radio morphology on arcsecond scales (from images with the Very Large Array at 6 and 2 cm) reveals a central core with two weak components located at opposite sides (Spencer et al. 1989; Stanghellini et al. 1998). At higher angular resolution, CTA 102 has been regularly observed since 1995 within the Very Long Baseline Array (VLBA) 2 cm Survey (e.g., Zensus et al. 2002) and its successor, the MOJAVE program (e.g., Lister et al. 2009). MOJAVE images show that the jet in CTA 102 extends toward the southeast up to ~15 mas

from the core, which corresponds to a de-projected distance of ~2.7 kpc using the estimated viewing angle of 2°.6 obtained by Jorstad et al. (2005).

Kinematic studies of the MOJAVE data report apparent velocities between $1.39c$ and $8.64c$ (Lister et al. 2013). Higher apparent speeds, up to $\beta_{app} \sim 18c$, have been reported in higher-resolution VLBA observations at 43 GHz by Jorstad et al. (2001, 2005). Apart from superluminal features, the jet of CTA 102 also displays standing features: two stationary components, A1 and C, have been observed at a distance of ~0.1 and 2 mas from the core, respectively (Jorstad et al. 2001, 2005), and interpreted as recollimation shocks (Fromm et al. 2013b).

Recent MOJAVE polarimetric multifrequency observations (Hovatta et al. 2012) reveal a rotation measure gradient across the jet width at 7 mas from the core, which suggests the presence of a helical magnetic field in the jet. A similar result is reported in Fromm et al. (2013b), where the different observing frequencies reveal bends and helical structures in many parts of the jet.

CTA 102 was detected by the *Fermi Gamma-ray Space Telescope* in the first Large Area Telescope (LAT) catalog with a flux ($E > 100$ MeV) of $14.70 \pm 0.97 \times 10^{-8}$ photons cm^{-2} s^{-1} (Abdo et al. 2010a) and confirmed in the second catalog (Ackermann et al. 2011). In late 2012, the blazar exhibited an extraordinarily bright γ-ray outburst detected by the LAT, reaching a flux of $5.17 \pm 0.44 \times 10^{-6}$ photons cm^{-2} s^{-1} between 0.1 and 200 GeV. During the 2012 event, an unprecedented optical and near-infrared (near-IR) outburst was observed, as reported by Larionov et al. (2012) and Carrasco et al. (2012), respectively.

In this paper, we perform a radio to γ-ray multi-wavelength analysis in order to study the flaring activity of CTA 102 during the 2012 event. In Section 2, we present the multi-wavelength data set collected for the analysis, and we describe the methods used to reduce the data. In Section 3, we describe the characteristics of the emission at the different frequencies during the 2012 flare event. In Section 4, we study the kinematics and the flux density variability of the parsec scale jet. In Section 5, we perform the discrete cross-correlation analysis between light curves. In Section 6, we analyze the polarized emission of the source at millimeter and optical wavebands. We present our discussions and conclusions in Sections 7 and 8.

We adopt the cosmological values from the most recent *Planck* satellite results (Planck Collaboration et al. 2014): $\Omega_m = 0.3$, $\Omega_\Lambda = 0.7$, and $H_0 = 68$ km s^{-1} Mpc^{-1}. With these values, at the redshift of CTA 102 ($z = 1.037$), 1 mas corresponds to a linear distance of 8.31 pc, and a proper motion of 1 mas yr^{-1} corresponds to an apparent speed of $55.2c$.

2. OBSERVATIONS AND DATA REDUCTION

We are interested in studying the multi-spectral behavior of CTA 102 during the γ-ray flare that occurred between 2012 September and October. For this, we have collected data from millimeter to γ-ray wavelengths, extending our study from 2004 June to 2014 June. In particular, the *Fermi* data extend from the start of the mission (2008 August) to 2013 September, X-ray and UV data cover the observing period from 2009 August to 2013 June, optical and NIR data from 2004 June to 2013 October, and the combined radio light curves cover the entire period from 2004 June to 2014 June.

In the millimeter-wave range, we use data at (1) 350 GHz (0.85 mm) and 230 GHz (1.3 mm), obtained with the Sub-millimeter Array (SMA) at Mauna Kea, Hawaii; (2) 230 GHz (1.3 mm) and 86.24 GHz (3.5 mm) with the 30 m Telescope of Institut de Radioastronomie Millimétrique (IRAM) at the Pico Veleta Observatory (Spain); (3) 43 GHz (7 mm) with the VLBA; and (5) 37 GHz (8 mm) with the 13.7 m Telescope at Metsähovi Radio Observatory of Aalto University (Finland).

NIR photometric data (JHK filters) were obtained at the Perkins Telescope at Lowell Observatory (Flagstaff, AZ) using the MIMIR instrument (Clemens et al. 2007) and at the 1.1 m Telescope of the Main Astronomical Observatory of the Russian Academy of Sciences located at Campo Imperatore, Italy (see Hagen-Thorn et al. 2008 for details).

We have collected optical photometric data in the *UBVRI* bands from numerous telescopes: (1) the 2.2 m Telescope of Calar Alto Observatory (Almería, Spain)[16]; (2) the 2 m Liverpool Telescope of the Observatorio del Roque de Los Muchachos (Canary Island, Spain); (3) the 1.83 m Perkins Telescope of Lowell Observatory (Flagstaff, AZ); (4) the 1.54 m and 2.3 m telescopes of Steward Observatory (Mt. Bigelow and Kitt Peak, AZ)[17]; (5) the 40 cm LX-200 Telescope of St. Petersburg State University (St. Petersburg, Russia); (6) the 70 cm AZT-8 Telescope of the Crimean Astrophysical Observatory (Nauchnij, Ukraine); (7) the 1.5 m Kanata Telescope in Higashi-Hiroshima Observatory (Japan)[18]; and (8) the Ultraviolet and Optical Telescope (UVOT) on board the *Swift* satellite. Optical data are in part also in polarimetric mode, mostly in the *R* band, except for items (4) and (5) listed above (see Schmidt et al. 1992; Hagen-Thorn et al. 2008, respectively, for details). In the UV range, we use UVOT data from *Swift* in the three available filters: UVW2 (2030 Å), UVM2 (2231 Å), and UVW1 (2634 Å). We have also obtained X-ray data in the energy range 0.3–10 keV from the X-ray Telescope on board the *Swift* satellite.

At the highest photon energies considered here, we have analyzed γ-ray data from the LAT of the *Fermi Gamma-ray Space Telescope*.

2.1. γ-Ray Data Analysis

We have analyzed the γ-ray data of the field containing CTA 102 from *Fermi* LAT from 2008 August to 2013 September, producing a light curve between 0.1 and 200 GeV with an integration time of 1 day. We used the *Fermi* Science Tools version v9r33p0 and instrument response function P7REP_SOURCE_V15, considering data inside a region of interest (ROI) of 15° radius centered on CTA 102. We followed the unbinned likelihood procedure as described at http://fermi.gsfc.nasa.gov/ssc/data/analysis/scitools/.

The procedure starts with the selection of good data and time intervals through the tasks *gtselect* and *gtmktime* and follows with the creation of an exposure map for each day (tasks *gtltcube*, *gtexpmap*) and the modeling of data through a maximum-likelihood method (*gtlike*). In this last step, we used a model that includes CTA 102 and 42 other point sources inside the ROI, according to the second *Fermi* Gamma-ray Catalog (2FGL; Ackermann et al. 2011). The model also takes

---

2

into account the diffuse emission from our Galaxy (*gll_iem_v05.fit*) and the extragalactic γ-ray background (*iso_source_v05.txt*). We searched for the flux normalization of CTA 102 by fixing the spectral index of the other point sources while varying both the flux and spectral index of our target. The γ-ray spectrum of CTA 102 was modeled with a log parabola curve corresponding to the spectral model given in the 2FGL catalog. We considered a successful detection when the test statistic TS $\geqslant$ 10, which corresponds to a signal-to-noise ratio $\gtrsim 3\sigma$ (Nolan et al. 2012).

2.2. X-ray, UV, Optical, and NIR

We collected X-ray and UV data from 2009 August to 2013 June from the *Swift* archive. The X-ray data in the energy range 0.3–10 keV were calibrated following the procedure described in Williamson et al. (2014). The UVOT data reduction was performed via the UVOTSOURCE tool, with a sigma value of 5 adopted to compute the background limit. Optical and NIR data were reduced and calibrated following the procedures outlined in Jorstad et al. (2010).

All of the magnitudes of the optical and NIR data have been corrected for Galactic extinction with values reported in the NASA Extragalactic Database[19] for each filter (Schlafly & Finkbeiner 2011). For the UV data, we obtained the absolute extinction value at each wavelength $A(\lambda)$ from Equation (1) in Cardelli et al. (1989). After the correction, we transformed magnitudes into fluxes using the formula reported in Mead et al. (1990) and Poole et al. (2008).

2.3. Photopolarimetric Millimeter VLBA and Single-dish Data

Multi-epoch very long baseline interferometer (VLBI) images provide ultra-high angular resolution that can be used to determine the location in the jet where flaring activity occurs. We therefore have collected data from the VLBA-BU-BLAZAR program,[20] which consists of monthly monitoring of γ-ray bright blazars with the VLBA at 43 GHz (7 mm). The data set consists of 80 total and polarized intensity images from 2007 June to 2014 June. We restore the images with a common convolving beam of 0.4 × 0.2 milliarcseconds (mas). Since the resolution of the longest baselines of the VLBA is less than half of these dimensions, we employ model fitting to define and determine the parameters of the very fine-scale structure. The data reduction was performed with a combination of the Astronomical Image Processing System (AIPS) and the Differential Mapping software (Difmap), as described in Jorstad et al. (2005). The electric vector position angle (EVPA) calibration follows the procedure discussed in Jorstad et al. (2005), which combines the comparison between VLA and VLBA integrated EVPA values at those epochs for which VLA data are available with the method of Gómez et al. (2002) that utilizes the stability of the instrumental polarization (D-terms).

The IRAM 30 m Telescope's total flux and polarimetric data in this paper were acquired under the POLAMI (Polarimetric AGN Monitoring at the IRAM 30 m Telescope) program (see I. Agudo et al. 2015, in preparation) and reduced and calibrated following the procedures introduced in Agudo et al. (2006, 2010, 2014).
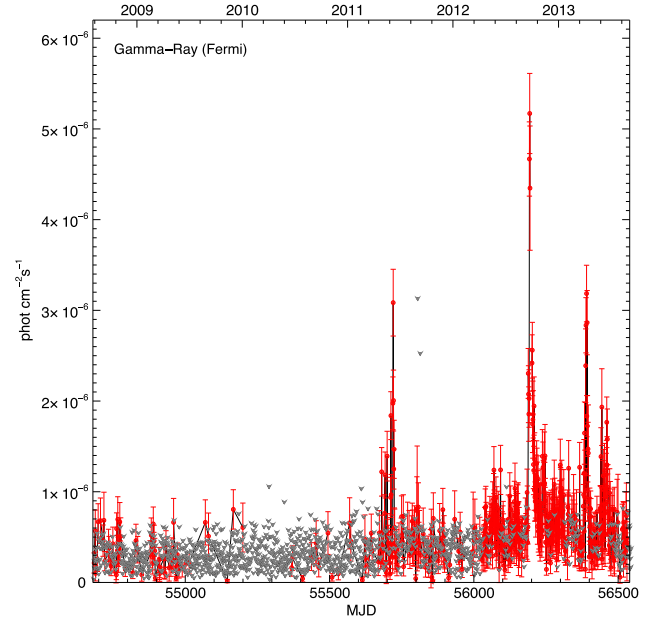
Figure 1. *Fermi* LAT γ-ray light curve between 0.1 and 200 GeV, with an integration time of 1 day. Red points represent the detections (TS > 10), and gray arrows correspond to upper limits when the source is not detected (TS < 10).

The Submillimeter Array data of CTA 102 came from an ongoing monitoring program at the SMA to determine the fluxes of compact extragalactic radio sources that can be used as calibrators at millimeter wavelengths (Gurwell et al. 2007). Observations of available potential calibrators are from time to time observed for 3–5 minutes, and the measured source signal strength are calibrated against known standards, typically solar system objects (Titan, Uranus, Neptune, or Callisto). Data from this program are updated regularly and are available at the SMA website.[21]

3. MULTI-WAVELENGTH OUTBURST

Figure 1 displays the γ-ray light curve of CTA 102 in the energy range 0.1–200 GeV during the period of major activity (2011 June–2013 April) obtained with an integration time of 1 day. Following Jorstad et al. (2013), we can define a γ-ray outburst as a period when the flux exceeds a threshold of 2×10^{-6} photons cm^{-2} s^{-1}. Although this is an arbitrary limit, it conforms to a visual inspection of the γ-ray light curve of CTA 102.

The first outburst takes place in 2011 June (MJD 55719–55721), when the source displays a one-day peak flux of $3.1 \pm 0.37 \times 10^{-6}$ photons cm^{-2} s^{-1}. The second, brightest outburst occurs at the end of 2012 September (2012.73), when the source remains above 2×10^{-6} photon cm^{-2} s^{-1} for 14 days (from MJD 56188 to 56202), reaching a peak of $5.2 \pm 0.4 \times 10^{-6}$ photons cm^{-2} s^{-1} on MJD 56193. During this outburst, the γ-ray flux increases by a factor of 10 in just 6 days. The third flare occurs in 2013 April (MJD 56387–56394) and lasts 8 days. On this occasion (MJD 56392), the blazar reaches a peak of $2.9 \pm 0.4 \times 10^{-6}$ photons cm^{-2} s^{-1}.

We compare the daily γ-ray light curve with the X-ray, UV, optical, NIR, and radio light curves in Figure 2. Table 1 lists
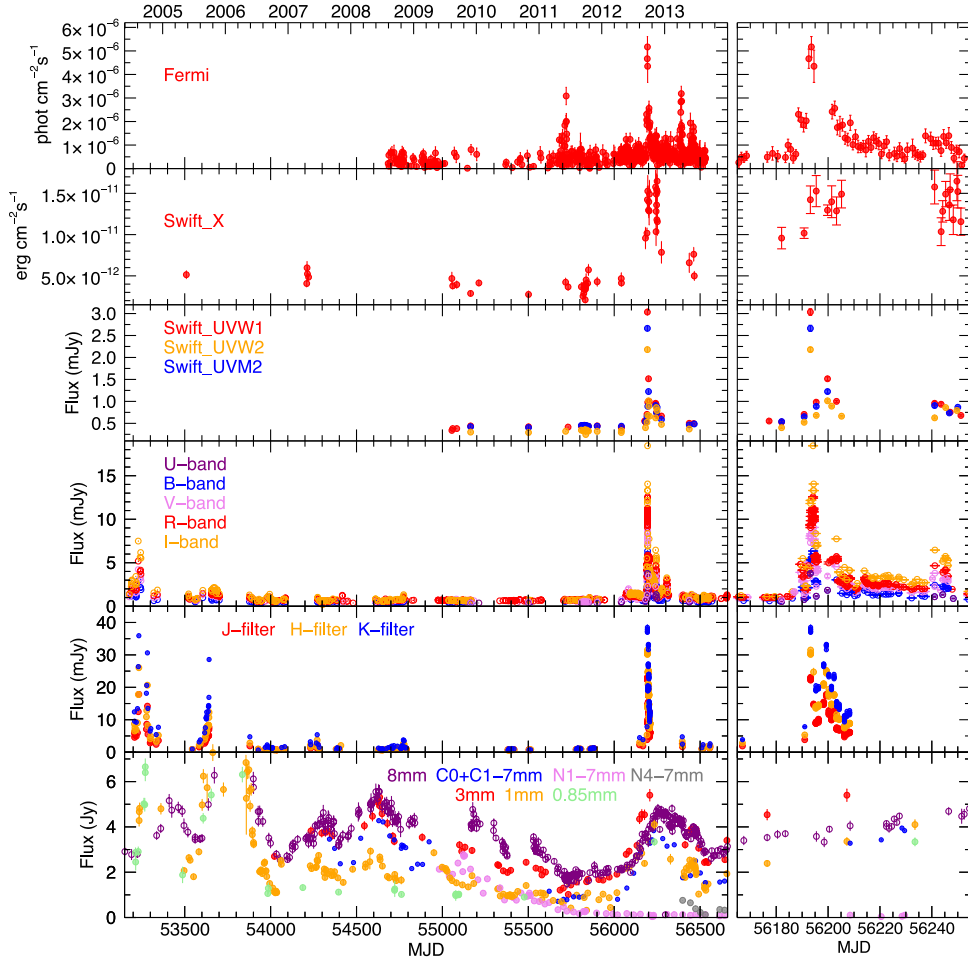
3

Figure 2. Light curves of CTA 102 from γ-ray to millimeter wavelengths. From top to bottom: γ-ray, X-ray, UV, optical, NIR, and millimeter-wave data. Left panel: data from 2004 May to 2014 January. Right panel: expanded view during the γ-ray outburst between 2012 August and November.

Table 1
Multi Wavelength Data

γ-Ray Data	Flux	Energy Band
Epoch		
(MJD)	(photons cm^{-2} s^{-1})	(GeV)
54684.2	2.15e-07 ± 1.11e-07	0.1–200
54688.2	5.68e-07 ± 2.30e-07	0.1–200
54689.2	10.00e-08 ± 8.30e-08	0.1–200

X-ray data		
Epoch	Flux	Energy Band
(MJD)	(photons cm^{-2} s^{-1})	(KeV)
53509.4	5.14e-12 ± 4.74e-13	0.3–10
54210.2	4.07e-12 ± 4.13e-13	0.3–10
54212.1	5.97e-12 ± 7.67e-13	0.3–10

(This table is available in its entirety in machine-readable form.)

the multi-wavelength data used in our analysis. The brightest γ-ray outburst, in 2012 September, is accompanied by similarly bright flares at all of the other wavebands. This is, however, not the case for the other two orphan γ-ray flares (γ-ray outbursts with no correspondence at any of the other observing bands),

with the exception of a millimeter-wave flare that follows the third γ-ray flare in 2013 April.

Analyzing the multi-wavelength flare in 2012, we observe that the X-ray light curve contains a double-peak structure, where the first peak is almost coincident with the γ-ray outburst and the second peak occurs ∼50 days later. The limited sampling of the X-rays prevents a deeper analysis of the overall X-ray behavior associated with this flare. The UV and optical bands exhibit a rapid and pronounced increase in the light curves coinciding with the γ-ray flare. In the optical light curve, we distinguish a secondary, weaker flare after ∼50 days, close to the second X-ray peak, as well as a third, smaller outburst that occurs ∼70 days after the second peak. In the UV it is also possible to distinguish a secondary flare delayed by ∼50 days with respect to the main flare, but the sampling of the data is insufficient to specify the behavior in more detail. In the NIR light curve, we observe a large flare coincident with the γ-ray flare, but there is no further sampling after this. A detailed analysis of the NIR flare shown in Figure 3 reveals that the event consists of three sub-flares covering almost the entire period of high γ-ray flux from MJD 56193 to 56202.

The radio light curve also exhibits an increase in flux density during the 2012 γ-ray outburst, but with a much longer timescale, lasting ∼200 days. The 1 mm light curve and 7 mm light curves of features C0 and C1 peak on ∼MJD 56230,
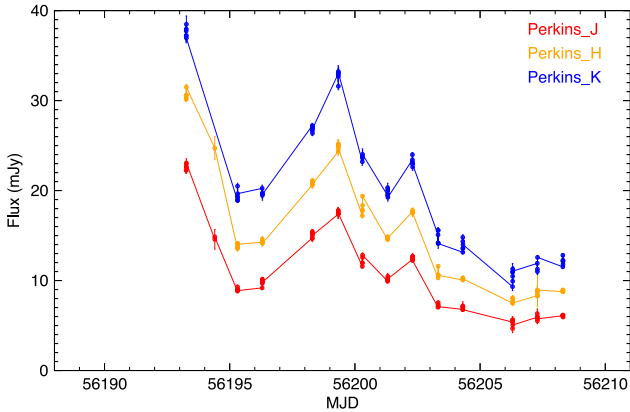
Figure 3. Expanded view of the NIR light curve in the *J*, *H*, and *K* bands during the period of the main γ-ray outburst.

about 1 month after the γ-ray flare. The 3 mm light curve follows a similar trend, starting to increase on ∼MJD 56000. Our limited time sampling between MJD 56208 and 56412 shows a peak on MJD 56207, very close to the γ-ray flare, although we cannot rule out the possibility that the actual peak is closer to that at 1 mm.

4. THE PARSEC-SCALE JET

4.1. Physical Parameters of Components

VLBA images of CTA 102 at some selected epochs are displayed in Figures 4–6. To carry out an analysis of the jet kinematics and flux density variability, we have fit with `Difmap` the complex visibilities with a model source consisting of components described by circular Gaussian brightness distributions. For each epoch, we obtained a model fit that provides information about the flux density (S), distance (r), and position angle (Θ) relative to the core and the FWHM size (a) of each component. The core (labeled C0), considered stationary over the entire period, is identified with the unresolved component in the northwestern (upstream) end of the jet. It is the brightest feature in the jet at most of the epochs. Polarization information has been obtained with an IDL program that calculates the mean values of the degree of polarization (m) and EVPA (χ) over the image area defined by the FWHM size of each component. The uncertainties of both m and χ correspond to the standard deviations of their respective distributions. Model-fit parameters for all components and epochs are reported in Table 2.

The accuracy of the model-fit parameters for each component depends on its brightness temperature, so that smaller uncertainties are expected for more compact components and higher flux densities. We have therefore established a criterion for quantifying the errors in the model-fit parameters that is directly related to the observed brightness temperature, $T_{\rm b} = 7.5 \times 10^8\, S/a^2$ (e.g., Jorstad et al. 2005), where $T_{\rm b}$ is measured in Kelvins (K), S in Janskys (Jy), and a in milliarcseconds (mas).

First, we select a representative sample of epochs and components with a wide range of S, a, and r values. For each one of these components, we compute the error in the fitted parameters by analyzing how the reduced χ^2 of the fit and resulting residual map change when varying the fitted parameters one at a time. We set a limit on the maximum

allowed variation of the reduced χ^2 of 20%, corresponding to an increase by a factor of ∼1.5 in the peak levels of the residual map. According to this criterion, we assign a series of uncertainties in position and flux density to the components in the sample. We then relate the derived uncertainties with the measured brightness temperature, obtaining the following relations:

$$\sigma_{xy} \approx 1.3 \times 10^4\, T_{\rm b}^{-0.6}, \tag{1}$$

$$\sigma_S \approx 0.09\, T_{\rm b}^{-0.1}, \tag{2}$$

where σ_{xy} and σ_S are the uncertainties in the position (R.A. or decl.) and flux density, respectively. These relations have been used to compute the errors in the position and flux density for all of the fitted components. To account for the errors in the flux calibration, we have added in quadrature a 5% error to the uncertainty in flux density. The uncertainties in the sizes of components are also expected to depend on their brightness temperatures. Following Jorstad et al. (2005), we have assigned a 5% error to the sizes of the majority of components (those with flux densities ⩾50 mJy and sizes of 0.1–0.3 mas) and a 10% error for more diffuse components.

Plots of separation and flux density versus time for the model-fit jet components, including the core, are presented in Figures 7 and 8. Besides the core, we have identified seven main components that could be traced reliably across multiple epochs. Component E1, located at ∼2 mas from the core, is a weak and extended feature that appears to be quasi-stationary across some epochs, or to move with a significantly slower velocity than other moving components (see Figure 7). A stronger and more compact component, C1, can be distinguished from the core at most of the observed epochs, located at a mean distance of $r \sim 0.1$ mas. Both quasi-stationary features have been observed previously by Jorstad et al. (2005) and Fromm et al. (2013a, 2013b) and interpreted as recollimation shocks in the jet. We identify five other moving components, N1, N2, N3, N4, and S1. Component S1 seems, however, to have a different nature: it appears to form in the wake of component N1 at a distance of ∼0.5 mas, and it is observed over only four epochs afterward. Its properties are similar to those expected and observed previously for trailing components (Agudo et al. 2001; Gómez et al. 2001; Jorstad et al. 2005). Linear fits of separation versus time have been obtained for the other moving components, N1, N2, N3, and N4, based on only those initial epochs at which an accurate position is obtained (see also Figure 7). This yields the estimates for the apparent velocities and times of ejection (epoch at which the component coincides with the core) listed in Table 3.

Since we cannot directly measure the radial velocities of the jet features, a common approach to disentangle the contributions of the component's Lorentz factor and viewing angle in the observed proper motion is the use of the flux variability (e.g., Jorstad et al. 2005; Hovatta et al. 2009). Following Jorstad et al. (2005), we use causality arguments to infer the variability Doppler factor

$$\delta_{\rm var} = \frac{sD_{\rm L}}{c\triangle t_{\rm var}(1 + z)}, \tag{3}$$

where s is the disk-equivalent angular diameter (where $s = 1.6a$ for a Gaussian component fit with FWHM = a measured at the
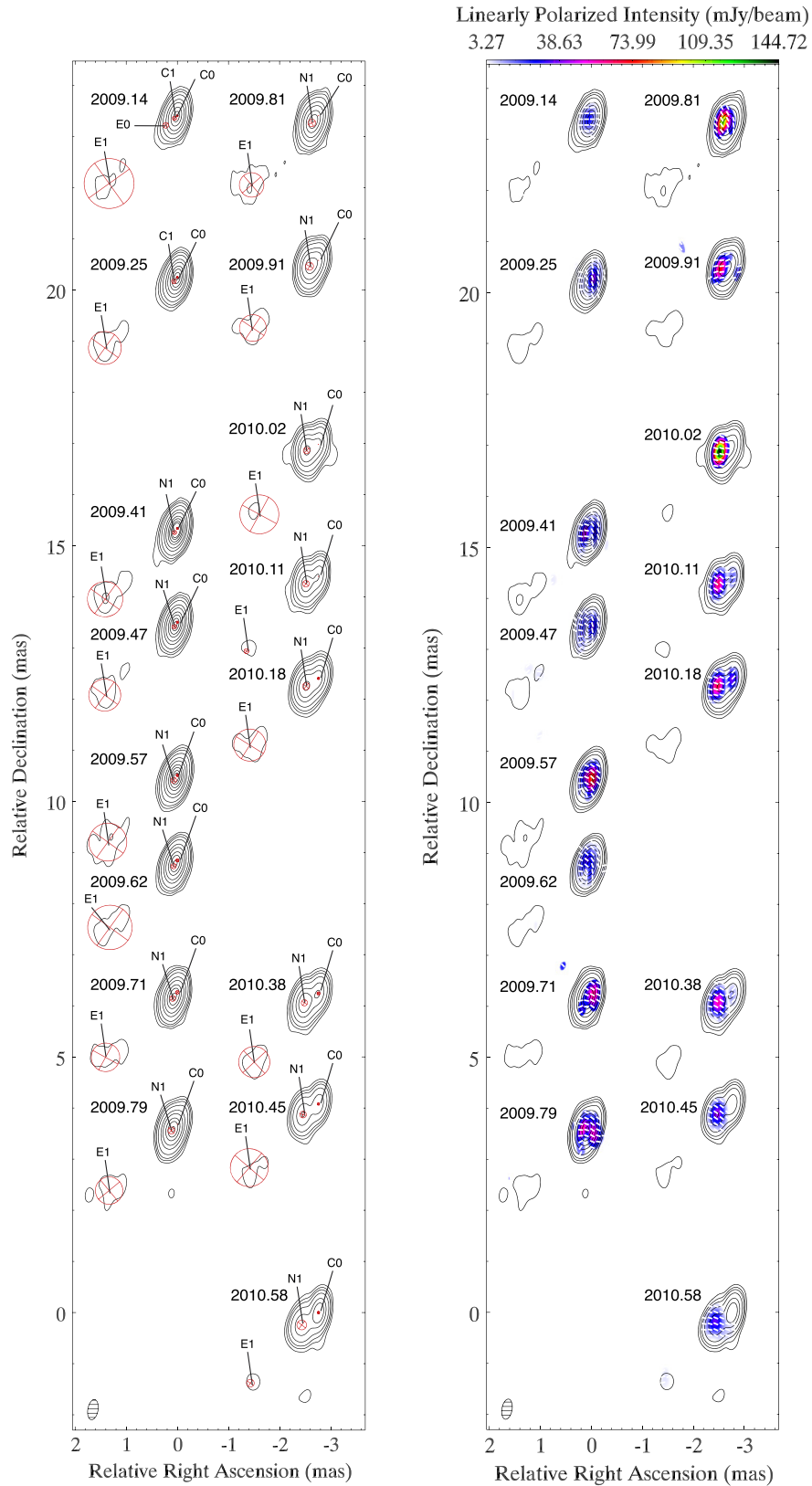
5

Figure 4. Sequence of 43 GHz VLBA images displaying epochs from 2009 February to 2010 August, when we observe the appearance of component N1. The images are restored with a common beam of 0.4 × 0.2 mas at −10° and are separated by a distance proportional to the time elapsed between observing epochs. Left panel: contours (total intensity) are traced at 0.003, 0.008, 0.04, 0.1, 0.3, 0.6, 1.2, 1.8, 2.5, and 3.0 Jy beam^{-1} and I_{peak} = 4.2 Jy beam^{-1}. Red circles represent model-fit components. Right panel: same contours (total intensity) as in the left panel plus colors that represent linearly polarized intensity and white sticks symbolizing linear polarization angle.
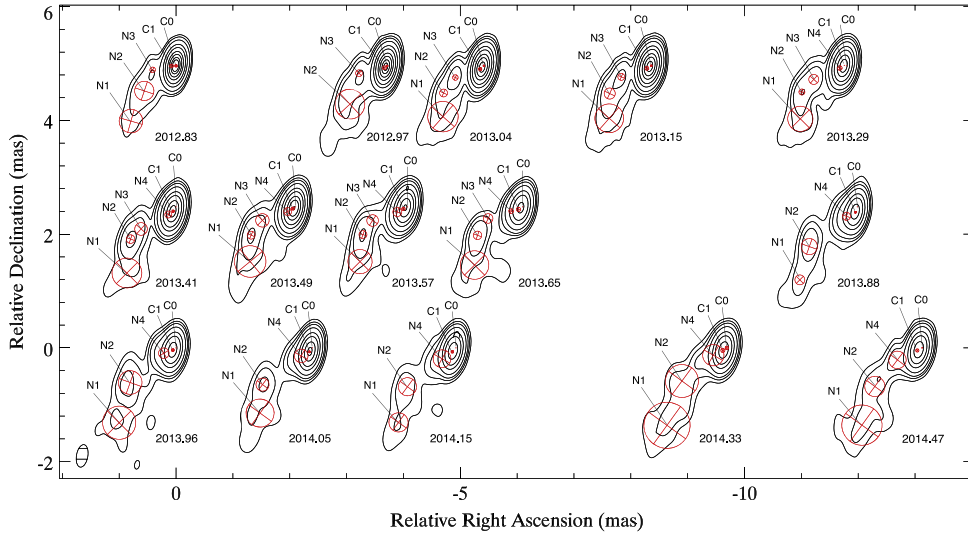
6

Figure 5. Sequence of total intensity 43 GHz VLBA images from 2012 October to 2014 June, covering the epochs from which we start observing component N4. Peak intensity is $I_{peak} = 3.6$ Jy beam^{-1} and contours are traced at 0.003, 0.008, 0.04, 0.1, 0.3, 0.6, 1.2, 1.8, 2.5, and 3.0 Jy beam^{-1}.
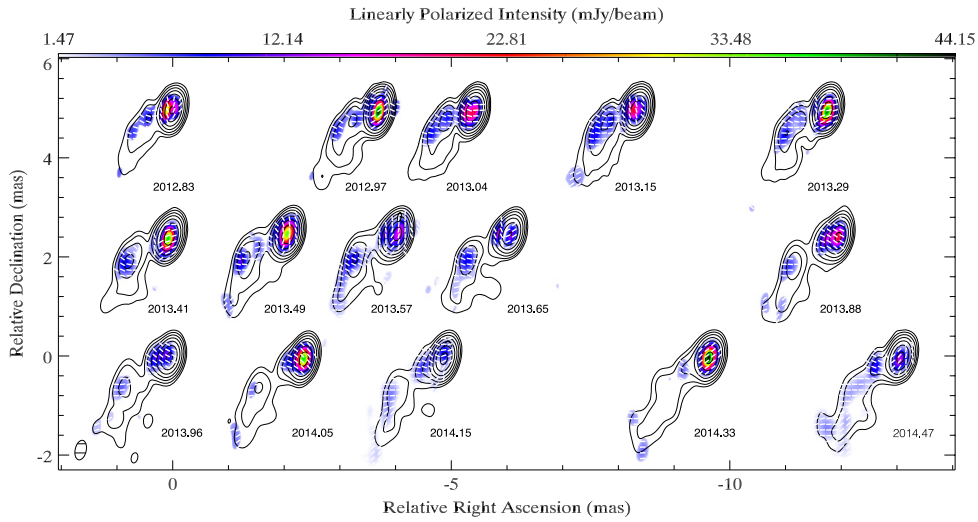

Figure 6. Same as Figure 5, but with linearly polarized intensity in colors and white sticks symbolizing linear polarization angle.

epoch of maximum flux), and D_L is the luminosity distance. The variability timescale is defined as $\triangle t_{var} = dt/\ln(S_{max}/S_{min})$, where S_{max} and S_{min} are the measured maximum and minimum flux densities, respectively, and dt is the time in years between S_{max} and S_{min} (Burbidge et al. 1974). This definition of δ_{var} is valid under the assumption that the flux density variability timescale corresponds to the light-travel time across the component, which is valid as long as the radiative cooling time is shorter than the light crossing time and expansion time. Combining the estimated value of δ_{var} with the measured apparent velocity, $\beta_{app} = \beta \sin\theta/(1 - \beta\cos\theta)$, where θ and β are the viewing angle and velocity (in units of the speed of light) of the component, we can calculate the variability Lorentz factor, Γ_{var}, and viewing angle, θ_{var}, using (Hovatta et al. 2009)

$$\Gamma_{var} = \frac{\beta_{app}^2 + \delta_{var}^2 + 1}{2\delta_{var}} \quad (4)$$

and

$$\theta_{var} = \arctan\frac{2\beta_{app}}{\beta_{app}^2 + \delta_{var}^2 - 1}. \quad (5)$$

Physical parameters of the moving components obtained from this method are reported in Table 4.

4.2. Kinematics and Flux Density Variability

By inspecting the light curves in Figure 8, we can identify two flaring periods in the core: a prolonged first event that extends from mid-2007 to the beginning of 2009, and a second one between mid-2012 and the beginning of 2013, in coincidence with the main γ-ray flare.

The peak flux of the first flare occurs between 2008 June and July, when both components C0 and C1 increase their flux densities, reaching a combined value of $\sim$4.2 Jy. Due to the proximity of C1 to the core, it is not always possible for the model-fitting routine to clearly distinguish the two components, leading to high uncertainties in the flux ratio of the two

7

Table 2
VLBA 43 GHz Model-fit Components' Parameters

Epoch (year)	Epoch (MJD)	Flux (mJy)	Distance from C0 (mas)	Pos. Angle (°)	Major Axis (mas)	Degree of Polarization (%)	EVPAs (°)
			Component C0				
2007.45	54264.5	3086 ± 313	⋯	⋯	0.017 ± 0.001	⋯	⋯
2007.53	54294.5	3423 ± 347	⋯	⋯	0.034 ± 0.002	1.5 ± 0.2	71.2 ± 5.7
2007.59	54318.5	2340 ± 239	⋯	⋯	0.038 ± 0.002	2.4 ± 0.1	76.4 ± 5.4
2007.66	54342.5	3163 ± 321	⋯	⋯	0.045 ± 0.002	1.6 ± 0.1	71.9 ± 6.6
2007.74	54372.5	2743 ± 279	⋯	⋯	0.045 ± 0.002	1.4 ± 0.1	82.9 ± 8.4
			Component C1				
2007.66	54342.5	296 ± 37	0.07 ± 0.01	119.2 ± 3.2	0.062 ± 0.003	1.6 ± 0.1	65.5 ± 7.1
2007.74	54372.5	307 ± 37	0.09 ± 0.01	104.4 ± 4.8	0.031 ± 0.002	2.2 ± 0.1	−80.8 ± 6.3
2007.83	54405.5	168 ± 25	0.13 ± 0.02	119.5 ± 3.2	0.116 ± 0.006	2.6 ± 0.2	79.3 ± 5.9
2008.04	54482.5	575 ± 64	0.08 ± 0.01	146.2 ± 1.9	0.070 ± 0.003	0.7 ± 0.1	37.8 ± 5.5
2008.16	54524.5	894 ± 96	0.09 ± 0.01	−166.3 ± 7.4	0.062 ± 0.003	0.5 ± 0.1	38.2 ± 5.6

(This table is available in its entirety in machine-readable form.)
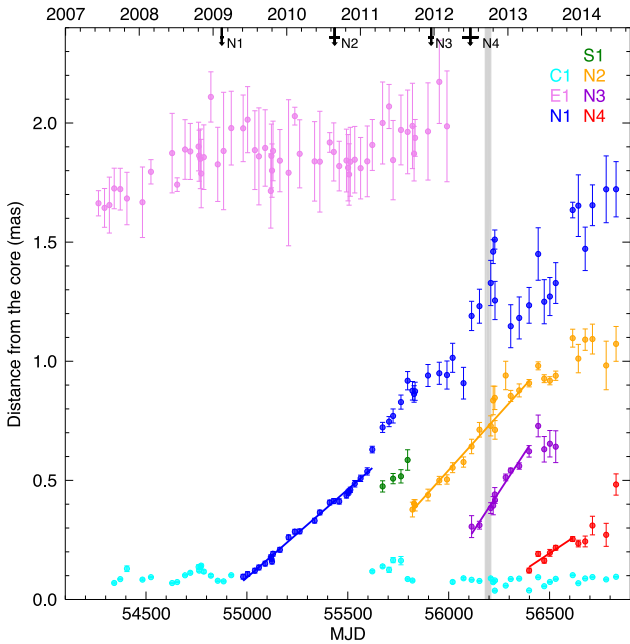

Figure 7. Distance from the core vs. time for the 43 GHz model-fit components, with linear fits overlaid. Downward black arrows mark the time of ejection of each component with the respective error bar. The gray vertical stripe indicates the epoch of the γ-ray flare.
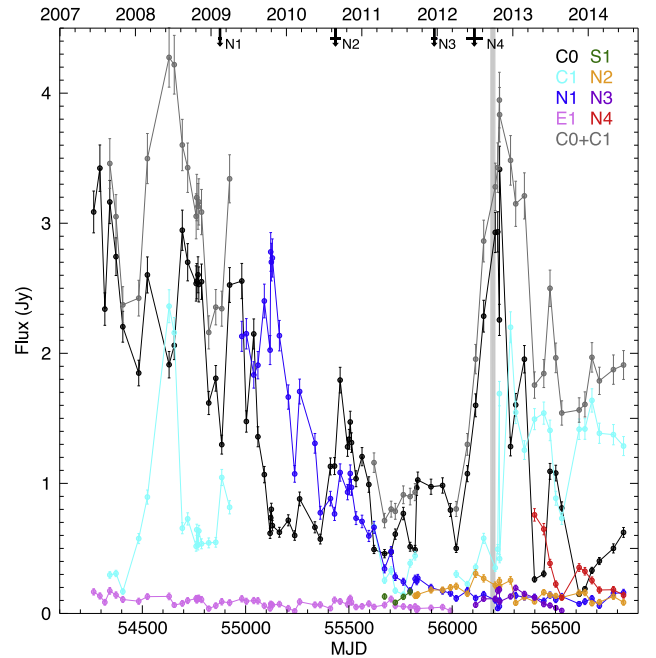

Figure 8. Light curves of 43 GHz model-fit components. Downward arrows and the gray vertical stripe indicate the same as in Figure 7.

Table 3
Kinematics of Moving Jet Features

Name	N.Epoch	μ (mas yr^{-1})	β_{app} (c)	T_{ej} (year)
N1	26	0.27 ± 0.01	14.9 ± 0.2	2009.12 ± 0.02
N2	18	0.35 ± 0.01	19.4 ± 0.8	2010.65 ± 0.07
N3	10	0.49 ± 0.03	26.9 ± 1.8	2011.96 ± 0.07
N4	6	0.21 ± 0.02	11.3 ± 1.2	2012.49 ± 0.11

features, as well as uncertainties in the position of C1. Because of this, Figure 8 also shows the combined flux density of the core and component C1, providing the data needed to follow the total flux density within the core region of CTA 102.

The second flare in the millimeter-wave core began in mid-2012, reaching its peak flux density at the end of 2012 October, close to the γ-ray flare (see Figure 8; Section 5). After the peak, the core region (C0 plus C1) remains in a high flux state until the last observing epoch, with a combined flux density oscillating around ∼2 Jy.

Both flares in the core region are associated with the appearance of subsequent superluminal components. In the case of the first such flare, component N1 appears as a bright

and well-defined feature that moves along the jet at 14.9 ± 0.2 c (see Figures 7–8 and Table 3). We also note that the ejection of component N1 corresponds to a change in the innermost structure of the compact jet, after which component C1 is no

Table 4
Physical Parameters of Moving Jet Features

Name	$\triangle t_{var}$ (year)	a_{max}[a] (mas)	δ_{var}	θ_{var} (°)	Γ_{var}
N1	0.70	0.14	14.6	3.9	14.9
N2	1.12	0.33	22.4	2.5	19.6
N3	0.28	0.09	26.1	2.2	26.2
N4	0.20	0.08	30.3	1.2	17.3

Note.
[a] FWHM of the model-fit component calculated at the epoch of maximum flux.

longer detected for almost two years. The second core flare leads to the ejection of component N4, which is significantly weaker than component N1 and has the slowest proper motion of the analyzed components (see Figures 7–8 and Table 3).

The values of the variability Doppler factors listed in Table 4 correspond to a progressive increase with time, from 14.6 for component N1 to 30.3 for component N4. Previous estimations of the variability Doppler factor in CTA 102 range between 15.6 (Hovatta et al. 2009) and 22.3 ± 4.5 (Jorstad et al. 2005), making N4 the superluminal knot with the highest Doppler factor to date. According to our analysis, this unusually large value is due to a progressive re-orientation in the direction of ejection of knots, from $\theta_{var} = 3°.9$ for component N1 to $\theta_{var} = 1°.2$ for N4, which travels almost directly along the line of sight. This change in the jet orientation is readily apparent when analyzing each component's position angle shortly after the time of ejection, as well as their subsequent trajectories, as shown in Figure 9.

This smaller viewing angle of the jet with respect to the observer during the second radio flare, which appears to last until the end of our VLBA data set (2014 June), is also in agreement with the significant differences observed between the ejections of components N1 and N4. While component N1 is clearly identified in the jet as a bright ($\gtrsim 2$ Jy) component soon after its ejection, most of the increase in the total flux density during the second radio flare appears to be associated with the core region (C0+C1), with component N4 representing only a small fraction of the flare. The smaller viewing angle of the jet also leads to a more difficult identification of component N4, which is not clearly discerned from the core until 2014 May (2014.33). Further support for the re-orientation of the jet toward the observed is also obtained from the analysis of the polarization, discussed in Section 6.

5. CROSS-CORRELATION ANALYSIS

To quantify the relationship among the light curves at the different wavebands, we perform a discrete cross-correlation analysis. The z-transformed discrete correlation function (ZDCF) described by Alexander (1997) has been designed for unevenly sampled light curves, as in our case. We use the publicly available zdcf_v1.2 and plike_v4.0.f90 programs,[22] with a minimum number of 11 points inside each bin, as recommended for a meaningful statistical interpretation. We compute the DCF between each pair of light curves, including data from 100 days before to 100 days after the main γ-ray outburst. Time sampling of the light curves ranges from one

day for the γ-ray data to tens of days in the case of some other wavebands (see Figure 2).

Figure 10 displays the ZDCF analysis for the optical-γ (upper panel) and UV-γ (lower panel) data. We find that the correlation peaks between the γ-ray light curve and the optical and UV light curves give a time lag of 0.70 ± 1 and $1.23^{+5.00}_{-4.09}$ days, respectively, where a positive lag means that the γ-ray variations lead. We therefore conclude that the variations at the three wavelengths are essentially coincident within the uncertainties.

The sparser sampling of the X-ray data, as well as its double-peaked structure, precludes a reliable ZDCF analysis. However, we note that the first X-ray data peak is coincident with the γ-ray flare, and the second brighter X-ray flare occurs ∼50 days later (see Figure 2). The triple-flare structure of the NIR light curve during the γ-ray flare (see Figure 3) also prevents a unique interpretation of a cross-correlation analysis. Nevertheless, from inspection of the light curves, we see that the first, brightest peak in the NIR light curve (56193 MJD) is simultaneous with the γ-ray outburst within an uncertainty of one day, corresponding to the time sampling of both light curves.

We obtain no significant correlation between the millimeter-wave and γ-ray light curves. This can be due to the different timescales associated with the emission at these wavebands, as also suggested for other blazars (e.g., 1156+295; Ramakrishnan et al. 2014). The rise time for the millimeter-wave band is of the order of months, while for the γ-rays it is of the order of a few days. We note, however, that the 1, 3, and 7 mm light curves contain a significant flare coincident with the γ-ray outburst.

6. POLARIZED EMISSION

Figure 11 shows the optical and millimeter-wave linear polarization between MJD 54000 and 56900, covering the period of the γ-ray flare. To solve for the $\pm n\pi$ ambiguity in the EVPA, we assume the slowest possible variation in time, applying a $\pm \pi$ rotation between two consecutive measurements when the magnitude of the EVPA change would otherwise exceed $\pi/2$.

No significant increase in the degree of polarization at millimeter wavelengths is observed during the γ-ray flare, but the EVPAs display a progressive rotation starting about one year prior to the γ-ray flare. Figure 11 shows that between 2007 and mid-2011 the EVPAs at 3 and 1 mm are distributed around a mean value of ∼100°. After this, the polarization at millimeter wavelengths starts a slow rotation by almost 80° in one year (from 2011 July to 2012 August) until the flare epoch. In coincidence with the γ-ray flare, the rate of EVPA rotation in the VLBI core and stationary component C1 increases significantly, leading to a rotation of almost 200° in one year. Subsequently, component N4 appears and the EVPAs of both C1 and N4 rotate again toward values similar to those at 1 and 3 mm, reaching ∼−100°. It is possible that during the flare, while the new superluminal component N4 is crossing the core zone, the EVPAs of the innermost region at 7 mm rotate due to the passage of the component. After this, when N4 can be distinguished from C1 and C0, the EVPAs at 7 mm again follow the general behavior of the EVPAs at shorter millimeter wavelengths. A similar discrepancy between the 1–3 and 7 mm EVPAs occurs between mid-2009 and mid-2010, when
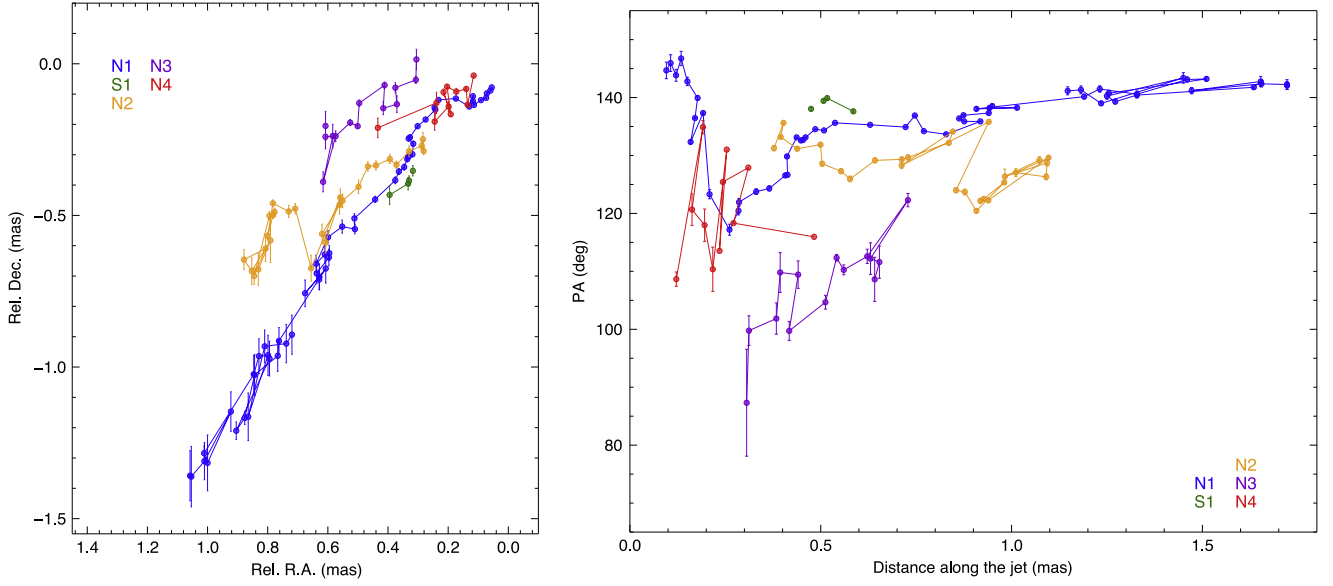
---
[22] http://www.weizmann.ac.il/weizsites/tal/research/software/

9

Figure 9. Trajectories (left panel) and position angles as a function of distance from the core (right panel) of the moving components in the jet.
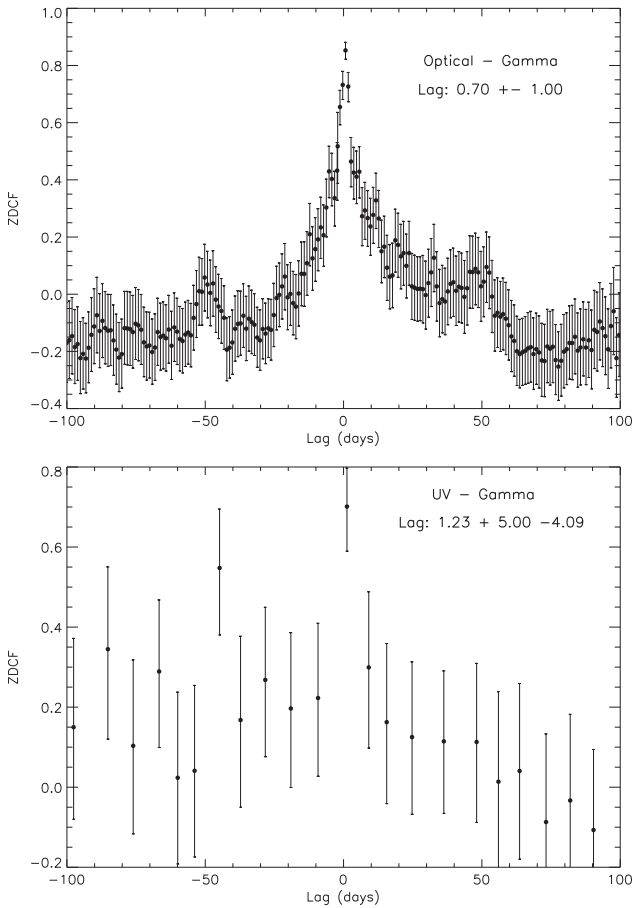

Figure 10. Z-transformed discrete correlation function between optical and γ-ray data (upper panel) and UV and γ-ray data (lower panel). In each panel, we report the time lag corresponding to the correlation peak with its respective 1σ error (see Alexander 2013 for more details).
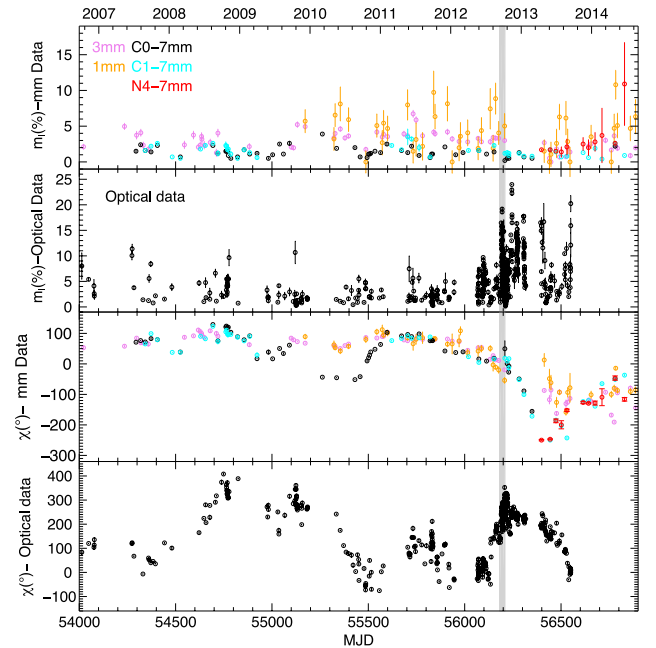

Figure 11. Optical and millimeter-wave linear polarization over the period MJD 54000–56800. The first two panels display the degree of millimeter-wave and optical polarization, respectively. The third and fourth panels display the EVPAs at millimeter and optical wavelengths, respectively. The gray vertical stripe indicates the epoch of the main γ-ray flare.

component N1 is ejected and becomes brighter than the core until mid-2010 (see Figure 8).

We can then distinguish the rapid rotation of polarization vectors observed in the VLBI components at 7 mm after the flare from the slower rotation observed at 1 and 3 mm. The latter leads to a rotation of the mm-EVPAs of ∼200° over 3 years (from 2011 July to 2014 August). This progressive
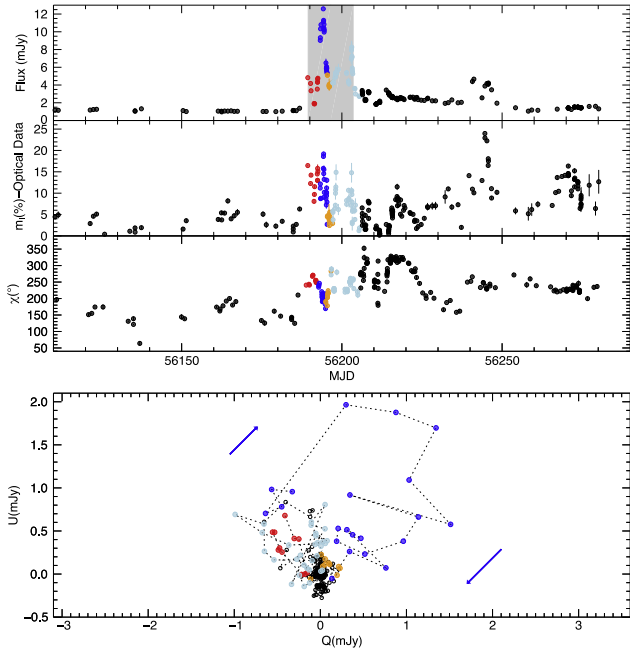
Figure 12. Upper panel displays, from top to bottom, the light curve, degree and time evolution of polarization, and EVPA at optical frequencies. Each colored mark corresponds to the period over which we plot the U and Q Stokes parameters in the lower panel. Blue points mark a clockwise rotation cycle that occurs in coincidence with the total intensity peak. The gray vertical stripe indicates the time range of the main gamma-ray flare.

Figure 13. Spectral energy distribution of CTA 102 from millimeter-wave to γ-ray frequencies during the brightest γ-ray flare (black) and at other observing epochs, as labeled in the figure and discussed in the text.

7. SPECTRAL ENERGY DISTRIBUTION

We have computed the spectral energy distribution (SED) of the source from millimeter to γ-ray wavelengths at several epochs (see Figure 13): two epochs between MJD 54720 and MJD 55055, corresponding to γ-ray quiescent states; the epochs of the first γ-ray flare (MJD 55715–55721), the main flare (MJD 56193), and the third γ-ray flare (MJD 56392–56398); one epoch of a quiescent state between the first and second flares (MJD 56040–56047), and a second one between the second and third flares (MJD 56273–56280). For the main γ-ray flare, all data are simultaneous except for the millimeter-wave data, which corresponds to MJD 56208. For the other epochs, we have considered a range of time (as indicated in Figure 13) in order to cover the entire energy range.

By examining Figure 13, we observe that, during the multiwavelength flare in 2012 (black points), both the synchrotron and the inverse-Compton peaks increased. The synchrotron peak frequency during the flare is close to 10^{14} Hz, at the upper end of the frequency range 10^{12}–10^{14} Hz of synchrotron peaks observed in luminous blazars (Ghisellini & Tavecchio 2008). At the same time, we also observe a shift in the inverse-Compton peak to higher frequencies, which leads to a hardening of the spectrum between 0.1 and 1 GeV. We note that neither of the other two, weaker γ-ray flares displays a similar shift in the peak of the inverse-Compton spectrum. In particular, the weaker first and third γ-ray flares display a very similar inverse-Compton spectrum, peaking at nearly the same frequency, with only a minor hardening toward higher energies during the third flare. The shift of the γ-ray peak toward higher frequencies during the main γ-ray flare can be explained by a change in the viewing angle—leading to an increase in Doppler factor—of the emitting region, in support of our hypothesis of a reorientation of the jet toward the line of sight during the multiwavelength flare (see Sections 4 and 6).

The ratio of the inverse-Compton to synchrotron peaks is of the order of 10, which is not sufficiently large to rule out synchrotron self-Compton (SSC) scattering as the main mechanism for the production of the γ-ray emission (e.g., Sikora et al. 2009).

rotation in the EVPAs can be produced by a change in the orientation of the innermost jet, which would be in agreement with the larger Doppler factor and smaller viewing angle of component N4 associated with the γ-ray event, as discussed previously (see Section 4).

The optical polarization executes rapid and pronounced changes in both degree of polarization and EVPA associated with the γ-ray flare. Figure 12 displays an expanded view of the optical polarization data near the time of the γ-ray flare, with four different time ranges marked in different colors. Before the peak at optical frequencies on MJD 56194, the source undergoes a period of rapid changes in both total and polarized emission (marked in red), and the EVPAs rotate by almost 30°. The plot of Stokes parameters U versus Q in Figure 12 reveals a clear clockwise rotation of the EVPAs (marked in blue), in coincidence with the main flare in total flux and a rapid change in the degree of polarization. This clockwise rotation has been previously reported by Larionov et al. (2013a).

If we assume a model in which a relativistic shock does not cover the entire cross-section of the jet and is moving down the jet following helical magnetic field lines, which also propagate downstream, then we expect to observe a rotation in the EVPA. This should be accompanied by a change in the degree of polarization, with a minimum in the middle of the rotation, where the flaring region contains magnetic field lines with opposite polarity (e.g., Vlahakis 2006; Marscher et al. 2008; Larionov et al. 2013b). Evidence of a helical magnetic field in CTA 102 jet can also be found in the detection of negative circular polarization (Gabuzda et al. 2008) and in a gradient in the rotation measure across the jet width at about 7 mas from the core (Hovatta et al. 2012), both in MOJAVE observations.
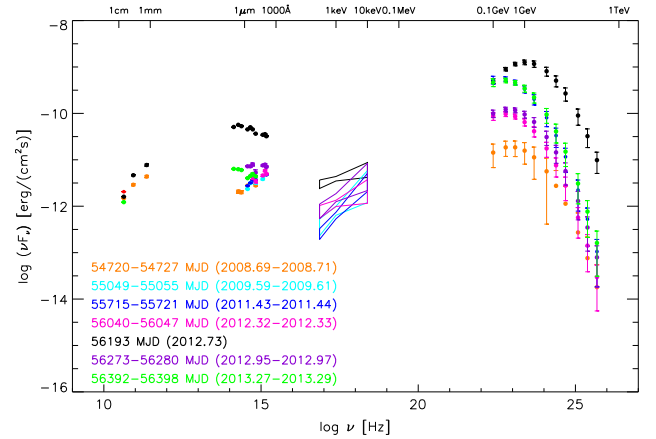
8. DISCUSSION AND RESULTS

We have presented a multi-wavelength polarimetric study of the quasar CTA 102 during an unprecedented γ-ray outburst that was observed between 2012 September 23 and October 2. We find that the γ-ray outburst occurred simultaneously with flares from millimeter to X-ray wavelengths, with the exception that the 1 and 7 mm light curves peak almost one month after the shorter-wavelength flares. However, all of the millimeter-wave light curves begin to increase before the shorter-wavelength outburst, but took longer times to reach maximum flux and then to decay.

Our DCF analysis confirms the coincidence between the γ-ray flare and the optical-UV flare. The same analysis does not provide unambiguous correlation between the X-ray or NIR and the γ-ray light curves because of the multi-peak structure of the flare at these two frequencies and the relatively sparse sampling.

The *Fermi* LAT daily light curve reveals two more γ-ray outbursts apart from that in 2012: one in 2011 June and the other in 2013 April. Both outbursts are weaker and "orphan." Only the bright outburst in 2012 September–October is coincident with flares at the other wavelengths and with the emergence of a new superluminal knot from the radio core.

We have combined our multi-wavelength study of light curves with an analysis of multi-epoch VLBA observations at 43 GHz that provide the necessary angular resolution to follow the evolution of the jet during the outburst. In the 43 GHz VLBA images, we observe the ejection of multiple superluminal knots from the radio core during the analyzed period, but only one of these knots, N4, is associated with a γ-ray flare. Component N4 was ejected in 2012.49 ± 0.11, within a time range between 47 and 127 days before the main γ-ray flare in 2012 (2012.73), when the radio core started to increase in flux density. The interaction between a traveling feature and the stationary radio core appears to have triggered a number of γ-ray outbursts in blazars (e.g., Morozova et al. 2014; Ramakrishnan et al. 2014) and radio galaxies (Grandi et al. 2012; Casadio et al. 2015). However, not every ejection of a new knot leads to a γ-ray flare. For instance, it is not clear why a γ-ray flare is associated with N4 in CTA 102 and not with the other moving radio components.

From the analysis of model-fit components at 43 GHz, we deduce that the jet changed its orientation with respect to the observer when component N4 was ejected. This is derived from an analysis of the variability Doppler factor and viewing angle, which indicates that a progressive increase in the Doppler factor occurred, caused by a re-orientation of the jet toward the line of sight. This led to a minimum viewing angle of $\theta \sim 1^\circ\!\!.2$ when component N4 was ejected during the γ-ray outburst. This change in the orientation of the jet is supported by the observed progressive, slow rotation of the millimeter-wave EVPAs starting almost one year before the ejection of N4 and the γ-ray flare. We therefore conclude that the γ-ray emission in CTA 102 is related to a decrease in the viewing angle of the jet.

This correlation between γ-ray activity and orientation of the jet has been already observed in other BL Lac objects (Marscher et al. 2008; Larionov et al. 2010; Rani et al. 2014), quasars (Abdo et al. 2010b; Raiteri et al. 2011; Jorstad et al. 2013), and radio galaxies (Casadio et al. 2015), although there are different interpretations regarding the cause of the change in orientation. Some authors consider a bent or precessing jet, while others suggest a helical jet with the radiating component following this helical path. A helical trajectory could also be the consequence of magnetic field lines twisting around a conical or parabolic jet (Vlahakis 2006).

In the case of CTA 102, there are indications of a helical magnetic field structure (Gabuzda et al. 2008; Hovatta et al. 2012). We associate the fast variability in the polarized optical emission, as well as the clockwise rotation displayed in the EVPAs during the outburst, with the helical path followed by the superluminal component in its motion along the outwardly propagating magnetic field lines. On the other hand, a number of similar rotations of the millimeter-wave and optical polarization vectors occurred in both the clockwise and counterclockwise directions over the entire 2004–2014 monitoring period. This can be interpreted in terms of random walks of a turbulent magnetic field (Jones 1988; D'Arcangelo et al. 2007; Marscher 2014). Early results from the RoboPol program show that, while many EVPA rotations related to γ-ray flares can be produced by a random walk process, some are not (Blinov et al. 2015). If the rotation associated with a γ-ray flare is caused by a helical geometry of the magnetic field, then future such outbursts should be accompanied by similar clockwise rotations.

The observed long-term rotation in millimeter-wave polarization vectors, together with the slower proper motion associated with component N4, suggests a change in the jet orientation, so that it becomes more closely aligned with the line of sight during the ejection of component N4 and the multi-wavelength flare.

The close timing of the γ-ray, X-ray, UV, and optical flares suggests co-spatiality of the emission at all these frequencies. Knot N4 was 0.025–0.07 mas downstream of the core when the γ-ray flare occurred, i.e., it had not yet reached the feature C1 at $\sim$0.1 mas. This is confirmed by the increase in flux density in the 7 mm core during the γ-ray outburst. Hence, we conclude that the bright γ-ray outburst occurred inside the millimeter-wave core region.

We observe component N4 for the first time in the VLBA images on 2013 April (MJD 56398), when it was located at $r \sim$ 0.12 mas. The γ-ray flare in 2013 April occurred between MJD 56387 and 56394. Therefore, a possible interpretation of this flare is the passage of component N4 through C1, interpreted by Fromm et al. (2013a) as a possible recollimation shock.

If the radio core were located within $\sim$1 pc of the black hole (BH), then the accretion disk or the broad-line region could provide the necessary photon field to explain the high-energy emission through external Compton scattering. The 43 GHz radio core in CTA 102 must be coincident with, or downstream of, the 86 GHz core that is located at a distance of 7.5 ± 3.2 pc ($\sim$8.5 × 10^4 gravitational radii for a BH mass of $\sim$8.5 × $10^8 M_\odot$; Zamaninasab et al. 2014) from the BH (Fromm et al. 2015). A similar scaled distance, $\sim$$10^4$–$10^5$ gravitational radii, has been determined also for two radio galaxies, 3C 111 and 3C 120 (Marscher et al. 2002; Chatterjee et al. 2009, 2011) and two blazars, BL Lac and 3C 279 (Marscher et al. 2008; Abdo et al. 2010b). For a mean viewing angle of the jet of CTA 102 of $2^\circ\!\!.6$ (Jorstad et al. 2005; Fromm et al. 2015), the distance of N4 from C0 is 4.6–13 pc, hence the γ-ray outburst took place more than 12 pc from the BH. At this location, there should be a negligible contribution of photons from the disk or the broad-line region, or from the dusty torus (located $\sim$1.6 pc from the BH; Pacciani et al. 2014), for

external Compton scattering to produce the high-energy flare. The lack of a suitably strong external source of photons favors SSC scattering of NIR to UV photons by electrons in the jet with energies $\sim$10 times the rest-mass energy as the source of the γ-ray emission. The ratio of γ-ray to infrared (synchrotron) luminosity is $\lesssim$10, sufficiently low to be consistent with the SSC process.

9. CONCLUSION

Our study of the time variability of the multi-wavelength flux and linear polarization of the quasar CTA 102 confirms its erratic blazar nature, revealing both strong connections across wavebands in one outburst and no obvious connections for other events. The bright γ-ray outburst in late 2012 was accompanied by contemporaneous flares at longer wavelengths up to at least 8 mm, with the increase in millimeter-wave flux starting before the γ-ray activity. The polarization vector at both optical and millimeter wavelengths rotated from the time of the γ-ray peak until $\sim$150 days later. A new superluminally moving knot, N4—the feature with the highest Doppler beaming factor during our monitoring, according to our analysis—was coincident with the core in the 43 GHz VLBA images 47–127 days prior to the γ-ray peak. We conclude that the outburst was so luminous because the jet (or, at least, the portion of the jet where most of the emission occurs) had shifted to a direction closer to the line of sight than was previously the case. The time delay between the epoch when N4 crossed the centroid of the core (feature C0) and the epoch of peak γ-ray emission implies that the main flare took place $\gtrsim$12 pc from the BH. At this distance, the only plausible source of seed photons for inverse-Compton scattering is NIR to UV emission from the jet itself. The ratio of γ-ray to infrared luminosity is only $\sim$10 at the peak of the outburst, low enough to be consistent with SSC high-energy emission.

Multiple superluminal knots appeared in the jet during the 7 years covered by our VLBA observations. These include a very bright component (N1) ejected in 2009.12 $\pm$ 0.02 and associated with a significant millimeter-wave flare in the core region ($\sim$4.2 Jy). Yet, only component N4 is related to a flare at γ-ray energies. Two strong "orphan" γ-ray flares have no apparent optical counterparts. A strong millimeter-wave event with neither a γ-ray nor optical counterpart can be explained by an inability of the event to accelerate electrons up to energies $\sim 10^4 mc^2$ needed to radiate at such frequencies, although the reason for this inability is unclear. Orphan γ-ray flares might be explained by a knot crossing a region where there is a higher local density of seed photons for inverse-Compton scattering (Marscher et al. 2010; MacDonald et al. 2015). Indeed, the second orphan flare corresponds to the time of passage of knot N4 through stationary feature C1 (located $\sim$0.1 mas from the core), which could be such a region.

During the multi-wavelength outburst we observe intra-day variability in the optical polarized emission, as well as a clockwise rotation in optical EVPAs. This rotation could be caused by a spiral path traced by the knot moving along helical magnetic field lines that propagate outwards relativistically. Alternatively, the various rotations of the polarization vector seen in our data set, which are in the clockwise and counterclockwise direction over different time ranges, could be mainly random walks caused by a turbulent magnetic field.

CTA 102 displays the complex behavior characteristic of the blazar class of active galactic nuclei. Nevertheless, we have found possible connections between variations in the multi-wavelength flux and polarization and in the structure of the jet in some events. Continued monitoring of CTA 102 and other bright blazars at multiple wavebands with as dense a sampling as possible, combined with millimeter-wave VLBI imaging, can eventually determine which connections are robust and the extent to which stochastic processes dominate the behavior of blazars.

REFERENCES

Abdo, A. A., Ackermann, M., Ajello, M., et al. 2010a, ApJ, 715, 429
Abdo, A. A., Ackermann, M., Ajello, M., et al. 2010b, Natur, 463, 919
Ackermann, M., Ajello, M., Allafort, A., et al. 2011, ApJ, 743, 171
Agudo, I., Gómez, J.-L, Marti, J.-M., et al. 2011, ApJL, 549, L183
Agudo, I., Krichbaum, T. P., Ungerechts, H., et al. 2006, A&A, 456, 117
Agudo, I., Molina, S. N., Gómez, J. L., et al. 2012, IJMPS, 8, 299
Agudo, I., Thum, C., Gómez, J. L., & Wiesemeyer, H. 2014, A&A, 566, A59
Agudo, I., Thum, C., Wiesemeyer, H., & Krichbaum, T. P. 2010, ApJS, 189, 1
Alexander, T. 1997, in Astrophysics and Space Science Library 218, Astronomical Time Series, ed. D. Maoz, A. Sternberg & E. M. Leibowitz (Dordrecht: Kluwer), 163
Alexander, T. 2013, arXiv:1302.1508
Blinov, D., Pavlidou, V., Papadakis, I., et al. 2015, MNRAS, 453, 1669
Burbidge, G. R., Jones, T. W., & Odell, S. L. 1974, ApJ, 193, 43
Cardelli, J. A., Clayton, G. C., & Mathis, J. S. 1989, ApJ, 345, 245
Carrasco, L., Luna, A., Porras, A., & Mayya, D. Y. 2012, ATel, 4442, 1
Casadio, C., Gómez, J. L., Grandi, P., et al. 2015, ApJ, 808, 162
Chatterjee, R., Marscher, A. P., Jorstad, S. G., et al. 2009, ApJ, 704, 1689
Chatterjee, R., Marscher, A. P., Jorstad, S. G., et al. 2011, ApJ, 734, 43
Clemens, D. P., Sarcia, D., Grabau, A., et al. 2007, PASP, 119, 1385

13

D'Arcangelo, F. D., Marscher, A. P., Jorstad, S. G., et al. 2007, ApJL, 659, L107
Fromm, C. M., Perucho, M., Ros, E., Savolainen, T., & Zensus, J. A. 2015, A&A, 576, A43
Fromm, C. M., Perucho, M., Ros, E., et al. 2011, A&A, 531, A95
Fromm, C. M., Ros, E., Perucho, M., et al. 2013a, A&A, 551, A32
Fromm, C. M., Ros, E., Perucho, M., et al. 2013b, A&A, 557, A105
Gabuzda, D. C., Vitrishchak, V. M., Mahmud, M., & O'Sullivan, S. P. 2008, MNRAS, 384, 1003
Ghisellini, G., & Tavecchio, F. 2008, MNRAS, 387, 1669
Gómez, J.-L., Marscher, A. P., Alberdi, A., Jorstad, S. G., & Agudo, I. 2001, ApJL, 561, L161
Gómez, J., Marscher, A., Alberdi, A., et al. 2002, Polarization Calibration of the VLBA Using the D-terms, Tech. Rep., National Radio Astronomy Observatory, VLBA Scientific Memo
Grandi, P., Torresi, E., & Stanghellini, C. 2012, ApJL, 751, L3
Gurwell, M. A., Peck, A. B., Hostler, S. R., Darrah, M. R., & Katz, C. A. 2007, in ASP Conf. Ser. 375, From Z-Machines to ALMA: (Sub) Millimeter Spectroscopy of Galaxies, ed. A. J. Baker et al. (San Francisco, CA: ASP), 234
Hagen-Thorn, V. A., Larionov, V. M., Jorstad, S. G., et al. 2008, ApJ, 672, 40
Hovatta, T., Lister, M. L., Aller, M. F., et al. 2012, AJ, 144, 105
Hovatta, T., Valtaoja, E., Tornikoski, M., & Lähteenmäki, A. 2009, A&A, 494, 527
Itoh, R., Fukazawa, Y., Tanaka, Y. T., et al. 2013, ApJL, 768, L24
Jones, T. W. 1988, ApJ, 332, 678
Jorstad, S. G., Marscher, A. P., Larionov, V. M., et al. 2010, ApJ, 715, 362
Jorstad, S. G., Marscher, A. P., Lister, M. L., et al. 2005, AJ, 130, 1418
Jorstad, S. G., Marscher, A. P., Mattox, J. R., et al. 2001, ApJS, 134, 181
Jorstad, S. G., Marscher, A. P., Smith, P. S., et al. 2013, ApJ, 773, 147
Larionov, V., Blinov, D., & Jorstad, S. 2012, ATel, 4397, 1
Larionov, V. M., Blinov, D. A., Jorstad, S. G., et al. 2013a, EPJWC, 61, 4019
Larionov, V. M., Jorstad, S. G., Marscher, A. P., et al. 2013b, ApJ, 768, 40
Larionov, V. M., Villata, M., & Raiteri, C. M. 2010, A&A, 510, A93
Lister, M. L., Aller, M. F., Aller, H. D., et al. 2013, AJ, 146, 120
Lister, M. L., Cohen, M. H., Homan, D. C., et al. 2009, AJ, 138, 1874
MacDonald, N. R., Marscher, A. P., Jorstad, S. G., & Joshi, M. 2015, ApJ, 804, 111

Maraschi, L., Ghisellini, G., Tanzi, E. G., & Treves, A. 1986, ApJ, 310, 325
Marscher, A. P. 2014, ApJ, 780, 87
Marscher, A. P., Jorstad, S. G., D'Arcangelo, F. D., et al. 2008, Natur, 452, 966
Marscher, A. P., Jorstad, S. G., Gómez, J.-L., et al. 2002, Natur, 417, 625
Marscher, A. P., Jorstad, S. G., Larionov, V. M., et al. 2010, ApJL, 710, L126
Mead, A. R. G., Ballard, K. R., Brand, P. W. J. L., et al. 1990, A&AS, 83, 183
Moore, R. L., & Stockman, H. S. 1981, ApJ, 243, 60
Morozova, D. A., Larionov, V. M., Troitsky, I. S., et al. 2014, AJ, 148, 42
Nolan, P. L., Abdo, A. A., Ackermann, M., et al. 2012, ApJS, 199, 31
Osterman Meyer, A., Miller, H. R., Marshall, K., et al. 2009, AJ, 138, 1902
Pacciani, L., Tavecchio, F., Donnarumma, I., et al. 2014, ApJ, 790, 45
Pica, A. J., Smith, A. G., Webb, J. R., et al. 1988, AJ, 96, 1215
Planck Collaboration, Ade, P. A. R., Aghanim, N., et al. 2014, A&A, 571, A16
Poole, T. S., Breeveld, A. A., Page, M. J., et al. 2008, MNRAS, 383, 627
Raiteri, C. M., Villata, M., Aller, M. F., et al. 2011, A&A, 534, A87
Ramakrishnan, V., León-Tavares, J., Rastorgueva-Foi, E. A., et al. 2014, MNRAS, 445, 1636
Rani, B., Krichbaum, T. P., Marscher, A. P., et al. 2014, A&A, 571, L2
Rantakyrö, F. T., Wiik, K., Tornikoski, M., Valtaoja, E., & Bååth, L. B. 2003, A&A, 405, 473
Savolainen, T., Wiik, K., Valtaoja, E., Jorstad, S. G., & Marscher, A. P. 2002, A&A, 394, 851
Schlafly, E. F., & Finkbeiner, D. P. 2011, ApJ, 737, 103
Schmidt, G. D., Stockman, H. S., & Smith, P. S. 1992, ApJL, 398, L57
Sikora, M., Stawarz, Ł., Moderski, R., Nalewajko, K., & Madejski, G. M. 2009, ApJ, 704, 38
Smith, P. S., Montiel, E., Rightley, S., et al. 2009, arXiv:0912.3621
Spencer, R. E., McDowell, J. C., Charlesworth, M., et al. 1989, MNRAS, 240, 657
Stanghellini, C., O'Dea, C. P., Dallacasa, D., et al. 1998, A&A, 131, 303
Vlahakis, N. 2006, in ASP Conf. Ser. 350, Blazar Variability Workshop II: Entering the GLAST Era, ed. H. R. Miller et al. (San Francisco, CA: ASP), 169
Williamson, K. E., Jorstad, S. G., Marscher, A. P., et al. 2014, ApJ, 789, 135
Zamaninasab, M., Clausen-Brown, E., Savolainen, T., & Tchekhovskoy, A. 2014, Natur, 510, 126
Zensus, J. A., Ros, E., Kellermann, K. I., et al. 2002, AJ, 124, 662

4.3   Summary and contextualization

4.3.1   3C 120 and CTA 102

The most important conclusion that we obtain by comparing the two previous multi-wavelength studies is that, despite belonging to very different classes of AGN, the radio galaxy 3C 120 and the blazar CTA 102 display similar properties during γ-ray outbursts.

In particular, in these two sources we found that γ-ray outbursts with a counterpart at millimeter wavebands (or in coincidence with flares at X-ray, UV, optical, and near-infrared frequencies, as occurs in CTA 102) are associated with the ejection of a new superluminal component, meaning the passage of the component through the mm-VLBI core. On the other hand, we found that not all ejections of new components are associated with γ-ray events.

In both sources we found evidence of changes in the direction of motion of super-luminal components, so that components associated with γ-ray outbursts are those moving in a direction closer to our line of sight. Therefore, we infer that γ-ray flares are detected when a new superluminal component is ejected at a smaller viewing angle.

In the case of CTA 102 we also observe an orphan γ-ray flare (i.e., without counterparts at other wavebands) and a minor γ-ray flare, without clear counterparts at the other wavelengths but probably associated with the passage of the superluminal component through a recollimation shock close to the core.

The γ-ray dissipation regions are located in both cases in the parsec-scale jet, close to the mm-VLBI core and far from the central engine. This supports the interpretation in which the mm-VLBI core corresponds to a recollimation shock, favoring the production of high-energy emission during the interaction of two shocks, the stationary associated with the mm-VLBI core and the moving associated with the superluminal component. The difficulty in having contribution from external photon fields at such distances from the central engine supports the synchrotron self Compton mechanism as responsible for the production of γ-ray photons.

4.3.2   Similar results in other AGN

Many blazars show properties similar to those described above during high-energy events. I report below some studies to which I have contributed and where we found

some of the behaviors described above.

We found evidences of γ-ray outbursts in coincidence with flares at millimeter wavelengths and triggered by the passage of a new superluminal component through the mm-VLBI core in multiple blazars, i.e. both FSRQ objects as 1156+295 (Ramakrishnan et al., 2014), PKS 1510-089 (Aleksić et al., 2014) and 3C 454.3 (Jorstad et al., 2013), and BL Lac objects as 0954+658 (Morozova et al., 2014). In two of them (Morozova et al., 2014; Ramakrishnan et al., 2014) we also found minor γ-ray flares associated with the passage of the superluminal knot through a standing recollimation shock close to the mm-VLBI core, as reported for CTA 102. The passage of a new emerging knot through three recollimation shocks inside the core is a possible scenario also to explain the triple structure of three γ-ray and optical flares observed in 3C 454.3 between autumn 2009 and autumn 2010 (Jorstad et al., 2013). In 3C 454.3 the repeated pattern suggests the same mechanism and location for all three flares, that happened in coincidence also with X-ray, optical and millimeter outbursts.

However, not always γ-ray flares have a counterpart at millimeter wavelengths; orphan flares have been observed in other blazars besides CTA 102. A good example can be found in Lico et al. (2014), where we analyzed 15, 24 and 43 GHz VLBA observations of the blazar Mrk 421 from January to December 2011 in coincidence with three γ-ray flares of similar intensity detected by *Fermi* in March, September and November 2011. We obtain that only the March event was associated with an increase in flux at all three radio wavelengths.

In many blazars, γ-ray and optical flares occur very close in time, e.g. 4C 38.41 and BL Lacertae (Raiteri et al., 2012, 2013), and often in coincidence also with millimeter and X-ray flares, as observed in 3C 454.3 (Jorstad et al., 2013) and 0954+658 (Morozova et al., 2014). But sometimes γ-ray and optical flares peak before their millimeter and X-ray counterparts that therefore should be produced downstream the location of the γ-ray event, as we found in OJ 248 (Carnerero et al., 2015) and BL Lacertae (Raiteri et al., 2013).

As we did in 3C 120 and CTA 102, we adopt a geometrical interpretation for observed γ-ray flares also in other blazars, i.e. OJ 248, BL Lacertae, and 4C 38.41 (Carnerero et al., 2015; Raiteri et al., 2012, 2013), considering that either the jet or the emitting regions change their orientation over time, and they result oriented closer to the line of sight during high energy events.

Changes in polarization in these objects are frequently observed during outbursts. We find evidence of both shocks, that produce an increase in the degree of polarization and a symptomatic change in the EVPAs orientation (see § 2.3), and plasma turbulence. This is the case of 3C 454.3, where the degree of optical linear polarization displays a general increase during an outburst but it drops significantly when the γ-ray peak happens (Jorstad et al., 2013). In other cases the increase in the degree of optical polarization is in coincidence with an optical and γ-ray flare, and a wide rotation of optical EVPAs is also observed during the outburst, as we found in OJ 248 (Carnerero et al., 2015) and 0954+658 (Morozova et al., 2014). In the latter, optical EVPAs are observed to rotate smoothly more than 300° in one direction and this can be related to the spiral path followed by the component along helical magnetic field lines, as we also suggested for CTA 102 (see sketch in Figure 4.1).
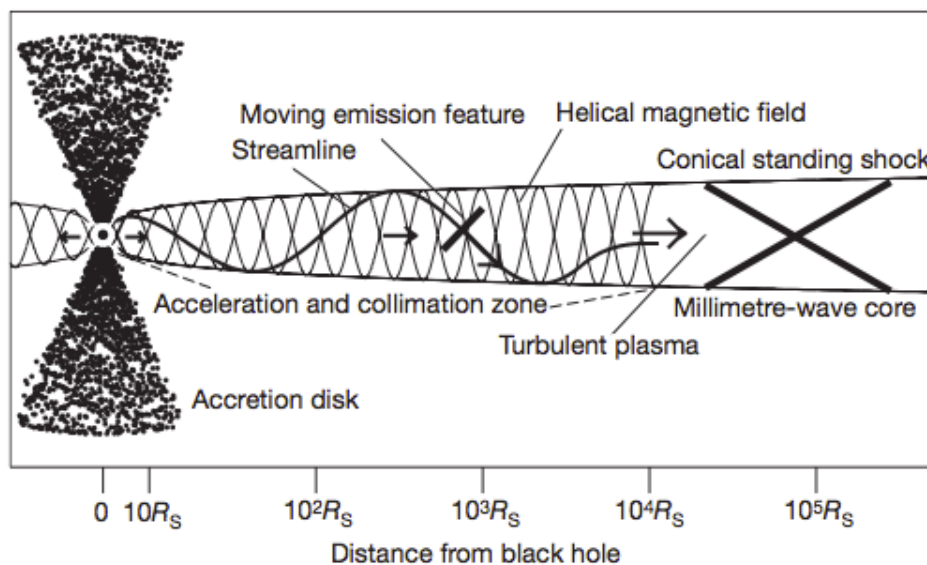

Figure 4.1: Inner jet model. A moving shock propagates along the jet following helical magnetic field lines. The millimeter core is here the first recollimation shock and in this sketch is located at almost 10^5 Schwarzschild radii (R_s), as for 3C 120 and CTA 102. Reproduced from Marscher et al. (2008).

For radio galaxies it is more difficult to draw general conclusions. This is mainly because radio galaxies are less powerful objects and they usually are oriented at larger viewing angle, therefore having non-favorable conditions for being detected at γ-ray

energies. Indeed, only a small fraction of radio galaxies has been detected at γ-ray frequencies. As mentioned in § 3.2, before our work on 3C 120, the connection between a γ-ray outburst and the ejection of a new superluminal component from the mm-VLBI core has been observed only in the FRII radio galaxy 3C 111 (Grandi et al., 2012). The radio galaxy 3C 120 is therefore the first FRI radio galaxy where we observe this kind of behavior. The other well known FRI radio galaxy, which has experienced many high energy (100 MeV<E<100 GeV energies) and very high energy (E>100 GeV) events over time, is M 87. Despite many flares registered from this source, no new components have been clearly observed emerging from the core during these events. Only indications of brightening in the region close to the core (Acciari et al., 2009) or time-lags between flaring peaks at 43 and 22 GHz (Hada et al., 2014) have been observed as evidence of new components in coincidence with VHE flares in 2008 and 2012, respectively. In Hada et al. (2014) we found that from February to March 2012, when M 87 exhibited a high activity state at VHE, the radio core at 22 and 43 GHz increased its flux density while the peculiar emitting region HST-1, which is a possible candidate site for the γ-ray photon production, was in a low state of flux. Another interesting result we obtained in Hada et al. (2014) is that the *Fermi* high-energy light-curve showed an increase before the VHE event, but came back to quiescence during such VHE event.

Similar distances between the central black hole and the mm-wave core, of the order of 10^4-10^5 R_s (see Figure 4.1), as those found for the case of 3C120 and CTA 102 (Marscher et al., 2002; Fromm et al., 2015), were also found in other blazars (Marscher et al., 2008, 2010; Agudo et al., 2011b) as well as in the radio galaxy 3C 111 (Chatterjee et al., 2011). However, the distance between the mm-wave core and the black hole in the nearby radio galaxy M 87 is very different. In this case, the 43 GHz core is located at few tens of Schwarzschild radii (Hada et al., 2011). We will focus our attention on this topic in the next Chapter.

Finally, it is worth mentioning as a general remark that the the common features outlined from all these multi-wavelength studies cannot be generalized as representative of the entire blazar class. The variety of behaviors of different blazars during γ-ray flares is so large (e.g. some showing sharp EVPA swings during gamma-ray flares and others not, or some showing orphan flares and other not) that it can be considered with certain guarantees that we are still far from understanding the blazar phenomenon, at least to with regard to high energy processes and emission mechanisms. Therefore, to gain a

deeper understanding of the physics of these objects, the future goal both of the entire community and as a natural continuation of this PhD thesis will be to extend these type of multi-wavelength studies over a wide sample of AGN to try extracting more general conclusions.

5

Polarimetric studies of the radio galaxies 3C 120 and M 87: searching for recollimation shocks

Because of their proximity to us, and therefore because of their brightness, radio galaxies 3C 120 and M 87 are very well known and well studied AGN. Their powerful and knotty jets, among other peculiarities, make them interesting subjects of study.

As discussed in Chapter 4, they are both gamma-ray emitters. M 87 is also a TeV emitter, although its jet is not oriented at a small viewing angle with regard to the line of sight. Therefore the detection of such gamma-ray emission is not favored by relativistic beaming, as we would expect in order to have emission up to very high energies. This, together with the lack of prominent low energy flares in nuclear regions during some VHE events, sets some doubts on the mechanism of the γ-ray emission observed in this source as well as on the location of the emission region. Previous studies have considered both the core and the peculiar emitting region HST-1 (see Figure 5.1), located at a de-projected distance $\gtrsim$ 120 pc downstream of the nucleus, as possible candidates for the γ-ray emission observed in this source. During the VHE event registered in 2005, radio, optical and X-ray outbursts have been registered from HST-1, while the nucleus was in a low activity state (Harris et al., 2006). Three more

events have been registered after 2005; in 2008, 2010 and 2012. The 2008 and 2012 events suggest the core as the possible site for the TeV emission, since the peculiar knot HST-1 remained quiescent at radio and X-rays frequencies (Acciari et al., 2009; Hada et al., 2014).
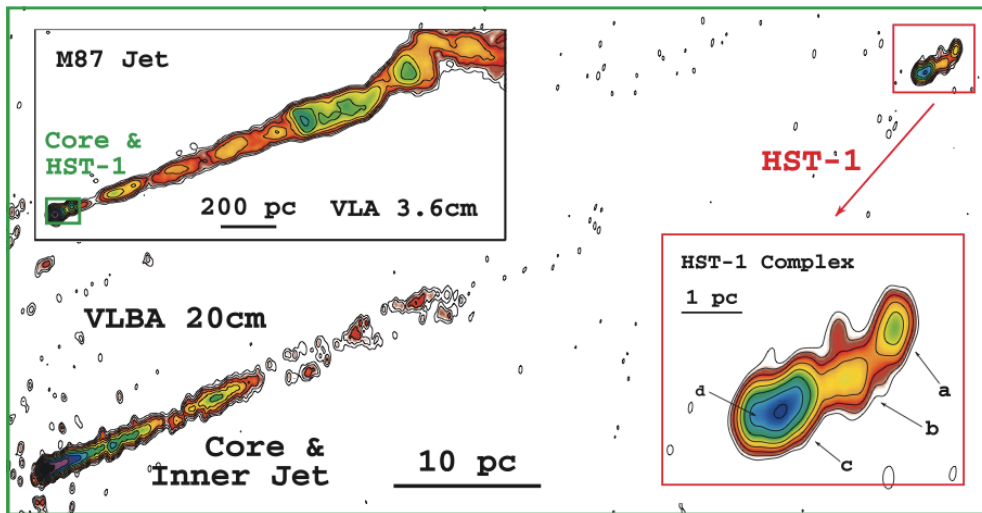

Figure 5.1: M 87 and HST-1 multi-scale images. Two images of the M 87 jet with the VLBA at 20 cm (main image) and with the VLA at 3.6 cm (upper left inset panel). In the VLA image a green box indicates the portion of the jet represented in the VLBA image. The red box on the bottom right displays a zoom of the HST-1 region in the VLBA image. Reproduced from Cheung et al. (2007).

The 2010 event complicated even more the interpretation of M87's behavior because no prominent low energy flares have been detected in the core, nor in the HST-1 region. A key aspect to consider here is the nature of the peculiar knot HST-1, which is still a matter of debate. With the resolution provided by VLBA observations we observe a jet that becomes progressively fainter with distance from the core because of radiative cooling until fading away. Surprisingly, the jet resumes after hundreds of parsecs at the location of HST-1, as can be seen in Figure 5.1. To explain the rebrightening of the jet at such large distances from the nucleus, a mechanism for particles acceleration is needed at the HST-1 region. A recollimation shock is a natural explanation here (see § 2.3).

The hypothesis of a recollimation shock is supported by many previous studies: Stawarz et al. (2006) found that a reconfinement nozzle is expected in the position of

HST-1 due to interaction of the jet with the external medium; also semi-analytical and numerical magneto-hydrodinamic (MHD) models support the hypothesis of the recollimation shock (Gracia et al., 2009; Bromberg & Levinson, 2009; Nalewajko, 2012), as well as VLBI observations by Asada & Nakamura (2012) showing that HST-1 corresponds to the location at which the jet in M 87 changes from a parabolic to a conical shape. There are, however, no conclusive observational indications for the existence of a stationary feature in HST-1 region associated with the recollimation shock as expected from numerical simulations (Gómez et al., 1995, 1997) and observed in other sources (Agudo et al., 2012; Cohen et al., 2014). Only in early 1.7 GHz VLBA observations by Cheung et al. (2007) the authors reported an upper limit of $0.25c$ for the apparent motion of the upstream region of HST-1 (labeled by these authors as HST-1d).
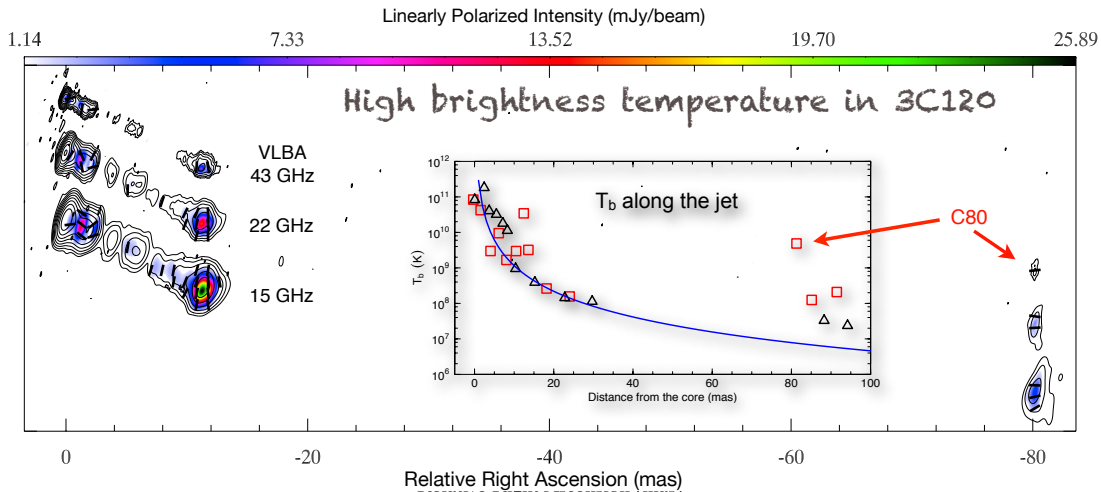

Figure 5.2: 3C 120 VLBA images containing its far away component C80. VLBA observations of 3C 120 in November 2007 at 43 (top), 22 (middle) and 15 (bottom) GHz; reproduced from Roca-Sogorb et al. (2010). The inset panel shows the observed brightness temperature for different components along the jet, with the red squares and black triangles representing different epochs. The blue line represents the expected decline with distance from the core.

Another radio galaxy where we find a similar peculiar region is the radio galaxy 3C 120. In this source the jet also resumes its emission at almost 80 mas from the core ($\gtrsim$140 pc, de-projected, considering a viewing angle $<20°$; Roca-Sogorb et al., 2010), see Figure 5.2. Our research group discovered for the first time the emitting region at

∼80 mas (named C80) from polarimetric VLBA observations of 3C 120 performed in November 2007. Roca-Sogorb et al. (2010) reported an unusually high brightness temperature for component C80 which was interpreted as produced by a strong stationary shock located in that region.

The bright jet of 3C 120 has a very rich structure, displaying both superluminal components and stationary features suggestive of a helical configuration seen in projection (Walker et al., 2001; Gómez et al., 2001b). Multi-wavelength observations of 3C 120 have also revealed a clear connection between the activity in the accretion disk and the subsequent appearance of new components in the radio jet, therefore establishing the accretion disk origin of the radio jet for the first time in AGN (Marscher et al., 2002). Polarimetric VLBI observations have also proven to be a powerful tool to study this peculiar radio galaxy, that reveals rapid changes in the total and linearly polarized emission associated with the interaction between the jet and interstellar clouds (Gómez et al., 2000). These clouds are also responsible for the localized high Faraday rotation seen at parsec scales in 3C 120 (Gómez et al., 2008, 2011).

In light of the findings reported in Roca-Sogorb et al. (2010) we decided to perform a detailed analysis of the C80 unusual emitting region through new multi-frequency polarimetric VLBA images (Agudo et al., 2012). In Agudo et al. (2012) we also compare observational properties with simulated images of conical recollimation shocks obtained by Dr. Timothy V. Cawthorne, who used the models described in Cawthorne & Cobb (1990) and Cawthorne (2006). I performed the calibration and imaging of most of the data presented in Agudo et al. (2012), following the procedure described in § 3.2.

5.1 A recollimation shock 80 mas from the core in the jet of the radio galaxy 3C 120: observational evidence and modeling

The following article has been published in *The Astrophysical Journal* on June 20th, 2012 and is reproduced here in its original format.

The reference for this article is: Agudo I., Gómez J. L., Casadio C., Cawthorne T. V., Roca-Sogorb M., 2012, ApJ, 752, 92.

The authors are: Iván Agudo, José L. Gómez, Carolina Casadio, Timothy V. Cawthorne and Mar Roca-Sogorb.

A RECOLLIMATION SHOCK 80 mas FROM THE CORE IN THE JET OF THE RADIO GALAXY 3C 120: OBSERVATIONAL EVIDENCE AND MODELING

Iván Agudo[1,2], José L. Gómez[1], Carolina Casadio[1], Timothy V. Cawthorne[3], and Mar Roca-Sogorb[1]
[1] Instituto de Astrofísica de Andalucía, CSIC, Apartado 3004, 18080 Granada, Spain; jlgomez@iaa.es
[2] Institute for Astrophysical Research, Boston University, 725 Commonwealth Avenue, Boston, MA 02215, USA
[3] School of Computing, Engineering and Physical Science, University of Central Lancashire, Preston PR1 2HE, UK
Received 2012 March 13; accepted 2012 April 12; published 2012 May 30

ABSTRACT

We present Very Long Baseline Array observations of the radio galaxy 3C 120 at 5, 8, 12, and 15 GHz designed to study a peculiar stationary jet feature (hereafter C80) located $\sim$80 mas from the core, which was previously shown to display a brightness temperature $\sim$600 times larger than expected at such distances. The high sensitivity of the images—obtained between 2009 December and 2010 June—has revealed that C80 corresponds to the eastern flux density peak of an arc of emission (hereafter A80), downstream of which extends a large ($\sim$20 mas in size) bubble-like structure that resembles an inverted bow shock. The linearly polarized emission closely follows that of the total intensity in A80, with the electric vector position angle distributed nearly perpendicular to the arc-shaped structure. Despite the stationary nature of C80/A80, superluminal components with speeds up to $3 \pm 1\, c$ have been detected downstream from its position, resembling the behavior observed in the HST-1 emission complex in M87. The total and polarized emission of the C80/A80 structure, its lack of motion, and brightness temperature excess are best reproduced by a model based on synchrotron emission from a conical shock with cone opening angle $\eta = 10°$, jet viewing angle $\theta = 16°$, a completely tangled upstream magnetic field, and upstream Lorentz factor $\gamma_u = 8.4$. The good agreement between our observations and numerical modeling leads us to conclude that the peculiar feature associated with C80/A80 corresponds to a conical recollimation shock in the jet of 3C 120 located at a de-projected distance of $\sim$190 pc downstream from the nucleus.

Key words: galaxies: active – galaxies: individual (3C 120) – galaxies: jets – polarization – radio continuum: galaxies

Online-only material: color figures

1. INTRODUCTION

The radio galaxy 3C 120 is a very active and powerful emitter of radiation at all observed wavebands. While classified as a Seyfert 1 (Burbidge 1967), its spectrum shows broad emission lines and a complex optical morphology which has been interpreted as the result of a past merger (García-Lorenzo et al. 2005). Variability in the emission lines has allowed reverberation mapping to yield a black hole mass of $\sim$3 × $10^7\, M_\odot$ (Wandel et al. 1999). In X-rays, it is the brightest broad-line radio galaxy, with the X-ray spectrum becoming softer when the intensity increases (Maraschi et al. 1991), suggesting that the soft X-rays are dominated by the disk instead of the beamed jet. This has made it possible to establish a clear connection between the accretion disk and the radio jet through coordinated X-ray and radio observations (Marscher et al. 2002; Chatterjee et al. 2009). Along with 3C 111, 3C 120 is one of only two broad-line radio galaxies detected by *Fermi*-LAT in the GeV photon energy range, such emission being most probably the result of beamed radiation from the relativistic jet observed at intermediate viewing angles (Kataoka et al. 2011).

At radio wavelengths, 3C 120 has a blazar-like one-sided superluminal radio jet extending up to hundreds of kiloparsecs (Walker et al. 1987, 1988; Muxlow & Wilkinson 1991). Due to its proximity ($z = 0.033$), and to its bright millimeter emission (Agudo et al. 2010), Very Long Baseline Array (VLBA) observations at high frequencies (22, 43, and 86 GHz) show a very rich inner jet structure containing multiple superluminal components with apparent velocities up to $6c$ (Gómez et al. 1998, 1999; Homan et al. 2001; Jorstad et al. 2005; Marscher

et al. 2007). Continued monthly monitoring with the VLBA at 22 and 43 GHz has revealed rapid changes in the total and linearly polarized intensity, interpreted as resulting from the interaction of the jet components with the external medium (Gómez et al. 2000, 2001). Longer wavelength very long baseline interferometry (VLBI) observations have shown evidence for the existence of an underlying helical jet structure (Walker et al. 2001), which has been interpreted as the result of jet precession (Hardee et al. 2005; Caproni & Abraham 2004)

Combination of the information from a sequence of 12 monthly polarimetric VLBA observations of 3C 120 at 15, 22, and 43 GHz has allowed imaging of the linearly polarized emission within the innermost $\sim$10 mas jet structure, revealing a coherent in time Faraday screen and polarization angles (Gómez et al. 2008). Gradients in Faraday rotation and degree of polarization across and along the jet are observed, together with a localized region of high ($\sim$6000 rad m^{-2}) Faraday rotation measure (RM) between approximately 3 and 4 mas from the core. The existence of this localized region of high RM, together with the observation of uncorrelated changes in the RM screen and RM-corrected polarization angles, suggests that a significant fraction of the Faraday RM found in 3C 120 originates in foreground clouds, rather than in a sheath intimately associated with the emitting jet (Gómez et al. 2011).

VLBA observations of 3C 120 in 2007 November revealed a component (hereafter C80) located at 80 mas (which corresponds to a de-projected distance of $\sim$190 pc for a viewing angle of $16°$) with a brightness temperature $T_b \approx 5 \times 10^9$ K, which is about 600 times higher than expected at such distances from the core (Roca-Sogorb et al. 2010). Analysis of
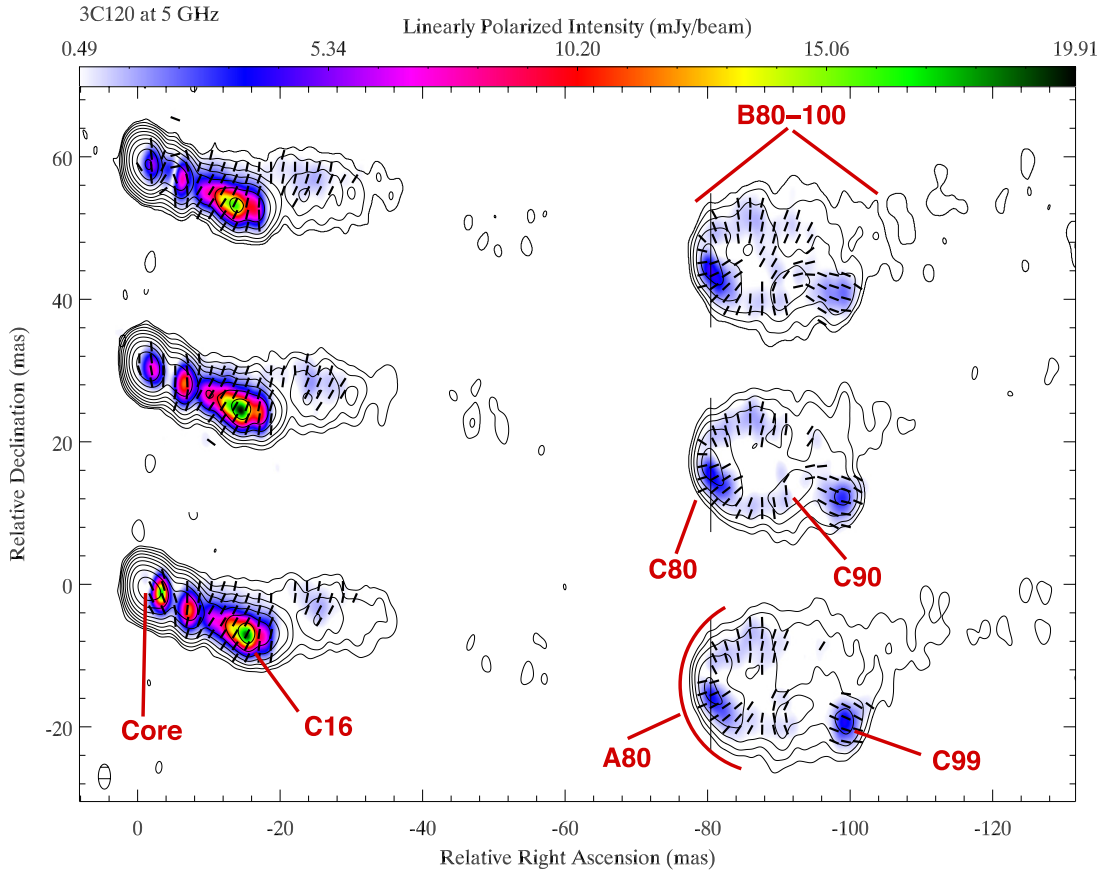
1

Figure 1. Sequence of VLBA images of 3C 120 at 5 GHz taken on 2009 December 14, 2010 March 14, and 2010 June 21 (from top to bottom). Vertical separations are proportional to the time difference between epochs. Total intensity contours are overlaid at 0.03%, 0.07%, 0.17%, 0.41%, 1.02%, 2.49%, 6.11%, 14.98%, 36.72%, and 90% of the total intensity peak at 1.53 Jy beam^{-1}. A common convolving beam of FWHM 3.5 × 1.7 mas at 0° was used for all images and is shown in the lower left corner. Gray-scale images (on a linear scale shown at the top) show the linearly polarized intensity. Black sticks (or unit length) indicate the polarization electric vector position angle, uncorrected for Faraday rotation. The vertical lines at ~80 mas from the core indicate the location where the transverse cuts of the fractional polarization of the jet shown in Figure 5 were performed.

(A color version of this figure is available in the online journal.)

previous observations (starting in 1982) shows that this component was not detected at frequencies higher than 5 GHz before 2007 April, when it was first observed at 15 GHz. After this epoch C80 appears in all images (even at the highest frequencies) at the same location without significant changes in its flux density. Roca-Sogorb et al. (2010) conclude that the unusually high T_b of C80 could be explained by a helical shocked jet model—and perhaps some flow acceleration—but it seems very unlikely that this corresponds to the usual shock that emerges from the core and travels downstream to the location of C80, requiring some other intrinsic process capable of providing a local amplification in the density of high energy particles and/or magnetic field.

Here we present the results from a new observing program designed to study the nature of the C80 feature. Such a study is complemented with semi-dynamical and semi-analytical simulations to help us interpret the structure of C80 and its surrounding jet region. The paper is organized as follows. In Section 2, we describe the new VLBA observations presented here and their data reduction procedures; in Section 3, we report on the results that are obtained directly from the observations; we present the numerical models used to reproduce these observations in Section 4. Finally, in Section 5 we summarize our main results and draw the conclusions from this work.

At the redshift of 3C 120, and under the standard ΛCDM cosmology (with $H_0 = 71$ km s^{-1} Mpc^{-1}, $\Omega_M = 0.27$, and $\Omega_\Lambda = 0.73$) that we assume in this work, an angular separation of 1 mas in the sky corresponds to a projected linear distance of 0.65 pc, and a proper motion of 1 mas yr^{-1} is translated to a superluminal speed 2.19 times larger than the speed of light.

2. OBSERVATIONS

The new multi-frequency and polarimetric VLBA images of the jet in 3C 120 presented in this paper were obtained from observations performed on 2009 December 14, 2010 March 14, and 2010 June 21. The corresponding observations, that employed all ten antennas of the VLBA, were performed at 5, 8, and 12 GHz (see Figures 1–3), and used a two-bit signal sampling to record in a 32 MHz bandwidth per circular polarization at a recording rate of 256 Mbits s^{-1}.

Calibration of the data was performed within the AIPS software package following the standard procedure for VLBI polarimetric observations (Leppänen et al. 1995). To correct for opacity effects on the higher frequency observations (>8 GHz) we used the recorded variation of the system temperature on every station to solve for the receiver temperature and zenith opacity. The final images were obtained following the standard hybrid-mapping procedure through an iterative process that
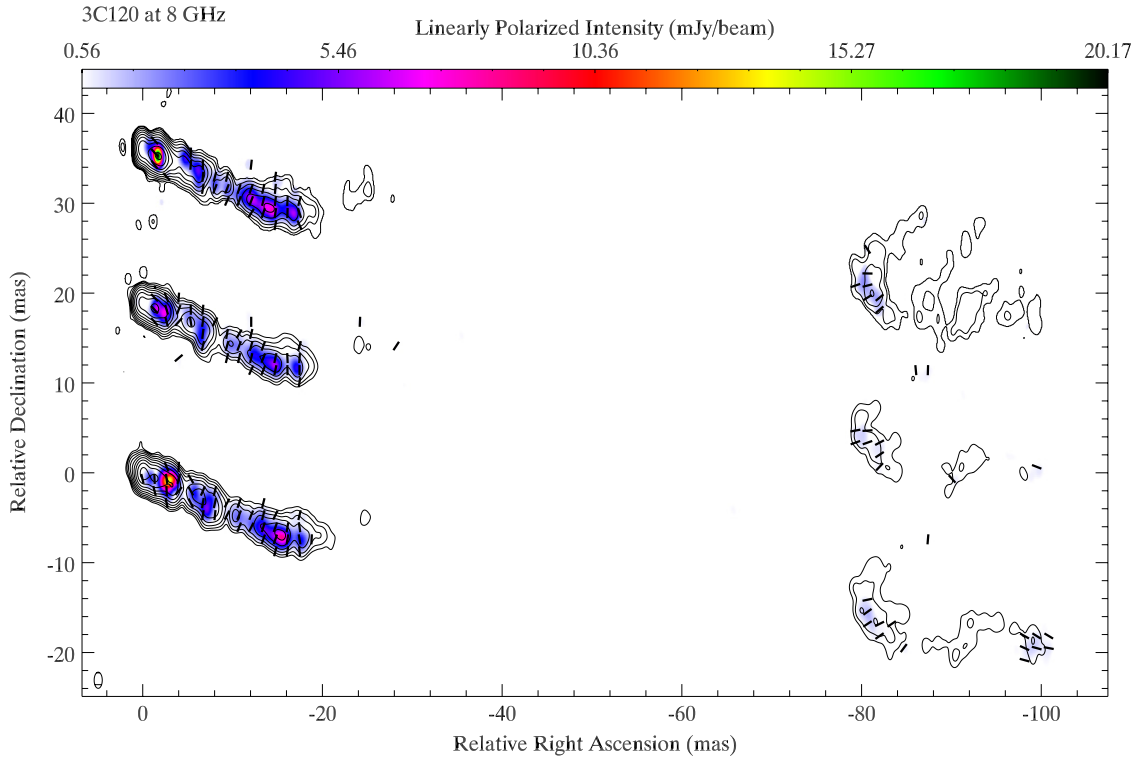
Figure 2. Same as Figure 1 but for the 8 GHz images. Contour levels are drawn at 0.11%, 0.23%, 0.49%, 1.03%, 2.17%, 4.58%, 9.64%, 20.30%, 42.74%, and 90% of the total intensity peak at 1.04 Jy beam^{-1}. A common convolving beam of FWHM 1.8 × 0.9 mas at 0° was used for all images.
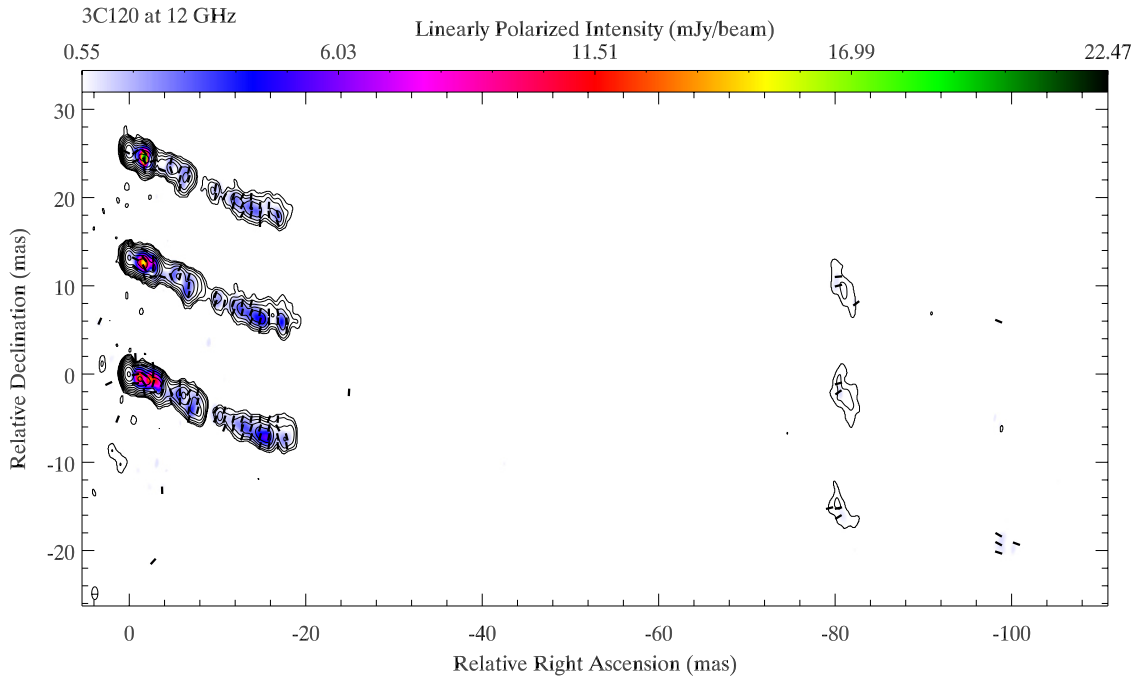(A color version of this figure is available in the online journal.)

Figure 3. Same as Figure 1 but for the 12 GHz images. Contour levels are drawn at 0.17%, 0.34%, 0.69%, 1.38%, 2.76%, 5.54%, 11.13%, 22.34%, 44.83%, and 90% of the total intensity peak at 0.75 Jy beam^{-1}. A common convolving beam of FWHM 1.5 × 0.7 mas at 0° was used for all images.
(A color version of this figure is available in the online journal.)

employed both AIPS and the DIFMAP package (Shepherd 1997).

For the calibration of the absolute orientation of the electric vector position angle (EVPA) we employed both a set of VLA observations of our polarization calibrators (NRAO150,

OJ287, 3C 279, and 3C 454.3) from the VLA/VLBA Polarization Calibration Program[4] and the information extracted by the comparison of the D-terms at different observing epochs

---

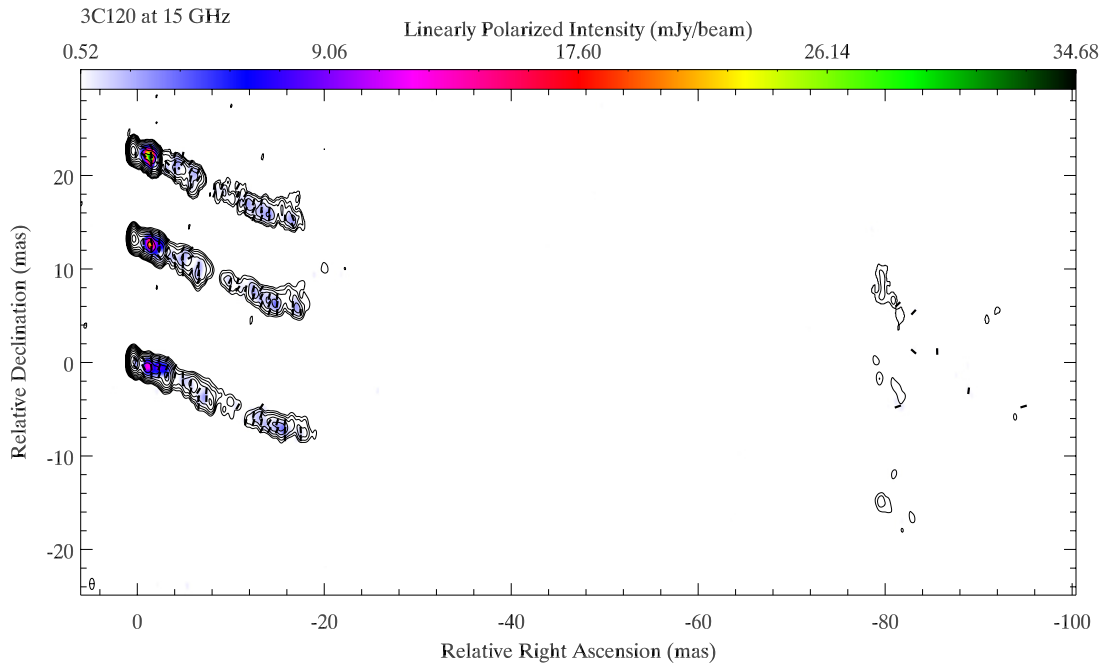[4] http://www.vla.nrao.edu/astro/calib/polar/

Figure 4. Same as Figure 1 but for the 15 GHz images obtained and calibrated by the MOJAVE team (see the text). From top to bottom, the three images correspond to VLBA observations performed on 2009 December 10, 2010 March 10, and 2010 July 12. Contour levels are drawn at 0.13%, 0.27%, 0.56%, 1.15%, 2.38%, 4.92%, 10.17%, 21.04%, 43.52%, and 90% of the total intensity peak at 0.73 Jy beam^{-1}. A common convolving beam of FWHM 1.2×0.5 mas at 0° was used for all images. (A color version of this figure is available in the online journal.)

(see Gómez et al. 2002). The useful input from the first of these two methods was rather limited in our case because the VLA/VLBA Polarization Calibration Program does not include data at 12 GHz, and the program was halted at the end of 2009 to focus on EVLA commissioning, hence preventing us from getting the calibration at 5 and 8 GHz for the latest two observing epochs in 2010. However, we verified that the 5 and 8 GHz D-terms were very stable during our three observations. Gómez et al. (2002) showed that in this case the D-terms can be used to calibrate those observing epochs without an independent EVPA calibration. This allowed us to calibrate the 5 and 8 GHz EVPAs of the latest two observing epochs by rotating their corresponding D-terms to match those of the fully calibrated first observing epoch.

At 12 GHz there are no available independent polarization data from our sources to estimate the adequate EVPA calibration. However, we used the publicly available total-intensity and linear-polarization 15 GHz VLBA images of 3C 120 taken (and calibrated) by the MOJAVE team[5] on dates close to those of our multi-frequency observations (see Figure 4). These 15 GHz EVPA images allowed us to calibrate our 12 GHz EVPA on nearby epochs by fitting Faraday rotation profiles at 5, 8, and 15 GHz to find the correct EVPA calibration at 12 GHz. The stability of the D-terms at 12 GHz was also used as a cross-check for the final calibration at this frequency. The final errors in our absolute calibration of the EVPA at all our observing frequencies are estimated to be ~5°.

3. RESULTS

3.1. The Inner ~20 mas of the Jet

Figures 1–4 show the new 5, 8, 12, and 15 GHz VLBA images of 3C 120 in total and linearly polarized intensity, as well as their

corresponding EVPA distribution. These new images show a straight jet within the inner ~20 mas that contains a bright and highly polarized knot at ~16 mas from the core (C16). The EVPA of C16 is distributed perpendicular to the jet axis. The same EVPA orientation is found in the C16 counterparts at 8, 12, and 15 GHz (see Figures 2–4) where the images show an increasingly rich structure of jet knots with observing frequency all along the innermost 20 mas of the jet. The multi-frequency polarization properties of C16 match those of the C12 jet feature reported by Gómez et al. (2011). This, together with the total flux dominance of both C16 and C12 in regions ≳10 mas from the core and the fact that C16 lies in the jet region expected from the position of C12 and the typical proper motions in the jet of 3C 120 (~2 mas yr^{-1}, Gómez et al. 2001), allows us to identify both components as representing the same jet moving knot.

3.2. Bright Emission Region between 80 and 100 mas from the Core: B80-100

The jet feature at ~80 mas from the core (C80) is detected in all new images presented in this work from 5 to 15 GHz (Figures 1–4). No other jet feature is detected in the jet downstream of C80 in the 12 and 15 GHz images presented here. However, the new 5 GHz images show an emission region in an arc from north to south around the eastern side of C80, having the shape of an inverted bow shock, similar to those observed at the end of the large-scale jets of FR-II radio galaxies (e.g., Perley et al. 1984). Perhaps because of the lack of sensitivity, this arc of emission (that we have labeled as A80) was not detected by our previous short-integration VLBA observations of the source at 5 GHz (see Roca-Sogorb et al. 2010; Gómez et al. 2011), where only the detection of C80, the brightest region in A80, was reported.

Together with C80/A80, the new 5 GHz images show a bubble-like extended emission—region larger than ~20 mas

---

along the jet axis—from the sharp edge near the location of C80, and ~20 mas across the jet axis. This emission structure will be called B80-100 hereafter (see Figure 1). Neither the total intensity nor the polarized emission is symmetric with regard to the jet axis in B80-100. The maxima in total and linearly polarized intensity are both located on the southern side of the bubble, which resembles the behavior of the jet in 3C 120 within the first ~10 mas (Gómez et al. 2000, 2001, 2008).

Further downstream from C80 (but still within B80-100), C90, a more extended jet region reported by Roca-Sogorb et al. (2010) and Gómez et al. (2011) at observing frequencies below 8 GHz, starts to be resolved in our new images (Figures 1 and 2). Our 8 GHz images in 2009 and 2010 show the jet emission around C90 as a slightly more extended and sparser jet region than in the image taken in 2007 November 30 by Gómez et al. (2011) at the same frequency. C90 is better observed in our 5 GHz images that map the entire B80-100 at higher sensitivity. This provides a reliable superluminal speed measurement of C90 ($v_{C90} = 3.4 \pm 1.0\,c$), which contrasts with the stationary character of C80 (Roca-Sogorb et al. 2010) located ~10 mas upstream in the jet.

Our new images also show a bright and compact jet region located ~99 mas from the core—reported here for the first time—that we have labeled C99. Our kinematic study of this feature also reveals superluminal proper motion ($v_{C99} = 3.0 \pm 1.1\,c$) of similar magnitude and direction downstream from the jet than C90. The superluminal character of the flow downstream from C80 resembles the behavior near the HST-1 knot in M87 as reported by Cheung et al. (2007), who suggested HST-1 as the site of a recollimation shock in the jet of M87 (see also Stawarz et al. 2006; Asada & Nakamura 2012).

Given the typical superluminal motions previously detected in 3C 120 on smaller jet scales (~4c; Gómez et al. 2001), we consider it unlikely that C90—as identified by Roca-Sogorb et al. (2010) and Gómez et al. (2011)—can be identified with C99 at earlier epochs, given the exceedingly large proper motion that would be needed ($\gtrsim 9c$, which has not previously been observed in the jet of 3C 120). Our 5 GHz images show that C99's flux density increases progressively from 2009 December 14 to 2010 June 21, which provides a better explanation for why C99 was not detected in our previous 5 GHz observations in 2007 November 30.

3.3. Arc of Emission at ~80 mas from the Core: A80

As shown in Figure 1 (see also Figures 2–4), the linearly polarized emission in A80 closely follows that of the total intensity, with values of the degree of polarization up to ~30% (see also Figure 5), and the EVPAs distributed nearly perpendicular to the arc-shaped structure of A80, as expected in the case of a shock front.

The observations presented here show a nearly constant flux density evolution of C80/A80, and confirm the large brightness temperature as well as its stationarity, both within our new observing epochs and with regard to the reported position of C80 at earlier epochs. These properties appear remarkably similar to those expected in the case of conical recollimation shocks (e.g., Cawthorne & Cobb 1990; Gómez et al. 1995, 1997; Agudo et al. 2001; Cawthorne 2006; Nalewajko 2009) and will be discussed in detail in the next session.

Interestingly, the region of B80-100 close to the jet axis and downstream from the sharp edge of A80 appears unpolarized in our 5 GHz images. In contrast, weak linear polarization emission (with EVPA nearly perpendicular to the local jet axis) starts to be
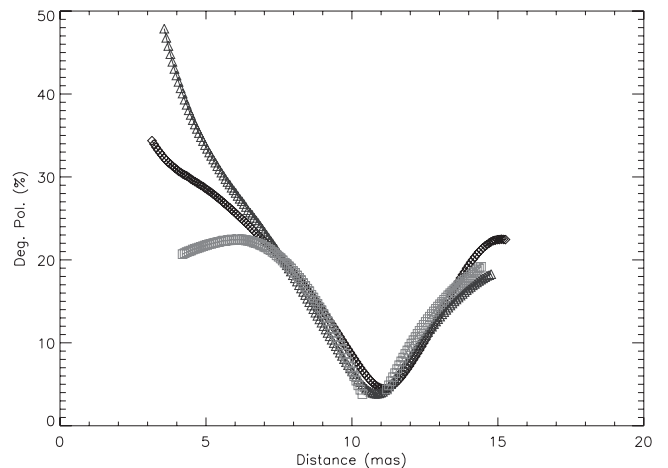

Figure 5. 5 GHz fractional polarization across the A80 jet structure through the slices (from south to north) marked in Figure 1. Diamonds correspond to epoch 2009 December 14, triangles to epoch 2010 March 14, and squares to 2010 June 21.

discerned further downstream at ~10 mas from the eastern edge of A80. The strong linear polarization emission of C99 shows its EVPA distribution parallel to the jet axis, which, together with the measured superluminal motion, may be an indication of a traveling plane shock wave perpendicular to the axis.

3.4. Faraday Rotation Screen Between 5 and 15 GHz

Figure 6 shows the RM image of 3C 120 for 2009 December made by combining the data between 5 and 15 GHz. The RM images for the other two epochs of our observations show very similar results to those for 2009 December and are therefore not shown. As can be seen in the inset panels of Figure 6, we obtain good fits to a λ^2 law of the EVPAs throughout the jet, except at longer wavelengths in the innermost ~4 mas, probably due to beam depolarization and opacity.

The RM screen shown in Figure 6 is in excellent agreement with that obtained for observations taken in 2007 November (see Figure 7 in Gómez et al. 2011), providing further confirmation for the stationarity of the Faraday screen in 3C 120 claimed previously (Gómez et al. 2008). Note, however, that relatively rapid changes (in scales of tens of months) in the RM have also been observed in the innermost ~2 mas of the jet (Gómez et al. 2011). Our new observations also confirm the negative gradient in RM with distance along the jet, including a sign reversal at ~8 mas from the core. The motion of component C16 along the jet during the two-year time span between the 2007 observations of Gómez et al. (2011) and ours have allowed the mapping of the RM further downstream, revealing an RM of -79 ± 2 rad m^{-2}, fully consistent with the RM gradient along the jet mentioned previously.

Component C80/A80 has a small RM of 20 ± 2 rad m^{-2}, leading to a Faraday rotation in the EVPAs at our longest observing wavelength of 6 cm (5 GHz) of $4°$, within the estimated error in our absolute calibration of the EVPAs. We therefore can conclude that our EVPA maps of C80/A80 are not affected by Faraday rotation.

4. A CONICAL SHOCK MODEL FOR A80

The structure and polarization of the A80 feature point toward an origin in the kind of shock that can occur when the internal pressure of a jet adjusts as a result of changes to its environment.
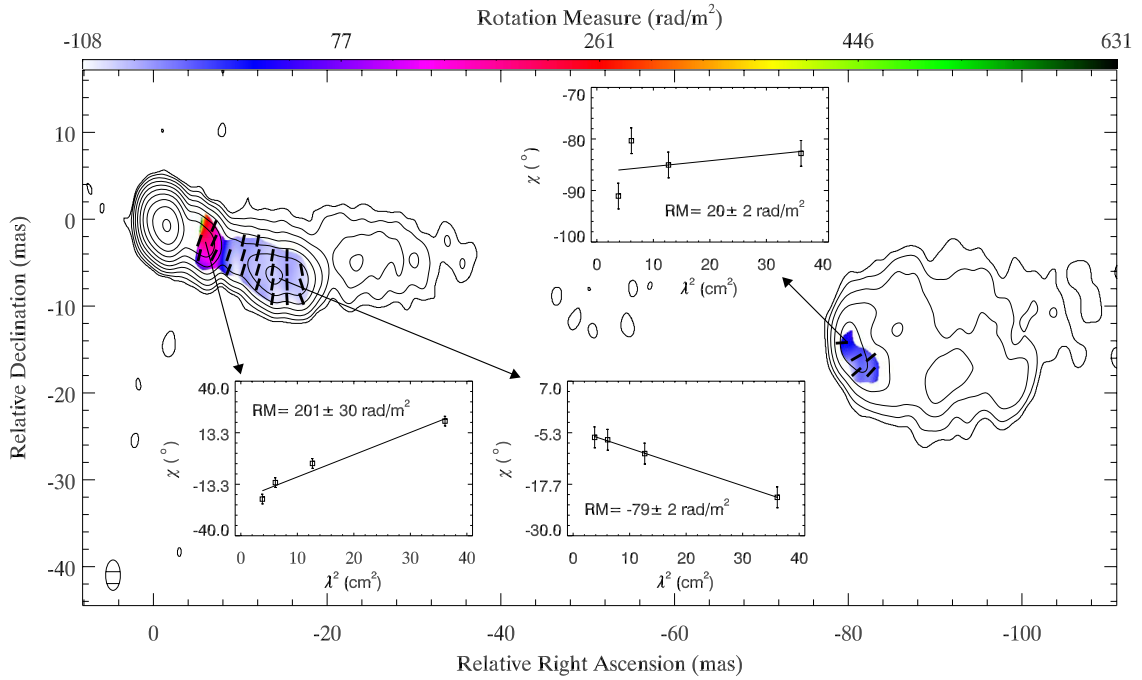
Figure 6. Rotation measure image of 3C 120 between 5 and 15 GHz for observations taken on 2009 December 14. Contours show the 5 GHz total intensity image (see Figure 1). Black sticks indicate the RM-corrected EVPAs. Inset panels show sample fits to a λ^2 law of the EVPAs at some particular locations. The convolving beam is shown in the lower left corner.

(A color version of this figure is available in the online journal.)

This type of structure has been suggested as the origin of the HST-1 knot in M87 (Stawarz et al. 2006; Asada & Nakamura 2012). A jet that is initially freely expanding may become underpressured and is therefore recollimated by a conical shock converging away from the nucleus. Such shocks may reflect from the jet axis, producing a second conical shock diverging away from the nucleus that further adjusts the collimation of the jet. The result is a structure consisting of a pair of point-to-point conical shocks that have been found to occur both in experiments and numerical simulations (e.g., Gómez et al. 1995). In A80, there is no evidence for a converging shock—the shape of the structure, particularly in polarized intensity, suggests a diverging cone that will divert the flow away from the axis causing a drop in pressure. This therefore appears to indicate that A80 has arisen because the jet has rapidly become overpressured, perhaps as a result of a sudden drop in external pressure at this point. Though this seems the most probable explanation it is possible that the jet has encountered a small object—perhaps a molecular cloud typical of the narrow-line emission regions in AGNs—near the axis of the jet, and that the conical shock represents the resulting wake. This explanation seems less probable because it depends on the lucky chance that the obstacle is near the jet axis, but it is in agreement with previous indications for a jet/cloud collision at distances closer to the core (Gómez et al. 2000).

Here, the A80 feature is modeled as a diverging conical shock using the models described by Cawthorne & Cobb (1990) and Cawthorne (2006). These models assume the plasma to be a relativistic gas with sound speed $c/\sqrt{3}$.

Previous monitoring of the proper motions in 3C 120 (e.g., Gómez et al. 2000, 2001; Walker et al. 2001; Homan et al. 2001; Marscher et al. 2002; Jorstad et al. 2005) shows that the maximum apparent velocity observed is $\sim 6c$. From this it is possible to estimate the maximum viewing angle, $\theta_{max} = 19°$, and the minimum Lorentz factor of the jet, $\gamma_u = 6$ (e.g., Gómez

et al. 2000). The value $\beta_{app} = 6$ is therefore assumed, being also relevant to the components labeled L5 to L8 by Walker et al. (2001) in the region upstream from C80. This value is used to constrain the properties of the upstream flow. The 5 GHz images presented in this paper are used to constrain the properties of the shock wave.

The projected semi-opening angle η_p of the conical shock is best estimated from the polarized intensity images presented earlier in this paper (Figure 1). The cone axis is taken to be a line inclined at approximately 7° from EW, pointing directly back to the radio core structure. The opening angle deduced from the distribution of polarized flux density is about 90°, but after convolution of model structures with the elliptical beam, the best fit to this is found from a projected opening angle in the region of 80° corresponding to $\eta_p = 40°$. The angle between the polarization rods on either side of the structure (measured where the polarized flux density is brightest) is in the region of 90°. Since the model polarization E rods are orthogonal to the projected edge of the conical structure, a value of $\eta_p = 40°$ corresponds to an angle of 100° between the polarization rods on the two sides. However, after convolution, this angle is reduced to approximately 90°, in agreement with the images, as a result of the influence of the polarized structure nearer the axis. A value of η_p much less than 40° would be hard to reconcile with both a symmetrical cone structure and an axis pointing back to the core region; if the axis is maintained at its inclination of 7° to EW, then the southern edge of the cone would then exclude much of the observed flux density. Values of η_p significantly greater than 40° result in simulated polarization images that are inconsistent with those observed in that they do not reproduce the observed saddle point between the two sides of the polarization image. Hence, a value for η_p in the region of 40° seems to offer the best chance of modeling the observed structure of A80 and is therefore used in what follows.
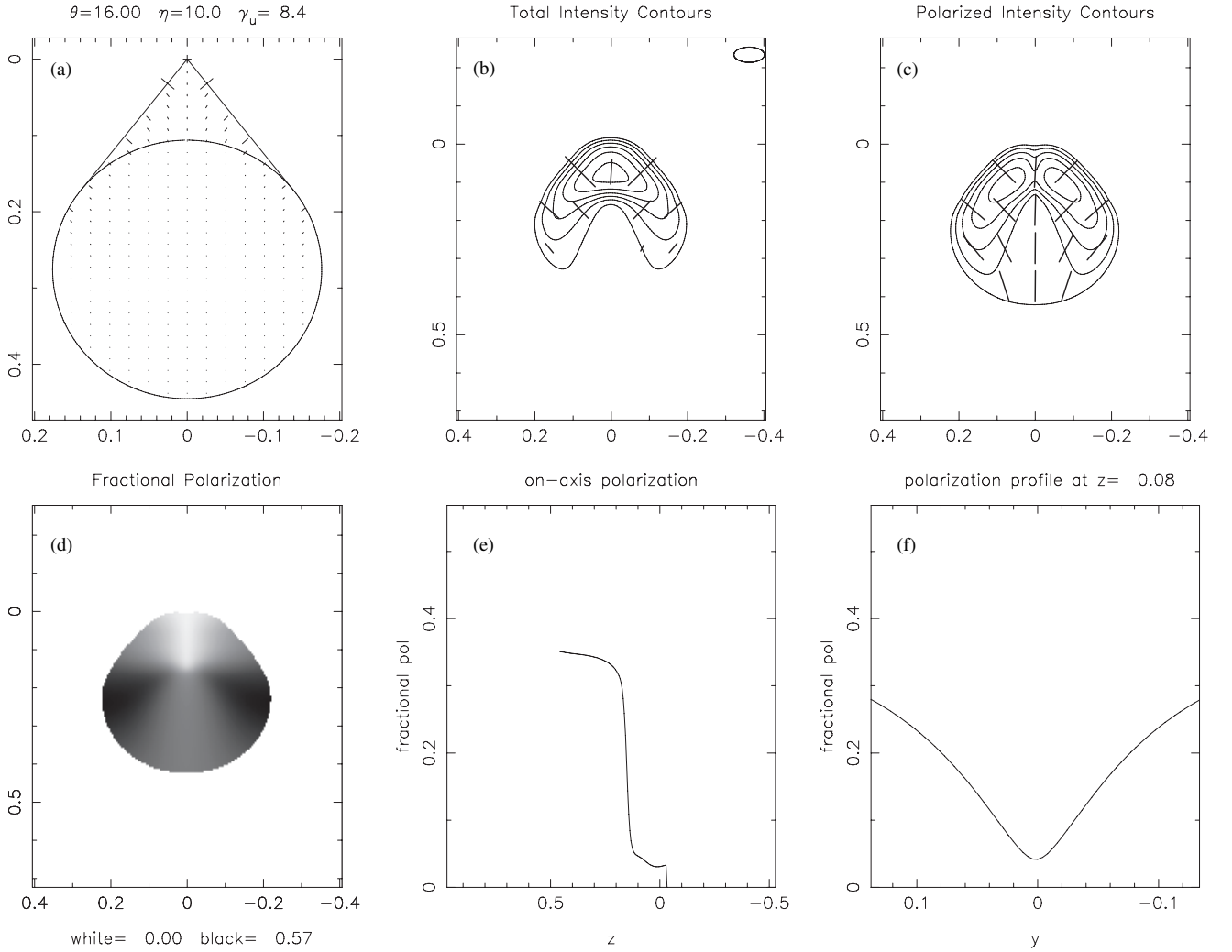
Figure 7. Simulated images and plots corresponding to model 3 (see Table 1). Plots of the six panels are as follows: (a) outline of the shock structure and the (unconvolved) polarization rods of length proportional to P, (b) contours of I after convolution with a beam chosen to match in shape that of the observations; the convolved polarization is shown by rods parallel to the E field and of length proportional to P, (c) contours of convolved P, with polarization angle χ shown by the orientation of rods of constant length, (d) variation of fractional polarization (from the convolved images), (e) along the jet axis, and (f) across the jet through the region of the I peak. In all six plots the units of distance are scaled so that the height of the cone (from apex to base) is unity.

The true semi-opening angle η is related to η_p by

$$\tan \eta_p = \frac{\tan \eta}{\cos \theta (1 - \tan^2 \theta \tan^2 \eta)^{1/2}}, \qquad (1)$$

which can be solved numerically for η in terms of η_p and θ.

A further constraint is provided by the requirement that, in the rest frame of the upstream flow, the shock wave must advance toward the stationary plasma at speed greater than the sound speed, $c/\sqrt{3}$. This requires that

$$\beta_u \gamma_u \sin \eta > 1/\sqrt{2}. \qquad (2)$$

For each value of θ, a unique model can be computed using the procedures described in Cawthorne (2006) provided inequality (2) is satisfied. Parameters appropriate to several models are given in Table 1 and the corresponding model images have been computed assuming that the upstream magnetic field is completely disordered. The plausible range of θ is quite restricted: values below about $10°$ are ruled out by inequality (2), while values above $18°.9$ cannot yield apparent superluminal speeds as high as $\simeq 6c$.

The simulated images corresponding to models 1–4 resemble the observations of A80 shown in Figure 1. The total intensity (I) images in Figure 7 show a bow wave pattern, while the simulated polarized intensity (P) images show a similar pattern that is divided by a saddle point at the position of maximum I. The polarization E rods in the two elongated P features are approximately perpendicular to the direction of elongation, which corresponds to the outline of the conical shock wave. Models 1–4 produce simulations that differ mainly in two ways: first, the structures become more compact as θ increases, because the emission from the far side of the shock wave becomes relatively weaker, and second, the degree of polarization increases as θ increases, mainly because the shock becomes stronger (the compression factor of the shock κ decreases) as a result of increasing values of η and the upstream flow velocity (β_u).

The model best matching the degrees of polarization found in the images is model 3. In this model, the degree of polarization rises to about 30% near the edges of A80 in the region of the peak in total intensity, and levels as high as this are seen in this region on the southern side of A80 (as shown in the profiles plot of Figure 5).

7

Table 1
Model Parameters for Different Values of θ

Model	θ (°)	β_u	η (°)	κ	ξ (°)	β_d	δ_u	$\delta_{d,\,max}$	$\delta_{d,\,max}/\delta_u$	R_1	R_2
(1)	(2)	(3)	(4)	(5)	(6)	(7)	(8)	(9)	(10)	(11)	(12)
1	12	0.9874	7.5	0.76	1.2	0.9849	4.63	4.73	1.02	2.9	3.0
2	14	0.9895	8.8	0.50	3.2	0.9826	3.62	5.33	1.47	40.3	27.5
3	16	0.9929	10.0	0.31	5.0	0.9815	2.61	5.26	2.02	600	395
4	18	0.9974	11.2	0.14	6.9	0.9810	1.40	5.19	3.71	68,900	39,300

Notes. For all these models the upstream magnetic field was assumed to be completely tangled. Columns are as follows: (1) model number; (2) angle θ between the axis and the line of sight; (3) β_u, upstream flow velocity as a fraction of c; (4) η, the (deprojected) semi-opening angle; (5) κ, the compression factor at the shock front; (6) ξ, the angle through which the flow is deflected; (7) β_d, the downstream flow velocity expressed as a fraction of c; (8) δ_u Doppler factor upstream of the conical shock; (9) $\delta_{d,max}$, maximum Doppler factor downstream of the conical shock; (10) $\delta_{d,max}/\delta_u$, ratio of maximum downstream to upstream Doppler factor; (11) intensity ratio R_1 between the downstream and upstream emission; and (12) a new estimate, R_2, of the downstream to upstream intensity with downstream intensity weighted by the Doppler shift.

The simulated images for model 3 are shown in Figure 7. The model is reasonably successful in reproducing the observed structure in the vicinity of the I peak. However, further downstream the observed polarization rods turn to become orthogonal to the axis, whereas the model polarization rods turn in the opposite sense. On axis, the model polarization rods are parallel to the axis, but where on-axis polarization is seen in the observations, at distances greater than about 10 mas from the working surface, the rods are either orthogonal or oblique to the axis. It seems that if the conical shock model is appropriate, then it is the dominant influence on the polarized emission only within about 10 mas of the apex.

Another way in which the model is successful is in its prediction of a very large ratio of upstream to downstream intensity. The observations of Roca-Sogorb et al. (2010) have shown that C80 (the brightest hot spot in A80) represents an increase in the intensity of emission with respect to the underlying jet by a factor of approximately 600, a figure that they found difficult to explain without invoking acceleration of the jet. If this is due to the formation of a shock structure, then the ratio of the upstream to downstream intensity should be about 600 or greater. If the Doppler factors of the upstream and downstream flows are δ_u and δ_d, respectively, and the compression ratio is κ, then the intensity ratio should be approximately

$$R_1 = \frac{I_d}{I_u} = \kappa^{(5\alpha-6)/3}\left(\frac{\delta_d}{\delta_u}\right)^{(2-\alpha)},$$

where $\alpha \simeq -1$ is the spectral index for C80 (Roca-Sogorb et al. 2010). In estimating the value of R_1 the largest downstream Doppler factor $\delta_{d,max}$ (for flow at angle $\theta - \xi$ to the line of sight) has been assumed. The values of κ, $\delta_{d,max}$ for the downstream flow closest to the line of sight and R_1 are shown in Table 1. Because $\delta_d < \delta_{d,max}$ for most of the downstream flow, R_1 is likely to be an overestimate of the intensity ratio, and so a second estimate based on an intensity-weighted average of the downstream Doppler factor, R_2, has also been included in the table.

Table 1 shows that as θ increases from 12° to 18°, so the downstream to upstream brightness ratios, R_1 and R_2, increase very rapidly. The greater part of this effect is due to the compression of the plasma (indicated by the value of κ) and its effect on the magnetic field and particle density. However the increase in the value of $\delta_{d,max}/\delta_u$ is also significant. This occurs because (1) δ_u is decreasing because θ is increasing and β is also

increasing in the regime where $\sin\theta > \gamma_u^{-1}$, and (2) because δ_d is varying only weakly, which occurs because although β_d decreases and θ_d increases, the shock becomes stronger and parts of the downstream flow are directed closer to the observer's line of sight.

From Table 1 it is clear that parameters similar to those of model 3 ($\theta = 16°$), which gave the closest match for the fractional polarization values, should have a downstream to upstream brightness ratio of order several hundred. It therefore seems likely that such models can reasonably reproduce both the observed polarization structures and the very high ratio of downstream to upstream intensity demanded by Roca-Sogorb et al. (2010).

A few variants on the models described here have been investigated to determine whether they might explain the transverse polarization rods seen on the downstream side of C80. First a poloidal magnetic field component was added, as described by Cawthorne (2006). The influence of the poloidal field on the polarization is strongest on the near side of the shock front, producing transverse polarization rods near the peak in I, where none are seen. The effect is negligible on the far side of the shock, which extends further downstream toward the region where transverse polarization rods would be desirable. The possibility that the upstream flow might be converging slightly has also been investigated, as suggested by Nalewajko (2009). The effect was to increase the degree of polarization at a given value of θ, but otherwise the simulated images were very similar. It seems that neither of these modifications helps to explain the larger scale polarization properties beyond A80. It is possible that allowing for a more complex upstream field structure might explain the entire polarization structure of B80-100 but, on the other hand, it seems likely that the conical shock is not the dominant influence on polarization toward the downstream edge of the B80-100 structure. Indeed, the superluminal motion found for C90 and C99 suggests that instead the polarization structure downstream of A80 may be the result of moving plane-perpendicular shock waves that appear in the wake of the A80 conical shock.

It is worth noting that, although the upstream Doppler factor is rather low in model 3 ($\simeq 2.6$) the jet to counterjet ratio is still reasonably high, giving

$$\frac{I_{\rm jet}}{I_{\rm counterjet}} = \left(\frac{1+\beta_u\cos\theta}{1-\beta_u\cos\theta}\right)^{2-\alpha} \simeq 1.2\times10^4$$

for $\alpha \simeq -0.5$, as expected nearer the core.

8

5. SUMMARY AND CONCLUSIONS

The first analysis of the properties of component C80 was carried out by Roca-Sogorb et al. (2010), who concluded that although a helical shocked jet model—including perhaps some bulk flow acceleration—could explain the unusually large brightness temperature, it appears unlikely that it corresponds to the usual shock that moves from the core to the location of C80. Rather, Roca-Sogorb et al. (2010) proposed the need for an alternative process capable of explaining the high brightness temperature of C80, its appearance in high-frequency images after 2007 April, and its apparent stationarity. One of the possible alternatives considered by these authors involved a stationary shock at the location of C80 with emission suddenly enhanced by the arrival of a region of enhanced particle number in the jet flow, such as the one proposed to explain the kinematic and flux evolution properties of the HST-1 knot in M87 (Stawarz et al. 2006).

The main goal of the new observations presented here is to further constrain the physical processes taking place in the jet of 3C 120 that have led to the extreme properties of C80. Thanks to the increased sensitivity achieved by our new observations we report on the existence of the A80 arc of total intensity and linear polarization associated with C80, as part of a larger bulge of emission that extends ∼20 mas along and across the jet. Most importantly, the polarization vectors are distributed perpendicularly to the semi-circular shape of A80, as would be expected for the case of a compression by a shock front. This evidence, together with the excess in brightness temperature displayed by C80/A80 and its stationarity in flux and position, supports the model suggested by Roca-Sogorb et al. (2010) in which C80/A80 corresponds to a standing shock. More specifically, our modeling suggests a conical recollimation shock. Indeed, our simulations based on the synchrotron emission from a conical shock, as described by Cawthorne (2006), reproduce quite closely the observed total and linearly polarized emission structure, the electric vector distribution, and the increased brightness temperature of C80/A80, allowing constraints on the values of the jet flow in 3C 120 and the geometry of the conical shock at ∼80 mas from the core. In particular, our simulations provide the cone opening angle $\eta = 10°$, the jet viewing angle $\theta = 16°$ at the location of A80, and the upstream Lorentz factor $\gamma_u = 8.4$.

An important issue to investigate further is the origin of the recollimation shock at such large distances from the core of emission in relativistic jets as in 3C 120 and presumably in M87. While for M87 it has been proposed that the recollimation originates from the transition between a parabolic to a conical shape (Asada & Nakamura 2012), in 3C 120 we suggest that the most plausible cause is a sudden drop in the external pressure, leading to the formation of a conical shock wave opening away from the nucleus.

The study of the nature of C80—and the structure of its related arc of emission A80—that we present in this paper was only possible thanks to the high angular resolution provided by the VLBA and its large sensitivity and good performance for polarimetric observations. The use of synthetic images of the total intensity and linear polarization of conical shocks has also proven to be a powerful tool to interpret the nature of jet structures, and to constrain the physical and geometrical properties of such structures and the jet plasma that forms them. Studies similar to that presented here can be carried out for a number of cases—additional potential examples might be the

HST-1 and K1 knots in M87 (Stawarz et al. 2006) and 3C 380 (Papageorgiou et al. 2006). Performing these studies will be important to obtain relevant information on the relativistic jets and their surrounding medium.

REFERENCES

Agudo, I., Gómez, J. L., Martí, J. M., et al. 2001, ApJ, 549, L183
Agudo, I., Thum, C., Wiesemeyer, H., & Krichbaum, T. P. 2010, ApJS, 189, 1
Asada, K., & Nakamura, M. 2012, ApJ, 745, L28
Burbidge, E. M. 1967, ApJ, 149, L51
Caproni, A., & Abraham, Z. 2004, MNRAS, 349, 1218
Cawthorne, T. V. 2006, MNRAS, 367, 851
Cawthorne, T. V., & Cobb, W. K. 1990, ApJ, 350, 536
Chatterjee, R., Marscher, A. P., Jorstad, S. G., et al. 2009, ApJ, 704, 1689
Cheung, C. C., Harris, D. E., & Stawarz, Ł. 2007, ApJ, 663, L65
García-Lorenzo, B., Sánchez, S. F., Mediavilla, E., González-Serrano, J. I., & Christensen, L. 2005, ApJ, 621, 146
Gómez, J. L., Marscher, A. P., & Alberdi, A. 1999, ApJ, 521, L29
Gómez, J. L., Marscher, A. P., Alberdi, A., Jorstad, S. G., & Agudo, I. 2001, ApJ, 561, L161
Gómez, J. L., Marscher, A. P., Alberdi, A., Jorstad, S. G., & Agudo, I. 2002, VLBA Scientific Memorandum 30 (http://www.vlba.nrao.edu/memos/sci/sci30memo.ps)
Gómez, J. L., Marscher, A. P., Alberdi, A., Jorstad, S. G., & García-Miró, C. 2000, Science, 289, 2317
Gómez, J. L., Marscher, A. P., Alberdi, A., Martí, J. M., & Ibáñez, J. M. 1998, ApJ, 499, 221
Gómez, J. L., Marscher, A. P., Jorstad, S. G., Agudo, I., & Roca-Sogorb, M. 2008, ApJ, 681, L69
Gómez, J. L., Martí, J. M., Marscher, A. P., Ibáñez, J. M., & Alberdi, A. 1997, ApJ, 482, L33
Gómez, J. L., Martí, J. M., Marscher, A. P., Ibáñez, J. M., & Marcaide, J. M. 1995, ApJ, 449, L19
Gómez, J. L., Roca-Sogorb, M., Agudo, I., Marscher, A. P., & Jorstad, S. G. 2011, ApJ, 733, 11
Hardee, P. E., Walker, R. C., & Gómez, J. L. 2005, ApJ, 620, 646
Homan, D. C., Ojha, R., Wardle, J. F. C., et al. 2001, ApJ, 549, 840
Jorstad, S. G., Marscher, A. P., Lister, M. L., et al. 2005, AJ, 130, 1418
Kataoka, J., Stawarz, Ł., Takahashi, Y., et al. 2011, ApJ, 740, 29
Leppänen, K. J., Zensus, J. A., & Diamond, P. J. 1995, AJ, 110, 2479
Lister, M. L., Aller, H. D., Aller, M. F., et al. 2009, AJ, 137, 3718
Maraschi, L., Chiappetti, L., Falomo, R., et al. 1991, ApJ, 368, 138
Marscher, A. P., Jorstad, S. G., Gómez, J. L., et al. 2002, Nature, 417, 625
Marscher, A. P., Jorstad, S. G., Gómez, J. L., et al. 2007, ApJ, 665, 232
Muxlow, T. W. B., & Wilkinson, P. N. 1991, MNRAS, 251, 54
Nalewajko, K. 2009, MNRAS, 395, 524
Papageorgiou, A., Cawthorne, T. V., Stirling, A., Gabuzda, D., & Polatidis, A. G. 2006, MNRAS, 373, 449
Perley, R. A., Dreher, J. W., & Cowan, J. J. 1984, ApJ, 285, L35
Roca-Sogorb, M., Gómez, J. L., Agudo, I., Marscher, A. P., & Jorstad, S. G. 2010, ApJ, 712, L160
Shepherd, M. C. 1997, in ASP Conf. Ser. 125, Astronomical Data Analysis Software and Systems VI, ed. G. Hunt & H. E. Payne (San Francisco, CA: ASP), 77
Stawarz, Ł., Aharonian, F., Kataoka, J., et al. 2006, MNRAS, 370, 981
Walker, R. C., Benson, J. M., & Unwin, S. C. 1987, ApJ, 316, 546
Walker, R. C., Benson, J. M., Unwin, S. C., et al. 2001, ApJ, 556, 756
Walker, R. C., Walker, M. A., & Benson, J. M. 1988, ApJ, 335, 668
Wandel, A., Peterson, B. M., & Malkan, M. A. 1999, ApJ, 526, 579

9

5.2 The radio galaxy M 87 and its peculiar knot at 900 mas from the core

In Giroletti et al. (2012) we presented the results from a monitoring program of the radio galaxy M 87 and its peculiar feature HST-1 combining new data taken with the European VLBI Network (EVN) and archival VLBA images, at 5 and 1.7 GHz respectively, for a total of 24 observations between November 2006 and October 2011. In Figure 5.3 we show the evolution in morphology of the HST-1 region from January 2007 to August 2011, with gaussian components obtained from the model-fits overlaid. The main results obtained in Giroletti et al. (2012) are as follows: i) the typical HST-1 extension in the radio band is of $\gtrsim$50 mas and it is formed by sub-structures on smaller angular scales, ii) two sub-components within HST-1 (*comp 1* and *comp 2* in Figure 5.3) moved regularly with superluminal velocity (v=4*c*) with a proper motion of ∼88 mas over the observing period – as we observe in Figure 5.4, iii) a slower moving component (*comp 2b*, in Figures 5.3 and 5.4) observed from August 2008 to May 2009 in the wake of the superluminal *comp 2*, resembling the characteristics of "trailing" components that appear behind a major flow disturbance in numerical simulations (Agudo et al., 2001) and have been observed in other sources (Gómez et al., 2001b; Jorstad et al., 2005), iv) after 2010 a new component (*comp 3*, in Figures 5.3 and 5.4) appeared upstream *comp 2* and in a position similar to that of the previous *comp 2b*.

As mentioned at the beginning of this chapter, a possible scenario to explain HST-1 phenomenon, is that of a recollimation shock located in the region which accelerates electrons that consequently emit via the synchrotron process. In order to test this hypothesis we performed relativistic hydrodynamical simulations using the *ratpenat* code (Perucho et al. 2010) involving the interaction between moving and standing recollimation shocks. To obtain a series of strong recollimation shocks the jet is launched with an initial over-pressure 10 times larger than the external medium. A magnetic field in equipartition with particle energy density and oriented predominantly in the direction of the jet axis is assumed. Figure 5.5 displays the rest-mass density, pressure, specific internal energy and Lorentz factor along the jet for the stationary model. When we introduce a perturbation, consisting of an increase by a factor of 8 in the pressure of the plasma injected into the jet, a shock wave forms. This shock moves along the jet
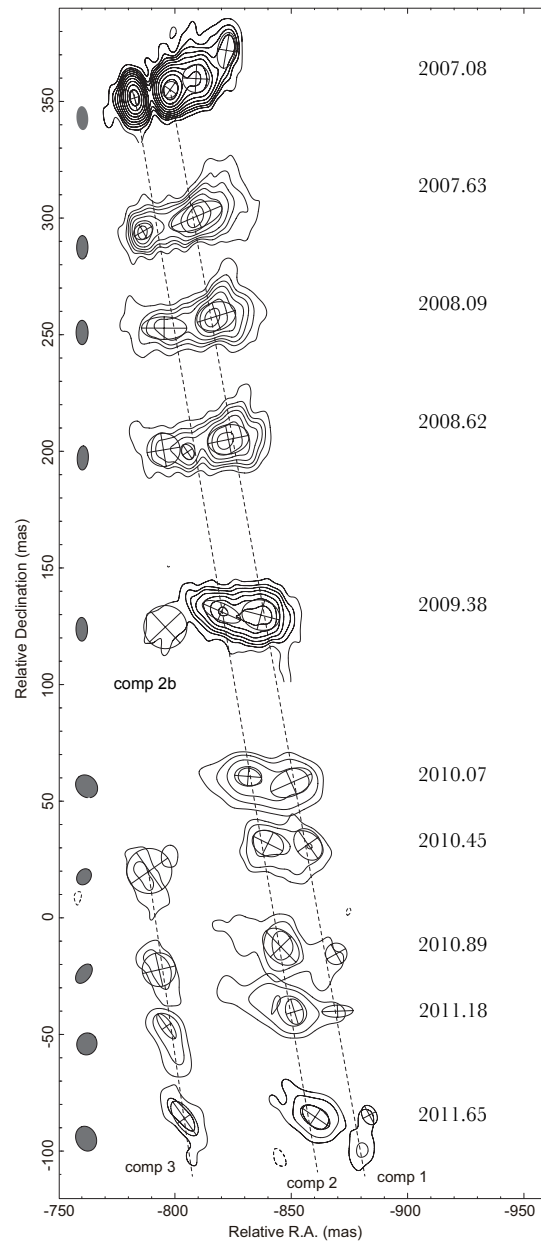
Figure 5.3: Total intensity images of HST-1 at 1.7 GHz (VLBA) from 2007.8 to 2009.38 and 5 GHz (EVN) from 2010.07 to 2011.65. Model-fit components are overlaid to the images. Images are spaced vertically proportionally to the time interval between the relative epochs. Adapted from Giroletti et al. (2012).
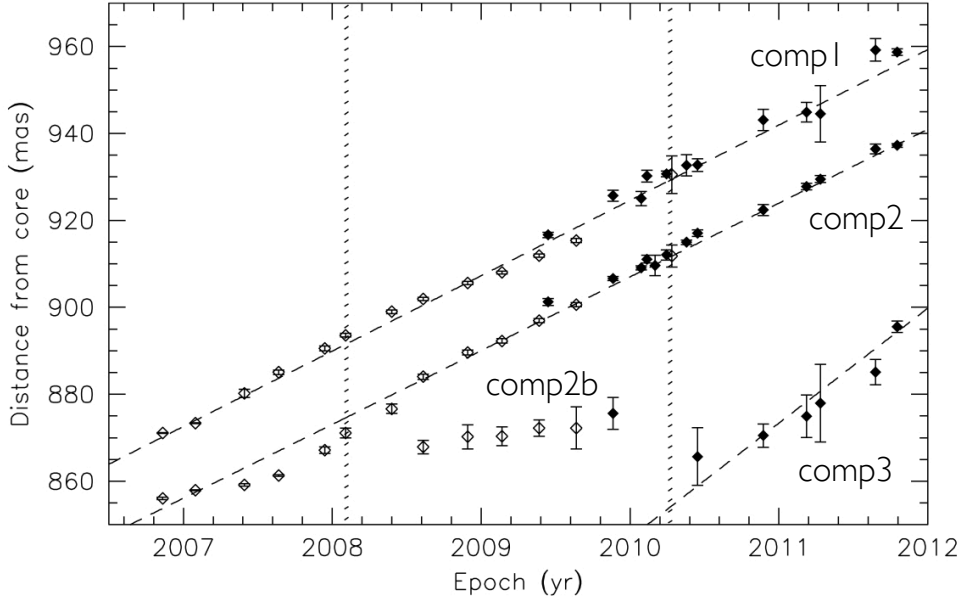
Figure 5.4: This plot represents the distance from the core of model-fit components within HST-1 as a function of time. Note the new component, *comp*3, appearing in late 2010 in a position similar of previous *comp 2b*. The two parallel linear fits matching the positions of *comp 1* and *comp 2* indicate that both components move regularly with the same velocity. From Giroletti et al. (2012).

and interacts with the second recollimation shock leading to a significant increase in pressure in that region, see Figure 5.6.

Synthetic synchrotron emission images are computed from the hydrodynamical simulation as input(see Gómez et al., 1995, 1997; Aloy et al., 2003, for details of the numerical model employed). We obtained a sequence of 15 total intensity images displayed in Figure 5.7. For the sake of clarity, we only show the portion of jet where the moving feature interacts with the recollimations shock. The interaction between both shocks (the stationary and the moving one) leads to a significant increase in the particle and magnetic field energy density and a new superluminal component appears in total intensity images, as can be seen in the third image from the top in Figure 2.11. The appearance of the new superluminal component is in agreement with our VLBI observations in Giroletti et al. (2012) where *comp 3* appears in a position similar to that of

previous *comp 2b* (see Figure 5.3).

It is important to note that, as shown in Figure 5.3 the quasi-stationary component associated with the recollimation shock (seen in the first five and last four images) is significantly fainter than the new superluminal component and its position shifts with the passage of the moving shock, as seen in previous numerical simulations (Gómez et al., 1997).
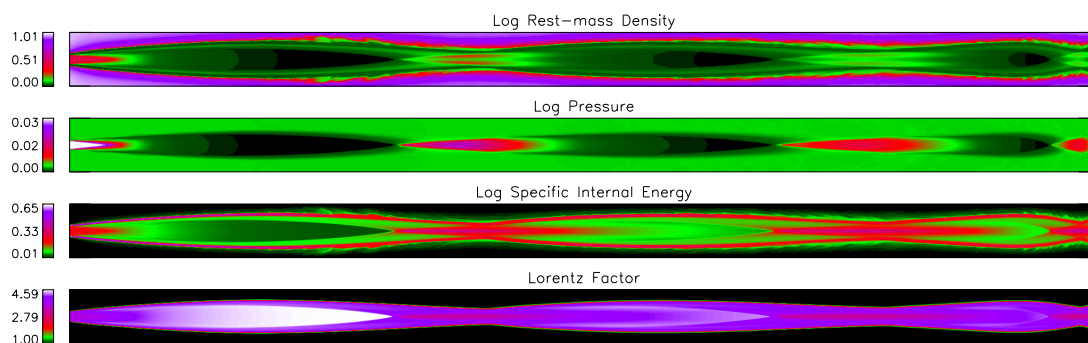

Figure 5.5: The stationary jet model in RHD simulation. Relativistic hydrodynamical simulation of a jet with an initial over-pressure 10 times larger than the external medium, leading to a set of recollimation shocks. Reproduced from Casadio et al. (2013).
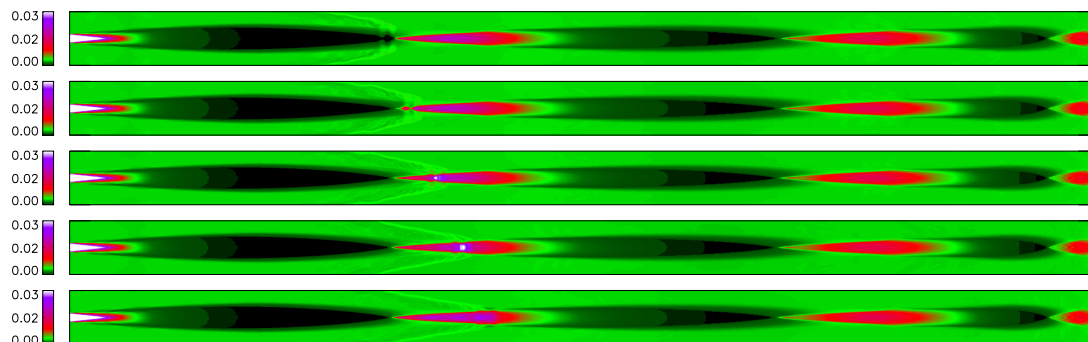

Figure 5.6: The jet model with the introduction of a moving shock wave. Five snap-shots in the time evolution (from top to bottom) of the jet particle pressure after the introduction of a perturbation, consisting in an increase by a factor of 8 in the jet inlet pressure. The perturbation interacts with the second recollimation shock leading to a significant increase in pressure. From Casadio et al. (2013).
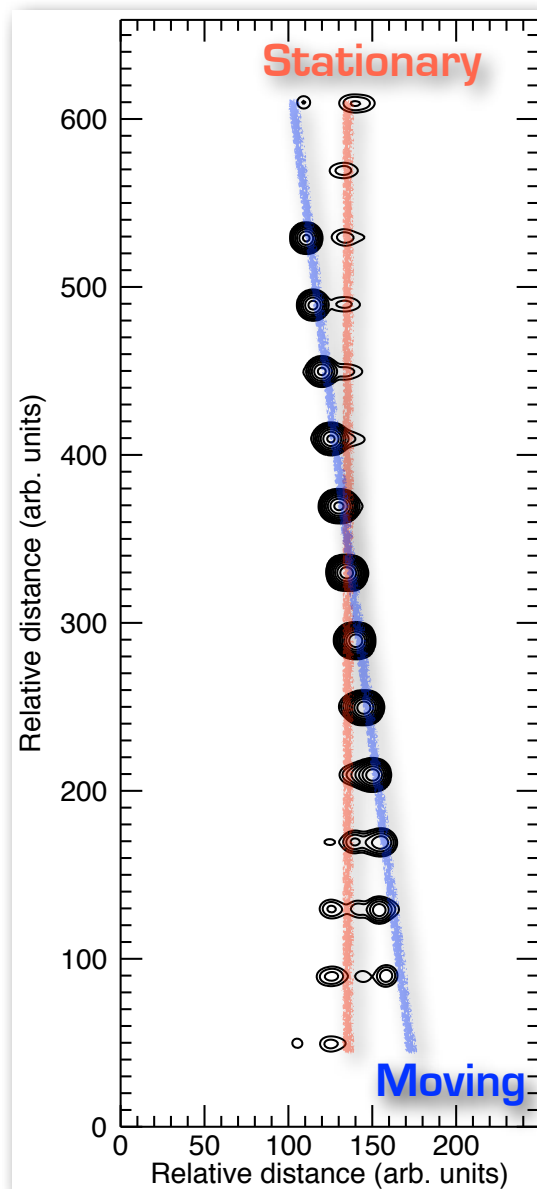
Figure 5.7: Simulated synchrotron emission maps. Fifteen snap-shots in the time evolution (from top to bottom) of the simulated synchrotron emission maps obtained using the relativistic hydrodynamical models shown in Figure 5.5 and 5.6 as input. Only the region corresponding to the interaction of the moving component with the recollimation shock is shown for clarity. Note that the passage of the perturbation through the recollimation shock (visible in the first five and last four epochs) leads to the appearance of a new superluminal component.
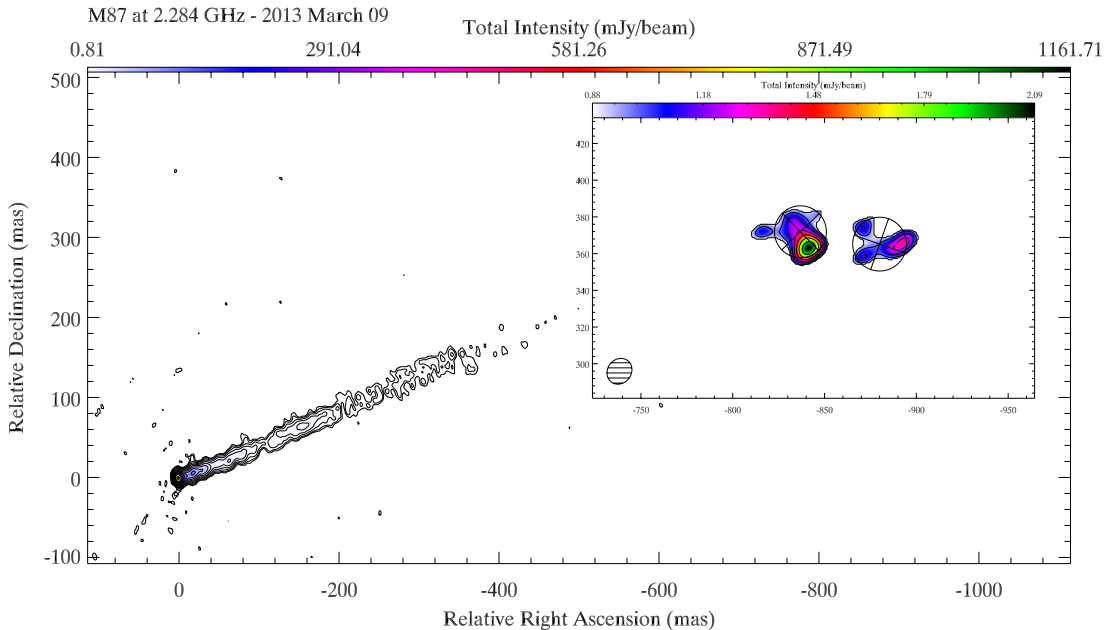
Figure 5.8: M 87 at 2.2 GHz (VLBA). VLBA observation at 2.2 GHz of M 87 in 9 March 2013. Total intensity is shown in contours and colors. Contours are plotted at 0.07, 0.13, 0.23, 0.42, 0.76, 1.38, 2.51, 4.56, 8.28, 15.03, 27.29, 49.56 and 90% of the peak brightness of 1.16 Jy/beam. The restoring beam is 8.8×4.61 mas at 15.8°. The panel inside the figure shows a zoom of the HST-1 region, obtained with a taper and resulting in a beam of 14.66×12.85 mas at -38.2°. Modelfits components in HST-1 are overlaid to the image and contours plot, whit contours plotted at 38.3, 44.2, 50.9, 58.7, 67.7, 78.1, 90% of the peak brightness of 2.1 mJy/beam.

To test this model we performed new polarimetric observations of the radio galaxy M 87 with the VLBA at 2.2 and 5 GHz (project BC210, PI Carolina Casadio) and with the JVLA at 15, 22 and 43 GHz in A-configuration (project 12B-153, PI Carolina Casadio). The VLBA at these two frequencies provides the necessary sensitivity to detect the faint emission associated with the recollimation shock in HST-1 and the necessary angular resolution to follow the kinematics and flux density evolution of subcomponents in that region. We performed three different VLBA observations, separated by 6 months each, 09 March 2013, 29 January 2014, and 14 July 2014. Here we present only the results corresponding to first epoch (09 March 2013); the analysis of the other epochs is in progress. Observations with the JVLA, providing lower resolution but a

larger field of view, were planned to study the fainter underlying emission and to probe the polarized emission structure along the jet of M 87, also in light of the results obtained in Agudo et al. (2012) on the radio galaxy 3C 120. They consist of 7 observing blocks, approximately three hours-long, observed between 2012 October 28 and 2012 December 22.
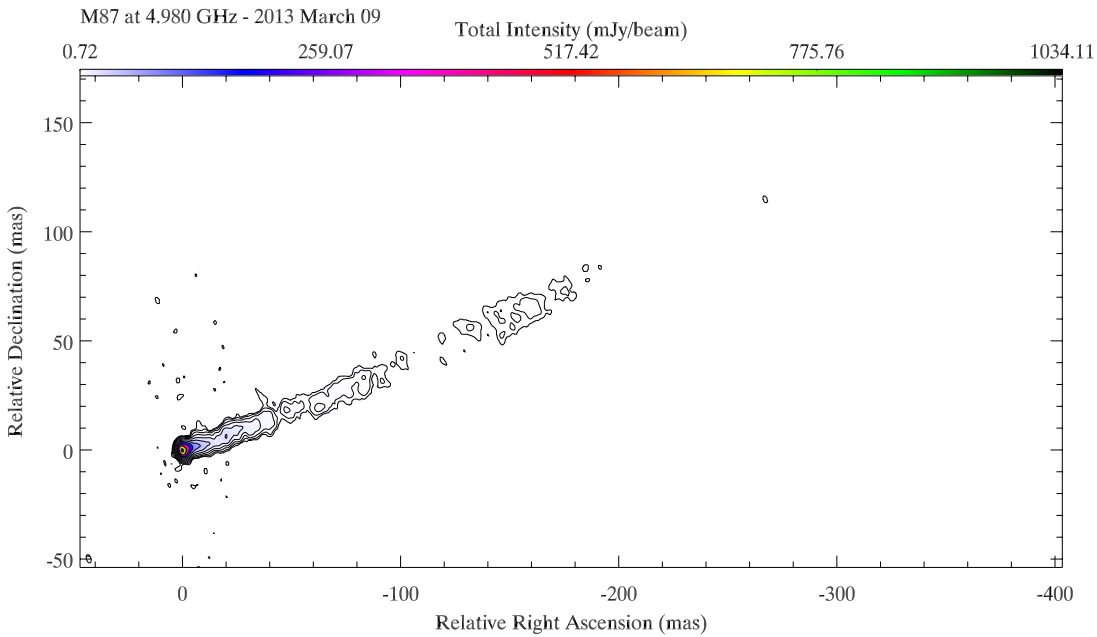

Figure 5.9: M 87 at 5 GHz (VLBA). VLBA observation at 5 GHz of M 87 in 9 March 2013. Total intensity is shown in contours and colors. Contours are plotted at 0.07, 0.14, 0.29, 0.6, 1.23, 2.51, 2.14, 10.51, 21.5, 43.99, 90% of the peak brightness of 1.034 Jy/beam. The restoring beam is 3.95×2.06 mas at 18.03°.

The calibration and imaging of the VLBA data was performed using a combination of `AIPS` and `Difmap` packages as described in § 3.2. During the hybrid imaging we applied a Gaussian taper to the visibility data at 2.2 GHz in order to detect the emission in the HST-1 region. The taper reduces the fringe visibility weight at long baselines, therefore increasing the sensitivity to extended structures but at lower angular resolution. Hence, the resulting beam in the HST-1 image at 2.2 GHz is bigger (14.66×12.85 mas) than the corresponding image of M 87 jet (8.8×4.61 mas) at the same frequency. The resolution in the 5 GHz image is even better (3.95×2.06 mas). It was not possible to detect emission in the HST-1 region at 5 GHz but, considering

the sensitivity achieved at both frequencies ($\sim$0.1-0.2 mJy/beam), we can estimate an upper limit for the peak flux density of HST-1 at 5 GHz of 0.5 mJy/beam ($\sim$ 5-σ).
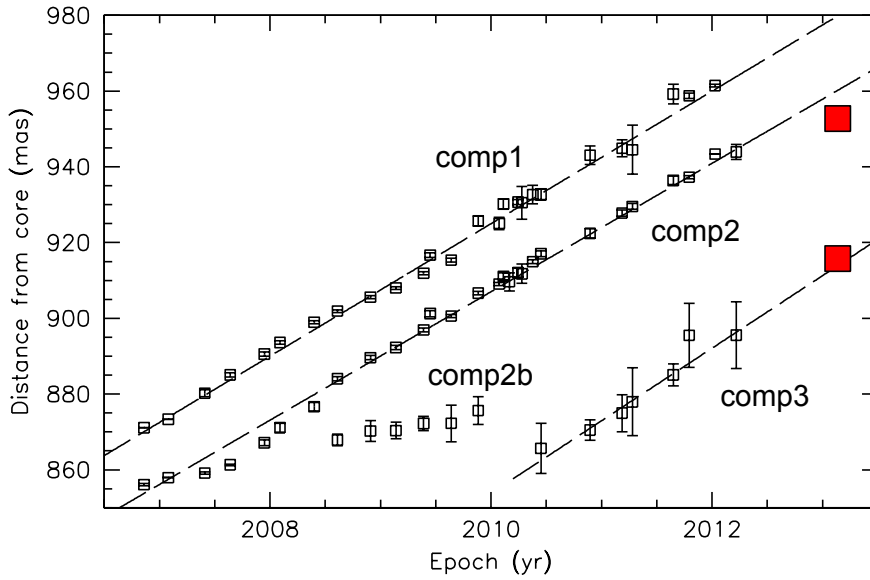

Figure 5.10: New subcomponents' positions in the HST-1 region. Distances of compact components in HST-1 as a function of time as registered in Giroletti et al. (2012). The two red squares represent the position of our two Gaussian model-fit components detected in HST-1 in the image at 2.2 GHz with the VLBA on 2013 March 9 (Figure 5.8).

The VLBA images at 2.2 and 5 GHz obtained on 09 March 2013 are shown in Figures 5.8 and 5.9, respectively. Figure 5.8 contains also an inset panel showing the HST-1 image obtained with the taper, together with circular components obtained fitting the visibility data. The HST-1 region at 2.2 GHz can be model fitted with two separated circular components, one located at $\sim$913 mas from the core and a second one at $\sim$953 mas. Comparing the positions of these two components with those detected in Giroletti et al. (2012) we find that they can be associated with *comp 3* and *comp 2*, respectively, as we observe in Figure 5.10. We obtained a peak flux density for HST-1 at 2.2 GHz of 2.1 mJy/beam, associated with *comp 3*, which is brighter than *comp 2* in this epoch.

If we compare the flux density values found with previous epochs (Giroletti et al., 2012) we find a significant decrease of HST-1 starting in 2011. This is also supported by
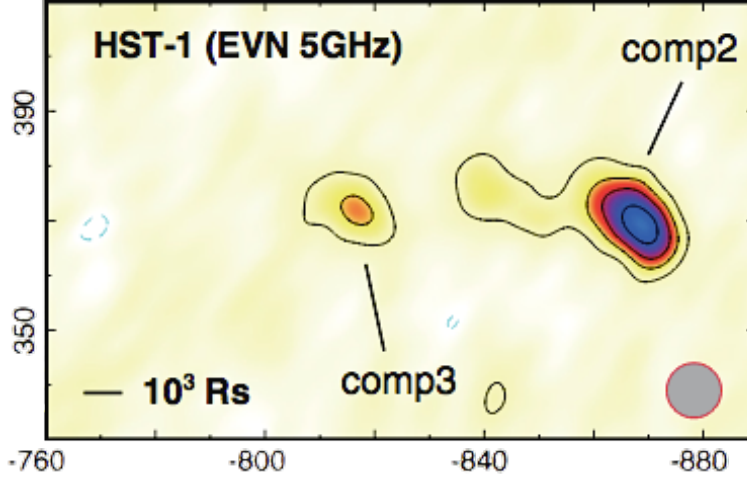
Figure 5.11: HST-1 at 5 GHz (EVN). EVN image of HST-1 at 5 GHz in 2012 March. Total intensity is shown in contours and colors. Contours are plotted at -1, 1, 2, 2.8, 4 times 3σ (0.24 mJy/beam). A 10.0 mas circular restoring beam is used. Reproduced from Hada et al. (2014).

the EVN image at 5 GHz of HST-1 in March 2012 (see Figure 5.11, Hada et al., 2014), where the peak flux density is <1 mJy/beam, despite the high activity at VHE displayed by M87 during that period. The main difference between March 2012 and March 2013 data is that in March 2012, *comp 2* is brighter than *comp 3*, while the opposite is found in March 2013. This, together with the lack of detection of *comp 1*, that appeared clearly in previous epochs (see Figure 5.3 and 5.4), suggests that subcomponents in the HST-1 region become weaker as they move downstream, probably because of adiabatic expansion.

The decrease in flux of HST-1 is also confirmed by our JVLA data. In Figure 5.12 we present the polarimetric JVLA image of M 87 at 15 GHz on 2012 November 25. In the image the core has a peak flux density of $\sim$2.9 Jy/beam and HST-1 a total flux of $\sim$9 mJy. The better sensitivity achieved by the new JVLA clearly stands up when we compare our image with an image obtained in 2006 with the old VLA at the same frequency in Figure 5.13. Comparison between flux density values obtained in 2012 and previous VLA archive data that we used to produce the images displayed in Figure 5.13 and 5.14, reveals a significant decrease in the flux density of HST-1 while the core remains stable or becomes even brighter with regard to previous epochs. In Figure 5.14 we report an image of HST-1 with the VLA in 2003 (left) and 2006 (right).
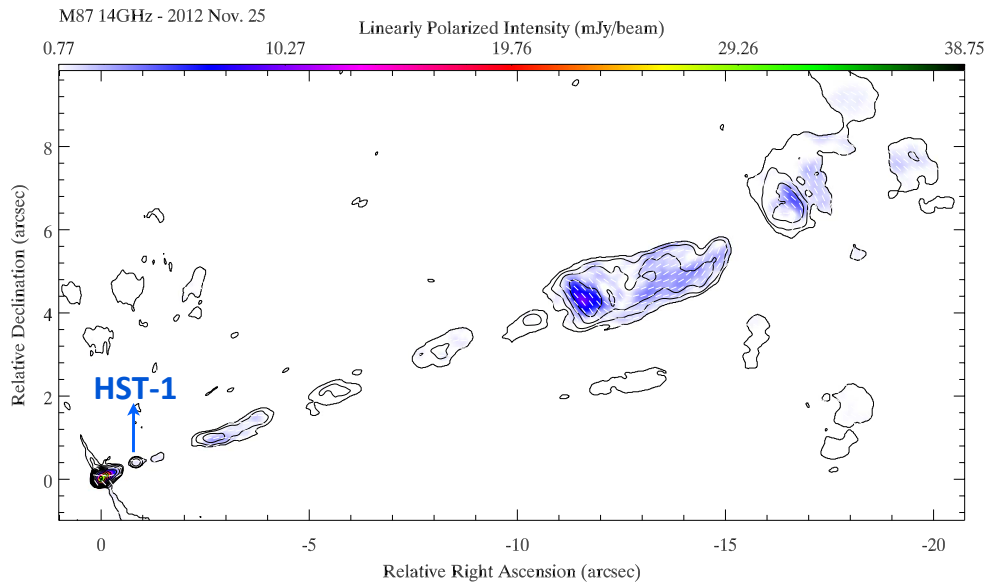
Figure 5.12: JVLA image at 15 GHz of M 87 in 2013 November 25. Total intensity is shown in contours and polarized flux in colors. White bars, of unit length, indicate the magnetic field direction (uncorrected for Faraday rotation). Contours are traced at 0.04, 0.09, 0.22, 0.52, 1.24, 2.91, 6.87, 16.19, 19.38, 17.90% of the peak brightness of 2.93 Jy/beam. The restoring beam is 0.17×0.165 arcseconds at -47°.
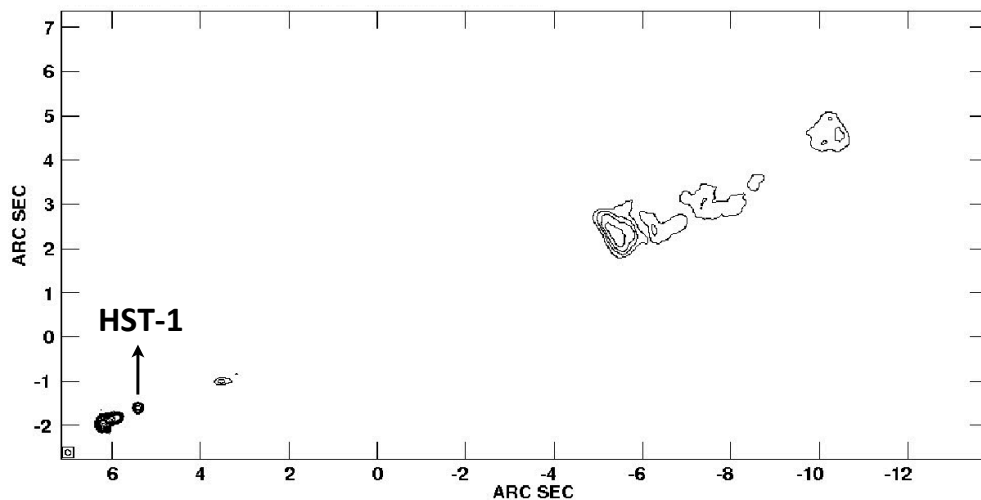

Figure 5.13: VLA image at 15 GHz of M 87 in 2006. Contours represent the total intensity and they are traced at -3, 3, 5, 7, 10, 15, 30, 50, 100, 300, 500, 1000, 1800 mJy/beam. The peak flux density is 1.9 Jy/beam.
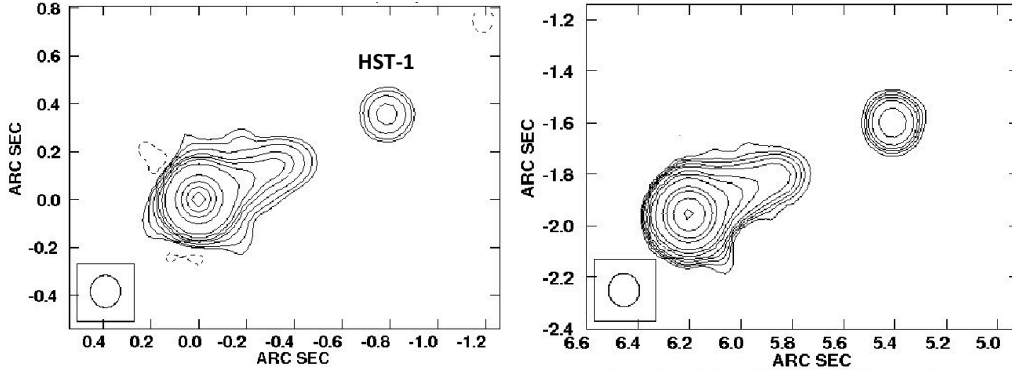
Figure 5.14: VLA observations at 15 GHz of M 87 in 2003 (left) and 2006 (right), reproduced using VLA archive data. Contours represent the total intensity and they are traced at -2, 3, 5, 10, 20, 30, 50, 100, 500, 1000, 1500, 2000 mJy/beam (left) and at -3, 3, 5, 7, 10, 15, 30, 50, 100, 300, 500, 1000, 1800 mJy/beam (right).

In those epochs the core has a peak flux density of 2.3 and 1.9 Jy/beam, respectively, hence fainter than our 2012 observation.

The HST-1 region was brighter in both previous epochs than in 2012, with a total flux of ~27 mJy in 2003 and ~52 mJy in 2006. In our JVLA image we also detect polarized emission up to ~20 arcseconds from the core, represented in colors in Figure 5.12. The peak of polarized flux is in the core of M 87, as expected in this source, but it is also interesting to note a region at ~12 arcseconds away with significant polarized flux. This emitting region at ~12 arcseconds, usually called knot A, has been interpreted by magnetohydrodynamic models as a relativistic shock launched from the HST-1 complex (Nakamura et al., 2010), but still not clear evidences about its nature and its relation with HST-1 have been observed so far.

We have also estimated the rotation measure (RM) due to Faraday rotation (see § 2.1.1.4) along the jet in M 87. For this purpose we analyzed archival JVLA data, corresponding to 8.4 GHz A-configuration observations, performed in June 2011 (program SB0514). We then used the 8, 15 and 22 GHz data to extract the information of the EVPA orientation along the jet at the three wavelengths. We finally obtained the rotation measure map shown in Figure 5.15. The inset panel in Figure 5.15 gives the rotation measure (RM=246±30 rad/m^2) for the region of knot A. Figure 5.15 shows the JVLA image at 8.4 GHz where EVPAs in knot A have been corrected by Faraday rotation.
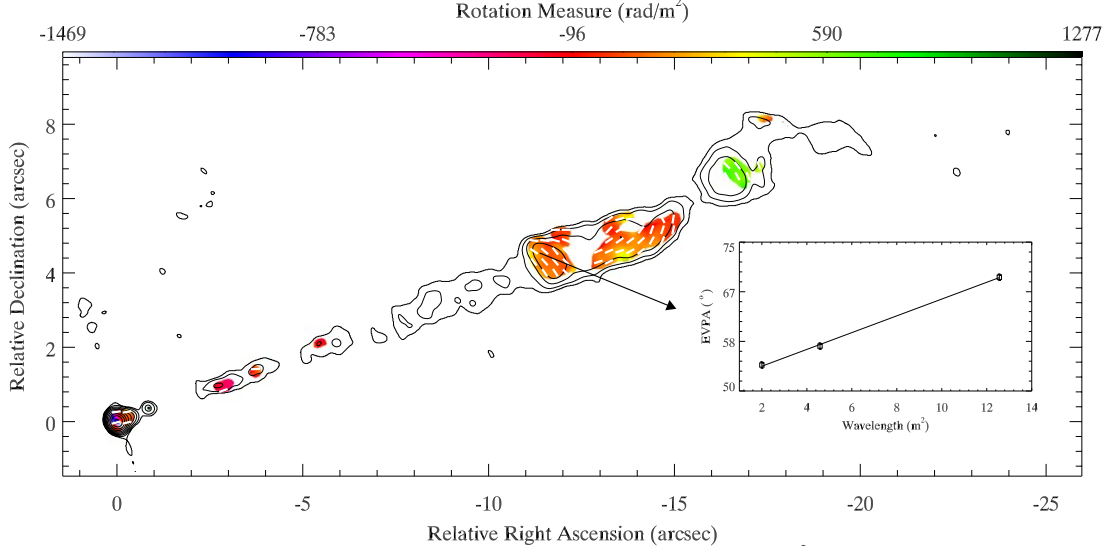
Figure 5.15: Rotation Measure map of M 87 jet. In contours we represent the JVLA image at 8.4 GHz in total intensity. The rotation measure map along the jet in M 87 is symbolized by the color scale. The white bars are the Faraday-corrected EVPAs. Inset panel shows the λ^2 fit to the EVPAs in the area of knot A, yielding RM=246±30 rad/m^2.

To conclude, our analysis of the flux evolution, morphology and velocity pattern of subcomponents in HST-1 region resembles what we observe in numerical simulations when a moving shock interacts with a stationary recollimation shock. This implies that HST-1 indeed may mark the location of a recollimation shock. The hypothesis of a recollimation shock is also supported by other previous studies, as discussed at the beginning of the chapter. Its location is coincident with the transition of the jet from a parabolic to a conical geometry, at $\sim 5 \times 10^5 R_s$ (Asada & Nakamura, 2012). This distance is similar to the separation between the central engine and the mm-VLBI core in several blazars and distant radio galaxies (see § 4.3). In some of these AGN (i.e., CTA 102, 3C 120, 3C 111) the core is interpreted as a recollimation shock to explain the high energy events associated with the ejection of new superluminal components from the core. Therefore, the jet section between the core and HST-1 in M87 may correspond to what we call the "core" in other sources located further away. This region, which is unresolved because of poorer linear resolution in further away sources,

may be imaged in M 87 because of its proximity (D$\sim$16.7 Mpc). In M 87 we have therefore the necessary linear resolution to distinguish between the mm-VLBI core and another possible recollimation shock at $\sim$5$\times$10^{5}R$_s$ (HST-1). This justifies to consider the core as responsible for some of the very high-energy events in M 87, and HST-1 in others. This supports the idea that a recollimation shock should be present in all AGN jets at 10^4-10^{5}R$_s$, since we observe the same behavior in radiogalaxies and blazars. It may happen that the mm-VLBI core is formed by many recollimation shocks, as indicated by higher resolution *RadioAstron* space VLBI observations of BL Lac (Gómez et al., 2016), 3mm VLBI observations of M 87 (Hada et al., 2016) and 7 mm VLBA observations of 3C454.3 (Jorstad et al., 2013).

5. Polarimetric studies of the radio galaxies 3C 120 and M 87: searching for recollimation shocks

6

Conclusions

This Thesis for the mention of Philosophiae Doctor (PhD) is focused on the study of relativistic jets in active galactic nuclei (AGN). These are produced by the mass accretion onto a super massive black hole (SMBH) lurking at the center of the host galaxy, and are well known for emitting profusely across the whole electromagnetic spectrum. They are also observed in other multiple astrophysical sites involving accretion onto compact objects, such as microquasars and GRBs. Despite decades of study, there are many aspects related to the physics of relativistic jets in AGN that still remain unclear. For instance, we do not know how jets are formed, accelerated, and collimated from the accretion disk around the SMBH. It is largely unknown what is the role played by the magnetic field in the jet dynamics, or in the actual jet formation. We do not know where the very high energy emission (γ-rays) is produced, and whether it is mainly due to synchrotron self-Compton, or inverse Compton scattering of ambient (external to the jet) photons. Thanks to the *Fermi* gamma-ray satellite, launched by NASA in 2008, we are extending our knowledge of the γ-ray activity in many AGN. We are also in the era of very high resolution mm-VLBI observations that give us the opportunity of studying deeper in the jet, to probe the regions where jets are formed. Multi-waveband

observations, combined with mm-VLBI observations, can therefore provide the information to determine how jets are formed and what are the sites and mechanisms for the production of γ-ray photons.

We performed two multi-wavelength studies, on the radio galaxy 3C 120 and the blazar CTA 102, during unprecedented γ-ray flares for both sources (Casadio et al., 2015a,b). The *Fermi* satellite registered in September-October 2012 an extraordinary bright γ-ray outburst in the blazar CTA102, and between December 2012 and October 2014 a prolonged γ-ray activity in the radio galaxy 3C120. In both studies the analysis of *Fermi* data has been compared with a series of 43 GHz VLBA images from the Boston University blazar monitoring program, with which our group collaborates. The images from this program provide the necessary spatial resolution to probe the parsec scale jet evolution during the high energy events. For the study of 3C 120 we also collected 15 GHz VLBA data from the MOJAVE program in order to extend the analysis of the radio jet to a wider observing period. In the case of CTA 102 our our observations covered the entire electromagnetic spectrum, from millimeter wavelengths, to infrared, optical, X and gamma-ray energies. Millimeter, near-infrared and optical data were collected as part of a large international collaboration in which many research groups, including our own, participate and in which I significantly contributed in the acquisition and analysis of the data.

From both multi-wavelength analyses we obtain that, despite representing very different classes of AGN, the radio galaxy 3C 120 and the blazar CTA 102 display very similar properties during γ-ray events. In particular we obtain that the γ-ray outbursts are associated with the passage of new superluminal components through the VLBI core. However, not all ejections produce detectable γ-ray flares and components responsible for the γ-ray emission are not necessary bright components. The key aspect to detect γ-ray emission seems to be the orientation of the emitting region. In fact, we find that components associated with the γ-ray flares move in a direction closer to our line of sight. This would lead to an increase in the Doppler factor, therefore enhancing the γ-ray emission above the flux detectable by *Fermi*. This new result is in agreement with the geometrical interpretation adopted to explain high energy flares observed in other studies in which I have participated (e.g. Raiteri et al., 2012, 2013; Carnerero et al., 2015). In the case of CTA 102 the hypothesis of a change in the jet orientation over time is also supported by the slow rotation over an extended period

($\sim$3 years) observed in the polarization vectors (EVPAs) at millimeter wavelengths. The analysis of the polarized emission at optical wavelengths shows instead intra-day variability and a clear clockwise rotation of the EVPAs during the γ-ray flare, which we associate with the path followed by the new superluminal component that moves along helical magnetic field lines. This is in agreement with theoretical models in which helical magnetic field are responsible for the jet formation, acceleration, and collimating (Blandford & Payne, 1982; Blandford & Znajek, 1977).

In both 3C 120 and CTA 102 the mm-VLBI core is located parsecs away from the black hole, at a distance of $\sim$10^4-10^5 Schwarzschild radii, in agreement also with findings for other AGNs (Marscher et al., 2008, 2010; Chatterjee et al., 2011). The location of the γ-ray dissipation zone close to the mm-VLBI core in both sources, at such distances from the black hole that is difficult to have contributions of photons from the disk or the broad line region and probably also from the molecular torus, lead us to suggest the synchrotron self Compton (SSC) mechanism for the production of γ-ray photons in both sources. Also the SED, in the case of CTA 102, is consistent with the SSC mechanism, and reveals also a different high energy spectrum for the bright γ-ray flare with respect to that of the "orphan flares".

Another consequence of locating the γ-ray emission in the mm-VLBI core, and far from the black hole, is that we need a mechanism to reaccelerate particles in situ, as for example happens in recollimation shocks. For this it is important to understand the nature of recollimation shocks and what could be the observational evidences associated with these shocks. For this purpose we have performed polarimetric studies of the jets in the radio galaxies 3C 120 (Agudo et al., 2012) and M 87 (Casadio et al., 2013); both aimed to understand the nature of the peculiar emitting regions C80 and HST-1, located hundreds of parsecs away from the core of the jet. With the improved sensitivity of our new polarimetric VLBA images of 3C 120, we analyzed in detail the observational properties of the emitting region at $\sim$80 mas from the core, whose detection was first reported in Roca-Sogorb et al. (2010). These authors suggest the possibility of a stationary shock at the location of C80 in order to explain the observed extreme properties, such as the unusually high brightness temperature. We discovered that C80 is the peak emission of a more extended structure whose upstream edge has an arc morphology (A80). The linearly polarized emission also follows this arc structure with polarization vectors distributed perpendicularly to the arc, as would be

expected in the case of a shock front, where the magnetic field component parallel to shock is compressed and amplified. This evidence, together with the high brightness temperature of C80 and the stationarity over time of C80/A80, while superluminal motions have been detected in the flow downstream C80/A80, supports the hypothesis of a recollimation shock. Moreover, the agreement between our findings and numerical simulations lead us to conclude that the emitting region C80 corresponds in fact to a recollimation shock located ∼190 pc from the core of the jet.

The situation observed in 3C 120 is very similar to what we find in the radio galaxy M 87 with its peculiar feature HST-1. In Giroletti et al. (2012) we observe that the extended emitting region named HST-1 is formed by superluminal subcomponents that seem to be released by the stationary upstream end of HST-1. This, and in the light of our findings for C80, lead us to suggest that HST-1 can also be associated with a recollimation shock. This implies that HST-1 may be the responsible for the high energy emission previously observed in M 87, although we rule out its implication in the TeV flare in March 2012, as we pointed out in Hada et al. (2014). In fact, between 2011 and 2013 HST-1 was found to be in a low flux state, confirmed also by our new VLBA and JVLA observations.

References

Abdo, A. A., Ackermann, M., Ajello, M., Allafort, A., Antolini, E., Atwood, W. B., Axelsson, M., Baldini, L., Ballet, J., Barbiellini, G., et al., 2010, ApJS, 188, 405 46

Abdo, A. A., Ackermann, M., Ajello, M., Atwood, W. B., Axelsson, M., Baldini, L., Ballet, J., Band, D. L., Barbiellini, G., Bastieri, D., et al., 2009, ApJS, 183, 46 46

Acciari, V. A., Aliu, E., Arlen, T., Bautista, M., Beilicke, M., Benbow, W., Bradbury, S. M., Buckley, J. H., Bugaev, V., Butt, Y., et al., 2009, Science, 325, 444 90, 94

Acero, F., Ackermann, M., Ajello, M., Albert, A., Atwood, W. B., Axelsson, M., Baldini, L., Ballet, J., Barbiellini, G., Bastieri, D., et al., 2015, ApJS, 218, 23 41, 46

Ackermann, M., Ajello, M., Allafort, A., Antolini, E., Atwood, W. B., Axelsson, M., Baldini, L., Ballet, J., Barbiellini, G., Bastieri, D., et al., 2011, ApJ, 743, 171 46

Ackermann, M., Ajello, M., Atwood, W. B., Baldini, L., Ballet, J., Barbiellini, G., Bastieri, D., Becerra Gonzalez, J., Bellazzini, R., Bissaldi, E., et al., 2015, ApJ, 810, 14 46

Agudo, I., Gómez, J. L., Casadio, C., Cawthorne, T. V., & Roca-Sogorb, M., 2012, ApJ, 752, 92 95, 96, 113, 123

Agudo, I., Gómez, J. L., Martí, J. M., Ibáñez, J.-M., Marscher, A. P., Alberdi, A., Aloy, M.-A., & Hardee, P. E., 2001, ApJ, 549, L183 107

Agudo, I., Jorstad, S. G., Marscher, A. P., Larionov, V. M., Gómez, J. L., Lähteenmäki, A., Gurwell, M., Smith, P. S., Wiesemeyer, H., Thum, C., et al., 2011a, ApJ, 726, L13 33

Agudo, I., Marscher, A. P., Jorstad, S. G., Larionov, V. M., Gómez, J. L., Lähteenmäki, A., Smith, P. S., Nilsson, K., Readhead, A. C. S., Aller, M. F., et al., 2011b, ApJ, 735, L10 90

Aleksić, J., Ansoldi, S., Antonelli, L. A., Antoranz, P., Babic, A., Bangale, P., Barres de Almeida, U., Barrio, J. A., Becerra González, J., Bednarek, W., et al., 2014, A&A, 569, A46 88

Aloy, M.-Á., Martí, J.-M., Gómez, J.-L., Agudo, I., Müller, E., & Ibáñez, J.-M., 2003, ApJ, 585, L109 109

REFERENCES

Antonucci, R., 1993, ARA&A, 31, 473 7

Asada, K., & Nakamura, M., 2012, ApJ, 745, L28 95, 118

Blandford, R. D., & Königl, A., 1979, ApJ, 232, 34 20, 23, 34

Blandford, R. D., & Levinson, A., 1995, ApJ, 441, 79 42

Blandford, R. D., & Payne, D. G., 1982, MNRAS, 199, 883 2, 34, 123

Blandford, R. D., & Rees, M. J., 1978, Phys. Scr, 17, 265 34

Blandford, R. D., & Znajek, R. L., 1977, MNRAS, 179, 433 2, 34, 123

Bonnoli, G., Tavecchio, F., Ghisellini, G., & Sbarrato, T., 2015, MNRAS, 451, 611 43

Bromberg, O., & Levinson, A., 2009, ApJ, 699, 1274 95

Carnerero, M. I., Raiteri, C. M., Villata, M., Acosta-Pulido, J. A., D'Ammando, F., Smith, P. S., Larionov, V. M., Agudo, I., Arévalo, M. J., Arkharov, A. A., et al., 2015, MNRAS, 450, 2677 88, 89, 122

Casadio, C., Gómez, J. L., Giroletti, M., Giovannini, G., Hada, K., Fromm, C., Perucho, M., & Martí, J.-M., 2013, in *European Physical Journal Web of Conferences*, volume 61 of *European Physical Journal Web of Conferences*, p. 6004 110, 123

Casadio, C., Gómez, J. L., Grandi, P., Jorstad, S. G., Marscher, A. P., Lister, M. L., Kovalev, Y. Y., Savolainen, T., & Pushkarev, A. B., 2015a, ApJ, 808, 162 iv, viii, xii, 33, 45, 56, 122

Casadio, C., Gómez, J. L., Jorstad, S. G., Marscher, A. P., Larionov, V. M., Smith, P. S., Gurwell, M. A., Lähteenmäki, A., Agudo, I., Molina, S. N., et al., 2015b, ApJ, 813, 51 iv, viii, xii, 45, 56, 122

Cawthorne, T. V., 2006, MNRAS, 367, 851 38, 96

Cawthorne, T. V., & Cobb, W. K., 1990, ApJ, 350, 536 38, 96

Chatterjee, R., Marscher, A. P., Jorstad, S. G., Markowitz, A., Rivers, E., Rothschild, R. E., McHardy, I. M., Aller, M. F., Aller, H. D., Lähteenmäki, A., et al., 2011, ApJ, 734, 43 33, 90, 123

Cheung, C. C., Harris, D. E., & Stawarz, Ł., 2007, ApJ, 663, L65 33, 94, 95

Cohen, M. H., Meier, D. L., Arshakian, T. G., Homan, D. C., Hovatta, T., Kovalev, Y. Y., Lister, M. L., Pushkarev, A. B., Richards, J. L., & Savolainen, T., 2014, ApJ, 787, 151 95

Dermer, C. D., Schlickeiser, R., & Mastichiadis, A., 1992, A&A, 256, L27 27

Donato, D., Ghisellini, G., Tagliaferri, G., & Fossati, G., 2001, A&A, 375, 739 28

Fanaroff, B. L., & Riley, J. M., 1974, MNRAS, 167, 31P 3

Fossati, G., Maraschi, L., Celotti, A., Comastri, A., & Ghisellini, G., 1998, MNRAS, 299, 433
  28

Fromm, C. M., Perucho, M., Ros, E., Savolainen, T., & Zensus, J. A., 2015, A&A, 576, A43 90

Gabuzda, D. C., Knuettel, S., & Reardon, B., 2015, MNRAS, 450, 2441 24

Ghisellini, G. (ed.), 2013, *Radiative Processes in High Energy Astrophysics*, volume 873 of
  Lecture Notes in Physics, Berlin Springer Verlag 11, 14, 26

Ghisellini, G., Celotti, A., Fossati, G., Maraschi, L., & Comastri, A., 1998, MNRAS, 301, 451
  28

Ghisellini, G., Tavecchio, F., Foschini, L., Ghirlanda, G., Maraschi, L., & Celotti, A., 2010,
  MNRAS, 402, 497 43

Giroletti, M., Hada, K., Giovannini, G., Casadio, C., Beilicke, M., Cesarini, A., Cheung, C. C.,
  Doi, A., Krawczynski, H., Kino, M., et al., 2012, A&A, 538, L10 v, viii, xii, 33, 107, 108,
  109, 114, 124

Gómez, J. L., Alberdi, A., & Marcaide, J. M., 1993, A&A, 274, 55 36

Gómez, J. L., Alberdi, A., Marcaide, J. M., Marscher, A. P., & Travis, J. P., 1994, A&A, 292,
  33 39

Gómez, J. L., Guirado, J. C., Agudo, I., Marscher, A. P., Alberdi, A., Marcaide, J. M., &
  Gabuzda, D. C., 2001a, MNRAS, 328, 873 33

Gómez, J. L., Lobanov, A. P., Bruni, G., Kovalev, Y. Y., Marscher, A. P., Jorstad, S. G.,
  Mizuno, Y., Bach, U., Sokolovsky, K. V., Anderson, J. M., et al., 2016, ApJ, 817, 96 119

Gómez, J. L., Marscher, A. P., Alberdi, A., Jorstad, S. G., & Agudo, I., 2001b, ApJ, 561, L161
  33, 96, 107

—, 2002, VLBA Scientific Memorandum No. 30 55

Gómez, J. L., Marscher, A. P., Alberdi, A., Jorstad, S. G., & García-Miró, C., 2000, Science,
  289, 2317 29, 96

Gómez, J. L., Marscher, A. P., Alberdi, A., Martí, J. M., & Ibáñez, 1998, ApJ, 499, 221 33

Gómez, J. L., Marscher, A. P., Jorstad, S. G., Agudo, I., & Roca-Sogorb, M., 2008, ApJ, 681,
  L69 24, 96

Gómez, J. L., Martí, J. M., Marscher, A. P., Ibáñez, J. M., & Alberdi, A., 1997, ApJ, 482, L33
  38, 95, 109, 110

REFERENCES

Gómez, J. L., Marti, J. M. A., Marscher, A. P., Ibanez, J. M. A., & Marcaide, J. M., 1995, ApJ, 449, L19 38, 95, 109

Gómez, J. L., Roca-Sogorb, M., Agudo, I., Marscher, A. P., & Jorstad, S. G., 2011, ApJ, 733, 11 96

Gracia, J., Vlahakis, N., Agudo, I., Tsinganos, K., & Bogovalov, S. V., 2009, ApJ, 695, 503 95

Grandi, P., Torresi, E., & Stanghellini, C., 2012, ApJ, 751, L3 90

Hada, K., Doi, A., Kino, M., Nagai, H., Hagiwara, Y., & Kawaguchi, N., 2011, Nature, 477, 185 38, 90

Hada, K., Giroletti, M., Kino, M., Giovannini, G., D'Ammando, F., Cheung, C. C., Beilicke, M., Nagai, H., Doi, A., Akiyama, K., et al., 2014, ApJ, 788, 165 v, ix, xiii, 90, 94, 115, 124

Hada, K., Kino, M., Doi, A., Nagai, H., Honma, M., Akiyama, K., Tazaki, F., Lico, R., Giroletti, M., Giovannini, G., et al., 2016, ApJ, 817, 131 119

Harris, D. E., Cheung, C. C., Biretta, J. A., Sparks, W. B., Junor, W., Perlman, E. S., & Wilson, A. S., 2006, ApJ, 640, 211 93

Högbom, J. A., 1974, A&AS, 15, 417 53

Homan, D. C., Attridge, J. M., & Wardle, J. F. C., 2001, ApJ, 556, 113 22

Homan, D. C., & Wardle, J. F. C., 1999, AJ, 118, 1942 22

Hughes, P. A., 1991, Journal of the British Astronomical Association, 101, 128 16, 21

Hughes, P. A., Aller, H. D., & Aller, M. F., 1985, ApJ, 298, 301 38, 39

—, 1989, ApJ, 341, 54 36

Jorstad, S. G., Marscher, A. P., Lister, M. L., Stirling, A. M., Cawthorne, T. V., Gear, W. K., Gómez, J. L., Stevens, J. A., Smith, P. S., Forster, J. R., et al., 2005, AJ, 130, 1418 29, 33, 36, 44, 58, 107

Jorstad, S. G., Marscher, A. P., Mattox, J. R., Aller, M. F., Aller, H. D., Wehrle, A. E., & Bloom, S. D., 2001, ApJ, 556, 738 42, 56, 58

Jorstad, S. G., Marscher, A. P., Smith, P. S., Larionov, V. M., Agudo, I., Gurwell, M., Wehrle, A. E., Lähteenmäki, A., Nikolashvili, M. G., Schmidt, G. D., et al., 2013, ApJ, 773, 147 57, 88, 89, 119

Jorstad, S. G., Marscher, A. P., Stevens, J. A., Smith, P. S., Forster, J. R., Gear, W. K., Cawthorne, T. V., Lister, M. L., Stirling, A. M., Gómez, J. L., et al., 2007, AJ, 134, 799 25, 39

Kellermann, K. I., 2013, Bulletin of the Astronomical Society of India, 41, 1 4

Kellermann, K. I., Sramek, R., Schmidt, M., Shaffer, D. B., & Green, R., 1989, AJ, 98, 1195 2

Konigl, A., 1981, ApJ, 243, 700 38

Leppanen, K. J., Zensus, J. A., & Diamond, P. J., 1995, AJ, 110, 2479 50

Lico, R., Giroletti, M., Orienti, M., Gómez, J. L., Casadio, C., D'Ammando, F., Blasi, M. G., Cotton, W., Edwards, P. G., Fuhrmann, L., et al., 2014, A&A, 571, A54 88

Lister, M. L., Aller, M., Aller, H., Hovatta, T., Kellermann, K. I., Kovalev, Y. Y., Meyer, E. T., Pushkarev, A. B., Ros, E., MOJAVE Collaboration, et al., 2011, ApJ, 742, 27 57

Lister, M. L., Aller, M. F., Aller, H. D., Homan, D. C., Kellermann, K. I., Kovalev, Y. Y., Pushkarev, A. B., Richards, J. L., Ros, E., & Savolainen, T., 2013, AJ, 146, 120 29

Lister, M. L., Cohen, M. H., Homan, D. C., Kadler, M., Kellermann, K. I., Kovalev, Y. Y., Ros, E., Savolainen, T., & Zensus, J. A., 2009, AJ, 138, 1874 29, 57

Lobanov, A. P., 1998, A&A, 330, 79 38

Lyutikov, M., Pariev, V. I., & Gabuzda, D. C., 2005, MNRAS, 360, 869 23

Marscher, A. P., 2005, Mem. Soc. Astron. Italiana, 76, 13 42

—, 2009, The Jet Paradigm - From Microquasars to Quasars, Lect. Notes Phys., 794, 175 36

—, 2014, ApJ, 780, 87 43

Marscher, A. P., & Gear, W. K., 1985, ApJ, 298, 114 38, 39

Marscher, A. P., Jorstad, S. G., Agudo, I., MacDonald, N. R., & Scott, T. L., 2012, Proceedings of Fermi & Jansky: Our Evolving Understanding of AGN - eConf C1111101 58

Marscher, A. P., Jorstad, S. G., Aller, M. F., McHardy, I., Balonek, T. J., Teräsranta, H., & Tosti, G., 2004, in *X-ray Timing 2003: Rossi and Beyond*, edited by P. Kaaret, F. K. Lamb, & J. H. Swank, volume 714 of *American Institute of Physics Conference Series*, pp. 167–173 58

Marscher, A. P., Jorstad, S. G., D'Arcangelo, F. D., Smith, P. S., Williams, G. G., Larionov, V. M., Oh, H., Olmstead, A. R., Aller, M. F., Aller, H. D., et al., 2008, Nature, 452, 966 33, 89, 90, 123

Marscher, A. P., Jorstad, S. G., Gómez, J. L., Aller, M. F., Teräsranta, H., Lister, M. L., & Stirling, A. M., 2002, Nature, 417, 625 90, 96

REFERENCES

Marscher, A. P., Jorstad, S. G., Larionov, V. M., Aller, M. F., Aller, H. D., Lähteenmäki, A., Agudo, I., Smith, P. S., Gurwell, M., Hagen-Thorn, V. A., et al., 2010, ApJ, 710, L126 27, 90, 123

Marti, J. M. A., Muller, E., Font, J. A., & Ibanez, J. M., 1995, ApJ, 448, L105 38

McKinney, J. C., & Blandford, R. D., 2009, MNRAS, 394, L126 35

Mittal, R., Porcas, R., Wucknitz, O., Biggs, A., & Browne, I., 2006, A&A, 447, 515 38

Morozova, D. A., Larionov, V. M., Troitsky, I. S., Jorstad, S. G., Marscher, A. P., Gómez, J. L., Blinov, D. A., Efimova, N. V., Hagen-Thorn, V. A., Hagen-Thorn, E. I., et al., 2014, AJ, 148, 42 88, 89

Nakamura, M., Garofalo, D., & Meier, D. L., 2010, ApJ, 721, 1783 117

Nalewajko, K., 2012, MNRAS, 420, L48 95

Pacholczyk, A. G., 1970, *Radio astrophysics. Nonthermal processes in galactic and extragalactic sources* 11, 16, 17, 18, 19, 21

Poutanen, J., & Stern, B., 2010, ApJ, 717, L118 58

Pushkarev, A., Lister, M., Kovalev, Y., & Savolainen, T., 2014, in *Proceedings of the 12th European VLBI Network Symposium and Users Meeting (EVN 2014). 7-10 October 2014. Cagliari, Italy.*, p. 104 57

Raiteri, C. M., Villata, M., D'Ammando, F., Larionov, V. M., Gurwell, M. A., Mirzaqulov, D. O., Smith, P. S., Acosta-Pulido, J. A., Agudo, I., Arévalo, M. J., et al., 2013, MNRAS, 436, 1530 88, 122

Raiteri, C. M., Villata, M., Smith, P. S., Larionov, V. M., Acosta-Pulido, J. A., Aller, M. F., D'Ammando, F., Gurwell, M. A., Jorstad, S. G., Joshi, M., et al., 2012, A&A, 545, A48 88, 122

Ramakrishnan, V., León-Tavares, J., Rastorgueva-Foi, E. A., Wiik, K., Jorstad, S. G., Marscher, A. P., Tornikoski, M., Agudo, I., Lähteenmäki, A., Valtaoja, E., et al., 2014, MNRAS, 445, 1636 33, 88

Readhead, A. C. S., Pearson, T. J., Cohen, M. H., Ewing, M. S., & Moffet, A. T., 1979, ApJ, 231, 299 34

Roca-Sogorb, M., Gómez, J. L., Agudo, I., Marscher, A. P., & Jorstad, S. G., 2010, ApJ, 712, L160 95, 96, 123

Rybicki, G. B., & Lightman, A. P., 1979, *Radiative processes in astrophysics* (New York, Wiley-Interscience) 11, 12, 26, 27

Schmidt, M., 1970, ApJ, 162, 371 6

Schwab, F. R., & Cotton, W. D., 1983, AJ, 88, 688 53

Sikora, M., Begelman, M. C., & Rees, M. J., 1994, ApJ, 421, 153 27

Sikora, M., Stawarz, Ł., Moderski, R., Nalewajko, K., & Madejski, G. M., 2009, ApJ, 704, 38 43

Sokolov, A., Marscher, A. P., & McHardy, I. M., 2004, ApJ, 613, 725 58

Stawarz, Ł., Aharonian, F., Kataoka, J., Ostrowski, M., Siemiginowska, A., & Sikora, M., 2006, MNRAS, 370, 981 94

Tavecchio, F., Becerra-Gonzalez, J., Ghisellini, G., Stamerra, A., Bonnoli, G., Foschini, L., & Maraschi, L., 2011, A&A, 534, A86 27, 43

Tavecchio, F., Ghisellini, G., Bonnoli, G., & Ghirlanda, G., 2010, MNRAS, 405, L94 43

Urry, C. M., & Padovani, P., 1995, PASP, 107, 803 7

Valtaoja, E., & Teraesranta, H., 1996, A&AS, 120, C491 56

Valtaoja, E., & Terasranta, H., 1995, A&A, 297, L13 56

Van der Wolk, G., Barthel, P. D., Peletier, R. F., & Pel, J. W., 2010, A&A, 511, A64 4

Wagner, S. J., & Witzel, A., 1995, ARA&A, 33, 163 29

Walker, R. C., Benson, J. M., Unwin, S. C., Lystrup, M. B., Hunter, T. R., Pilbratt, G., & Hardee, P. E., 2001, ApJ, 556, 756 96

Wardle, J. F. C., 2013, in *European Physical Journal Web of Conferences*, volume 61 of *European Physical Journal Web of Conferences*, p. 6001 24

Whitney, A. R., Shapiro, I. I., Rogers, A. E. E., Robertson, D. S., Knight, C. A., Clark, T. A., Goldstein, R. M., Marandino, G. E., & Vandenberg, N. R., 1971, Science, 173, 225 29

Williamson, K. E., Jorstad, S. G., Marscher, A. P., Larionov, V. M., Smith, P. S., Agudo, I., Arkharov, A. A., Blinov, D. A., Casadio, C., Efimova, N. V., et al., 2014, ApJ, 789, 135 57

Zwicky, F., 1963, AJ, 68, 301 6

—, 1965, ApJ, 142, 1293 5